



A Theoretical Analysis of Super-Earths and Sub-Neptunes

Author:

Darius Modirrousta-Galian

Supervisor:

Prof. Giuseppina Micela

DOCTOR OF PHILOSOPHY IN PHYSICS

University of Palermo (UNIPA)

The National Institute for Astrophysics (INAF)

*A thesis submitted in fulfillment of the requirements for the degree of Doctor
of Philosophy in Physics.*

Declaration of Authorship

I, Darius Modirrousta-Galian, declare that this thesis titled, "Theoretical Exoplanetology" and the work presented in it are my own. I confirm that where information has been derived from other sources it has been indicated in the thesis.

Signed:

Date:

In part III of Jonathan Swift's *Gulliver's Travels*, the main character visits the city of Balnibarbi after the flying island of Laputa. Here, he comes across "*a most ingenious doctor*" who had "*very usefully employed his studies, in finding out effectual remedies for all diseases.*" This doctor had a rather unorthodox opinion on fixing the local political system; he suggested cutting the politicians' brains in half and then mixing them amongst each other to reconcile their conflicting opinions. Without realizing it, the author Jonathan Swift had metaphorically described how scientists collaborate and make discoveries. When we lack knowledge on a specific subject, we should 'discard' the incorrect part of our brain and replace it with another researcher's who knows better. Throughout my thesis, I have tried to follow the advice of this ingenious doctor in the hope that I could attain "*moderation, as well as regularity of thinking.*"

To JONATHAN SWIFT, a man I admire most profoundly.

Acknowledgements

I want to express my deepest gratitude to my supervisor Professor Giuseppina Micela for always supporting me and encouraging me to do my best. I had some of the most wonderful experiences that range from observing at the telescopes in La Palma, España, to presenting at Ariel conferences to some of the brightest exoplanetary scientists of our time. I am also grateful to Dr. Daniele Locci for teaching me how to model X-ray and ultraviolet induced photoevaporation and Dr. Jesus Maldonado for showing me how to operate telescopes. I must also mention Professor Giovanna Tinetti for introducing me to the field of Exoplanetology for which I am much indebted. Additionally, I am most thankful to Professor David J. Stevenson for welcoming me to attend his lectures at the California Institute of Technology. This experience was eye-opening because I learned theoretical planetology, focusing on the physics of planetary interiors and their evolutions. I also appreciate the constructive comments made by the anonymous referees. Special thanks should also be given to the Department of Fisica e Chimica at the Università Degli Studi Di Palermo and INAF - Osservatorio astronomico di Palermo for providing me all the resources I required for my research. Finally, I would like to thank my family and friends for supporting me entirely during the preparation for my Doctor of Philosophy in Physics.

Abstract

In this thesis, a theoretical analysis of super-Earths and sub-Neptunes is presented. Knowing how to interpret the available data of extra-solar worlds is particularly important as, within the next few years, several new and powerful astronomical instruments will become available such as Ariel¹ and JWST². A careful analysis of this data makes it possible to infer how planetary systems form, evolve, and behave independently or interact with other objects like stars. Accordingly, we will explore exoplanet population trends, individual exoplanets, and several theoretical concepts to see how they compare with observational data. We focus on three main topics: (1) the physics of X-ray and ultraviolet induced photoevaporation, (2) how to constrain the interior structure of airless magma ocean super-Earths, and (3) how to constrain the interior structure of super-Earths with hydrogen-rich envelopes.

Keywords – Exoplanets, Super-Earths, Sub-Neptunes

¹Atmospheric Remote-sensing Infrared Exoplanet Large-survey

²James Webb Space Telescope

Contents

1	Introduction	1
1.1	First Discoveries	1
1.2	Inferences on Exoplanet Interiors	3
1.3	Understanding Atmospheric Spectroscopy	4
1.4	Exoplanet Trends and Explanations	8
1.4.1	Core-powered Atmospheric Mass Loss	9
1.4.2	Differing Geological Compositions	11
1.4.3	Stellar X-ray and Ultraviolet (XUV) Irradiation	13
1.5	Scientific Impact and Layout of the Thesis	16
2	XUV-induced Evaporation	18
2.1	The Physics of XUV-induced Evaporation	18
2.1.1	First Approach: The Energy-Limited Equation	18
2.1.2	Second Approach: Strong Atmospheric Evaporation	20
2.1.3	Summary of the Physics of Mass-Loss	22
2.2	Exoplanet Population Evolution Model	23
2.3	Why Remnant Cores Matter	30
2.4	The Curious Case of 55 Cancri e	32
2.5	GJ 357 b: A Super-Earth Orbiting an Extremely Inactive Host Star	35
2.6	Future Works On Photoevaporation	39
3	Constraining Airless Super-Earths	48
3.1	Compositional Degeneracies	48
3.2	Exploring Super-Earth Surfaces	50
3.2.1	Defining Terms	51
3.2.2	Explaining the Problem	51
3.2.3	Modelling Exotic Reflective Magmas	53
3.2.4	The Surface Wave Density	59
3.2.5	The Waveheight	61
3.2.6	The Albedo Simulator	63
3.2.7	Summary	69
3.2.8	Future Work	69
4	Constraining Super-Earths with Envelopes	71
4.0.1	Two Ultra-Hot Jupiters	71
4.0.2	Three Hot Jupiters	73
4.0.3	Two Hot Sub-Neptunes	74
4.0.4	One Warm Super-Earth	74
4.1	Opacities and the RAPOC Code	75
4.1.1	Comparison With Values in the Literature	78
4.1.2	Limitations with Rosseland and Planck Mean Opacities	83
4.1.3	Summary and Conclusion	83
4.2	Exploring Super-Earth Interiors	84
4.2.1	How Core Erosion Works	87
4.2.2	Modeling Core Erosion	90

5	A Note on Astrobiology	95
5.1	Motivation	95
5.2	Of Aliens and Exoplanets: Why the search for life, probably, requires the search for water	96
5.2.1	Cosmochemical level	98
5.2.2	Planetary level	99
5.2.3	Micropalaeontological level	101
5.2.4	Earth is the average planet	101
5.2.5	Physicochemical level	103
5.2.6	Conclusion	106
6	Future Work	107
7	Summary and Conclusion	109
	References	111
	Appendix	132
A	Equations	132
A.1	Why Remnant Cores Matter – Calculation	132
A.1.1	Simple Radiative Model (after; Stevenson, 1982a)	132
A.1.2	Radius Derivation (after; Stevenson, 1982b)	134
A.1.3	Well-Mixed Model (after; Stevenson, 1982b)	135
A.1.4	Cored Model	136
A.2	Derivation of Compressed Cores	138
A.3	Derivation of the Rayleigh Number	139
A.4	Classical vs Ultimate Theory of Rayleigh-Bénard Convection	141
A.4.1	Classical Derivation	141
A.4.2	Ultimate Derivation	143

List of Figures

- 1.1 *Left:* one of the first distributions of exoplanet radii. It became evident, even when there were strong biases against smaller exoplanets, that sub-Neptunian bodies are abundant (Fig. 4 from [Batalha et al., 2013](#)). "B11" and "New" indicate the old and new datasets at the time of writing. *Right:* with more exoplanets discovered, the distribution of exoplanet sizes got further refined (Fig. 4 from [Burke et al., 2014](#)). The grey color indicates the previously known exoplanets, whereas the newer Kepler candidates are represented by red. 3
- 1.2 The bimodal distribution in exoplanet radii for orbital periods less than 100 days (Fig. 7 from [Fulton et al., 2017](#)). 'typical uncert.' refers to the average uncertainty in the radius. The light grey line for planets with $R < 1.14 R_{\oplus}$ indicates the region suffering from a lack of data so is more prone to biases. 4
- 1.3 The mass and radius models from [Zeng et al. \(2016\)](#) and [Zeng and Sasselov \(2013\)](#) plotted with their respective distributions ([Fulton et al., 2017](#)). Diagram from [Zeng et al. \(2019\)](#). 5
- 1.4 Emission and transmission spectroscopy of hydrogen. The yellow circle is the star, the black circle is the planet with its surrounding envelope, and the red line is the orbital path of the planet. 6
- 1.5 The relationship between the vaporized atmospheric surface pressure, surface temperature, and surface composition (Fig. 1 from [Schaefer and Fegley, 2009](#)). 7
- 1.6 The vaporized atmospheric composition as a function of temperature for a Bulk Silicate Earth (BSE) surface composition (Fig. 2 from [Schaefer and Fegley, 2009](#)). 8
- 1.7 The sub-Jovian desert with the radius valley shown by the red dashed lines. Note how the valley vanishes at greater periods. Figure adapted from [Owen and Lai \(2018\)](#). 10
- 1.8 The temporal evolution of L_X of dM stars (solid lines; [Penz et al., 2008](#)) and dG stars (dashed lines; [Penz and Micela, 2008](#)). The thick lines give the median value, whereas the shaded areas are the dispersions. This graph is from [Penz et al. \(2008\)](#). 14
- 1.9 The trend in the X-ray and EUV luminosity of selected stars in the sample analysed by [Sanz-Forcada et al. \(2011\)](#). This image is from [Sanz-Forcada et al. \(2011\)](#). 15
- 2.1 *Left:* The y-axis is the ratio between the Energy-limited (E.L.) equation and a full hydrodynamic model, and the x-axis is the Jeans parameter (Λ) that describes the ratio between the thermal and gravitational effects acting on atmospheric particles; μ_H is the mass of a hydrogen atom and κ_B is Boltzmann's constant. The green line is the Hydro-based model, the red line is the value at one, and the blue lines are the values at 0.2 and 5. This image has been adapted from Figure 3 in [Kubyskhina et al. \(2018a\)](#). *Right:* The simple model given by Eq. 2.16. Whereas it does not perfectly match the figure on the left, it follows a similar trend, diverges at small values of Λ , and converges to unity at greater Jeans parameters. 21
- 2.2 Flowchart showing the path our code took when evolving the exoplanets. 24

2.3	Relative XUV flux of G-type and M-type stars. The red shaded region marks the measurements from Penz and Micela (2008) , Penz et al. (2008) and Sanz-Forcada et al. (2011) . The black line is the average measured XUV flux. The blue dashed line shows the step function we adopted in our model.	25
2.4	The final (blue line) and initial (red line) distributions of exoplanet radii for periods ≤ 100 days, as obtained by our model. The gray lines show the two peaks and the minimum discovered by Fulton et al. (2017) . The data points with the uncertainties correspond to the values given in Table 3 and Figure 7 of Fulton et al. (2017) . The light-red, light-yellow, and light-blue regions correspond only to the final radius distribution's rocky first peak, the remnant core (mega-Earth)-rich region, and the hydrogen-rich worlds of the second peak, respectively. For each region, we report the statistics of the envelope abundances.	26
2.5	The predicted final (blue) and initial (red) mass distributions of exoplanets whose radii are distributed according to Fig. 2.4. All planets have periods ≤ 100 days.	27
2.6	A comparison between the sub-Jovian desert from observational data (left) and our simulations (right, Modirrousta-Galian et al., 2020a). Both graphs have 787 data points.	28
2.7	Mass and radius distribution of 500 of our synthetic exoplanets after undergoing photoevaporation. All mass and radius curves come from Zeng and Sasselov (2013) and Zeng et al. (2016) except for the cold H ₂ curve, which originated from the equations of state by Becker et al. (2014) that were then adapted by Zeng et al. (2019) . The scale parameter of the laplacian function of the radii was set to 0.05 (i.e., a standard deviation of $\sqrt{2}/20$).	29
2.8	A simplified illustration of the atmospheric distribution predicted on some hot super-Earths with primordial atmospheres. This image does not show the atmospheric density at different latitudes.	34
2.9	Mass vs. radius for GJ 357 b using the coreless rocky (red dotted line), Earth-like (dark red dashed line), rocky with a 50 wt.% iron core (purple dash-dot line), and pure iron (grey line) models from Zeng and Sasselov (2013) and Zeng et al. (2016) . The values for the mass and radius and their uncertainties are those from Luque et al. (2019, purple) and Jenkins et al. (2019, blue)	35
2.10	X-ray luminosity vs. age and the angular momentum evolution models of Matt et al. (2015) . The empirical scaling law from Penz and Micela (2008) is shown. Two M stars with known ages, Barnard's star (GJ 699) and Kapteyn's star (GJ 191), are added to the plots for reference.	36
2.11	Synthetic spectra of GJ 357 b generated using the TauREx code. Our diagram includes the synthetic spectra of 100% CO ₂ (red), 100% SO ₂ (yellow), and a mixed atmosphere with 75% N ₂ along with 1% H ₂ O and 24% CO ₂ (blue). We show these forward models for the cloud-free case (top) and in the presence of opaque grey clouds at 0.01 bar (bottom).	38

- 2.12 *Top*: The initial primordial gas mass fraction distributions tested (from left to right: Gaussian, exponential decay, and uniform). All were truncated at an upper limit of 50% primordial gas. Increasing the mass fraction beyond this limit did not change the results unless one dealt with values close to ten times the core mass. All distributions gave rise to the same radius distribution after photoevaporation. *Bottom*: the radius distribution of super-Earths and sub-Neptunes immediately after photoevaporation. The gray lines mark the location of the two peaks and the minimum discovered by [Fulton et al. \(2017\)](#). The data points with the uncertainties correspond to the values given in Table 3 and Figure 7 of [Fulton et al. \(2017\)](#). The light-red, light-yellow, and light-blue regions correspond (approximately) to the typically quoted location of rocky worlds (e.g., [Jin and Mordasini, 2018](#)), the transition region ([Swain et al., 2019](#)), and hydrogen-rich worlds (e.g., [Modirrousta-Galian et al., 2020a](#)), respectively. For each region, we report the population composition. This result is not consistent with the observations of [Fulton et al. \(2017\)](#). 42
- 2.13 The radius distribution immediately after photoevaporation if the initial primordial gas mass fractions (i.e., the size of the initial atmospheres) are very large. The light-red, light-yellow, and light-blue regions correspond (approximately) to the typically quoted location of rocky worlds ([Jin and Mordasini, 2018](#)), the transition region ([Swain et al., 2019](#)), and hydrogen-rich worlds ([Modirrousta-Galian et al., 2020a](#)), respectively. Note that whereas a bimodal distribution forms, it deviates from the observations of [Fulton et al. \(2017\)](#) (the black data points). 43
- 2.14 The effects of the critical mass on the final radius distribution (after outgassing); all other parameters were left the same. From left to right, the critical masses are $3M_{\oplus}$, $5M_{\oplus}$, $7M_{\oplus}$, and $1 - 11M_{\oplus}$. The light-red, light-yellow, and light-blue regions correspond (approximately) to the typically quoted location of rocky worlds (e.g., [Jin and Mordasini, 2018](#)), the transition region ([Swain et al., 2019](#)), and hydrogen-rich worlds (e.g., [Modirrousta-Galian et al., 2020a](#)), respectively. Note how all distributions result in a bimodal trend. 44
- 2.15 The effects of the core mass on the final radius distribution (after outgassing); all other parameters were left the same. From left to right, the core mass distributions are a Rayleigh function ([Owen and Wu, 2017](#)), broken power laws ([Ginzburg et al., 2018](#); [Modirrousta-Galian et al., 2020a](#)), and a uniform distribution. The light-red, light-yellow, and light-blue regions correspond (approximately) to the typically quoted location of rocky worlds (e.g., [Jin and Mordasini, 2018](#)), the transition region ([Swain et al., 2019](#)), and hydrogen-rich worlds (e.g., [Modirrousta-Galian et al., 2020a](#)), respectively. Note how all distributions result in a bimodal trend. 45

2.16	The radius distribution of super-Earths and sub-Neptunes after late-stage outgassing. The gray lines show the two peaks and the minimum discovered by Fulton et al. (2017) . The data points with the uncertainties correspond to the values given in Table 3 and Figure 7 of Fulton et al. (2017) . The light-red, light-yellow, and light-blue regions correspond (approximately) to the typically quoted location of rocky worlds (e.g., Jin and Mordasini, 2018), the transition region (Swain et al., 2019), and hydrogen-rich worlds (e.g., Modirrousta-Galian et al., 2020a), respectively. For each region, we report the population composition; our data does not support the presence of the transition region. This result is consistent with the observations of Fulton et al. (2017)	46
3.1	<i>Top</i> , the transit method showing a planet traversing across the line of sight of a star and how this is coeval with the drop in the observed stellar flux (credit: Hans Deeg). <i>Bottom</i> , a sketch showing how the planet’s gravity causes the star to also orbit around the center of mass of the system. This stellar ‘wobble’ brings about a Doppler shift that can, in some cases, be detected by astronomers (credit: Alysa Obertas).	49
3.2	<i>Left</i> : solidified carbonatite from Jacupiranga Estado de São Paulo, Brazil (credit: Eurico Zimbres). The black minerals are magnetite (Fe_3O_4), the white are calcite (CaCO_3), and the green are olivine ($[\text{Mg}, \text{Fe}]_2 \text{SiO}_4$). <i>Right</i> : solidified komatiite from the Komati River in South Africa (credit: I. P. Vtorov). The long skeletal texture is called spinifex, and it is caused by the constrained growth of olivine or pyroxene crystals during magma solidification.	52
3.3	A comparison of the model by Lazányi and Szirmay-Kalos (2005) , Schlick’s approximation with n_{sy} , and the Fresnel equations.	55
3.4	Cartoon showing how a wavier surface will induce greater angles of incidence for incoming light.	56
3.5	Cartoon showing how taller waves can cause light rays to reflect multiple times and eventually get absorbed by the material.	57
3.6	A demonstration of how halving the side lengths causes the mass to decrease by a factor of four.	58
3.7	A demonstration of how halving the side lengths decreases the mass by a factor of three.	58
3.8	The unsmoothed fractal surface of an ocean whose wave heights are not adjusted. This surface was generated for a Hurst exponent of 0.7. The circled area magnifies the 0 – 1 m region by a $\times 100$	60
3.9	A 3-D rendition of a magma ocean surface generated using the methods given in sect. 3.2.4 and 3.2.5. Note that the x-axis and y-axis do not have the same scale, so surface features may seem distorted. It is also important to consider that in our albedo simulator, we used 2-D surfaces as they were less computationally expensive.	62
3.10	The planar albedo as a function of the synthetic refractive index (n_{sy}) and the Hurst exponent (H). This figure was generated with Eq. 3.12a and 3.12b.	64
3.11	The spherical albedo values of common Earth minerals and rocks, metals and metalloids, metal oxides, and two carbonaceous minerals, for a Hurst exponent of 0.8. The light-blue section is Kepler’s band-pass. This figure was generated with Eqs. 3.14, Eq. 3.12a, 3.12b, 3.13a, and 3.13b.	66

- 3.12 The spherical albedo for a terrestrial planet with an initial composition corresponding to the BSE that has been evolved due to chemical interactions between the magma and the mineral atmosphere. Four different spherical albedo spectrums are shown corresponding to varying levels of vaporization. The BSE composition is from [O'Neill and Palme \(1998\)](#), while the vaporized compositions were taken from [Kite et al. \(2016\)](#). The light-blue section is Kepler's band-pass. This figure was generated with Eqs. 3.14, Eq. 3.12a, 3.12b, 3.13a, and 3.13b. 67
- 3.13 The spherical albedo of a coreless terrestrial planet with the composition given by [Elkins-Tanton and Seager \(2008\)](#). The red dotted line is the average coreless spherical albedo value for $H = 0.8$, the red shaded region represents the uncertainty, and the black line is for the spherical albedo value of a cored BSE planet [O'Neill and Palme \(1998\)](#). The light-blue section is Kepler's band-pass. This figure was generated with Eqs. 3.14, Eq. 3.12a, 3.12b, 3.13a, and 3.13b. 68
- 4.1 Comparison between [Kurosaki et al. \(2014\)](#), [Abu-Romia and Tien \(1967\)](#), [Hottel \(1954\)](#), and RAPOC. The shaded lines in both plots represent the raw data loaded from *ExoMol's* water opacities ([Polyansky et al., 2018](#)). The blue lines are Rosseland mean opacities with the filled lines being from [Kurosaki et al. \(2014\)](#), the dash-dotted line from [Abu-Romia and Tien \(1967\)](#), and the dashed lines from RAPOC. The red lines are Planck Mean Opacities with the filled lines being from [Kurosaki et al. \(2014\)](#), the dash-dotted line from [Abu-Romia and Tien \(1967\)](#), the dash-dot-dotted line from [Hottel \(1954\)](#), and the dashed lines from RAPOC. The black dotted line is the median value of the raw wavelength dependent opacities. The left panel is for the visible wavelength range (0.3 to 0.7 μm) and right panel is for the IR wavelength range (0.7 to 50 μm). Both panels use the same pressure (1.01325 bar) and temperature (1500 K). 80
- 4.2 Comparison between [Abu-Romia and Tien \(1967\)](#), [Hottel \(1954\)](#), and RAPOC. The shaded lines in all plots represent the raw data loaded from *ExoMol's* carbon dioxide opacities ([Yurchenko et al., 2020](#)). The blue lines are Rosseland mean opacities with the dash-dotted lines being from [Abu-Romia and Tien \(1967\)](#), and the dashed lines from RAPOC. The red lines are Planck Mean Opacities with the dash-dot-dotted lines being from [Hottel \(1954\)](#), the dash-dotted lines from [Abu-Romia and Tien \(1967\)](#), and the dashed being from RAPOC. The black dotted line is the median value of the raw wavelength dependent opacities. The three panels refer to different gas temperatures: right is for $T = 1500 K$, center is for $T = 2000 K$, and left is for $T = 2500 K$. All panels use the same pressure (1.01325 bar). 81

4.3	Comparison between Badescu (2010) and RAPOC estimates. The shaded lines in all plots represent the raw data loaded from <i>ExoMol</i> 's carbon dioxide opacities (Yurchenko et al., 2020). The blue lines are Rosseland Mean Opacities with the filled lines from Badescu and the dashed lines from RAPOC . The red dashed lines are RAPOC 's Planck Mean opacities, and the black dotted lines are the median value of the raw wavelength dependent opacities. The left column is for low pressure ($567 \cdot 10^{-3}$ bar) and the right column is for high pressure (11.467 bar); both columns use the same temperature (300 K). The wavelength range is different in the two rows as the top row uses 0.5 to 50 μm range, while the bottom row uses 5 to 10 μm .	82
5.1	<i>Left:</i> $\times 20$ transmitted light photo of haematite strings. <i>Right:</i> $\times 50$ reflected light photo of haematite strings.	95
5.2	If we plotted the properties of life-bearing planets on a graph, Earth would most probably be located somewhere in the center. Note, this figure assumes that such properties would be distributed in a Gaussian-like manner; the actual distribution is unknown.	102
5.3	The physicochemical properties of water can be explained by the high electronegativity of oxygen, and the low electronegativity of hydrogen, which give it two dipoles capable of hydrogen bonding. The polar nature of the molecule is due to the 104.5° angle that forms.	104
5.4	The most thermodynamically favourable shapes for amphiphilic molecules to take in water are micelles, bilayer sheets and liposomes. These forms are driven by the hydrophobic effect and may have facilitated the evolution of cellular membranes.	105
A.1	Not-to-scale cartoon depicting the classical vs. ultimate theory of Rayleigh-Bénard convection. L is the thickness of the convective section, whereas δ is the thickness of the boundary layer.	141

List of Tables

3.1	Parameters for Eq. (3.12a) and (3.12b)	63
4.1	Retrieved atmospheric composition of WASP-76 b from transmission and emission spectroscopy	72
4.2	Retrieved atmospheric composition of WASP-127 b, WASP-62 b and WASP-62 b from transmission spectroscopy	73
5.1	The cosmochemical composition of our solar-system according to Lodders (2010)	98

Terms and Acronyms

Abiogenesis – The formation of life from non-living matter.

AMOSE – Airless Magma Ocean Super-Earth.

Bolometric flux – The total flux emitted over all wavelengths.

Bond albedo – The fraction of reflected irradiance divided by the total incoming irradiance. Sometimes the spectral irradiance is used instead of the total irradiance.

CPAML – Core Powered Atmospheric Mass Loss.

Degeneracy – The ability of various mechanisms or properties leading to the same observable outcome.

Endmember – A pure compound that contributes to the compositional mixture of minerals.

Fractal – A mathematical construct whose fractal dimension (or Hausdorff dimension) is greater than its topological dimension.

Fractal dimension – A measure of how the complexity of a fractal changes as a function of the the scale it is measured in.

Geometric albedo – The observed reflected component of an object at zero phase angle relative to a Lambertian surface.

Hausdorff dimension – see *Fractal dimension*.

Hurst exponent – A measure of the coherence (or self-similarity) of a system.

Imaginary refractive index – A measure of the attenuation of electromagnetic radiation through a material.

Jeans parameter – The gravitational potential energy of a gas particle in an atmosphere relative to its kinetic energy.

Lambertian surface – An ideal fully reflective perfectly diffusing surface.

Non-uniqueness – See *Degeneracy*.

Nusselt Number – The ratio of the convective to conductive heat flux at a boundary layer in a fluid.

Planck mean opacity – The arithmetic mean of the wavelength-dependent opacity weighted by the Planck black-body radiation energy density distribution.

Polytrope – A solution of the Lane–Emden equation in which the pressure of a system is proportional to the density raised to a given exponent.

Primordial atmosphere – A hydrogen-rich atmosphere that has not experienced much processing and is therefore close to its stellar composition.

Rayleigh number – The ratio of the diffusion to advection thermal timescales.

Real refractive Index – The ratio of the speed of light in a vacuum to its speed in a material.

Reflectance – A directional parameter that quantifies the reflective properties of a surface. It depends on the incident and emerging angles, the wavelength of light, the composition, and the roughness of the surface.

Remnant core – A planet that once had a large primordial atmosphere that was lost through atmospheric evaporation. The primordial atmosphere compressed the core resulting in it having a significantly high density.

RMS height – The root mean squared height of vertical perturbations on a surface.

Rosseland mean opacity – The harmonic mean of the wavelength-dependent opacity weighted by the temperature derivative of the Planck black-body radiation energy density distribution.

Secondary atmosphere – An atmosphere that has been processed by exogenous and endogenous mechanisms such as volcanism and planetesimal impacts.

Spherical albedo – See *Bond albedo*.

Sub-Neptune – Loosely defined as a planet with a mass less than ten times the mass of Earth that hosts a hydrogen-rich atmosphere.

Super-Earth – Loosely defined as a planet with a mass less than ten times the mass of Earth that does not host a hydrogen-rich atmosphere.

Synthetic refractive Index – Defined as a refractive index that accounts for the real and imaginary components.

XUV – X-ray and Ultraviolet.

1 Introduction

1.1 First Discoveries

The first exoplanet discovered around a main-sequence star was 51 Pegasi b in 1995 (Mayor and Queloz, 1995). Current observations place the mass and radius at $0.46_{-0.01}^{+0.06}$ M_J and $1.9 \pm 0.3 R_J$ respectively (Martins et al., 2015), with an effective temperature > 1000 K; in other words, 51 Pegasi b is a hot Jupiter. Relative to other planets, hot Jupiters are the most straightforward to discover due to their favorable properties; their great masses cause their host stars to wobble, a motion that can be easily detected with radial velocity measurements. Furthermore, their large cross-sectional areas and close orbits result in a significant fraction of the incoming stellar light getting blocked and a higher probability of transits occurring, both of which allow for radius measurements to be made. Because astronomical instrumentation and data processing techniques have improved, the rate at which extra-solar planets get discovered has significantly increased. Most detections are from the transit method, although radial velocity, direct imaging, microlensing, and pulsar timing have also played important roles. The present statistics of exoplanet discovery techniques are as follows³:

1. *Transit* ($\sim 75\%$) – Measuring the drop in the apparent stellar luminosity, providing the radius of the orbiting planet.
2. *Radial Velocity* ($\sim 20\%$) – Measuring the Doppler shift in the star’s spectrum, gives information on the planetary mass.
3. *Microlensing* ($\sim 3\%$) – Measuring the degree of gravitational lensing in the light from a background source by the orbiting planet, providing the planetary mass.
4. *Imaging* ($\sim 1\%$) – Detecting young far-orbiting planets by their faint thermal emissions. This provides loose constraints on their masses.
5. *Other* ($\sim 1\%$) – Transit timing variations, eclipse timing variations, pulsar timing, orbital brightness modulation, pulsation timing variations, disk kinematics, and astrometry.

³Data from the NASA Exoplanet Archive (Accessed on February 2nd 2022)

Considering the dominance of the transit method, for most planets, we only have radius measurements, meaning that their compositions and structures cannot be reasonably constrained. Because of this, the planets of most interest have mass and radius measurements available, as their bulk densities can then be used to make inferences about their interiors. Unfortunately, determining the mass of an exoplanet is difficult. For example, to know the amount of Doppler shift present in the stellar spectrum, one needs the star to be reasonably bright so enough photons can be collected. Furthermore, small exoplanets such as super-Earths and sub-Neptunes induce (relatively) small oscillations on their host stars, meaning that performing a radial velocity analysis is challenging. One must, therefore, also consider the host star, as it strongly dictates how observable a planet is.

When the Kepler space telescope entered service on the 12th May 2009, an explosion in exoplanetary discoveries occurred. Thousands of new planets were discovered, making it possible to perform statistical analyses on the data and better understand our stellar neighborhood. Newer data sets showed that Jupiter-sized planets are relatively rare, whereas sub-Neptunian bodies are common. One of the first statistical analyses of exoplanet properties came from [Batalha et al. \(2013\)](#), who found that exoplanets with radii of $\sim 1.8 R_{\oplus}$ were abundant. [Burke et al. \(2014\)](#) then improved on the known exoplanet radius distribution by correcting for the observational biases against smaller bodies (see Fig. 1.1). The newly discovered set of exoplanets that are larger than Earth ($> 1 R_{\oplus}$) but smaller than Neptune ($< 3.88 R_{\oplus}$) are called super-Earths and sub-Neptunes. While there is no formal definition for super-Earths and sub-Neptunes, it has become common to define them as having radii between $1 - 1.75 R_{\oplus}$ and $1.75 - 3.5 R_{\oplus}$ respectively ⁴. This classification was first proposed by [Fulton et al. \(2017\)](#), who analyzed exoplanet population data and resolved the bimodal trend in their sizes (shown in Fig. 1.2). Additionally, [Fulton et al. \(2017\)](#) confirmed that there is a deficit of exoplanets located at $\sim 1.75 R_{\oplus}$, which was confounding at the time because it was not predicted by planetary formation models (e.g., [Schlichting et al., 2013](#); [Simon et al., 2016](#)). However, before progressing further with the radius distribution, it is crucial to understand how researchers constrain the compositions of exoplanets.

⁴This definition is used throughout the thesis.

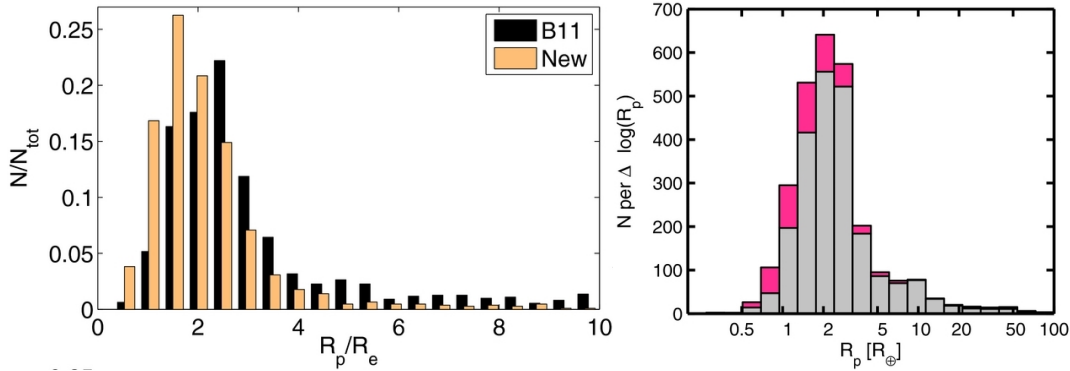


Figure 1.1: *Left:* one of the first distributions of exoplanet radii. It became evident, even when there were strong biases against smaller exoplanets, that sub-Neptunian bodies are abundant (Fig. 4 from [Batalha et al., 2013](#)). "B11" and "New" indicate the old and new datasets at the time of writing. *Right:* with more exoplanets discovered, the distribution of exoplanet sizes got further refined (Fig. 4 from [Burke et al., 2014](#)). The grey color indicates the previously known exoplanets, whereas the newer Kepler candidates are represented by red.

1.2 Inferences on Exoplanet Interiors

In the literature, the most common approach for understanding the interior structure of exoplanets is to infer the bulk planetary composition based on polytropic mass-radius trends (see Fig. 1.3 and sect. 3.1 for a more thorough explanation). Planetary equations of state are readily produced (e.g., [Zapolsky and Salpeter, 1969](#); [Stevenson, 1982b](#); [Valencia et al., 2006, 2007b](#); [Fortney et al., 2007](#); [Seager et al., 2007](#); [Sotin et al., 2007](#); [Rogers and Seager, 2010](#); [Madhusudhan et al., 2012](#)), with [Zeng and Sasselov \(2013\)](#) and [Zeng et al. \(2016\)](#) being widely cited due to providing tables and analytic approximations. Whereas polytropic analyses provide some clues on the geochemistry and structure of exoplanets, they suffer from significant degeneracies (e.g., [Valencia et al., 2013](#); [Dorn et al., 2017](#)). For instance, 55 Cancri e has a mass and radius ($7.99^{+0.32}_{-0.33}M_{\oplus}$ and $1.875 \pm 0.029R_{\oplus}$, respectively, [Bourrier et al., 2018a](#)) that could be compatible with a coreless rocky body ([Bourrier et al., 2018a](#)), a water world ([Zeng and Sasselov, 2013](#); [Zeng et al., 2016](#)), a graphitic planet ([Madhusudhan et al., 2012](#)), a silicate carbide planet ([Miozzi et al., 2018](#)), a rocky body with a massive nitrogen atmosphere ([Zilinskas et al., 2020](#)), and a rocky body with a core and a primordial hydrogen envelop ([Crida et al., 2018](#); [Modirrousta-Galian et al., 2020b](#)). This non-uniqueness problem could be reduced by analyzing the atmospheric composition of these bodies. For example, in the case of 55 Cancri e, studies have found

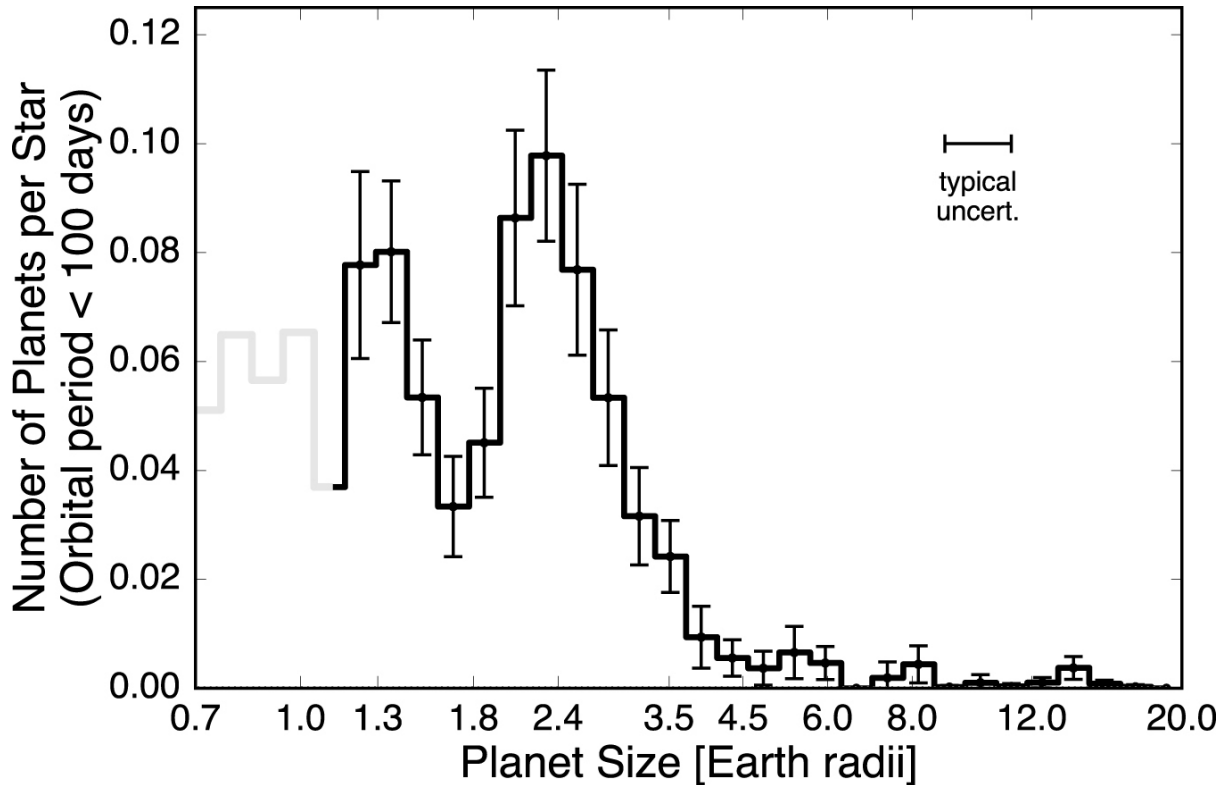


Figure 1.2: The bimodal distribution in exoplanet radii for orbital periods less than 100 days (Fig. 7 from [Fulton et al., 2017](#)). ‘typical uncert.’ refers to the average uncertainty in the radius. The light grey line for planets with $R < 1.14 R_{\oplus}$ indicates the region suffering from a lack of data so is more prone to biases.

spectral signatures corresponding to hydrogen ([Tsiaras et al., 2016](#); [Esteves et al., 2017](#)), mineral species ([Ridden-Harper et al., 2016](#)), and no water ([Esteves et al., 2017](#)). These studies, therefore, strongly suggest that 55 Cancri e is a rocky planet with a hydrogen atmosphere. Even so, the atmospheric composition of 55 Cancri e is still disputed, with new findings being consistent with the presence of a secondary atmosphere ([Jindal et al., 2020](#); [Zhang et al., 2021](#)). Nevertheless, precisely analyzing the spectra of large exoplanet populations is currently not possible due to instrumental limitations.

1.3 Understanding Atmospheric Spectroscopy

Spectroscopy can be used to constrain the internal structure and composition of exoplanets with atmospheres. This method involves the search for spectral features that reveal the chemistry present in an exoplanet’s atmosphere; this can be done in emission or transmission depending on the location of the exoplanet relative to its host star (see Fig. 1.4). In most cases, atmospheres have a mixture of elements, making it difficult

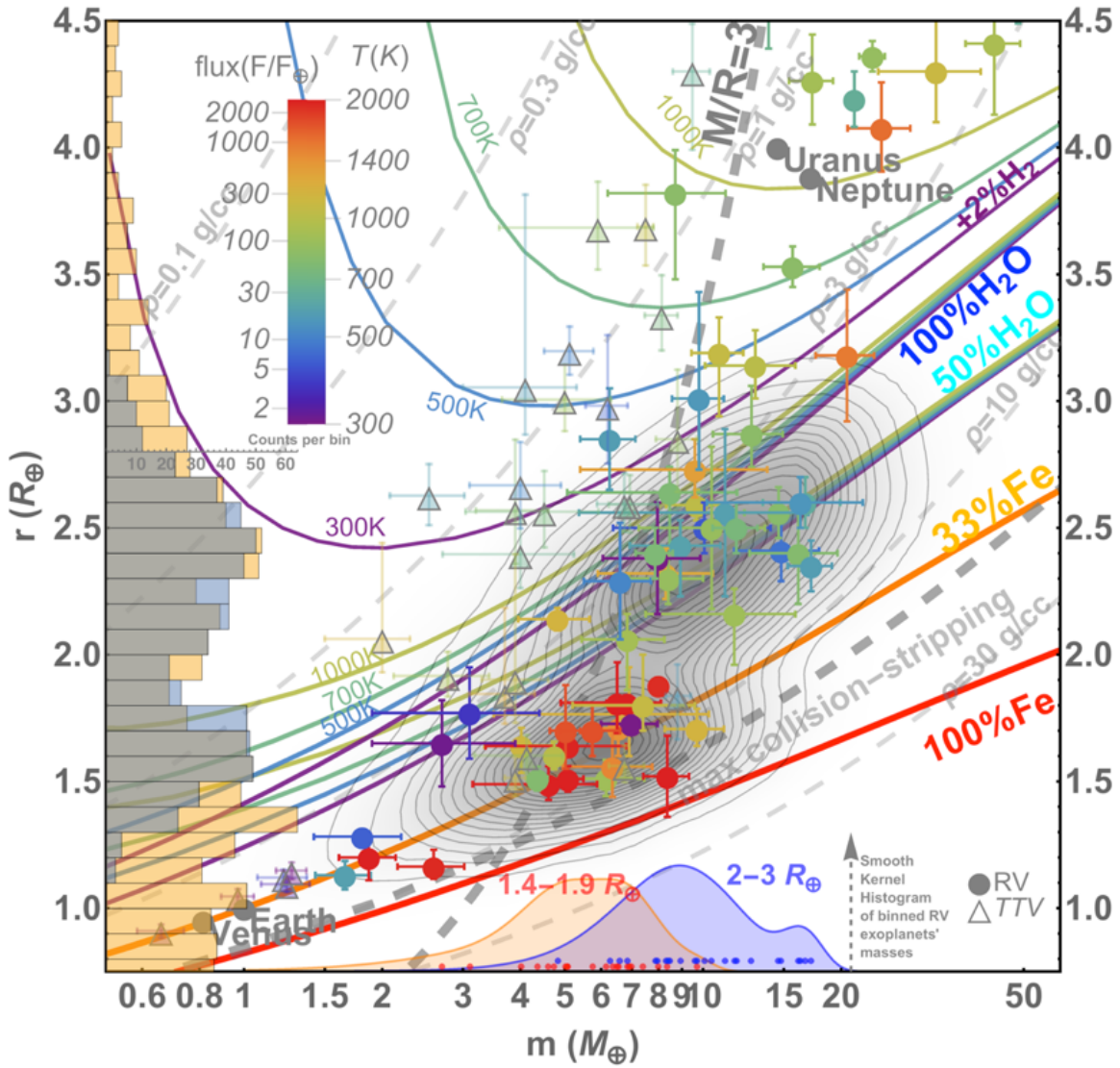


Figure 1.3: The mass and radius models from Zeng et al. (2016) and Zeng and Sasselov (2013) plotted with their respective distributions (Fulton et al., 2017). Diagram from Zeng et al. (2019).

to isolate the individual species present as the various spectral lines are entangled. The first exoplanet characterized with spectroscopy was the hot Jupiter HD 209458 b (Charbonneau et al., 2002); by comparing its spectrum with a theoretical one, the presence of sodium was confirmed. Because of its relatively low mass ($0.682^{+0.014}_{-0.015} M_J$), inflated radius ($1.359^{+0.016}_{-0.019} R_J$), and high temperature ($\simeq 1500$ K), HD 209458 b has a large scale height, making its atmosphere easier to analyze (Bonomo et al., 2017). Since 2002, the available astronomical instrumentation and statistical tools have drastically improved, thus allowing for more thorough analyses of exoplanetary atmospheres. For example, new research suggests that it may be possible to characterize the mineral vaporized atmospheres of

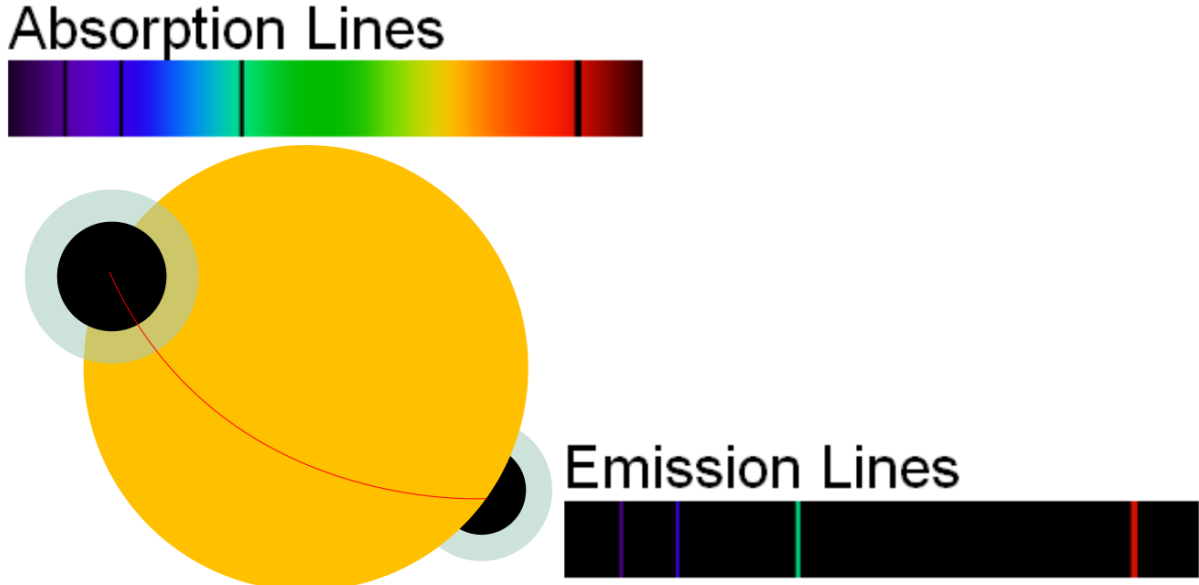


Figure 1.4: Emission and transmission spectroscopy of hydrogen. The yellow circle is the star, the black circle is the planet with its surrounding envelope, and the red line is the orbital path of the planet.

highly irradiated super-Earths (Ito et al., 2021) because at effective temperatures $\gtrsim 1500$ K, surface magma vaporizes and remains stably in a gaseous phase. The chemistry of the resultant mineral atmosphere is therefore helpful for understanding the composition and internal structure of these planets (e.g., Schaefer and Fegley, 2009; Schaefer et al., 2012; Ito et al., 2015).

To illustrate the utility of atmospheric spectroscopy, we reference CoRoT-7b that has a mass, radius, and equilibrium temperature of $5.74 \pm 0.86 M_{\oplus}$, $1.585 \pm 0.064 R_{\oplus}$, and 1756 ± 27 K (Barros et al., 2014), respectively. Assuming that it has a surface composition similar to the BSE (bulk silicate Earth), vaporization models predict a tenuous sodium-dominated atmosphere with a surface pressure of ~ 1 Pa (e.g., Schaefer et al., 2012; Ito et al., 2015); this prescription provides a direct connection between the atmospheric and surface composition. Furthermore, an improved understanding of planetary atmospheres could even reveal whether recent catastrophic impacts have taken place. Modeling terrestrial meteorite impacts shows that for velocities greater than ~ 15 km s $^{-1}$, the entire impactor and a portion of the target could vaporize as temperatures over $\sim 10,000$ K are possible (Collins et al., 2005). The 28 km diameter Mistastin Lake crater in Canada is thought to be the result of a meteorite that upon impact reached a temperature of ~ 2640 K (Timms et al., 2017); this is the highest recorded crustal temperature on

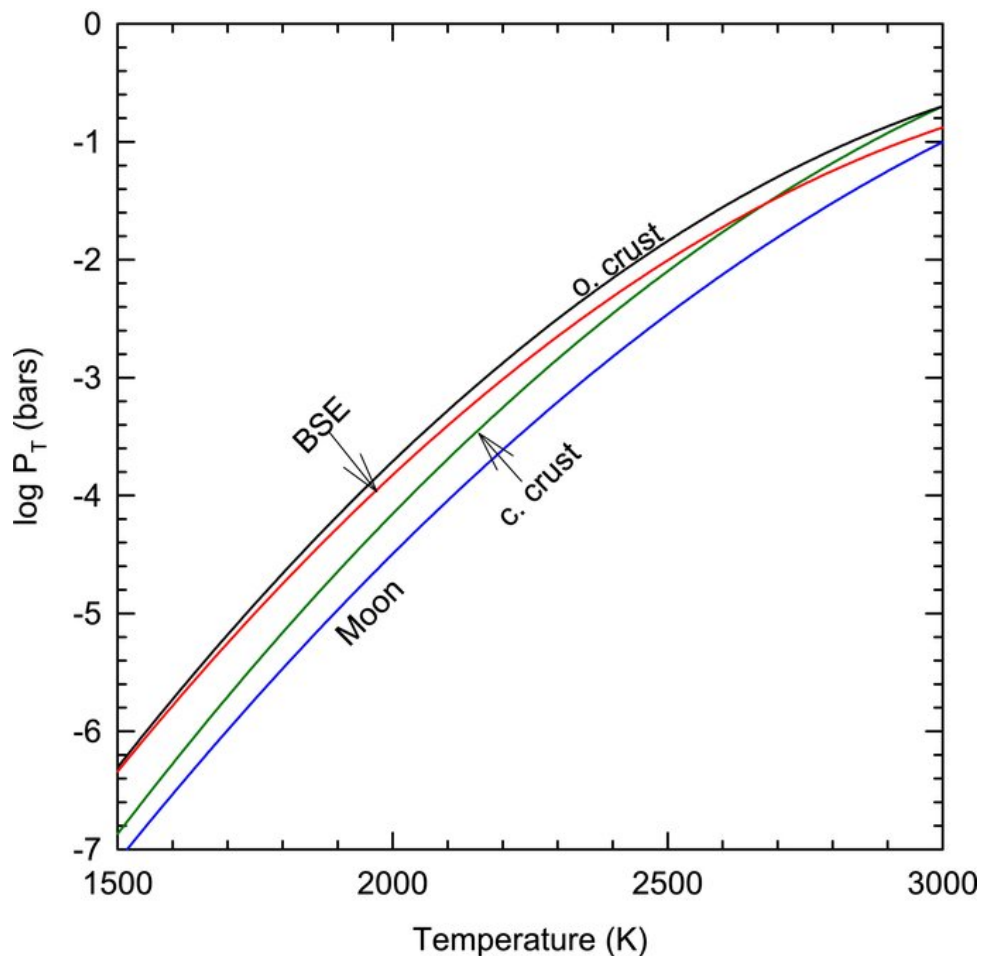


Figure 1.5: The relationship between the vaporized atmospheric surface pressure, surface temperature, and surface composition (Fig. 1 from [Schaefer and Fegley, 2009](#)).

Earth. [Lupu et al. \(2014\)](#) explored the way terrestrial exoplanet atmospheres could be affected by post-formational giant impacts; they found that after an impact, the resultant atmospheres would be CO_2 - and H_2O -rich with small amounts of HF, HCl, NaCl, and SO_2 . The elevated temperatures would increase the brightness of the planet, making the system easier to analyze for $10^5 - 10^6$ years after the impact. In addition, geophysical modeling shows that the cores of planetesimals could vaporize when they collide with super-Earths leading to an increase in the metal-enrichment of the crust ([Kraus et al., 2015](#)). These studies are consistent in suggesting a possible link between the atmospheric and surface compositions of post-impact planets; we explore this idea further in sect 3.2.2.

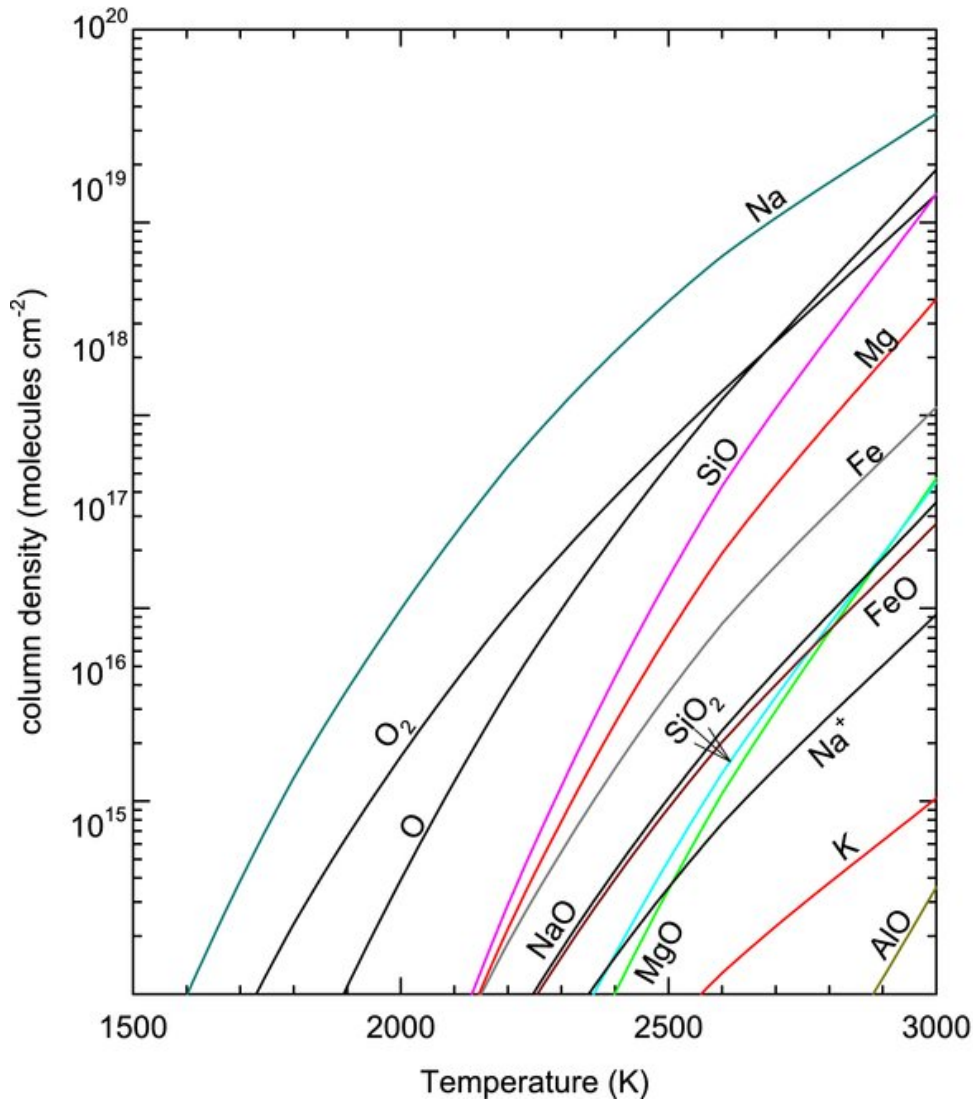


Figure 1.6: The vaporized atmospheric composition as a function of temperature for a Bulk Silicate Earth (BSE) surface composition (Fig. 2 from [Schaefer and Fegley, 2009](#)).

1.4 Exoplanet Trends and Explanations

As of the writing of this thesis, three competing major models explain the bimodal behavior of exoplanet radii:

1. Core-powered atmospheric mass loss (CPAML; e.g., [Ginzburg et al., 2016](#); [Gupta and Schlichting, 2019](#); [Ginzburg et al., 2018](#)).
2. Differing geological compositions ([Zeng et al., 2019](#)).
3. Stellar XUV-induced photoevaporation (e.g., [Lecavelier Des Etangs, 2007](#); [Ehrenreich and Désert, 2011](#); [Lammer et al., 2013](#); [Owen and Wu, 2013](#); [Jin et al., 2014](#); [Owen and Wu, 2017](#); [Kubyskhina et al., 2018b](#); [Modirrousta-Galian et al., 2020a](#)).

Whereas these models are not mutually exclusive, they each involve different physics that will be explored in the following. It is important to note that with core-powered atmospheric mass loss (CPAML), ‘core’ refers to the interior embryo and not the geological term for the planet’s iron-rich nucleus that has the same name. Nevertheless, these three models predict different observable trends. CPAML is, by definition, independent of the host star and the planet-star separation, so the bimodal trend should also be observable at any semi-major axis. The geologically-centered model by [Zeng et al. \(2019\)](#) instead predicts that the bimodal trend is independent of age because the first and second peaks are composed of rocky and icy planets, respectively. Finally, the XUV-evaporation model argues that high-energy irradiation from the host-star strongly affects primordial atmospheres so that the bimodal behavior would be dependent on the orbital distance, age, size of the planet, and spectral type of the star. Below, each of these models is explored in more detail.

1.4.1 Core-powered Atmospheric Mass Loss

This model proposes that if the interior’s heat capacity were significantly greater than the atmosphere’s, the primordial atmosphere would be stripped away (e.g., [Ginzburg et al., 2016](#); [Gupta and Schlichting, 2019](#); [Ginzburg et al., 2018](#)). One advantage of CPAML is that super-Earths and sub-Neptunes with extended atmospheres have been observed (e.g., [Masuda, 2014](#); [Jontof-Hutter et al., 2016](#); [Benatti et al., 2019](#)) that can only be explained by the presence of large interior heat budgets. CPAML, however, argues that the evaporation of an exoplanet’s atmosphere is independent of its distance from the star; this is not observed because astronomical data instead suggests that there is a sub-Jovian desert ([Owen and Lai, 2018](#), see Fig. 1.7): a region with a paucity of exoplanets of intermediate radii (i.e., the second peak) with orbital periods less than ~ 3 days. The CPAML model cannot explain the lack of planets in the second peak because of its orbital distance independence. Notwithstanding, this model still poses an interesting mechanism that warrants further mathematical analysis. The main argument by [Ginzburg et al.](#) is that the internal energy from the core and atmosphere triggers the removal of atmospheric gases so

$$\frac{dE_c}{dt} + \frac{dE_{atm}}{dt} \gtrsim \frac{dE_{grav}}{dt}. \quad (1.1a)$$

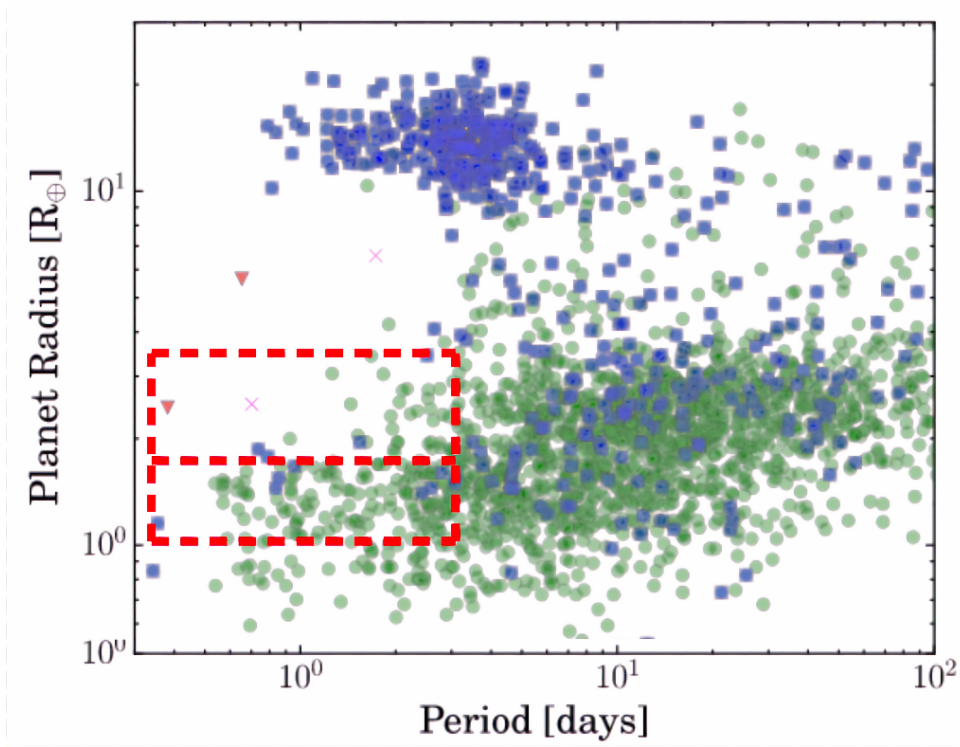


Figure 1.7: The sub-Jovian desert with the radius valley shown by the red dashed lines. Note how the valley vanishes at greater periods. Figure adapted from [Owen and Lai \(2018\)](#).

The above equation describes the requirement for CPAML in which the energy loss from the core and atmosphere is equal to or greater than the gravitational binding energy of the atmosphere. To be more specific,

$$M_c c_{p,c} \frac{dT_c}{dt} + M_{atm} c_{p,atm} \frac{dT_{atm}}{dt} \gtrsim \frac{GM_c}{R_c} \frac{dM_{atm}}{dt}, \quad (1.1b)$$

where the subscript c and atm are for the core and atmosphere respectively, M is the mass, c_p is the specific heat, T is the temperature, G is the gravitational constant, R is the radius, and t is the time elapsed. Assuming thermal equilibrium and a convecting core leads to $dT_{core}/dt \sim dT_{atm}/dt$, such that

$$(M_c c_{p,c} + M_{atm} c_{p,atm}) \frac{dT}{dt} \gtrsim \frac{GM_c}{R_c} \frac{dM_{atm}}{dt}. \quad (1.1c)$$

This can be simplified further,

$$\left(\frac{R_c}{GM_c} \right) dT \gtrsim \left(\frac{1}{M_c c_{p,c} + M_{atm} c_{p,atm}} \right) dM_{atm}, \quad (1.1d)$$

whence,

$$\frac{M_{atm}}{M_c} \lesssim \frac{c_{p,c}}{c_{p,atm}} \left(e^{\frac{R_c c_{p,atm} \Delta T}{GM_c}} - 1 \right). \quad (1.1e)$$

In the limit where $R_c c_{p,atm} \Delta T / GM_c \ll 1$ we can Taylor expand and simplify,

$$\frac{M_{atm}}{M_c} \lesssim \frac{R_c c_{p,c} \Delta T}{GM_c} \quad (1.1f)$$

for the realistic choices of $c_{p,c} \sim 10^3 \text{ J kg}^{-1} \text{ K}^{-1}$, $\Delta T \sim 10^3 \text{ K}$, $M_c \sim M_{\oplus}$, and $R_c \sim R_{\oplus}$,

$$\frac{M_{atm}}{M_c} \lesssim 2\%. \quad (1.1g)$$

In other words, an atmosphere less than a few percent of the total planetary mass will be removed by the internal luminosity of the core; this is consistent with the value of 5% given in [Ginzburg et al. \(2018\)](#). Despite the above approach being more simple than the one prescribed by [Ginzburg et al. \(2018\)](#), it illustrates the fundamental physics taking place. There are, however, a few aspects that make the predictions by Ginzburg et al. questionable. For instance, it is assumed that all of the interior energy gets used in fueling mass-loss; the interior heat of the core could instead fuel the core erosion process (see sect. 4.2) because the bottom atmospheric boundary is where energy gets transferred from the core to the atmosphere and, also, where core erosion primarily takes place. Furthermore, they assume that the core is isothermal, which is incorrect as a timescale longer than the universe's age would be required. Considering all of the above, whereas this model may provide a possible prescription for how some planets evolve, it remains highly speculative with fundamental theoretical issues to be resolved.

1.4.2 Differing Geological Compositions

The [Zeng et al. \(2019\)](#) model suggests that the bimodal distribution is the result of different geological compositions; the first peak is composed of terrestrial planets and the second of half-ice and half-silicate planets. In addition to ice-rich super-Earths having not been established⁵, this model makes testable predictions not supported by observational data. For example, if most planets in the second peak were composed of water, strong

⁵Super-Earths with densities consistent with ice have been detected, but it is uncertain whether they are ice-rich or rocky planets with hydrogen-rich envelopes. Whereas exoplanets hosting hydrogen-rich atmospheres have been established, ice-rich super-Earths remain speculative.

spectral absorption lines would be expected. Closely-orbiting planets would show evidence of the ionization and dissociation of water molecules; this has not been observed. Note that whereas water has been detected in several small exoplanets such as K2-18 b (Tsiaras et al., 2019; Benneke et al., 2019), HD 106315 c (Guilluy et al., 2021), HD 3167 c (Guilluy et al., 2021), and LHS 1140 b (Edwards et al., 2021), they all have primordial envelopes in which water is a minor component, so they do not fit the description of being ice planets as prescribed by Zeng et al. (2019).

Another major inconsistency is that the Zeng model is unable to reproduce the sub-Jovian desert (Owen and Lai, 2018). Unlike primordial atmospheres on rocky planets, H₂O atmospheres on ice-rich planets are much harder to remove because the instant vaporization of the core would cause a negative feedback mechanism regenerating the atmosphere. Therefore, to match observations, almost all water would need to be removed, requiring energy comparable to the planetary gravitational binding energy $\sim GM_p^2/R_p$. The total XUV energy available is many orders of magnitude too low to make this plausible (Hunten et al., 1987; Zahnle and Kasting, 1986; Luger and Barnes, 2015).

Several exoplanets with densities greater than iron, called remnant cores, have been observed (Swain et al., 2019). Kepler-131 c and K2-38 b are two examples of such planets that are approximately two (Sinukoff et al., 2017) and ten (Marcy et al., 2014) times denser than iron at room temperature and pressure. Whereas the reason for their high densities is still not well understood, it is generally accepted to be caused by the compression from a previously existent $1 - 10M_{\oplus}$ envelope (Mocquet et al., 2014). Some of these cores would remain compressed for geologically long timescales (Mocquet et al., 2014), thus explaining why the unusually high densities are detectable. The Zeng et al. (2019) model is unable to provide a mechanism for the presence of remnant cores, while the XUV-induced photoevaporation model can.

Furthermore, the Zeng model is inconsistent with the formation of mega-Earths, massive terrestrial exoplanets that are at least ten times the mass of Earth. According to planetary formation models, once a planet reaches a critical mass of $\sim 10M_{\oplus}$ (approximately), it can undergo runaway accretion (Ida and Lin, 2004, 2005, 2008). This prescription describes how a body acquires a primordial atmosphere and grows in mass to become a gas giant. During this time, heavy materials such as rock and ice (Shiraishi and Ida,

2008) would also get sequestered; they would then sink into the central embryo, causing its growth. Photoevaporation models predict that some massive planets will lose their envelopes (Kubyskhina et al., 2018b), leaving behind a large (remnant core) mega-Earth. For example, Kepler-145 b and K2-66 b are rocky bodies with masses and radii of $37.1 \pm 11.6M_{\oplus}$, $2.65 \pm 0.08R_{\oplus}$ (Xie, 2014) and $21.3 \pm 3.6M_{\oplus}$, $2.49 \pm 0.30R_{\oplus}$ (Sinukoff et al., 2017), respectively. Without the presence of a previously existent primordial envelope and the sequestration of heavy materials during its growth, the origin of mega-Earths is difficult to explain. We note, however, that planets undergoing runaway gas accretion tend to become massive ($\gtrsim 100M_{\oplus}$), so the complete removal of their envelopes is an active area of research. Furthermore, the sinking of heavy elements to the core is matter of debate because planetary data and models are consistent with a significant fraction remaining diluted in the envelope.

In addition to observational inconsistencies, the Zeng model does not consider the effects of surface vaporization on the equations of state. Due to observational biases, most observed small exoplanets are hot or warm. Hence, tight-orbiting, water-rich planets would experience surface vaporization, resulting in large hydrospheres. Beneath the radiative-convective boundary of these atmospheres, the pressures and temperatures may be high enough to cause water vapor to undergo a phase transition to a supercritical state. The equations of state allow for such systems to have enlarged radii without the need for hydrogen; the models by Zeng et al. (2019) do not include this critical effect, whereas other models, such as those of Mousis et al. (2020), make these considerations and arrive at vastly different mass-radius relations.

Having explored the Zeng et al. (2019) model, we argue that there are significant observational and theoretical problems that need to be resolved before further analysis can be made.

1.4.3 Stellar X-ray and Ultraviolet (XUV) Irradiation

This section will briefly describe the role of XUV radiation in shaping the histories and evolutions of exoplanets. For a specific analysis of XUV-induced photoevaporation, see chapter 2. X-rays and ultraviolet radiation are high-energy electromagnetic radiation in the wavelengths of $10^{-12} - 10^{-8}$ m and $10^{-8} - 4 \times 10^{-7}$ m, respectively. The high-

energy emission from stars is due to the hot corona: a thin plasma located above the photosphere. This emission is caused by thermal Bremsstrahlung powered by the star's magnetic dynamo; the strength of the dynamo depends on the stellar convection and rotation that is dependent on age. This mechanism, in its entirety, is ubiquitous for solar-type stars (from late-dF to dM; see [Vaiana et al., 1981](#)) and is an active area of research. We instead focus on the expected luminosity from G- and M-type stars that are two representative spectral types (see Fig. 1.8). Because of their simplicity and accuracy,

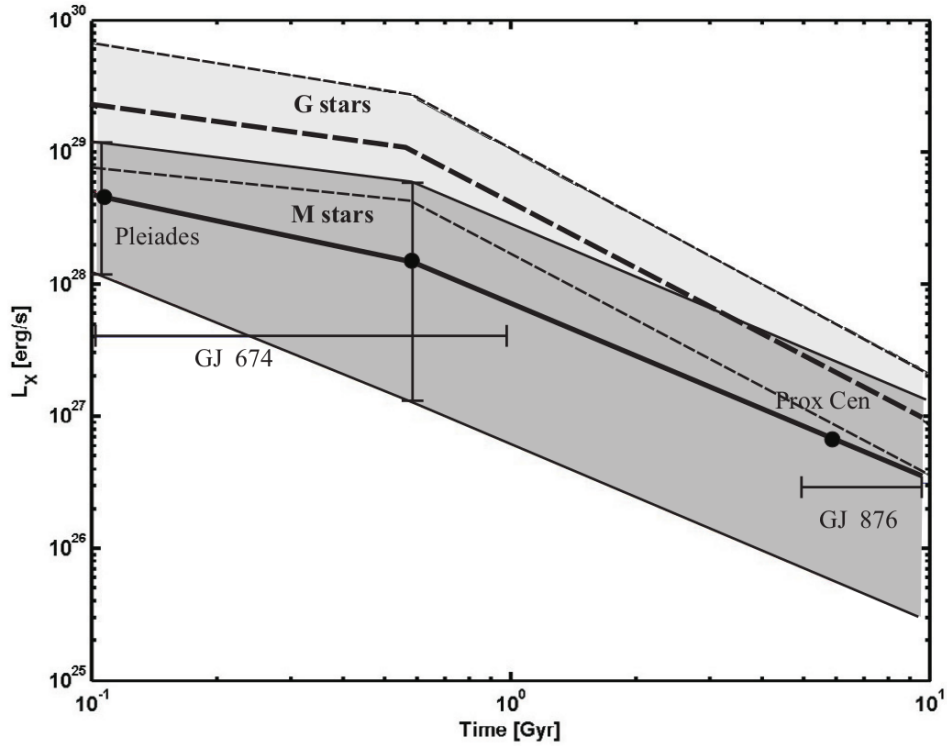


Figure 1.8: The temporal evolution of L_X of dM stars (solid lines; [Penz et al., 2008](#)) and dG stars (dashed lines; [Penz and Micela, 2008](#)). The thick lines give the median value, whereas the shaded areas are the dispersions. This graph is from [Penz et al. \(2008\)](#).

$$L_{X,G} = \begin{cases} 0.375L_{G,0}t^{-0.425}, & t \leq 0.6 \text{ Gyr} \\ 0.190L_{G,0}t^{-1.690}, & t > 0.6 \text{ Gyr} \end{cases}, \quad (1.2)$$

and

$$L_{X,M} = \begin{cases} 0.17L_{M,0}t^{-0.77}, & t \leq 0.6 \text{ Gyr} \\ 0.13L_{M,0}t^{-1.34}, & t > 0.6 \text{ Gyr} \end{cases}, \quad (1.3)$$

are widely used scaling laws for G-type (Penz et al., 2008) and M-type (Penz and Micela, 2008) stars. $L_{G,0} = 10^{29.35}$ erg s⁻¹ and $L_{M,0} = 10^{28.75}$ erg s⁻¹ are the mean log luminosities for G-type and M-type stars in the Pleiades, respectively. Note that L_x has an intrinsic spread around the mean value (the grey bands in Fig. 1.9). To find the X-ray luminosity, the relationship between X-ray and ultraviolet radiation is required; this was investigated by Sanz-Forcada et al. (2011) who provided the following function:

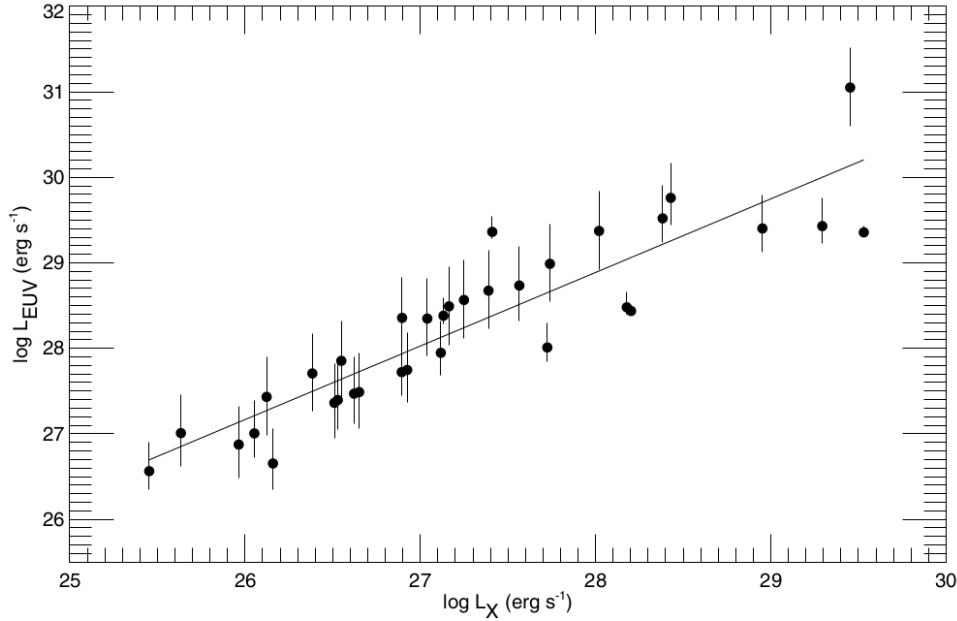


Figure 1.9: The trend in the X-ray and EUV luminosity of selected stars in the sample analysed by Sanz-Forcada et al. (2011). This image is from Sanz-Forcada et al. (2011).

$$L_{UV} = 10^{4.80 \pm 1.99} L_X^{0.860 \pm 0.073}, \quad (1.4)$$

whence the total XUV luminosity is

$$L_{XUV} = L_X + L_{UV}. \quad (1.5)$$

Planets exposed to high-energy radiation experience atmospheric evaporation; in sect. 2, this mechanism is explored thoroughly.

1.5 Scientific Impact and Layout of the Thesis

Exoplanetary observational data are limited, giving rise to degeneracies on the properties of super-Earths and sub-Neptunes; a robust understanding of planetary science is required to avoid ambiguities in our interpretation of the data. In light of this problem, this thesis analyzes super-Earth and sub-Neptune exoplanets from a theoretical perspective by considering data sets from various origins. The layout is as follows: in sect. 2, the effects of XUV-induced evaporation are indagated to explore how they shape the histories and future evolutions of planets hosting hydrogen-rich atmospheres. The aim of this section is to show how star-planet interactions play a crucial role that should not be overlooked when evaluating the characteristics of exoplanets. Observations and theory suggest that a star may fully erode away the primary and, potentially, secondary atmosphere of its host planet. Atmospheric spectroscopy is, therefore, impossible because such planets show (at most) a tenuous vaporized mineral atmosphere. These airless exoplanets remain elusive, which is the motivating factor of sect. 3 of this thesis, where we explore a novel technique wherein the Bond albedo of airless super-Earths can be used to make inferences on their internal structures and compositions.

Observations suggest that most exoplanets host atmospheres, so it is also necessary to discuss and explore their properties. The preponderance of such bodies has lead to a strong international movement focusing on the characterization of their atmospheres, so that their bulk properties can be constrained. It is commonly assumed that from the atmospheric spectroscopy of a sub-Neptune's photosphere, it is possible to predict the composition of the entire envelope. This assumption, however, is most probably incorrect because cloud formation and photochemistry lead to compositional stratification. For example, Earth's atmosphere is mostly nitrogen and oxygen, but above ~ 500 km, it is dominated by hydrogen and helium. Such issues are explored in sect. 4, where we first discuss atmospheric spectroscopy, and we then explore how atmospheric enrichment can be used to determine the processes occurring within.

Connecting the atmospheric composition of a planet with its surface or internal properties may, first, elucidate our poor understanding of their internal properties and how they evolve through time, and, second, reveal what planets are habitable or inhabited. The latter postulation is the motivating factor for sect. 5, where we focus on the presence

of alien life in extra-solar worlds and why water is the best medium for abiogenesis. In sect 6 potential future research is discussed in relation to the work presented in this thesis, and, finally, in sect 7, all the previously given information is discussed and summarized. Extra information and the derivations of some mathematical expressions are given in the appendix.

2 XUV-induced Evaporation

In this chapter, XUV-induced photoevaporation and its role in shaping the radius distribution will be analyzed. The work reported has been published in [Modirrousta-Galian et al. \(2020a\)](#), [Modirrousta-Galian et al. \(2020b\)](#), and [Modirrousta-Galian et al. \(2020c\)](#).

Chapter 1 discussed the core-powered atmospheric mass loss model and the geological-centered model as a possible cause of the bimodality. In this chapter we focus on the XUV-induced evaporation of primordial atmospheres and the expected influence on planet population trends. Unlike the other models, this mechanism has been observed for individual planets such as GJ 436 b (e.g., [Ehrenreich et al., 2015](#); [Bourrier et al., 2018c](#)). Before the effects of this mechanism are explored, it is necessary to discuss the underlying physics.

2.1 The Physics of XUV-induced Evaporation

2.1.1 First Approach: The Energy-Limited Equation

XUV-induced photoevaporation is a complex phenomenon, and the specific physics at work are highly situational. In the following, I will discuss the main processes presented in the literature. The way an exoplanet loses mass because of high-energy irradiation has not been settled yet. To begin understanding the physics of XUV-induced photoevaporation, we begin by analyzing the simplest form of atmospheric evaporation: the energy-limited equation that is derived from the first law of thermodynamics,

$$dU = Q - W \tag{2.1}$$

Where dU , Q , and W is the change in the internal energy, heat, and work, respectively. The assumption made is that there is no change in the internal energy of the system ($dU \simeq 0$), such that

$$Q \simeq W. \tag{2.2}$$

It is then assumed that the heat entering the system (Q) is given by the incoming high-energy photons,

$$\begin{aligned} Q &\simeq \varepsilon F_{XUV} A dt \\ &\simeq \varepsilon F_{XUV} \pi R_{XUV}^2 dt, \end{aligned} \quad (2.3)$$

where F_{XUV} is the energy flux from incoming XUV photons, A is the cross-sectional area of the planet, dt is a small unit of time, R_{XUV} is the radius at which the average XUV photon is absorbed (i.e., where the optical depth is 1 for XUV photons), and ε is the efficiency factor that accounts for effects such as the planetary albedo and molecular rotations. For mass to get lost, it has to be transported from R_{XUV} to the boundary of the Hill's sphere R_H (the location where particles are no longer gravitationally bound to the planet). This prescription can be expressed as,

$$W \simeq \frac{GM_p dM}{R_{XUV}} - \frac{GM_p dM}{R_H}, \quad (2.4)$$

where G , M_p , and dM are the gravitational constant, the mass of the planet, and a small unit of mass to be removed. To simplify this equation, we can define the parameter $K = 1 - R_{XUV}/R_H$,

$$W \simeq \frac{GM_p K dM}{R_{XUV}}. \quad (2.5)$$

Putting this all together gives,

$$\varepsilon F_{XUV} \pi R_{XUV}^2 dt \simeq \frac{GM_p K dM}{R_{XUV}}, \quad (2.6)$$

such that

$$\frac{dM}{dt} \simeq \varepsilon \frac{\pi R_{XUV}^3 F_{XUV}}{GM_p K}. \quad (2.7)$$

Because R_{XUV} is hard to calculate, it is common to approximate $R_{XUV} \rightarrow R_P$, so that

$$\frac{dM}{dt} \sim \varepsilon \frac{\pi R_P^3 F_{XUV}}{GM_p K}. \quad (2.8)$$

This is the most common form of the energy-limited formula. Although this method is well suited for gaseous giants, it generally fails when applied to super-Earths and sub-Neptunes. For example, it does not consider that particles have a velocity distribution, fast winds

can form, and that the planet's effective temperature influences mass loss.

2.1.2 Second Approach: Strong Atmospheric Evaporation

When thermal effects are included, the atmosphere inflates and experiences high-speed winds. Once these winds become supersonic, atmospheric gases may quickly achieve escape velocities, so the atmosphere ‘boils off’ (Owen and Wu, 2016; Kubyshkina et al., 2018b; Mordasini, 2020). In this scenario, the point at which gases have supersonic velocities is inside the atmosphere. By definition, because the speed of sound has been surpassed, information can no longer travel downwards, so mass-loss is independent of the exospheric properties. One must therefore perform a fluid-dynamical simulation to encapsulate the thorough complexity of this mass-loss regime (see Watson et al., 1981; García Muñoz, 2007; Tian et al., 2008);

$$\frac{\partial}{\partial t} (r^2 \rho_s) = -\frac{\partial}{\partial r} [r^2 \rho_s (u + u_s)] + r^2 \dot{\rho}_s, \quad (2.9a)$$

$$\frac{\partial}{\partial t} (r^2 \rho u) = -\frac{\partial}{\partial r} [r^2 (\rho u^2 + P)] + r^2 \rho f_{ext} + 2Pr, \quad (2.9b)$$

$$\frac{\partial}{\partial t} (r^2 \rho E) = -\frac{\partial}{\partial r} [r^2 (\rho E + P) u + r^2 q] + r^2 (\rho u f_{ext} + Q_{net}), \quad (2.9c)$$

where Eq. 2.9a, 2.9b and 2.9c are the equations of continuity, motion, and energy, respectively, for a spherically symmetric flow of an inviscid, multicomponent gas. t is the time elapsed, r is the radial distance from the center of the planet, ρ_s is the mass density of gas species s , ρ is the total mass density, u is the bulk velocity, u_s is the diffusion velocity of species s , P is the pressure, E is the total energy density, f_{ext} is the external force, q is the heat flux, and Q_{ext} is the net energy deposition rate. Solving the above equations shows that the true mass-losses may be up to $\sim 10^9$ times greater than those predicted by the energy-limited equation. From Fig. 2.1, it can be seen that once the Jeans parameter, Λ , is smaller than ~ 30 , the Energy-limited and Hydro-based models begin diverging. Therefore, to an adequate approximation, the Energy-limited equation can be used for $\Lambda \gtrsim 30$, and the Hydro-based equation for $\Lambda \lesssim 30$.

To conceptually explain why the two models deviate, we consider the limiting case where XUV photons are no longer the dominant heating factor; in this scenario, the bolometric

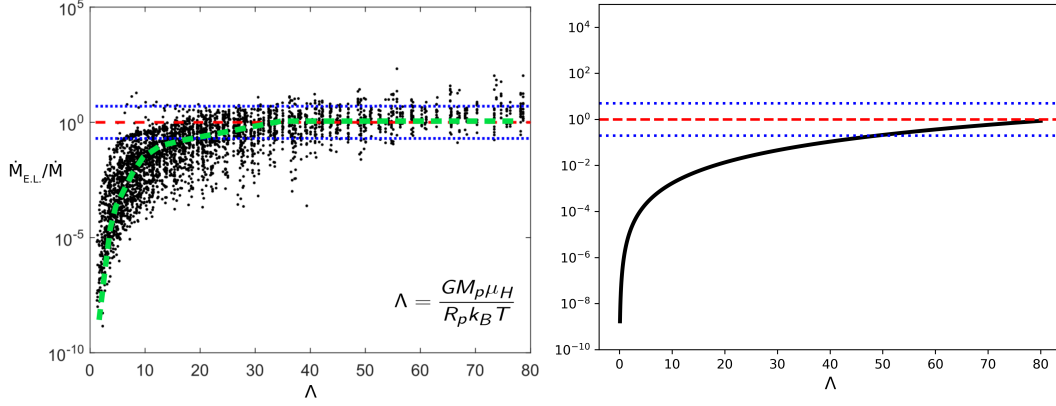


Figure 2.1: *Left:* The y-axis is the ratio between the Energy-limited (E.L.) equation and a full hydrodynamic model, and the x-axis is the Jeans parameter (Λ) that describes the ratio between the thermal and gravitational effects acting on atmospheric particles; μ_H is the mass of a hydrogen atom and κ_B is Boltzmann's constant. The green line is the Hydro-based model, the red line is the value at one, and the blue lines are the values at 0.2 and 5. This image has been adapted from Figure 3 in [Kubyshkina et al. \(2018a\)](#). *Right:* The simple model given by Eq. 2.16. Whereas it does not perfectly match the figure on the left, it follows a similar trend, diverges at small values of Λ , and converges to unity at greater Jeans parameters.

flux heats the atmosphere and causes its boil off. Because gases attain supersonic radial velocities, the Brownian motion of individual particles can be ignored, so escaping winds cannot directly interact with the hydrostatic gases below. The mass-loss rate is, therefore, given by,

$$\frac{dM}{dt} = 4\pi R_p^2 \mu n \bar{v}, \quad (2.10)$$

where μ is the mean molecular mass of the atmosphere, n is the particle number density at distance R_p , and \bar{v} is the average wind velocity. Note that \bar{v} does not need to be the escape velocity, v_{esc} , because the bolometric flux is heating up the gas and constantly causing its expansion. The velocity is found through the following relation,

$$\bar{v} = \frac{P}{F}, \quad (2.11)$$

where P is the incoming bolometric power and F is given by the gravitational force F_G . Whence,

$$\bar{v} = \frac{\pi R_p^2 F_{bol}}{F_G}, \quad (2.12)$$

but we know that the gravitational force is balanced by the kinetic gas pressure,

$$F_G = F_{gas}, \quad (2.13)$$

where,

$$F_{gas} = 4\pi R_p^2 n k_B T, \quad (2.14)$$

and k_B is Boltzmann's constant. Note that the gravitational and gas forces being balanced does not mean that the system is static; it instead suggests that gases are not constantly accelerating. Inputting Eq. 2.12 and Eq. 2.14 into Eq. 2.10 gives,

$$\frac{dM}{dt} = \frac{\epsilon \pi R_p^2 F_{bol} \mu}{k_B T}, \quad (2.15)$$

where ϵ is the efficiency factor that accounts for effects like the Bond albedo. Dividing Eq. 2.8 by Eq. 2.15 gives,

$$\frac{\dot{M}_{E.L.}}{\dot{M}} = \left(\frac{\epsilon}{\epsilon}\right) \left(\frac{F_{XUV}}{F_{bol}}\right) \Lambda^{-1}. \quad (2.16)$$

The above equation can be misleading because it gives the impression that the ratio is inversely proportional to Λ . However, $F_{bol} \propto T^4 \propto \Lambda^{-4}$, so the relationship is more complicated. By plotting Eq. 2.16 for adequately chosen parameters, the same trend is found as the figure on the left of Fig. 2.1. This simple prescription shows the difference between the assumptions made in the Energy-limited model and the Hydro-based model.

2.1.3 Summary of the Physics of Mass-Loss

Whereas our theoretical understanding of XUV-induced photoevaporation is still in its infancy, two major approaches have come to fruition: the Energy-limited and Hydro-based models. The former is more appropriate for systems where atmospheric gases are more strongly gravitationally bound to their host planet, such as gas giants. However, the latter approach incorporates more effects like variable particle velocities, wind formation, and thermal effects. Therefore, the Hydro-based equation better models super-Earths and sub-Neptunes, particularly when hot and having small masses.

2.2 Exoplanet Population Evolution Model

In this section I explore if XUV-induced photoevaporation is responsible for the bimodal radius distribution observed by [Fulton et al. \(2017\)](#).

In ([Modirrousta-Galian et al., 2020a](#)), 10^6 synthetic exoplanets with orbital period smaller than 100 days were evolved by exposing them to XUV irradiation from synthetic zero-age main-sequence stars. For each planet a different interior composition was set that ranged from 100 wt% Fe, through to 100 wt% MgSiO₃, and to 100 wt% H₂O ice, with varying hydrogen envelope sizes that varied from 0 wt% (a negligible envelope) to 100 wt% (a negligible core). The adopted mass-radius models for exoplanets before their evolution are shown below,

pure iron ([Zeng and Sasselov, 2013; Zeng et al., 2016](#)),

$$\frac{R_{\text{Fe}}}{R_{\oplus}} = 0.815 \times \left(\frac{M_p}{M_{\oplus}} \right)^{1/4.176}, \quad (2.17a)$$

rocky with ~ 1 wt% H₂-rich envelope ([Zeng and Sasselov, 2013; Zeng et al., 2016](#)),

$$\frac{R_{\text{Rock+H}_2}}{R_{\oplus}} = 1.410 \times \left(\frac{M_p}{M_{\oplus}} \right)^{1/3.905}, \quad (2.17b)$$

and 100 wt% cold H₂ planet ([Becker et al., 2014; Zeng et al., 2019](#)),

$$\frac{R_{\text{H}_2}}{R_{\oplus}} = 4.106 \times \left(\frac{M_p}{M_{\oplus}} \right)^{1/5.010}. \quad (2.17c)$$

The post-evolution mass-radius models are: remnant cores ([Mocquet et al., 2014](#)),

$$\frac{R_{\text{Remnant Core}}}{R_{\oplus}} = 0.469 \times \left(\frac{M_p}{M_{\oplus}} \right)^{1/3}, \quad (2.18a)$$

Earth-like planet ([Zeng and Sasselov, 2013; Zeng et al., 2016](#)),

$$\frac{R_{\text{Rock}}}{R_{\oplus}} = 1.007 \times \left(\frac{M_p}{M_{\oplus}} \right)^{1/3.7}, \quad (2.18b)$$

and pure H₂O planet (Zeng and Sasselov, 2013; Zeng et al., 2016),

$$\frac{R_{\text{H}_2\text{O}}}{R_{\oplus}} = 1.410 \times \left(\frac{M_p}{M_{\oplus}} \right)^{1/3.905}. \quad (2.18c)$$

We understand that planets show more complexity than what the above-shown polytropic relations portray; for example, inflated hydrospheres (water-rich atmospheres; Mousis et al., 2020) and hot enlarged rocky planets (Jespersen and Stevenson, 2020) are possible configurations that are not considered in our simple model. We also adopted the planetary ages, orbital parameters, and masses in accordance with current exoplanet statistics as given in the NASA Exoplanet Archive; full details can be found in sect. 2 and Table 3 of (Modirrousta-Galian et al., 2020a). Nevertheless, the simple prescription adopted allows for an analysis of atmospheric evaporation to determine the evolution of super-Earths and sub-Neptunes. The following algorithm is used,

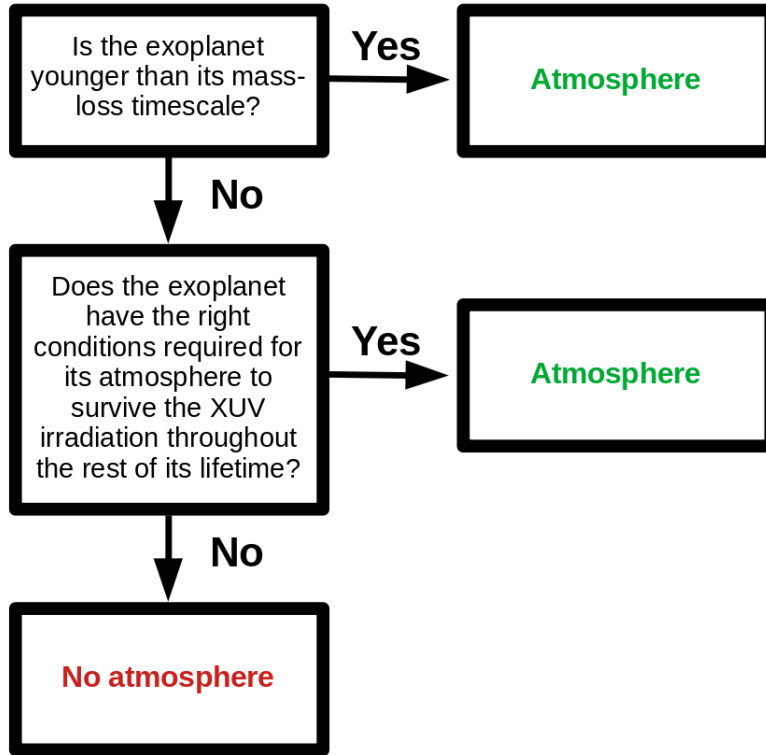


Figure 2.2: Flowchart showing the path our code took when evolving the exoplanets.

The mass-loss timescale is defined as

$$\tau = \frac{M_{env}}{\dot{M}_{env}}, \quad (2.19)$$

where τ is the timescale, M_{atm} is the mass of the hydrogen-rich envelope, and \dot{M}_{env} is the mass-loss rate given by the models of [Kubyskhina et al. \(2018a\)](#). Therefore, if a planet's age were shorter than the mass-loss timescale, the planet would still host its atmosphere. The second condition concerns whether a planet would eventually lose its atmosphere, this is not the same as the first condition as a star's X-ray and ultraviolet (XUV) luminosity drops precipitously with age. Therefore, Eq. 2.19 is only applicable when XUV irradiation is significant, as seen in Fig. 2.3. To evaluate the second condition,

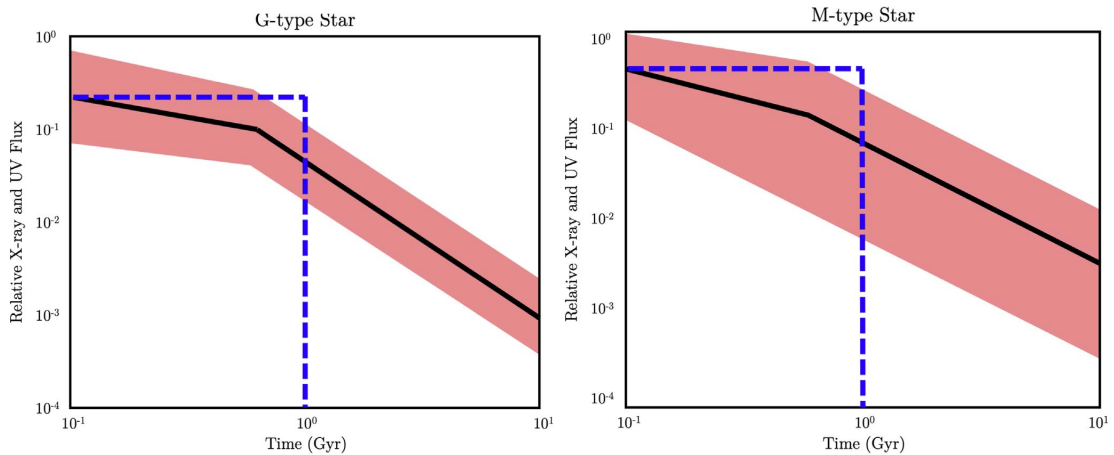


Figure 2.3: Relative XUV flux of G-type and M-type stars. The red shaded region marks the measurements from [Penz and Micela \(2008\)](#), [Penz et al. \(2008\)](#) and [Sanz-Forcada et al. \(2011\)](#). The black line is the average measured XUV flux. The blue dashed line shows the step function we adopted in our model.

we adopted the models by [Locci et al. \(2019\)](#) that provide the evolutionary pathways of gaseous planets as they experience X-ray and ultraviolet irradiation. Whereas [Locci et al. \(2019\)](#) uses the Energy-limited equation, the planets in our simulation for which this model applies are those with higher Jeans parameters, making the Energy-limited approach an appropriate approximation. As explained later in sect. 2.6, we can use the [Locci et al. \(2019\)](#) approach because our planetary models are oversimplified; they do not consider the interior heat flux and, therefore, do not produce very enlarged radii. Because of this assumption, the Jeans parameters of super-Earths and sub-Neptunes with medium or low XUV irradiances are large enough for the difference between the Hydro-based and Energy-limited models to be small. Given the above, for our simulation setup, the [Locci et al. \(2019\)](#) model makes it possible to predict what planets will be resilient to XUV irradiation throughout their lifetimes.

The last step of the algorithm stated that the remaining planets would lose their primordial

envelopes.

Our simulations replicate the bimodal distribution of exoplanet radii (see Fig. 2.4). We find that the majority of planets in the first peak are rocky, which is compatible with the results from [Owen and Adams \(2019\)](#), [Jin and Mordasini \(2018\)](#), and [Swain et al. \(2019\)](#). Moreover, we also find that the $\sim 2.4R_{\oplus}$ radius peak mainly comprises exoplanets with large primordial envelopes.

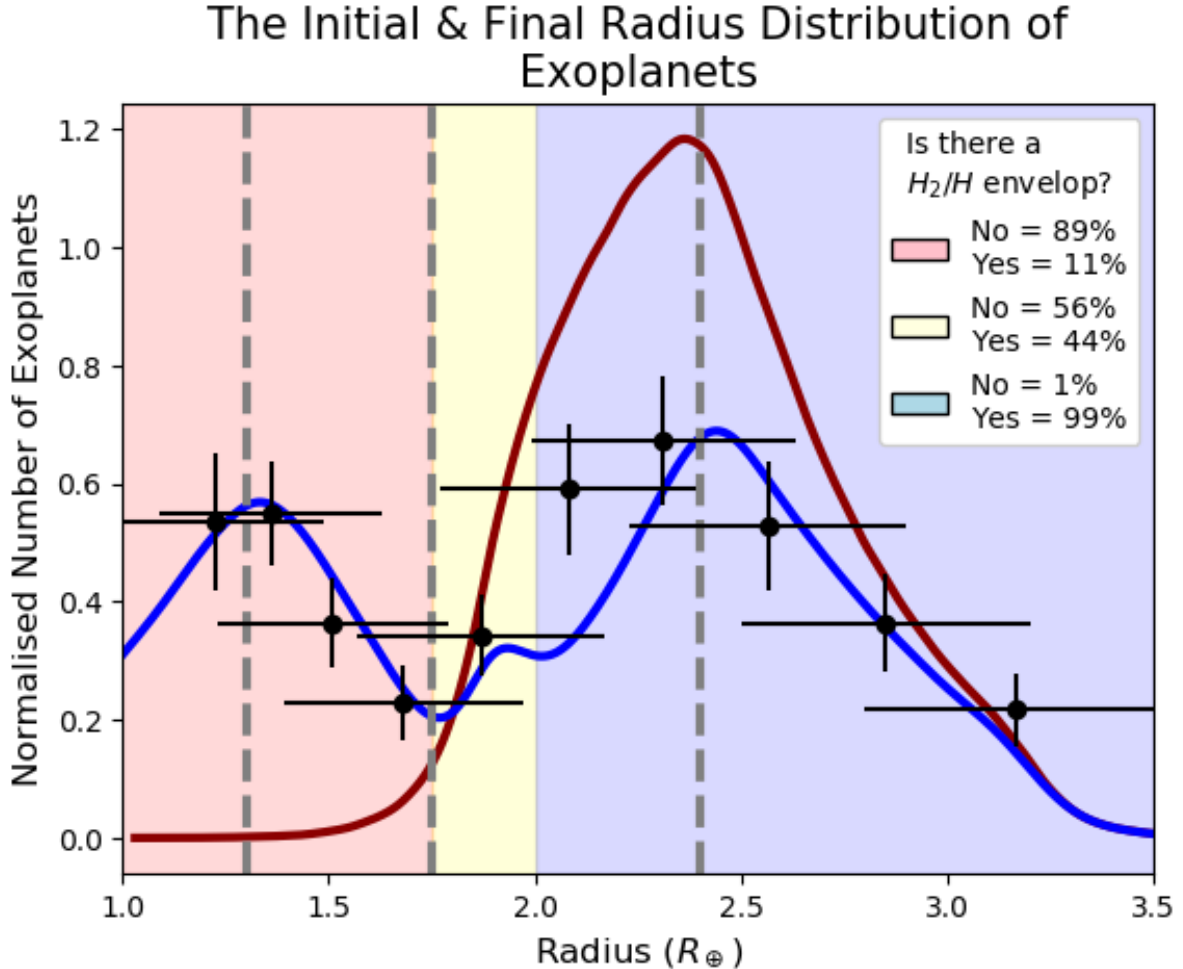


Figure 2.4: The final (blue line) and initial (red line) distributions of exoplanet radii for periods ≤ 100 days, as obtained by our model. The gray lines show the two peaks and the minimum discovered by [Fulton et al. \(2017\)](#). The data points with the uncertainties correspond to the values given in Table 3 and Figure 7 of [Fulton et al. \(2017\)](#). The light-red, light-yellow, and light-blue regions correspond only to the final radius distribution’s rocky first peak, the remnant core (mega-Earth)-rich region, and the hydrogen-rich worlds of the second peak, respectively. For each region, we report the statistics of the envelope abundances.

Furthermore, we argue that in order to reproduce the distribution by ([Fulton et al., 2017](#)), a paucity of exoplanets with masses above $\sim 8M_{\oplus}$ is necessary. Additionally, our

best-fit result predicts an initial flat distribution in exoplanets for $M_P \lesssim 8M_\oplus$ with a strong deficiency at $\lesssim 3M_\oplus$ (see Fig. 2.5). Another significant result is that we reproduce

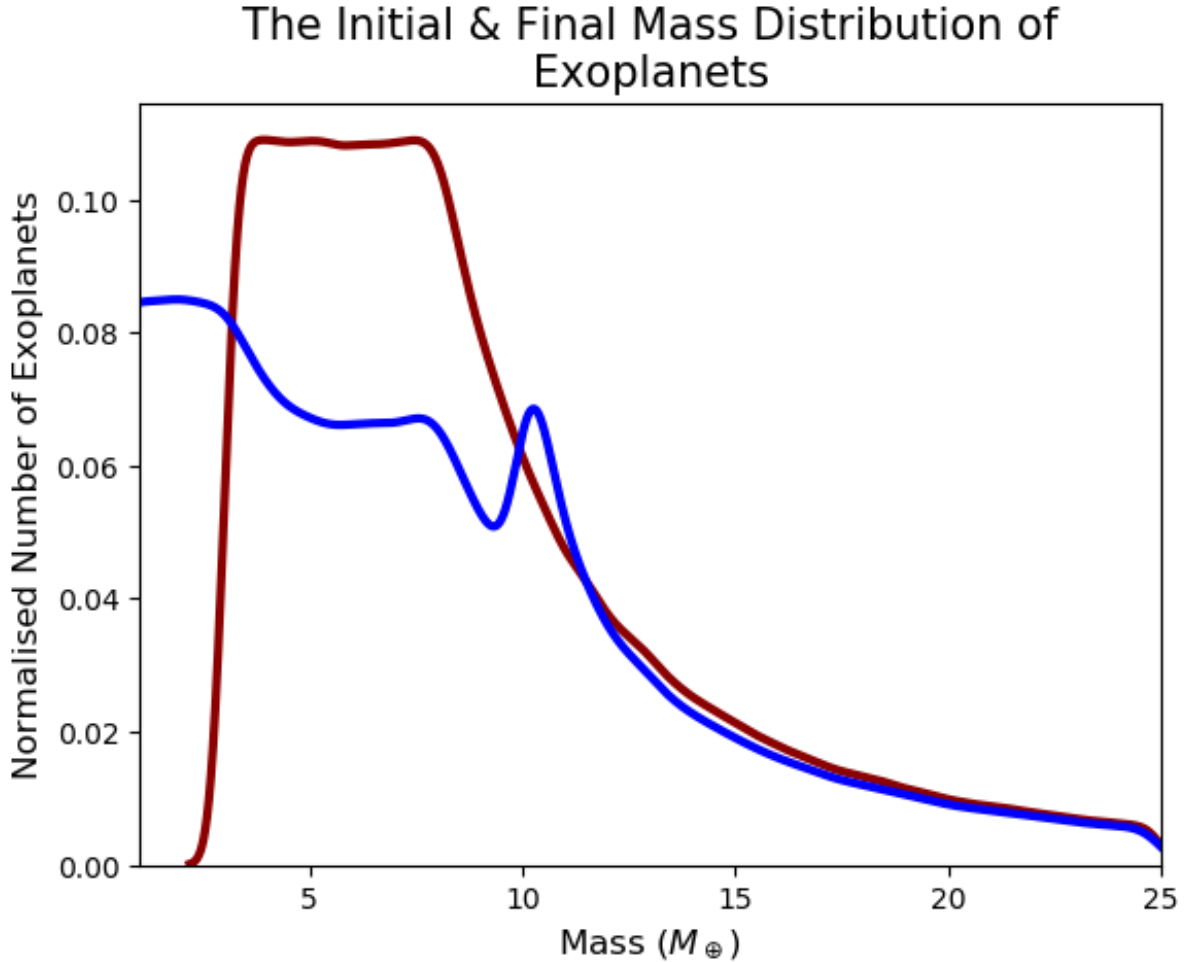


Figure 2.5: The predicted final (blue) and initial (red) mass distributions of exoplanets whose radii are distributed according to Fig. 2.4. All planets have periods ≤ 100 days.

the sub-Jovian desert as shown in Fig. 2.6. Nevertheless, our model is novel in several ways. For one, it adopts the Hydro-based mass-loss equation instead of the energy-limited equation (or a variant of it). Adopting a more complete mass-loss model is essential when dealing with irradiated super-Earths and sub-Neptunes as thermal effects play an important role in atmospheric removal (Lammer et al., 2016; Owen and Wu, 2016; Fossati et al., 2017; Kubyskhina et al., 2018a, for a more thorough explanation see sect. 2.1). In addition, we make predictions for the mass distribution of super-Earths and sub-Neptunes that are compatible with observational data (e.g., Howard et al., 2010; Marcy et al., 2014; Malhotra, 2015), even though we acknowledge that the masses of small exoplanets are not well constrained. Our results are also compatible with planetary formation models because

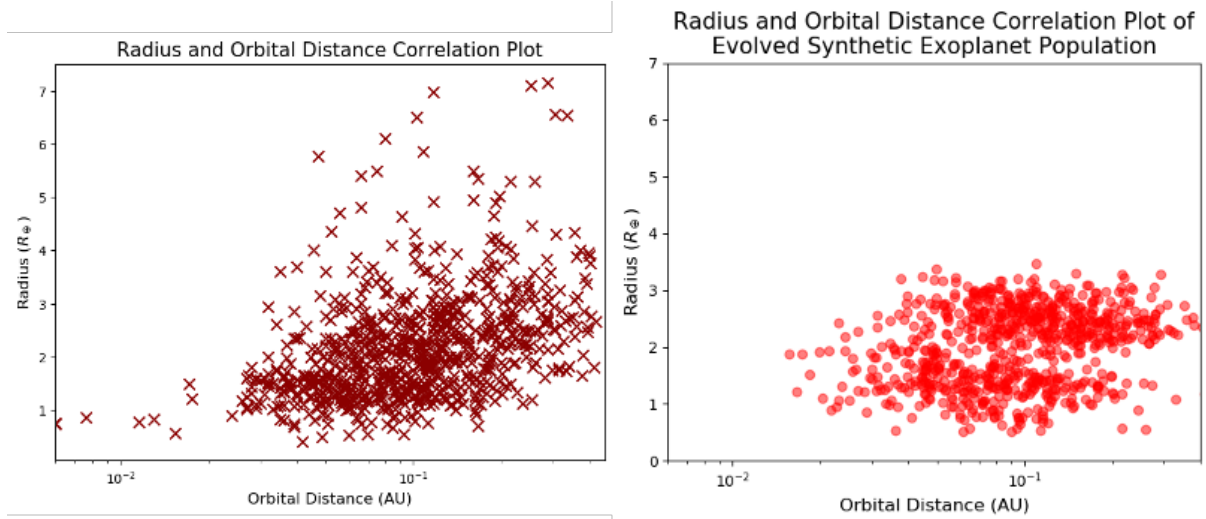


Figure 2.6: A comparison between the sub-Jovian desert from observational data (left) and our simulations (right, [Modirrousta-Galian et al., 2020a](#)). Both graphs have 787 data points.

a reduction in the frequency of exoplanets with masses $\gtrsim 10M_{\oplus}$ has long been predicted (e.g., [Ida and Lin, 2004, 2005, 2008](#); [Mordasini et al., 2009](#)). This drop in frequency is thought to occur as the result of the limited temporal interval available to form a core of critical mass before the dispersal of the disk gas (e.g., [Bitsch et al., 2015](#); [Johansen et al., 2019](#)). Because of this mechanism, planetary formation models predict that there should be fewer planets with masses between $\sim 10M_{\oplus}$ and $\sim 100M_{\oplus}$, which our models also predict.

Curiously, our model also predicts that there is a paucity in the number of planets with masses $\lesssim 3M_{\oplus}$. This paucity is probably due to instrumental limitations because it becomes exceedingly difficult to detect planets with small radii. However, the most interesting claim we make is the presence of a transition region from $1.75 - 2R_{\oplus}$ and the presence of remnant cores. As shown in Fig. 2.4, there is approximately an equal number of bodies with and without primordial atmospheres in the transition region. This transition region is corroborated by observational data ([Swain et al., 2019](#)).

Remnant cores are bodies that initially had large primordial atmospheres and then fully or partially lost them. Their original atmospheres were massive enough to cause a substantial compression of their interior embryos. Therefore, whereas many planets may have originally hosted hydrogen-rich atmospheres and then lost them, remnant cores are unique as they have densities greater than what is expected from a typical geochemical

composition (Mocquet et al., 2014). After a long enough time, however, these bodies may decompress and exhibit more typical densities (Mocquet et al., 2014). Some of the remnant cores may also be mega-Earth candidates; telluric planets with masses greater than $10M_{\oplus}$. These planets have masses greater than the previously mentioned critical mass, so a sizeable primordial atmosphere was likely initially accreted. Our simulations predict a noticeable contribution of ultra-dense cores (see Fig. 2.7) and mega-Earths (the 1% abundance of telluric planets in the second peak shown in Fig. 2.4 and the small peak in Fig. 2.5).

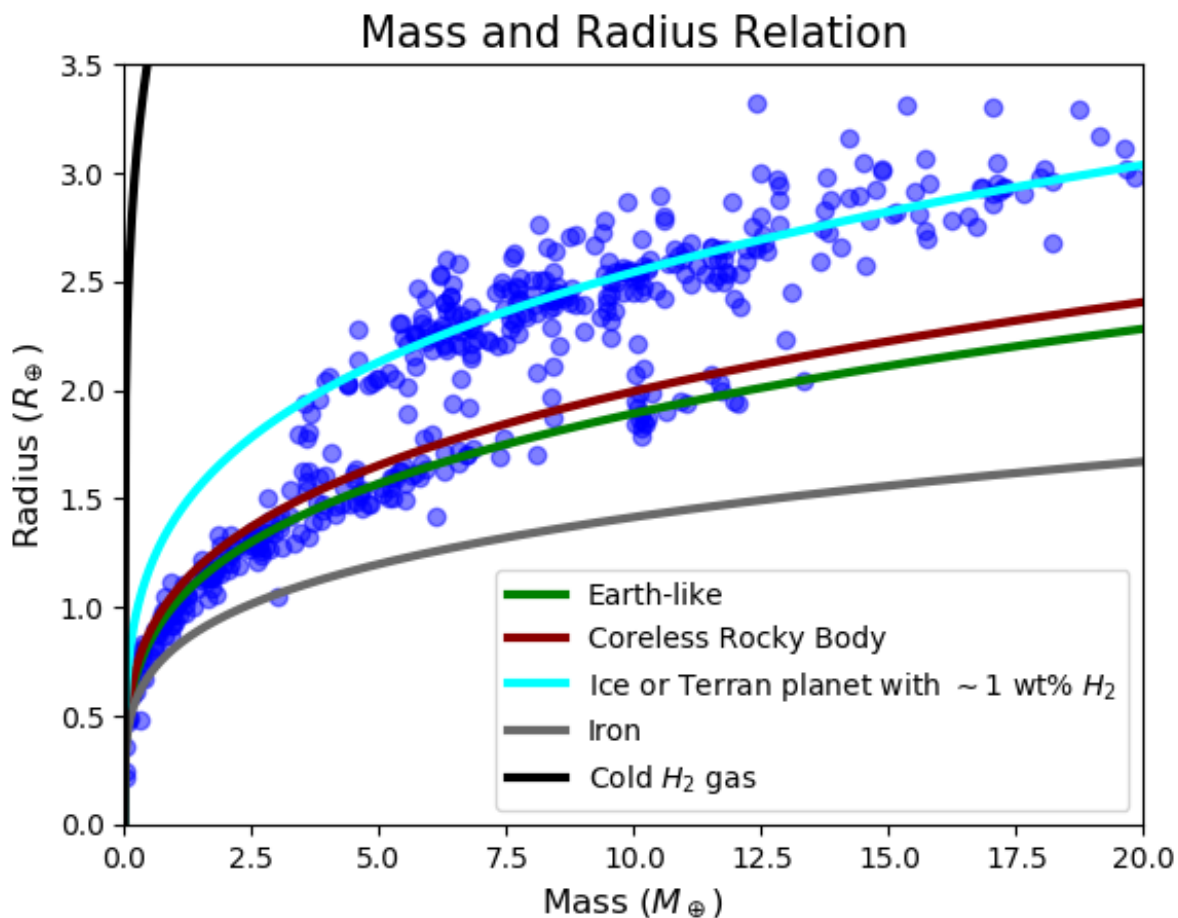


Figure 2.7: Mass and radius distribution of 500 of our synthetic exoplanets after undergoing photoevaporation. All mass and radius curves come from Zeng and Sasselov (2013) and Zeng et al. (2016) except for the cold H_2 curve, which originated from the equations of state by Becker et al. (2014) that were then adapted by Zeng et al. (2019). The scale parameter of the laplacian function of the radii was set to 0.05 (i.e., a standard deviation of $\sqrt{2}/20$).

Several mega-Earth candidates have been observed such as BD + 20594 b that has a mass and radius of $16.3 \pm 6.0M_{\oplus}$ and $2.2 \pm 0.1R_{\oplus}$ (Espinoza et al., 2016), K2-66 b with

$21.3 \pm 3.6 M_{\oplus}$ and $2.50 \pm 0.3 R_{\oplus}$ (Simukoff et al., 2017), and Kepler-145b with $37.1 \pm 11.6 M_{\oplus}$ $2.65 \pm 0.08 R_{\oplus}$ (Xie, 2014), respectively. In addition, there are several planets with extreme densities that could be remnant cores such as TOI-849b (Armstrong et al., 2020) and GJ 357 b (Jenkins et al., 2019, although there is ambiguity in the mass and radius measurements, see Luque et al. (2019)). Remnant cores are of great interest to the exoplanetary community as they could reveal insights on the interior structure and formation of gaseous bodies like Jupiter or Saturn.

2.3 Why Remnant Cores Matter

This section discusses the importance of remnant cores to understand the interior structure of gaseous bodies like Jupiter or Saturn⁶.

There is a symbiotic relationship between solar system and exoplanet science. For example, whereas exoplanet scientists rely on the geological, atmospheric, and formational models initially developed for planets in our solar system, the large number of exoplanets makes it possible to test these models statistically. In this section, a summary is given on the physics of Jupiter and Saturn and how this relates to remnant core exoplanets.

A thorough analysis of the historical (theoretical) research on Jupiter’s interior can be found in Stevenson (2020). We instead begin by discussing Perri and Cameron (1974): one of the first models that focused on the formation of Jupiter from the primordial solar nebula model. Based on the assumption that Jupiter formed adiabatically, they predicted that its embryo has a mass of $50 - 100 M_{\oplus}$; only with an embryo of this size would the surrounding nebular gas become hydrodynamically unstable and collapse to form the atmosphere. However, this is incorrect for two critical reasons; first, Jupiter did not form adiabatically. An adiabatic formation means that no energy is lost, so when the surrounding protoplanetary disk dissipated (usually in ~ 10 Myr), there would have been an imbalance between the pressure inside of Jupiter and outside. Therefore, it is essential for energy to be lost during the formation process so that a planet can remain in hydrostatic equilibrium once the nebular gas is lost. The second reason is that the radiative energy emitted from such a formational path would have been greater than our

⁶The content of this section is inspired by Stevenson (1982b) and the Ge131: Planetary Structure and Evolution classes taught at the California Institute of Technology.

Sun’s luminosity (Stevenson, 1982a); this is not physically possible.

A more correct model assumes that Jupiter formed radiatively (Mizuno et al., 1978; Mizuno, 1980; Stevenson, 1982a) because this would allow for some energy to be lost. This model still lacks many complexities found in more modern studies, such as phase changes, helium rain, and rotational effects. However, this prescription is still useful for getting an inference on the interior structure of Jupiter. As shown by the calculations in sect. A.1.1 of the appendix, a radiative formation would suggest that an embryo larger than $\sim 10M_{\oplus}$ undergoes runaway accretion and become a gas giant. Therefore, as a rough approximation, it can be assumed that Jupiter’s embryo is of this mass, but what happened to it once the planet was fully formed? Perhaps, the embryo became very dense and remained roughly intact; another possibility, however, is that the surrounding envelope eroded it and intimately mixed its constituent materials within the envelope. Both of these models can be tested for the case of Jupiter to see if they can provide testable predictions. The equation of state of large gaseous (hydrogen-rich) bodies, is approximately given by (French et al., 2012; Stevenson, 2020)⁷

$$P \simeq K\rho^2, \quad (2.20)$$

where P is the pressure, K is a compositional constant ($2.1 \times 10^5 \text{ kg}^{-1} \text{ m}^5 \text{ s}^{-2}$), and ρ is the density. The simple nature of the polytrope is purely coincidental because it is one of the only polytropic indices that is analytically solvable. Solving Eq. 2.20 (see sect. A.1.2 for the full derivation) provides the radius of a synthetic pure gaseous body with a Sun-like abundance of hydrogen and helium,

$$R_{H_2/He} = \sqrt{\frac{\pi K}{2G}}. \quad (2.21)$$

By assuming a well-mixed model, the following simple equation for the radius is attained,

$$R_{H_2/He} = (1 - z)\sqrt{\frac{\pi K}{2G}}, \quad (2.22)$$

where z is the heavy material mass fraction. The full derivation can be found in sect. A.1.3.

⁷This formula is an adequate approximation for the interior of Jupiter, but it fits poorly near the surface: a more correct model is $P \simeq K_1\rho^2 + K_2\rho^{1.45}$ (Markham and Stevenson, 2018). However, for illustrative purposes, we will adopt the simpler model.

Note that Eq. 2.22 is independent of the mass but strongly dependent on the heavy material mass fraction. In other words, Saturn has a smaller radius than Jupiter because it is substantially more enriched. Applying Eq. 2.22 to Saturn shows that it is consistent with a heavy material mass fraction of $\sim 16M_{\oplus}$, whereas Jupiter has a significantly lower enrichment.

For reference, a contrasting model can be tested in which all the heavy materials are located in a central core. Incidentally, the radius predicted with this approach is not only almost identical to the one given by Eq. 2.22, but the radius also has the same functional form. In other words, this shows that it is not possible to determine the distribution of elements in gas giants with only the mass and radius values. The complete derivation for this cored model is found in sect. A.1.4 of the appendix.

As explained in [Stevenson \(2020\)](#), knowing the moment of inertia can help to constrain the distribution of matter inside of a planet. In the case of Jupiter, a diffuse core better fits the observed data than a solid core or a well-mixed interior (see, [Leconte and Chabrier, 2012](#)). However, for exoplanets, it is generally not possible to know their moments of inertia, so it is difficult to determine their interior structures. Instead, by analyzing the statistics of remnant cores, it may be possible to resolve physical trends that give clues on their histories. If planetary embryos usually get destroyed in gas giants, remnant cores would be rare. Conversely, if the embryos remain mostly intact, one would expect a population of either very dense bodies or mega-Earths ([Mocquet et al., 2014](#); [Armstrong et al., 2020](#)). This prescription shows the intimate connection between the exoplanetary and solar system fields.

2.4 The Curious Case of 55 Cancri e

In the previous section, we presented our XUV-evaporation model. Whereas our model may explain the general behavior of sub-Neptunian planets with primordial atmospheres, it cannot explain the anomalous behavior of bodies like 55 Cancri e. Having a mass and radius of $8.58 \pm 0.43M_{\oplus}$ and $1.947 \pm 0.038R_{\oplus}$, respectively, its density is consistent with a rocky core engulfed by a primordial atmosphere (e.g., [Bourrier et al., 2018a](#); [Crida et al., 2018](#)). Additionally, spectroscopic signatures further support this hypothesis (e.g., [Tsiaras et al., 2016](#); [Esteves et al., 2017](#)), although some dispute these claims ([Jindal et al., 2020](#);

Zhang et al., 2021). The phase-curve data from 55 Cancri e appears contradictory as the day-side is consistent with not having an atmosphere due to its temperature being similar to the black-body model (~ 2300 K), whereas the night-side is compatible with a large envelope because of its high temperature of ~ 1400 K (Demory et al., 2016). Furthermore, given its tight orbit with its host star, strong atmospheric evaporation would be expected at a level that should be observable with currently available instruments, but XUV-induced atmospheric evaporation has not been detected so far (e.g., Ehrenreich et al., 2012; Bourrier et al., 2018b).

One potential solution is that 55 Cancri e has a large hydrogen reservoir dissolved in its magma oceans (Chachan and Stevenson, 2018) that leaks into the atmosphere and replenishes the lost gases. This mechanism is built on Henry’s law because it suggests that when a planet is young and hot, global magma oceans dissolve primordial gases within them. In the case of 55 Cancri e, it is estimated that ten times more hydrogen could be stored in the magma oceans than in the overlying envelope. Therefore, when one models the expected mass-losses, 55 Cancri e could have enough stored hydrogen to withstand the stellar irradiation for the remainder of its star’s lifespan. However, Chachan and Stevenson (2018) used the energy-limited mass-loss equation, which fails when applied to hot super-Earths like 55 Cancri e. This is because for low-mass low-density bodies, thermal effects play an important role in the evaporation of their primordial atmospheres (Lammer et al., 2016; Owen and Wu, 2016; Fossati et al., 2017; Kubyshkina et al., 2018a, ; for a more thorough explanation see sect. 2.1). Therefore, it is necessary to use a more complete model like the hydrodynamic approach (Kubyshkina et al., 2018a) that is based on fluid dynamical simulations. Using the model from Kubyshkina et al. (2018a), it can be shown that the predicted evaporation rates are high enough to remove the entire hydrogen reservoir in a few million years. Therefore, the storage of primordial atmospheres in magma oceans cannot explain why 55 Cancri e has a primordial atmosphere.

Another proposed solution involves a combination of tidal forces with orbital and rotational centrifugal forces. In Modirrousta-Galian et al. (2020b), it is argued that these effects could confine a hydrogen-rich atmosphere to the night-side, where it would be protected from the XUV irradiation. For this mechanism to take effect, there are two requirements; first, the bulk atmospheric composition would have to be primarily volcanic with a

smaller hydrogen component, and second, 55 Cancri e should have become tidally locked before losing its atmosphere. This prescription would result in the heavier species getting confined to latitudes $\lesssim 80^\circ$, while hydrogen is light enough to overcome the tidal, orbital, and rotational forces. Because of this disparity, hydrogen would have to slowly diffuse through the volcanic atmosphere to traverse into the day-side; this would lead to slow hydrogen leakage from the night-side to the day-side inhibiting atmospheric evaporation (see Fig. 2.8).

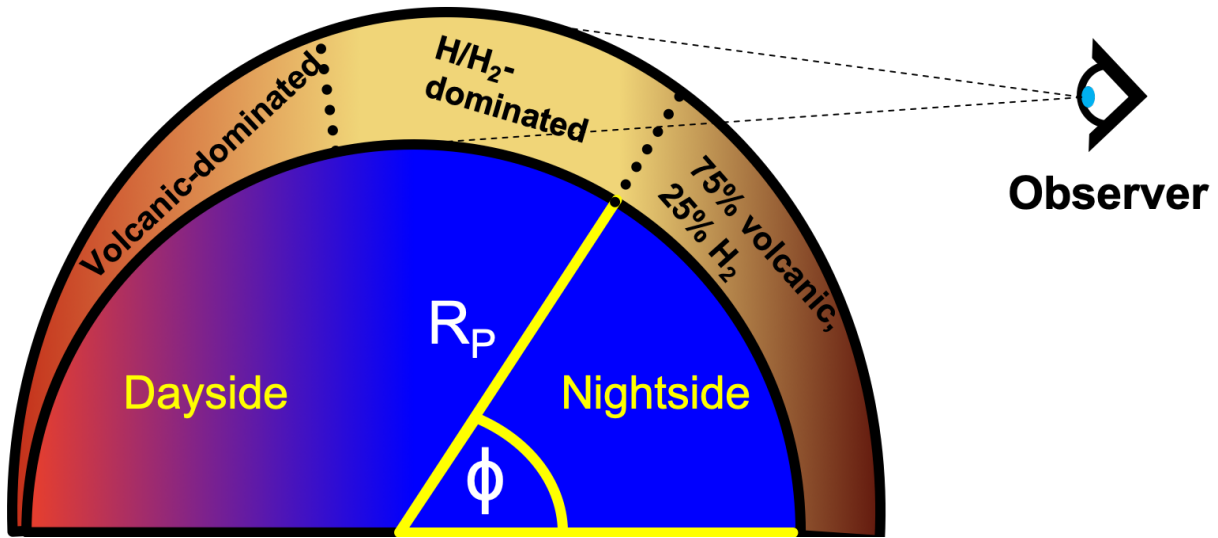


Figure 2.8: A simplified illustration of the atmospheric distribution predicted on some hot super-Earths with primordial atmospheres. This image does not show the atmospheric density at different latitudes.

This model is compatible with spectroscopic analyses suggesting that 55 Cancri e has a hydrogen-rich atmosphere (Tsiaras et al., 2016; Esteves et al., 2017), while also explaining why other studies have been unable to detect a significant evaporation rate (Ehrenreich et al., 2012; Bourrier et al., 2018b). However, it is important to note that Modirrousta-Galian et al. (2020b) adopts a two-dimensional geometry where the forces neatly couple together; a more rigorous approach would use three dimensions with spherical harmonics (Peale, 1999). This is a non-trivial problem that could be solved semi-analytically or through full hydrodynamic simulations.

55 Cancri e is a complex planet that warrants further research. Its curious nature and observability make it a focal point of future atmospheric characterization missions such as Ariel. Without better data, however, its nature will continue to remain nebulous.

2.5 GJ 357 b: A Super-Earth Orbiting an Extremely Inactive Host Star

In sect. 2.2 we discussed how XUV-induced photoevaporation could explain the bimodal distribution of exoplanet radii, and in sect. 2.4 we proposed a solution for the anomalous behavior of 55 Cancri e. To test the applicability of our models, we consider the super-Earth GJ 357 b, for which we have measurements of its host star's X-ray luminosity. With a mass, radius, and effective temperature of $1.84 \pm 0.31M_{\oplus}$, $1.22 \pm 0.08R_{\oplus}$, 525 ± 10 K, respectively, GJ 357 b is most probably a telluric planet, as shown in Fig. 2.9. GJ 357 b

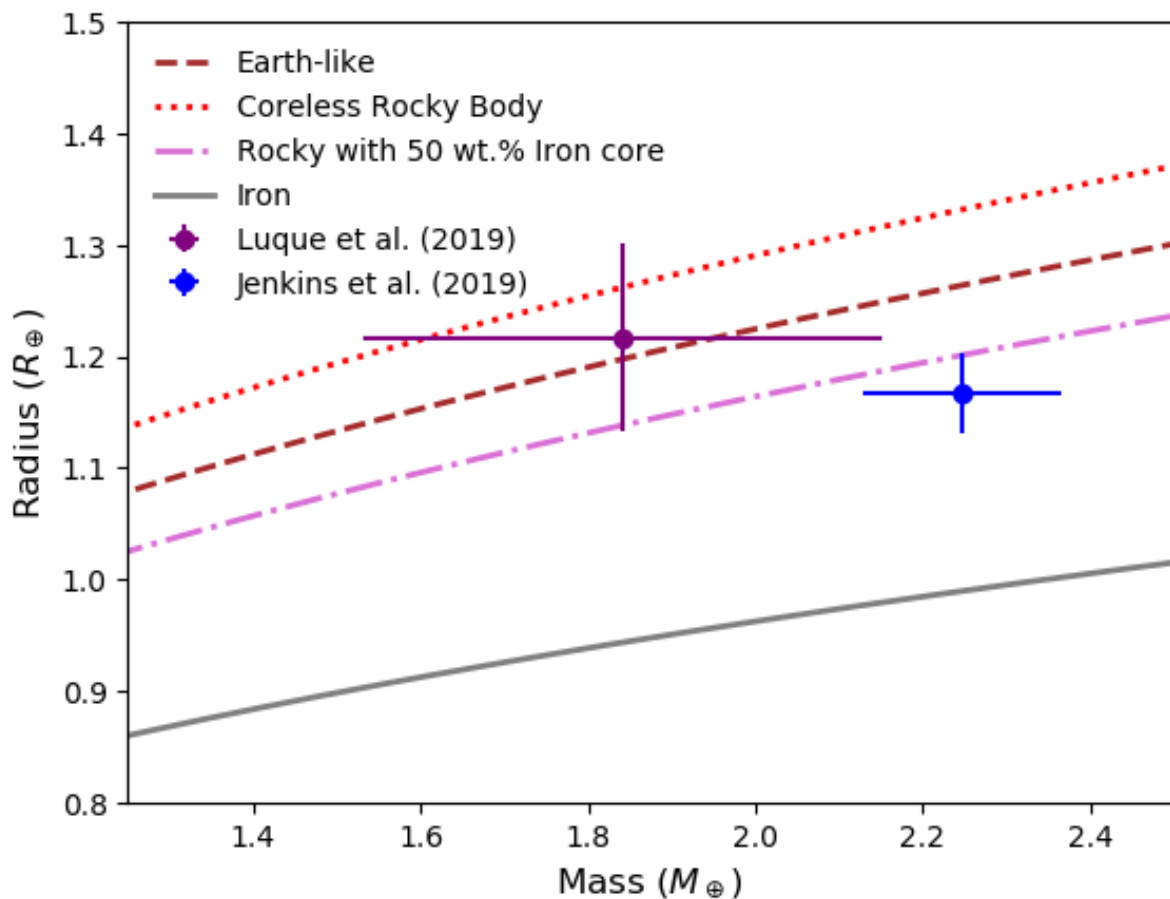


Figure 2.9: Mass vs. radius for GJ 357 b using the coreless rocky (red dotted line), Earth-like (dark red dashed line), rocky with a 50 wt.% iron core (purple dash-dot line), and pure iron (grey line) models from [Zeng and Sasselov \(2013\)](#) and [Zeng et al. \(2016\)](#). The values for the mass and radius and their uncertainties are those from [Luque et al. \(2019, purple\)](#) and [Jenkins et al. \(2019, blue\)](#).

is unique in our super-Earth catalogs as it orbits a star with one of the lowest X-ray luminosities ever observed (see Fig. 2.10): $\sim 10^{-6} L_x/L_{\text{bol}}$. The luminosity data was

acquired from a recent XMM-Newton observation (19th May 2019, Obs-ID 0840841501, PI: Stelzer). Based on this value, it is worth considering how such an inactive star would interact with its planet.

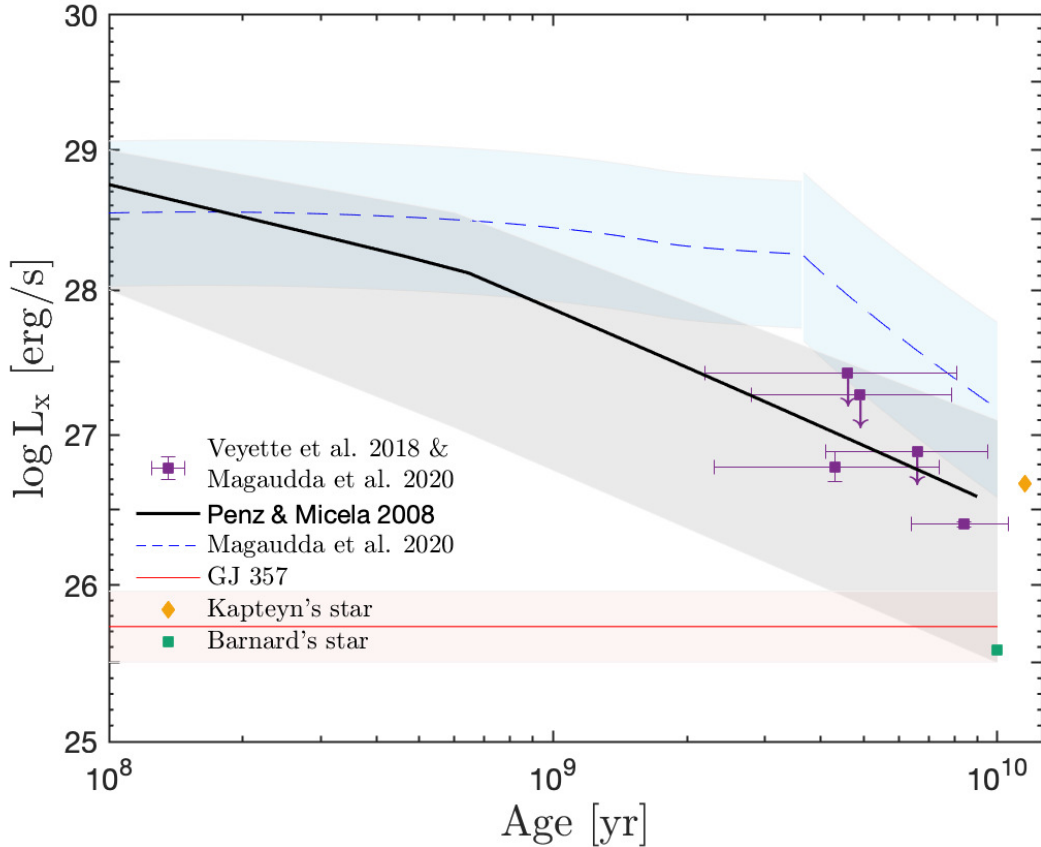


Figure 2.10: X-ray luminosity vs. age and the angular momentum evolution models of [Matt et al. \(2015\)](#). The empirical scaling law from [Penz and Micela \(2008\)](#) is shown. Two M stars with known ages, Barnard’s star (GJ 699) and Kapteyn’s star (GJ 191), are added to the plots for reference.

From the X-ray luminosity and the X-ray–age relationship from [Penz and Micela \(2008\)](#), shown in Fig. 2.10), the age of the star can be inferred. Assuming that the planet’s age is coeval with its host star’s, we estimated that GJ 357 b is at least ~ 5 Gyr old. Therefore, one can now do a backward reconstruction of the total hydrogen mass that could have been lost due to XUV-irradiation. It is important to note that this maximum hydrogen mass is probably not the primordial atmospheric reservoir GJ 357 b had in its early stages. Instead, this is the maximum mass possible, as any value greater than this would have survived through the irradiation history of the host star and would therefore not be consistent with the predicted telluric composition.

It is important to model the radius and mass evolution, the X-ray and ultraviolet radiation, and consider thermal effects to perform this backward reconstruction. For the radius evolution, we adopted the analytic model from [Lopez and Fortney \(2014\)](#),

$$R_p = R_c + 2.06R_{\oplus} \left(\frac{M_p}{M_{\oplus}} \right)^{-0.21} \left(\frac{f_{env}}{5\%} \right)^{0.59} \left(\frac{F_p}{F_{\oplus}} \right)^{0.044} \left(\frac{age}{5 \text{ Gyr}} \right)^{-0.18} \quad (2.23)$$

where R_p , R_c and R_{\oplus} are the planetary radius, the core's radius, and Earth's radius, respectively. M_p is the planetary mass, M_{\oplus} is Earth's mass, f_{env} is the atmospheric mass fraction, F_p is the amount of irradiation received by the planet, F_{\oplus} is the amount of irradiation received by Earth, and age is the age of the planet. As of writing, this is one of the most advanced mass-radius models for super-Earths as it includes the interior heat flux (via the age parameter), but it only works for ages greater than 100 Myr. Since XUV-evaporation occurs from as early as ~ 10 Myr, we assume a flat radiogenic flux from 10 – 100 Myr. For the X-ray evolution, we use the models from [Penz and Micela \(2008\)](#), whereas the scaling laws from [Sanz-Forcada et al. \(2011\)](#) are used for ultraviolet irradiation. Moreover, for the mass-loss model, we adopt the Hydro-based evaporation model from [Kubyskhina et al. \(2018a\)](#) as it includes thermal effects that are important for small and warm planets like GJ 357 b. Our models predict that GJ 357 had an initial X-ray luminosity of $\sim 10^{29}$ erg s $^{-1}$ and GJ 357 b could have hosted a theoretical maximum initial atmospheric mass of $\sim 38M_{\oplus}$ with a radius of $\sim 14R_{\oplus}$. Any initial mass smaller than $\sim 38M_{\oplus}$ would have been lost due to XUV-induced evaporation and would have therefore been compatible with the current telluric composition.

However, just because GJ 357 b may have lost its primordial atmosphere does not negate the possibility of hosting a secondary one; a secondary atmosphere can reveal much information on the interior structure and composition of super-Earths and sub-Neptunes. For instance, Saturn's moon, Titan, has an atmosphere rich in nitrogen ($\sim 95\%$) and methane ($\sim 5\%$) that is believed to originate from geological outgassing ([Tobie et al., 2006](#)). This is compatible with Titan most probably being composed of equal parts silicates and ices ([Fortes, 2012](#)). Similarly, the composition of a secondary atmosphere on GJ 357 b could reveal insights into the internal structure, the redox state of the mantle, and its history. Therefore, performing a spectroscopic analysis would be the next step in constraining the composition of GJ 357 b. To demonstrate the possible future

observability of GJ 357 b, we generated three synthetic atmospheric spectra; 100% CO₂, 100% SO₂, and 75% N₂, 24% CO₂ and 1% H₂O, using the TauRex code (Al-Refaie et al., 2019). Our synthetic spectra are presented in two ways: cloudless and with grey clouds (see Fig. 2.11). A full description of how we built our atmospheric spectra is present in Modirrousta-Galian et al. (2020c).

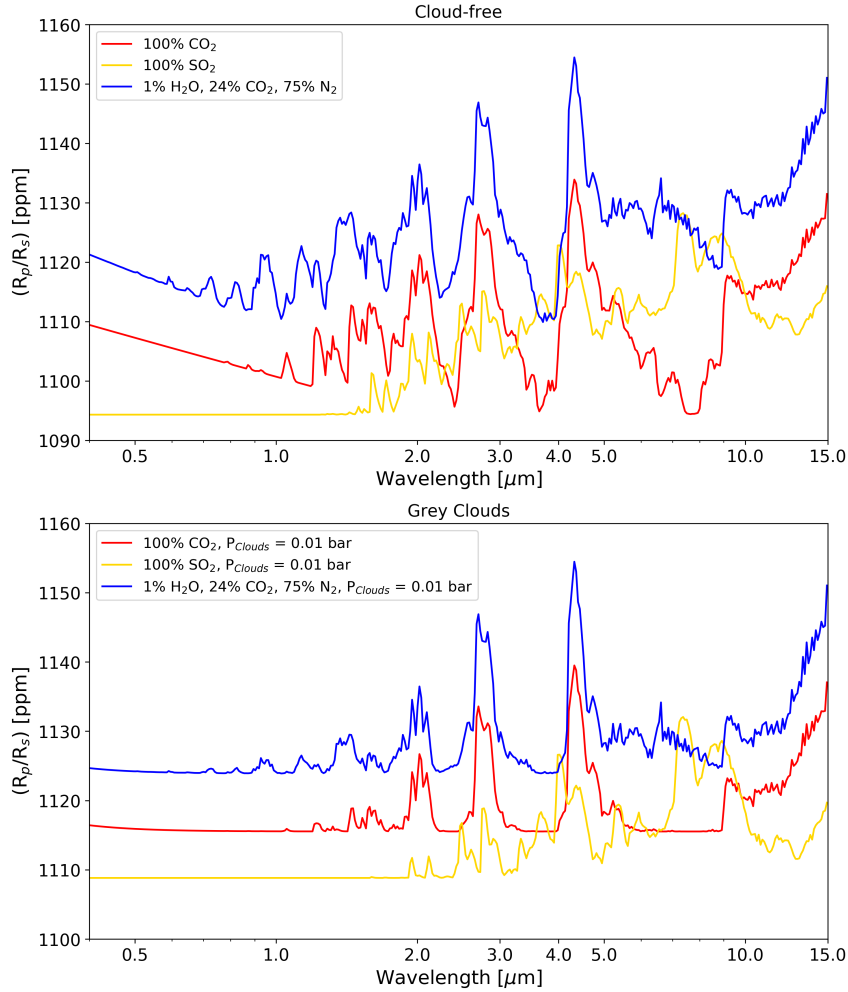


Figure 2.11: Synthetic spectra of GJ 357 b generated using the TauREx code. Our diagram includes the synthetic spectra of 100% CO₂ (red), 100% SO₂ (yellow), and a mixed atmosphere with 75% N₂ along with 1% H₂O and 24% CO₂ (blue). We show these forward models for the cloud-free case (top) and in the presence of opaque grey clouds at 0.01 bar (bottom).

We find that even with a low abundance of water, future instruments such as Ariel, JWST, and Twinkle, would be able to detect it. Because of this, we believe that GJ 357 b is one of the best targets for future atmospheric analyses, as its atmosphere should be relatively easy to characterize.

2.6 Future Works On Photoevaporation

A recurring problem in exoplanet photoevaporation models is that they usually focus on some aspects of photoevaporation while making crude assumptions on the physics outside of those aspects. Ironically, this has resulted in a bimodal distribution of photoevaporation papers, with half focusing on geophysics (e.g., [Ginzburg et al., 2016, 2018](#); [Gupta and Schlichting, 2019](#); [Zeng et al., 2019](#)) and the other half focusing on atmospheres (e.g., [Owen and Wu, 2013, 2017](#); [Kubyskhina et al., 2018a,b](#)); a more appropriate approach, however, would be to consider both coevally. As of the writing of this thesis, efforts are in place to create a more complete model that incorporates the various factors pertinent to atmospheric evaporation. The upcoming work is the result of a collaboration between stellar astrophysicists, atmospheric scientists, and geophysicists. We briefly discuss its findings below.

Our novel approach improves on [Modirrousta-Galian et al. \(2020a\)](#) in three ways: we use more flexible and accurate planetary equations of state, we are more rigorous with our XUV-induced photoevaporation models, and we incorporate the geodynamical state of super-Earth and sub-Neptune interiors. With regards to the equations of state, we use the models from [Lopez and Fortney \(2014\)](#),

$$R_p = R_c + 2.06R_{\oplus} \left(\frac{M_p}{M_{\oplus}} \right)^{-0.21} \left(\frac{f_{env}}{5\%} \right)^{0.59} \left(\frac{F_p}{F_{\oplus}} \right)^{0.044} \left(\frac{age}{5 \text{ Gyr}} \right)^{-0.18} + \Delta R, \quad (2.24)$$

where ΔR is the radiative layer thickness (only important for the most highly-irradiated exoplanets; under most conditions of interest it can be generally ignored),

$$\Delta R = 9 \left(\frac{k_B T}{\mu g} \right), \quad (2.25)$$

where k_B is Boltzmann's constant, T is the effective temperature, μ is the mean molecular mass of the atmosphere, and g is the gravitational acceleration. For the radius of the core, R_c , we include the effects of atmospheric-induced compression,

$$\frac{R_c}{R_{\oplus}} = \frac{1.07 - 0.21 \cdot f_{Fe}}{(1 + 1.2 \cdot (M_{atm}/M_c))^{0.1}} \left(\frac{M}{M_{\oplus}} \right)^{1/3.7}, \quad (2.26)$$

where the derivation of Eq. 2.26 is found in sect. A.2 of the appendix. These equations of

state predict enlarged planets when young due to their significant interior luminosities; astronomical observations support this (e.g., [Benatti et al., 2019](#)).

The evolution of a planet's interior heat flux is not well understood because it depends on multiple factors such as its formation history (e.g., [Ikoma et al., 2000](#); [Ikoma and Hori, 2012](#)) and its convective regime (e.g., [Korenaga, 2010](#); [O'Rourke and Korenaga, 2012](#)). Experimental data from Earth (e.g., [Cloud, 1972](#); [Li and Agee, 1996](#); [Richter et al., 1997](#)) and modeling (e.g., [Matsui and Abe, 1986a,b](#); [Abe, 1993](#); [Korenaga, 2021](#)) suggests that planets are most luminous during their first hundred million years. This is the time frame during which planets have inflated atmospheres ([Lopez and Fortney, 2014](#)). Furthermore, XUV observations show that stars are also most active during their first hundred million years (e.g., [Sanz-Forcada et al., 2011](#); [Penz and Micela, 2008](#); [Penz et al., 2008](#)), suggesting that most atmospheric evaporation takes place during the first hundred million years and then decreases precipitously. Because of the early catastrophic mass loss, in our new mass loss model, we use the following step function,

$$M_{atm} \approx \begin{cases} 0, & \frac{M_{atm,0}}{\dot{M}_{H.B.} \cdot \tau} \leq 1 \\ M_{atm,0} - (\dot{M}_{H.B.} \cdot \tau), & \text{otherwise} \end{cases}, \quad (2.27)$$

where $M_{atm,0}$ is the initial atmospheric reservoir, $\dot{M}_{H.B.}$ is the Hydro-based mass-loss rate, and $\tau = 100$ Myrs. The adopted stellar properties and orbital distances are almost identical to [Modirrousta-Galian et al. \(2020a\)](#), except for the previously mentioned atmospheric evaporation cut-off time of 100 Myrs instead of 1 Gyrs. For the planetary parameters, we considered more variables than in [Modirrousta-Galian et al. \(2020a\)](#). The Bond albedo values were distributed uniformly between 0.1 and 0.9; this accounts for the large variability in the observed albedos of super-Earths and sub-Neptunes (e.g., [Demory, 2014](#); [Malavolta, 2018](#); [Modirrousta-Galian et al., 2021](#)). To calculate the effective temperatures, we applied the Blackbody approach with a correction for the Bond albedo as shown in Eq. 2.28; T_* is the stellar temperature, A_B is the Bond albedo, R_* is the stellar radius and a_p is the orbital distance of the planet.

$$T = T_*(1 - A_B)^{1/4} \left(\frac{R_*}{2a_p} \right)^{1/2} \quad (2.28)$$

The atmospheric mass fraction is a free parameter defined as the atmosphere’s mass divided by the total planetary mass. We calculated the total planetary mass by modeling the core mass distribution and adding the atmospheric mass; the core mass distribution is also a free parameter. We assumed that all cores have a terrestrial composition (Mg-perovskite/post-perovskite mantle with an Fe center) with radii given by the bi-layer (i.e., Fe-rock) polytropic model from [Zeng et al. \(2016\)](#).

With the simulation setup complete, we evolved one million super-Earths and sub-Neptunes. We find that almost all ($> 99\%$) exoplanets lose their primordial envelopes (see Fig. 2.12). Furthermore, complete evaporation typically occurs in less than one million years; exceptions are planets with atmospheres greater than ten times the mass of their cores, although these are uncommon. Notwithstanding, even if one assumes that all planets are born with massive atmospheres, which is not consistent with our current understanding of planetary formation (e.g., [Safronov and Zvjagina, 1969](#); [Hayashi et al., 1977](#); [Ida and Lin, 2004, 2005](#); [Ikoma and Hori, 2012](#)), a bimodal distribution will form with the larger peak erroneously located at $\sim 4R_{\oplus}$ (see Fig. 2.13). In other words, the details of the initial atmospheric mass fractions are unimportant, as most super-Earths and sub-Neptunes lose their atmospheres. Furthermore, we also find that the initial core mass distribution is unimportant as it has a minor effect on the number of planets located in the second peak ($1.75 - 3.5R_{\oplus}$) and only shifts the location of the first peak ($1 - 1.75R_{\oplus}$).

We, therefore, argue that for the bimodal distribution to form, an additional mechanism is required that we suggest is geological outgassing of previously dissolved primordial gas ([Chachan and Stevenson, 2018](#); [Kite et al., 2020](#)). We find that if planets above a critical mass, M_{cri} , can outgas, the bimodal distribution will always form; this is shown in Fig. 2.14 and 2.15. Our best fit critical mass, shown in Fig. 2.16, ranged between $3M_{\oplus} < M_{cri} < 8.5M_{\oplus}$. The critical mass range is not an uncertainty but an intrinsic dispersion caused by the different internal structures, masses, and composition of super-Earths and sub-Neptunes. The critical mass range was found by fitting the observed bimodal trend to our XUV evaporation simulation. However, the critical mass range can also be predicted through geophysical arguments. Fluid dynamical simulations (e.g., [Iyer et al., 2020](#)) and experimental data (e.g., [Urban et al., 2011](#); [He et al., 2012](#); [Doering et al.,](#)

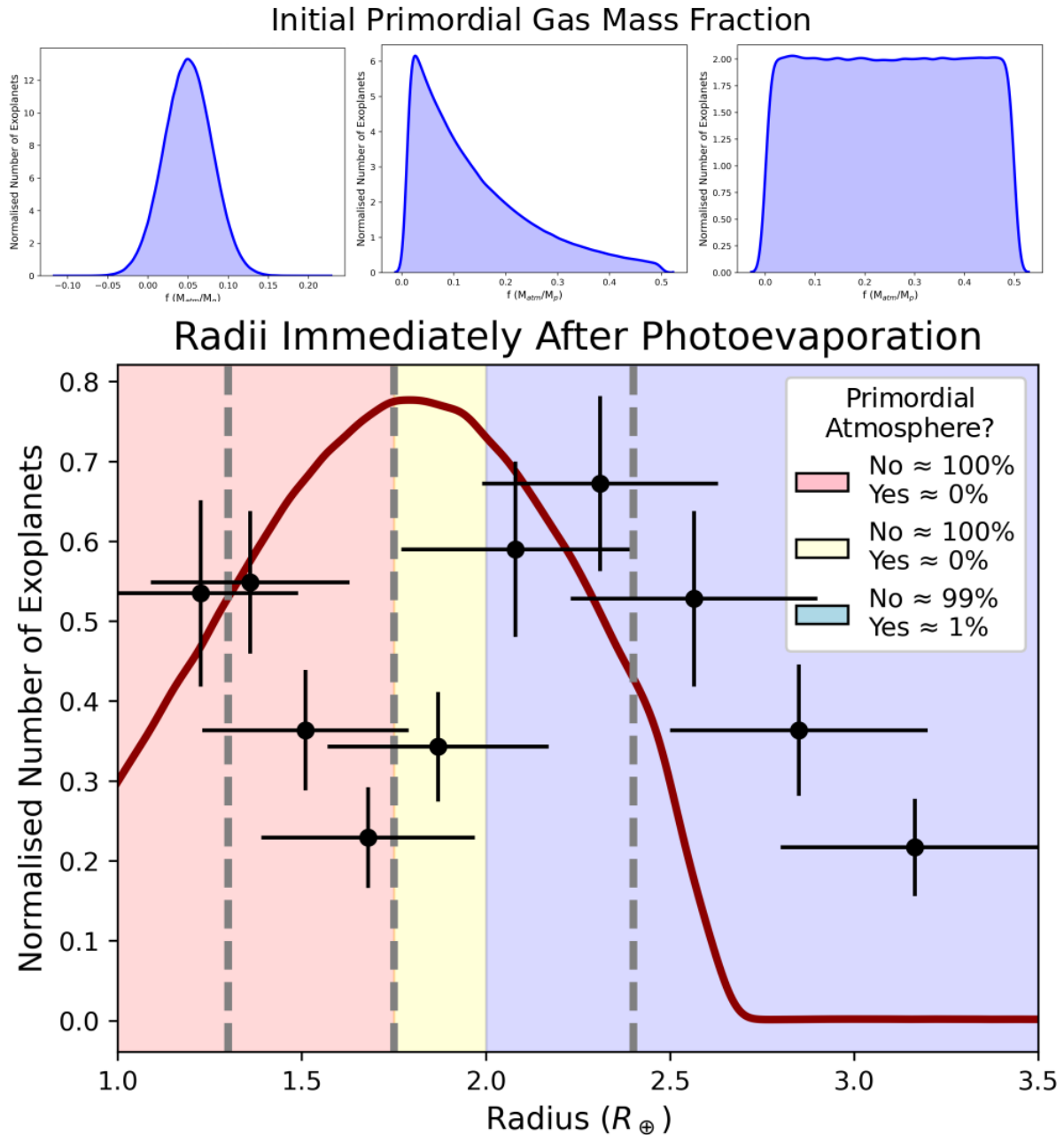


Figure 2.12: *Top:* The initial primordial gas mass fraction distributions tested (from left to right: Gaussian, exponential decay, and uniform). All were truncated at an upper limit of 50% primordial gas. Increasing the mass fraction beyond this limit did not change the results unless one dealt with values close to ten times the core mass. All distributions gave rise to the same radius distribution after photoevaporation. *Bottom:* the radius distribution of super-Earths and sub-Neptunes immediately after photoevaporation. The gray lines mark the location of the two peaks and the minimum discovered by [Fulton et al. \(2017\)](#). The data points with the uncertainties correspond to the values given in Table 3 and Figure 7 of [Fulton et al. \(2017\)](#). The light-red, light-yellow, and light-blue regions correspond (approximately) to the typically quoted location of rocky worlds (e.g., [Jin and Mordasini, 2018](#)), the transition region ([Swain et al., 2019](#)), and hydrogen-rich worlds (e.g., [Modirrousta-Galian et al., 2020a](#)), respectively. For each region, we report the population composition. This result is not consistent with the observations of [Fulton et al. \(2017\)](#).

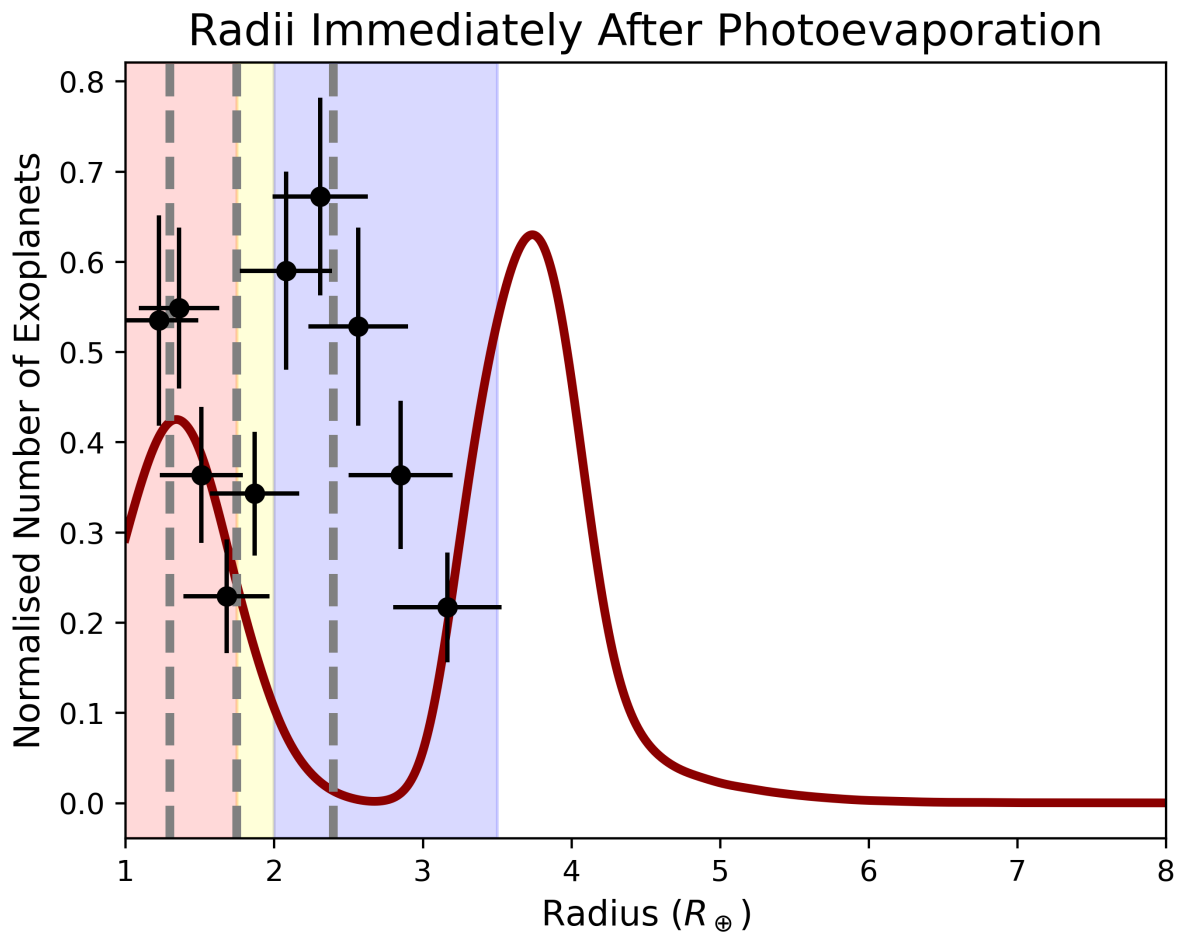


Figure 2.13: The radius distribution immediately after photoevaporation if the initial primordial gas mass fractions (i.e., the size of the initial atmospheres) are very large. The light-red, light-yellow, and light-blue regions correspond (approximately) to the typically quoted location of rocky worlds (Jin and Mordasini, 2018), the transition region (Swain et al., 2019), and hydrogen-rich worlds (Modirrousta-Galian et al., 2020a), respectively. Note that whereas a bimodal distribution forms, it deviates from the observations of Fulton et al. (2017) (the black data points).

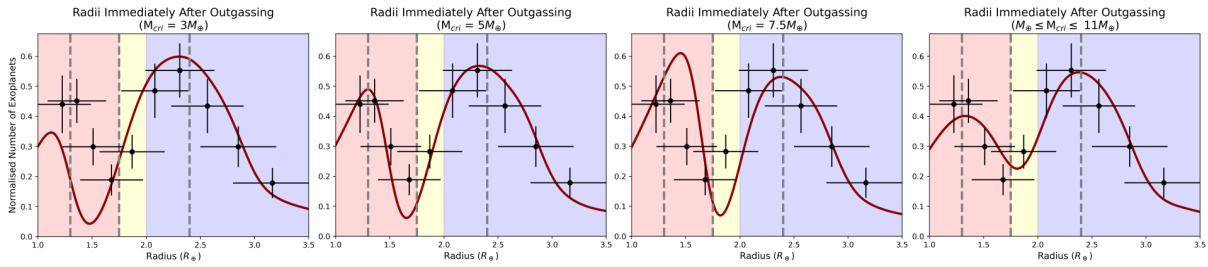


Figure 2.14: The effects of the critical mass on the final radius distribution (after outgassing); all other parameters were left the same. From left to right, the critical masses are $3M_{\oplus}$, $5M_{\oplus}$, $7M_{\oplus}$, and $1 - 11M_{\oplus}$. The light-red, light-yellow, and light-blue regions correspond (approximately) to the typically quoted location of rocky worlds (e.g., [Jin and Mordasini, 2018](#)), the transition region ([Swain et al., 2019](#)), and hydrogen-rich worlds (e.g., [Modirrousta-Galian et al., 2020a](#)), respectively. Note how all distributions result in a bimodal trend.

[2019; Doering, 2020](#))⁸ suggest that for convection to occur, a gravitational instability at a boundary layer has to initiate; this is illustrated in Fig. A.1 of sect. A.4 in the appendix. The important boundary layer is located at the bottom for fluid systems with only basal heating, like a kettle. However, the important boundary layer is at the top for planets because other heat sources such as radioactivity make the top boundary layer more significant than the bottom one. The top boundary layer is called the lithosphere and, on Earth, it is composed of the crust and the portion of the upper mantle that behaves elastically. Whereas Earth’s lithosphere is divided into various subducting plates, Venus’ and Mars’ lithospheres are rigid and do not partake in interior convection. The reason why Earth has plate tectonics and not a stagnant lid like the other known terrestrial planets is disputed. Among the various explanations for plate tectonics, two are relevant to the planets of interest to this study: negative buoyancy and mantle hydration.

The first mechanism involves generating a dense lithosphere that is gravitationally unstable, and founders; [O’Rourke and Korenaga \(2012\)](#) explored this idea for super-Earths and found that increasing the planetary mass also increases the eclogite mass fraction in the lithosphere. Because eclogite is a dense phase of mafic rock (basalt or gabbro), it may instigate gravitational instabilities in the lithosphere that allow the planet to remain geologically active for billions of years. Through simulations and scaling arguments, [O’Rourke and Korenaga \(2012\)](#) found that the fraction of crust in the eclogite stability field follows a simple analytic formulation (their Eq. 37), suggesting, for example, that a

⁸Note that [He et al. \(2012\)](#) states that they find evidence for the ultimate state of convection but, as explained in [Doering \(2020\)](#), their experimental data instead supports the classical regime.

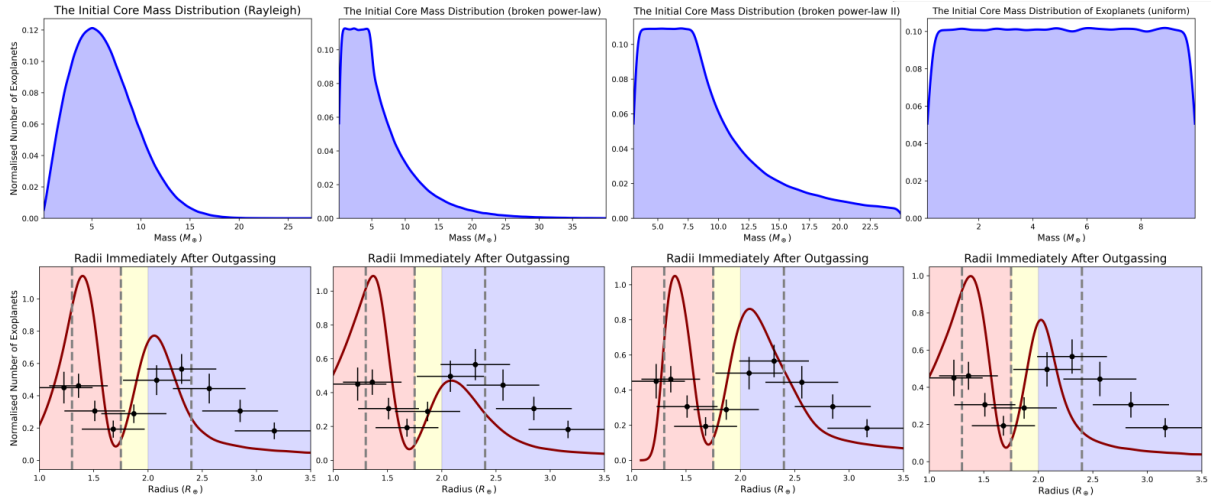


Figure 2.15: The effects of the core mass on the final radius distribution (after outgassing); all other parameters were left the same. From left to right, the core mass distributions are a Rayleigh function (Owen and Wu, 2017), broken power laws (Ginzburg et al., 2018; Modirrousta-Galian et al., 2020a), and a uniform distribution. The light-red, light-yellow, and light-blue regions correspond (approximately) to the typically quoted location of rocky worlds (e.g., Jin and Mordasini, 2018), the transition region (Swain et al., 2019), and hydrogen-rich worlds (e.g., Modirrousta-Galian et al., 2020a), respectively. Note how all distributions result in a bimodal trend.

$10M_{\oplus}$ rocky planet can have $\sim 75\%$ more eclogite in its lithosphere than a Venus-sized planet. Although geodynamical simulations are so far limited for this mechanism, it provides an intuitive and straightforward process that may be relevant to the terrestrial super-Earths of interest in this study.

The second argument focuses on the stress required to make the lithosphere transition from elastic to plastic deformation (i.e., the yield stress), with the latter facilitating lithospheric subduction and recycling. For Earth, the mechanism responsible for lowering the yield stress below the convective stress has not been settled yet (e.g., Bercovici, 2003). Among the proposed explanations, mantle hydration through thermal cracking provides a straightforward and convincing method for enabling the wholesale recycling of the lithosphere (Moresi and Solomatov, 1998; Korenaga, 2007, 2017). However, its applicability to super-Earths and sub-Neptunes may appear limited due to their high surface temperatures. However, the crucial point to recognize is that mantle hydration occurs because of the H^+ dipole in H_2O molecules that influences mantle rheology by perturbing the ionic bonds that are characteristic of all rocks. The dissolution of primordial gas in planetary interiors could replicate this hydration process due to a portion of the dissolved hydrogen interacting with iron oxides to form water. Because the lithospheric

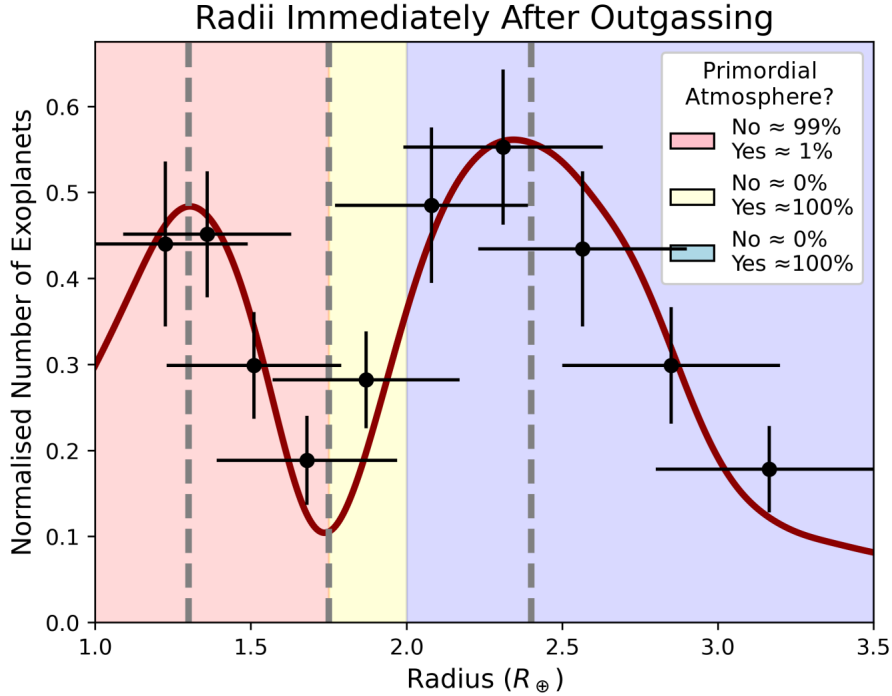


Figure 2.16: The radius distribution of super-Earths and sub-Neptunes after late-stage outgassing. The gray lines show the two peaks and the minimum discovered by [Fulton et al. \(2017\)](#). The data points with the uncertainties correspond to the values given in Table 3 and Figure 7 of [Fulton et al. \(2017\)](#). The light-red, light-yellow, and light-blue regions correspond (approximately) to the typically quoted location of rocky worlds (e.g., [Jin and Mordasini, 2018](#)), the transition region ([Swain et al., 2019](#)), and hydrogen-rich worlds (e.g., [Modirrousta-Galian et al., 2020a](#)), respectively. For each region, we report the population composition; our data does not support the presence of the transition region. This result is consistent with the observations of [Fulton et al. \(2017\)](#).

mass scales with the area ($\sim M_p^{1/2}$) and the fraction of water scales with the mass⁹, larger planets are more likely to have hydrated lithospheres with lower yield strengths. Combining this effect with the greater convective vigor pertinent to more massive planets ([Valencia et al., 2007a](#); [Korenaga, 2010](#)) would suggest that brittle failure and, thus, an unstable stagnant lid are more probable when the mass increases.

The aforementioned mechanisms are consistent in providing a pathway for generating lithospheric instabilities at greater planetary masses. An unstable stagnant lid maintains planets in a geologically active state so that they can slowly release their previously dissolved primordial gas reservoirs. In other words, whereas XUV-induced photoevaporation removes the atmospheres of most planets (leading to the first peak),

⁹Assuming that the water abundance scales with the hydrogen abundance. Because of Henry’s law, the hydrogen abundance scales with the surface pressure, which is a function of the planetary mass. It, therefore, follows that the water abundance scales with the planetary mass.

geological outgassing generates atmospheres for planets with cores greater than the critical mass (producing the second peak). The next stage in our analysis is to explore the effects of the oxidation state of the mantle on sequestering and preserving the dissolved hydrogen to evaluate how the interior planetary conditions influence the properties of exoplanet populations. This paper is a work in progress.

3 Constraining Airless Super-Earths

3.1 Compositional Degeneracies

To determine the radius of a planet, it is necessary to carry out a transit observation. This detection technique, based on photometry, measures the drop in the perceived brightness of a star as the planet traverses across our line of sight; a more significant drop in the perceived stellar flux suggests a larger planetary radius. It is typically much more challenging for astronomers to obtain the mass than the radius as this requires detecting minuscule stellar oscillations caused by the planet's gravity. This type of observation is called the radial velocity method (see Fig. 3.1 for a visual representation) and it is based on spectroscopy, thus requiring large telescopes.

For most known exoplanetary systems, only the planetary radius is known, so very few inferences can be made on the bulk geochemical composition. The only exceptions are planets with very large radii because hydrogen must be present in large quantities. As explained in sect. 1.2, for the subsample where the planetary mass and radius are known, the interior composition can be constrained by considering the bulk density. Using the bulk density with planetary equations of state, it is possible to understand how materials behave under geological conditions so that mass-radius relations for endmember¹⁰ geochemical compositions can be determined. Throughout the years, several studies have produced synthetic planetary mass-radius relations (e.g. [Zapolsky and Salpeter, 1969](#); [Stevenson, 1982b](#); [Valencia et al., 2006, 2007b](#); [Fortney et al., 2007](#); [Seager et al., 2007](#); [Sotin et al., 2007](#); [Madhusudhan et al., 2012](#); [Zeng and Sasselov, 2013](#); [Zeng et al., 2016, 2019](#)), but similar results can be retrieved through a simple review of polytropes. A polytrope is defined as an equation of state that follows the equation

$$P \propto \rho^n. \tag{3.1a}$$

We note that in the astrophysical literature, it is more common to use the exponent of $n + 1/n$. However, this makes it hard to describe rocky and icy planets, so instead,

¹⁰An endmember is a pure compound that contributes to the compositional mixture of minerals. MgSiO_4 , for example, is an endmember of olivine, a mineral that makes up a large portion of Earth's crust and mantle.

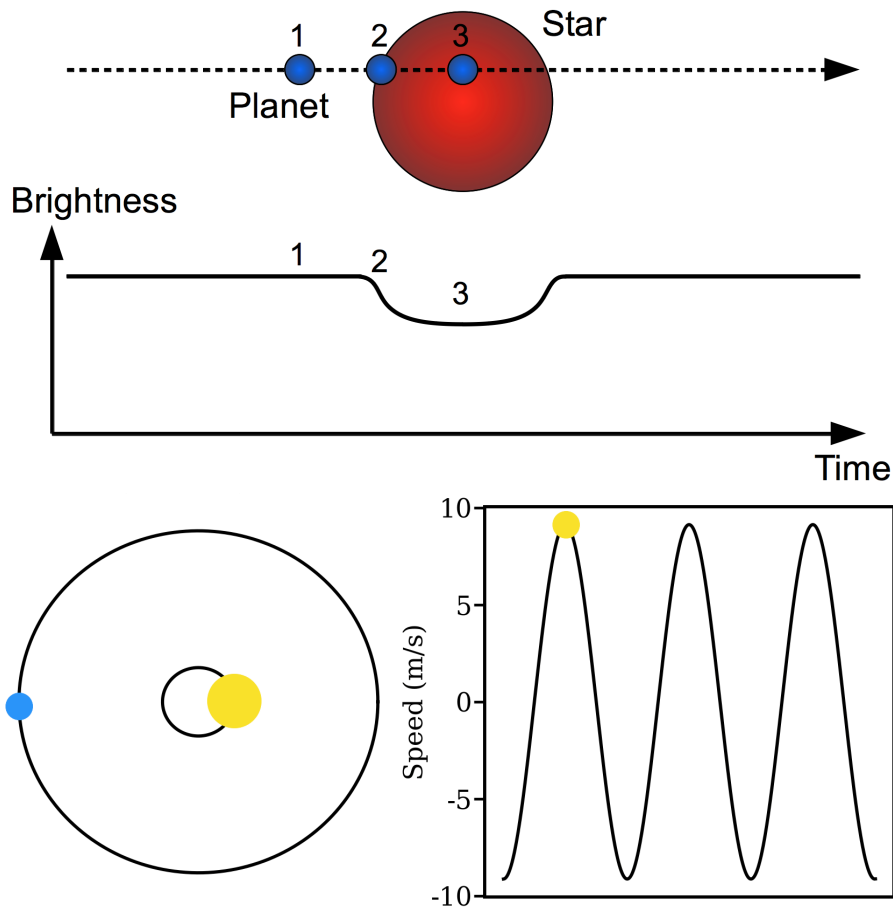


Figure 3.1: *Top*, the transit method showing a planet traversing across the line of sight of a star and how this is coeval with the drop in the observed stellar flux (credit: Hans Deeg). *Bottom*, a sketch showing how the planet's gravity causes the star to also orbit around the center of mass of the system. This stellar 'wobble' brings about a Doppler shift that can, in some cases, be detected by astronomers (credit: Alysa Obertas).

we adopt an index of n , as used by D. J. Stevenson and others, due to its practicality. Eq. 3.1a can, therefore, be evaluated so that the mass-radius relationships are retrieved. To do this, we substitute in $P \propto M^2/R^4$ and $\rho \propto M/R^3$:

$$\left[\frac{M^2}{R^4} \right] \propto \left[\frac{M}{R^3} \right]^n. \quad (3.1b)$$

This is now solved for the radius in terms of the mass so that

$$R \propto M^{\frac{2-n}{4-3n}}. \quad (3.1c)$$

Eq. 3.1c is the commonly used form for the mass-radius relationship of planets, where different values of n correspond to different compositions and internal structures:

- $n = 1$ is for the *singular isothermal sphere of gas*, which has been used to model the initial conditions for protostellar collapse. Despite its simplicity, it is not an accurate model (e.g. [Whitworth et al., 1996](#)).
- $n \simeq 2$ provides an accurate description of cold gas-giants like Jupiter.
- $n \simeq 3$ adequately describes rocky planets with small hydrogen atmospheres (~ 1 wt.%) or H₂O ice planets (i.e., cold water-worlds).
- $n \simeq 4$ is appropriate for very iron-rich bodies.
- $n \simeq 5$ roughly corresponds to planets with an Earth-like composition.
- $n \simeq \infty$ operates well for small bodies like the Moon or Pluto, where the internal pressures are small enough for materials not to undergo phase-transitions or sufficient density changes.

Planetary models have become exceedingly advanced and even include effects like adiabatic heating and radioactivity. However, as explained previously, degeneracies persist, such as those between H₂O planets and rocky worlds with small primordial envelopes. Therefore, to understand exoplanets' interior structures and composition, more data is required. The following sections discuss how the albedo values of molten, airless super-Earths are tell-tale signs for their chemical compositions. This work has been published on [Modirrousta-Galian et al. \(2021\)](#).

3.2 Exploring Super-Earth Surfaces

The concept behind this idea is straightforward; in the same way that humans can infer the composition of everyday objects by their appearance, the same should hold for exoplanets. The specific details differ because humans judge based on preconceived stereotypes, such as looking at a chair and deducing that it is probably strong enough to sustain one's weight. However, when analyzing exoplanets, a more objective approach can be taken where, for example, one can look at the reflectance of a surface at different wavelengths. By determining how reflective a surface is and how this changes with different wavelengths, it is possible to infer the composition of the surface.

3.2.1 Defining Terms

Before we can progress with an explanation of our model, it is essential to define the relevant terms: the reflectance, R , is a directional quantity that depends on the incident and emerging angles, as well as the wavelength of the light and the composition (through the refractive indices) and roughness of the surface. The spherical albedo, A_S , is the total fraction of incident radiance scattered by a body in all directions. The planar (or plane) albedo, A_{pla} , is the spherical albedo of a planar surface of the planet. Finally, the bolometric Bond albedo, A_B , is the spherical albedo integrated across all wavelengths.

3.2.2 Explaining the Problem

Several experimental studies have measured material reflectances to predict the composition of airless (or near-airless) magma-ocean super-Earths. For instance, [Essack et al. \(2020\)](#) measured the reflectance of basalt and feldspar lavas by recording how much light, from a precisely calibrated light source, was reflected to the spectrometer. They found that, whereas the reflectance at latitudes close to the equator is very high, the bulk average reflected component is only $\sim 10\%$. This disparity occurs because the high albedo regions account for a small portion of the total planetary surface, so their contribution is minor. These results are consistent with older studies that observed low albedos (also $\sim 10\%$) on solidified Martian lava flows ([Edgett and Rice, 1997](#)). The problem, however, is that the inferred Bond albedo values of certain super-Earths are significantly higher than the ones predicted by experimentation. For instance, some hot super-Earths have Bond albedos that possibly exceed $\sim 50\%$ ([Rouan et al., 2011](#); [Demory, 2014](#)).

Explanations for the observed high albedos of magma-ocean super-Earths come in two forms: highly reflective atmospheres ([Hamano et al., 2015](#); [Pluriel et al., 2019](#)) and exotic magmas ([Rouan et al., 2011](#)). Data from our solar system supports the first explanation. For example, Venus has a Bond albedo of 75% caused by its highly reflective atmosphere. It follows that some of these exoplanets may have heavy volcanic atmospheres that result in high albedos. The only problem with this model is that hosting an atmosphere for very close molten exoplanets should be difficult due to intense stellar irradiation. For instance, Kepler 10 b has an estimated Bond albedo of $\sim 48\%$ and, due to being tidally locked, has a day-side and night-side temperature of ~ 3000 K and ~ 50 K respectively ([Rouan](#)



Figure 3.2: *Left:* solidified carbonatite from Jacupiranga Estado de São Paulo, Brazil (credit: Eurico Zimbres). The black minerals are magnetite (Fe_3O_4), the white are calcite (CaCO_3), and the green are olivine ($[\text{Mg}, \text{Fe}]_2\text{SiO}_4$). *Right:* solidified komatiite from the Komati River in South Africa (credit: I. P. Vtorov). The long skeletal texture is called spinifex, and it is caused by the constrained growth of olivine or pyroxene crystals during magma solidification.

et al., 2011). The strong temperature gradient implies that a significant atmosphere is not present as there must be little thermal circulation.

Furthermore, the vaporized mineral atmosphere formed on the day-side would rapidly traverse into the night-side and condense. Therefore, while a highly reflective atmosphere may explain the observed albedos on certain super-Earths, it cannot explain it for all observed cases. For a more thorough explanation of the importance of atmospheres on the albedo, see *Modirrousta-Galian et al.* (2021).

For the rest of this chapter, we only focus on exotic magmas that have also been observed in our solar system, notably on Earth, such as carbonatite lava from the *Ol Doinyo Lengai volcano in Tanzania*. Carbonatite melt is only ~ 800 K, which is substantially colder than typical basaltic melts that usually have temperatures of ~ 1500 K. Furthermore, as the name suggests, carbonatite is composed of carbonates: mainly Nyerereite ($\text{Na}_2\text{Ca}(\text{CO}_3)_2$) and Gregoryite ($[\text{Na}_2, \text{K}_2, \text{Ca}]\text{CO}_3$). Another exotic magma is komatiite that is believed to no longer naturally exist on Earth. Having an eruption temperature of ~ 2000 K, komatiite was Earth's hottest ultramafic lava; its geochemical composition is classified as 40 – 45 wt.% SiO_2 and > 18 wt.% MgO . Fig 3.2 is a photograph of solidified carbonatite and komatiite minerals.

3.2.3 Modelling Exotic Reflective Magmas

Intuition would suggest that if Earth has exotic magmas, exoplanets may have them as well. Three main parameters would affect the reflectance of magma: the geochemical composition, the angle of incidence of the incoming light, and the wavelength of light. By using the indices of refraction, geochemical effects can be incorporate. There is a real (n) and imaginary (k) part, where the first describes the speed of light in a material (this is fundamental for understanding how much refraction occurs), while the second handles the attenuation (i.e., energy losses); together, these two indices can describe how much light gets reflected. For instance, in the case of normal incident light, the following equation can be used to calculate the reflectance (Abraham and Becker, 1950),

$$R = \left(\frac{|n_1 - n_2|^2 + |k_1 - k_2|^2}{|n_1 + n_2|^2 + |k_1 + k_2|^2} \right). \quad (3.2)$$

For the situations of interest, planets are airless or nearly airless, so only the magma's indices of refraction need to be considered. Hence, Eq. 3.2 can be simplified to,

$$R = \left(\frac{|n - 1|^2 + |k|^2}{|n + 1|^2 + |k|^2} \right). \quad (3.3)$$

Eq. 3.3 shows that two different materials can be equally reflective if they had the right combination of n and k . In other words, there is a degeneracy where we can only obtain R from observations and not the refractive indices alone, so this equation is not useful in its current form. Because of this, we can create a new parameter n_{sy} that we define as the synthetic refractive index. This parameter accounts for the effects of the real and imaginary indices to reproduce the same reflectance:

$$R = \left(\frac{n_{sy} - 1}{n_{sy} + 1} \right)^2. \quad (3.4a)$$

Because we have defined n_{sy} as a real index that can produce the same reflectance, Eq. 3.3 can be equated with Eq. 3.4a so that

$$\left(\frac{n_{sy} - 1}{n_{sy} + 1} \right)^2 = \left(\frac{|n - 1|^2 + |k|^2}{|n + 1|^2 + |k|^2} \right). \quad (3.4b)$$

Solving for n_{sy} gives

$$n_{sy} = \frac{\left(\frac{|n-1|^2+|k|^2}{|n+1|^2+|k|^2}\right)^{1/2} + 1}{1 - \left(\frac{|n-1|^2+|k|^2}{|n+1|^2+|k|^2}\right)^{1/2}}, \quad (3.4c)$$

where Eq. 3.4a describes the reflectance of a surface as a function of the synthetic refractive index, and Eq. 3.4c tells us the synthetic refractive index as a function of the real and imaginary refractive indices. To find how the reflectance depends on the wavelength of light and composition of the material, their effects on the synthetic refractive index must be quantified. To a rather crude approximation (and in many cases, it is incorrect), the Sellmeier equation provides this relationship,

$$n_{sy} \sim \left[A + \sum_i \frac{B_i \lambda^2}{\lambda^2 - C_i} \right]^{1/2}, \quad (3.5)$$

where λ is the wavelength with A , B , and C being experimentally or theoretically determined constants that account for the composition of the material (see [Polyanskiy \(2010\)](#) and [Grainger et al. \(2014\)](#) for raw numerical data). For more accurate equations, see table 5 of [Modirrousta-Galian et al. \(2021\)](#). Combining experimentally derived equations such as Eq. 3.5, with Eq. 3.4a, provides a purely analytic equation for the reflectance of a flat surface when the light is arriving perpendicular to the plane. To include the effects of non-perpendicular light, Eq. 3.4a has to be replaced with the Fresnel equations:

$$R_s = \left| \frac{n_{sy} \cos \theta_i - \sqrt{1 - (n_{sy} \sin \theta_i)^2}}{n_{sy} \cos \theta_i + \sqrt{1 - (n_{sy} \sin \theta_i)^2}} \right|^2, \quad (3.6a)$$

$$R_p = \left| \frac{n_{sy} \sqrt{1 - (n_{sy} \sin \theta_i)^2} - \cos \theta_i}{n_{sy} \sqrt{1 - (n_{sy} \sin \theta_i)^2} + \cos \theta_i} \right|^2, \quad (3.6b)$$

and

$$R_{eff} = \frac{1}{2} (R_s + R_p), \quad (3.6c)$$

where θ_i is the angle of incidence of the light and R_s , R_p , and R_{eff} are the s-polarised, p-polarised, and effective (total) reflectances, respectively. The Fresnel equations are, however, computationally expensive, especially if iterative ray-tracing simulations are run. Because of this, approximations can be used that, under certain circumstances,

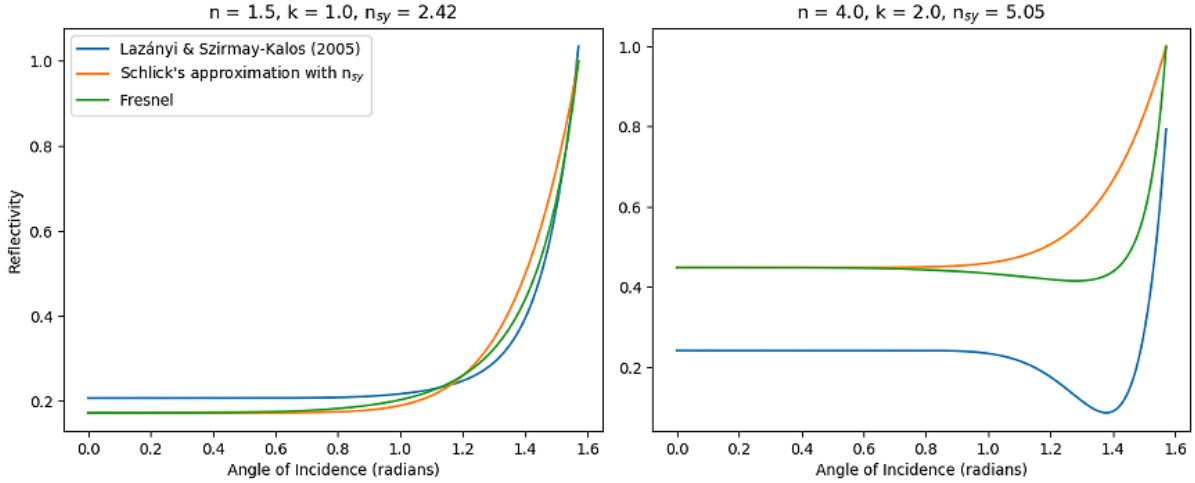


Figure 3.3: A comparison of the model by [Lazányi and Szirmay-Kalos \(2005\)](#), Schlick’s approximation with n_{sy} , and the Fresnel equations.

adequately model the behavior of light. One such model is [Lazányi and Szirmay-Kalos \(2005\)](#) that functions well for low n and k values. We decided not to adopt this model as it overestimates the reflectance at small angles of incidence, and it becomes inaccurate at high indices of refraction (see Fig. 3.3). Another commonly used model is the Lommel-Seeliger Law ([Seeliger, 1884](#)); this is a simple analytical approach that well approximates diffuse reflection. Unfortunately, it fails for Bond albedo values larger than $\simeq 0.20$ ([Fairbairn, 2005](#)), so it does not apply to the very reflective super-Earths of interest. An alternative approach is to use the Hapke model ([Hapke, 2012](#)) that is a semi-empirical analytical method for estimating the Bond albedo of airless bodies. We decided not to use this method as it is adapted for regolith surfaces such as asteroids, but not fluids like magmas. The approximation most suitable for highly reflective molten airless super-Earths is Schlick’s approximation ([Schlick, 1994](#)),

$$R = R_0 + (1 - R_0)(1 - \cos \theta_i)^5, \quad (3.7)$$

where R_0 is given by Eq. 3.4a. Even for unusually high indices of refraction, Schlick’s approximation closely matches the results predicted by the Fresnel equations for most angles of incidence (see Fig. 3.3); only at high angles of incidence do the deviations become noticeable. Even so, this method is the most accurate approximation; it is therefore adopted in our simulations.

As seen by Eq. 3.7, the angle of incidence has a strong influence on the reflectance of the

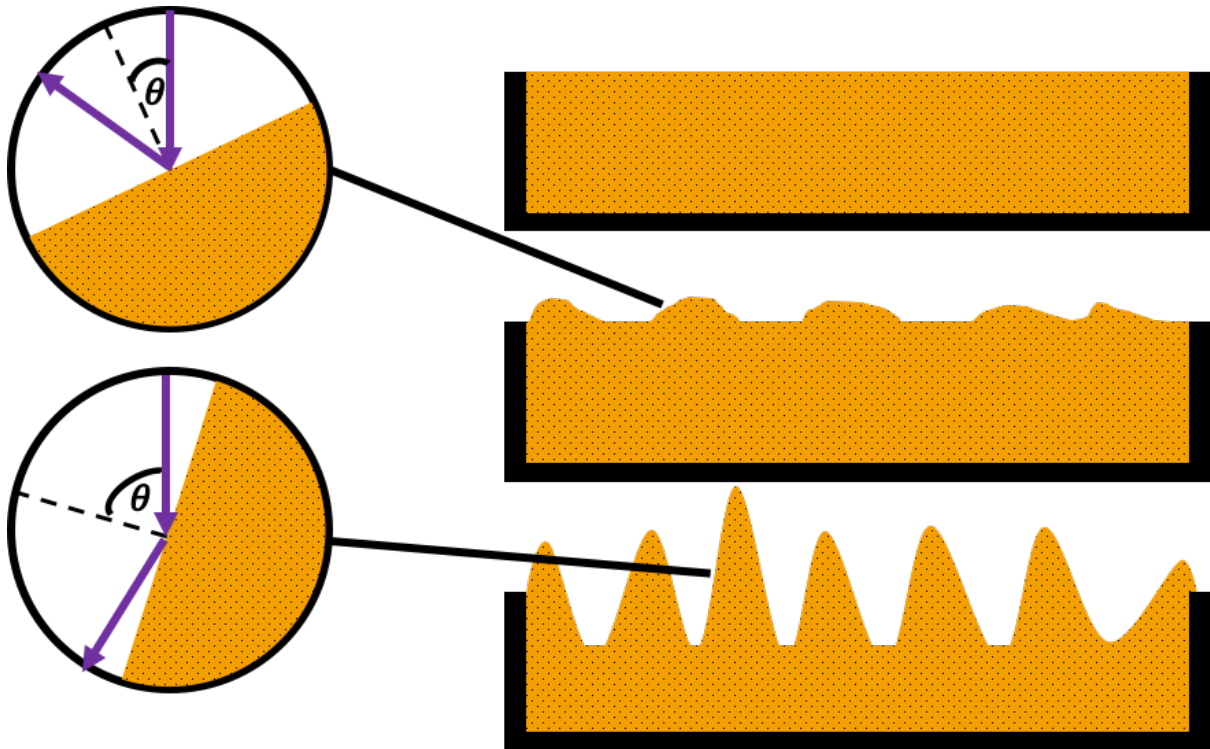


Figure 3.4: Cartoon showing how a wavier surface will induce greater angles of incidence for incoming light.

surface. Because of this, surface topography/roughness should play a considerable role on the Bond albedo of the planet. On the one hand, a magma ocean with larger and more frequently forming waves will result in greater angles of incidence; this would increase the Bond albedo (see Fig. 3.4). On the other hand, waves will act like concavities that trap light-rays and thus result in multiple internal reflections, which decrease the Bond albedo (see Fig. 3.5). The second effect cannot be explored analytically so, to determine the Bond albedo of a surface, ray-tracing simulations are required. The complexity of this problem shows that the topography of a surface is important, so it must be modeled realistically to avoid biasing the data. One potential approach is to adopt a simple mathematical construct like a sine wave; however, this model poorly matches real fluid systems. A more appropriate approach would be to use fractal mathematics.

A fractal is defined as an entity with a fractal (or Hausdorff) dimension greater than its topological dimension. To explain this concept, let us first consider a square material with a side of length 8 cm and a negligible thickness. If one scales the length by half, the mass will drop to a quarter of the original. Fig. 3.6 illustrates this concept, while Eq. 3.8 shows

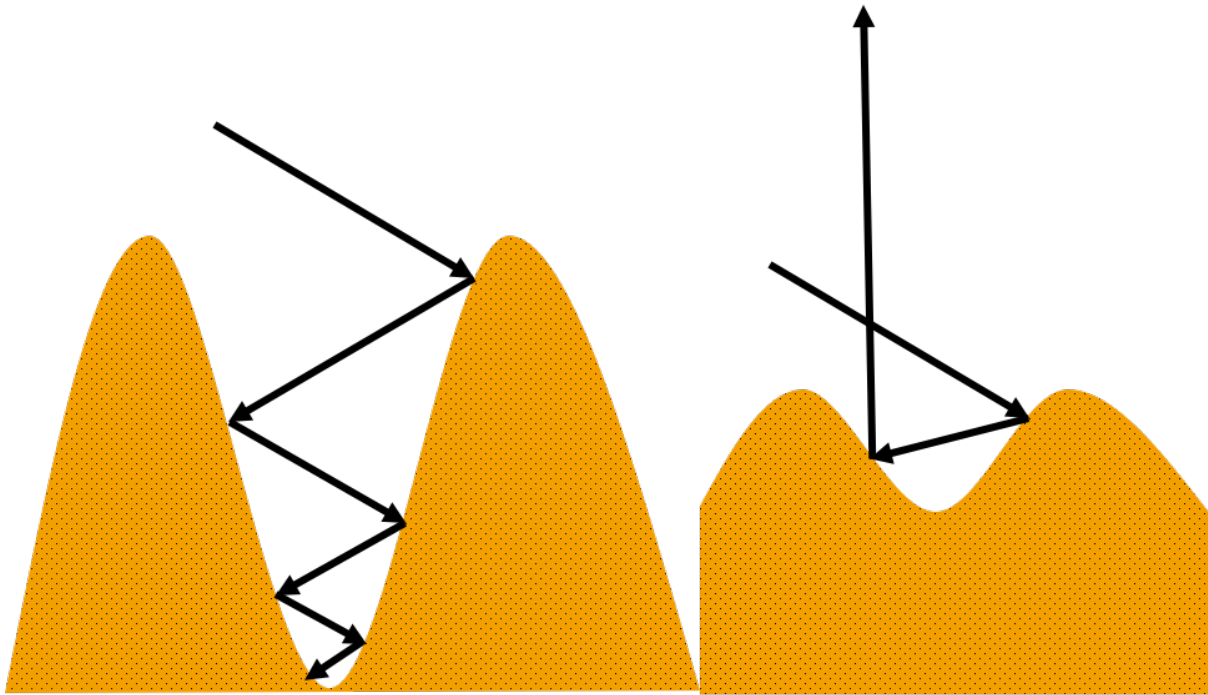


Figure 3.5: Cartoon showing how taller waves can cause light rays to reflect multiple times and eventually get absorbed by the material.

the generalised mathematical relation:

$$M \propto L^D, \quad (3.8)$$

where M is the mass, L is the length, and D is the dimension. For a square, D is 2, but for a cube, it is 3; halving the sides of a cube would, therefore, make the mass eight times smaller. One can now consider a fractal like the Sierpiński triangle (see Fig. 3.7) that is composed of 1-D lines, so it has a topological dimension of 1. By looking at Fig. 3.7, it can be seen that halving the side length makes the mass decrease by a factor of three. Therefore, for Eq. 3.8 to be satisfied, the dimension must be $D = \log_2 3 \approx 1.585$. This value is the fractal dimension, which is greater than the previously mentioned topological dimension (exactly 1), so the Sierpiński triangle fulfills the criteria required to be a fractal.

Fractals may give the impression of being idealized mathematical constructs, but they generally model nature better than non-fractals (e.g., Mandelbrot, 1975; Stiasnie, 1991; Stiasnie et al., 1991). The fractal dimension measures the geometric complexity of a system so that, from a geological perspective, information is provided on the surface

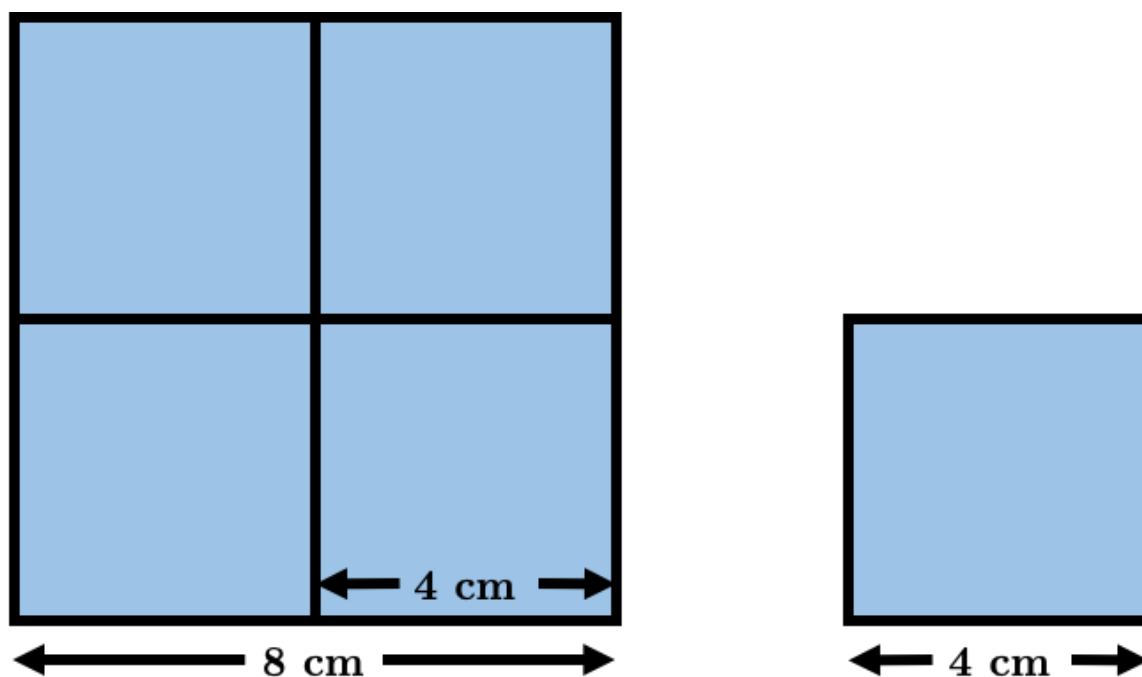


Figure 3.6: A demonstration of how halving the side lengths causes the mass to decrease by a factor of four.

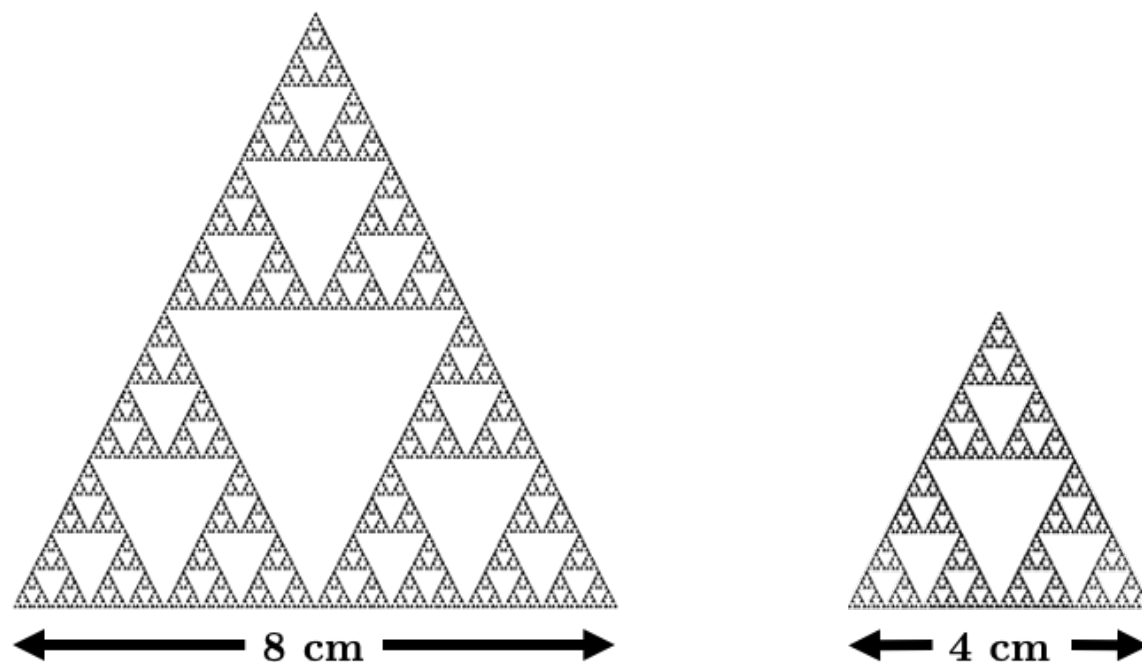


Figure 3.7: A demonstration of how halving the side lengths decreases the mass by a factor of three.

roughness. For instance, Earth's oceans have calculated fractal dimensions of ~ 2.3 (Stiassnie, 1991; Stiassnie et al., 1991), which means that, due to surface inhomogeneities, Earth's actual surface area is several orders of magnitude greater than what a perfect spherical model would predict. The waviness of a magma ocean can also be quantified with the fractal dimension, denoted as F . For the situations where the local and global properties are interlinked (like most of nature), the fractal dimension can be substituted by $F = 3 - H$, where H is the Hurst exponent that measures the coherence of a surface and has a value between zero and one. The Hurst exponent is constant regardless of the dimension one is working in, so it is a more useful parameter to adopt. Two essential properties must now be included: (1) the spatial density of waves and (2) the size of those waves. A calm magma ocean will have few waves, with each wave being smaller in size, whereas a turbulent ocean will have many waves with large amplitudes. These two properties must be considered separately, so first, we begin with the surface wave density.

3.2.4 The Surface Wave Density

To model the surface wave density, we used the `fbm 0.3.0` python package with the Davies and Harte (1987) fractional Gaussian noise (fGn) method. This technique is theoretically exact in generating discretely sampled fGn numerical values for a given fractal dimension. A thorough explanation of the Davies and Harte method is found on page 412 of Wood and Chan (1994). We chose to model the magma ocean surfaces as a collection of different points with elevations given by fGn to approximate the random motions induced from the vaporized atmospheric winds (see sect. C of the appendix in Modirrousta-Galian et al. (2021) for a mathematical relationship of the wind energies and the surface roughness). However, this approach assumes that each point is independent of its neighbors, which would only be valid for a zero viscosity fluid (i.e., a superfluid) that lacks surface tension. Magmas have viscosities, so the non-continuous, sharp terrains would be unrealistic. Fig. 3.8 is an example of a pre-smoothed, unrealistic surface.

To smooth these surfaces, we applied a Gaussian filter from the Astropy package (Astropy Collaboration et al., 2013, 2018) with a standard deviation of 100 pixels (equivalent to 1 m). The process of smoothing the surface is analogous to adding a viscosity that, by definition, will act against the fluid flow. We chose to smooth out perturbations smaller than 1 m as this closely matches the waves we observe on Earth's oceans (see sect. 5.5 of

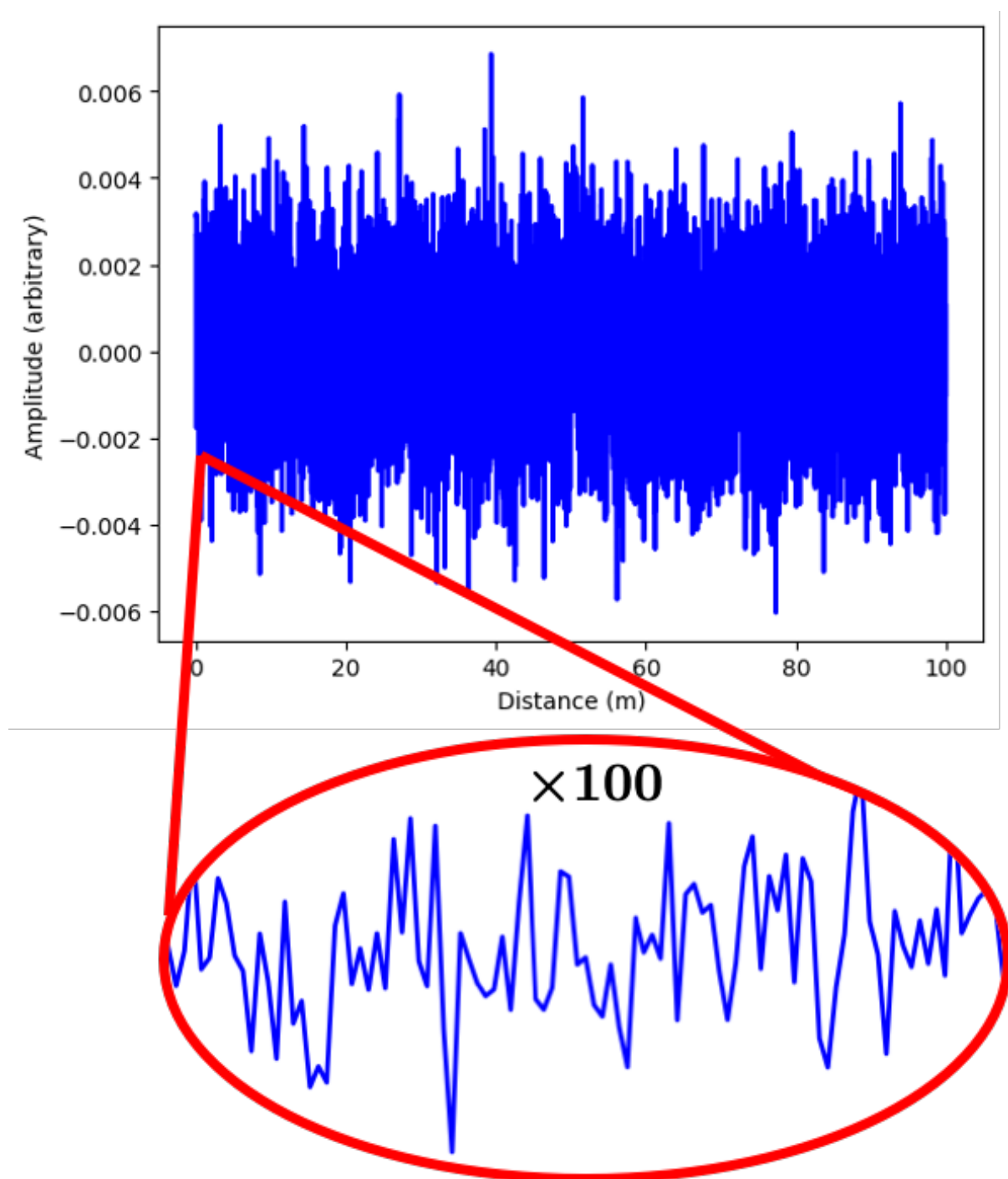


Figure 3.8: The unsmoothed fractal surface of an ocean whose wave heights are not adjusted. This surface was generated for a Hurst exponent of 0.7. The circled area magnifies the 0 – 1 m region by a $\times 100$.

Modirrousta-Galian et al. (2021) for a justification of why the Earth’s ocean waves are an appropriate analog for the roughness of the magma ocean on Kepler-10 b and other hot super-Earths). From a mathematical perspective, the act of smoothing perturbations smaller than 1 m means that fractal behavior ceases at small scales; this behavior is expected for natural systems instead of idealized mathematical constructs.

By combining the fGn package with the Gaussian filter, we now had a method of modeling the surface wave density as a function of the Hurst exponent (H). Now we needed to find the relationship between the Hurst exponent and the wave height.

3.2.5 The Waveheight

Concerning the average wave amplitude, we adopted the empirical relationship discovered by Durst et al. (2011) between the fractal dimension and the root mean square (RMS) height:

$$RMS \approx h_0 (F - 2), \quad (3.9)$$

where F is the fractal dimension and h_0 is an experimentally derived height constant. Using the previously mentioned relation, we can convert the fractal dimension into the Hurst exponent,

$$RMS \approx h_0 (1 - H). \quad (3.10)$$

To determine h_0 , we adopt Earth’s oceans as an analog that have an average Hurst exponent of ≈ 0.7 (Stiassnie, 1991; Stiassnie et al., 1991) with a root mean squared average waveheight of $RMS \approx 1.5$ m (Met Office, 2010). Therefore, the height constant can be constrained to $h_0 \approx 5$ and Eq. 3.10 can be written as,

$$RMS \approx 5 (1 - H). \quad (3.11)$$

We assume that h_0 is constant and equal for the Earth and Kepler-10 b. This assumption is made because the viscosity of magma at high temperatures is similar to that of water; we explain this point further in sect. 5.5 of Modirrousta-Galian et al. (2021). Now that we have the tools to model the wave heights and the surface wave density, we generate realistic magma ocean surfaces (see Fig. 3.9).

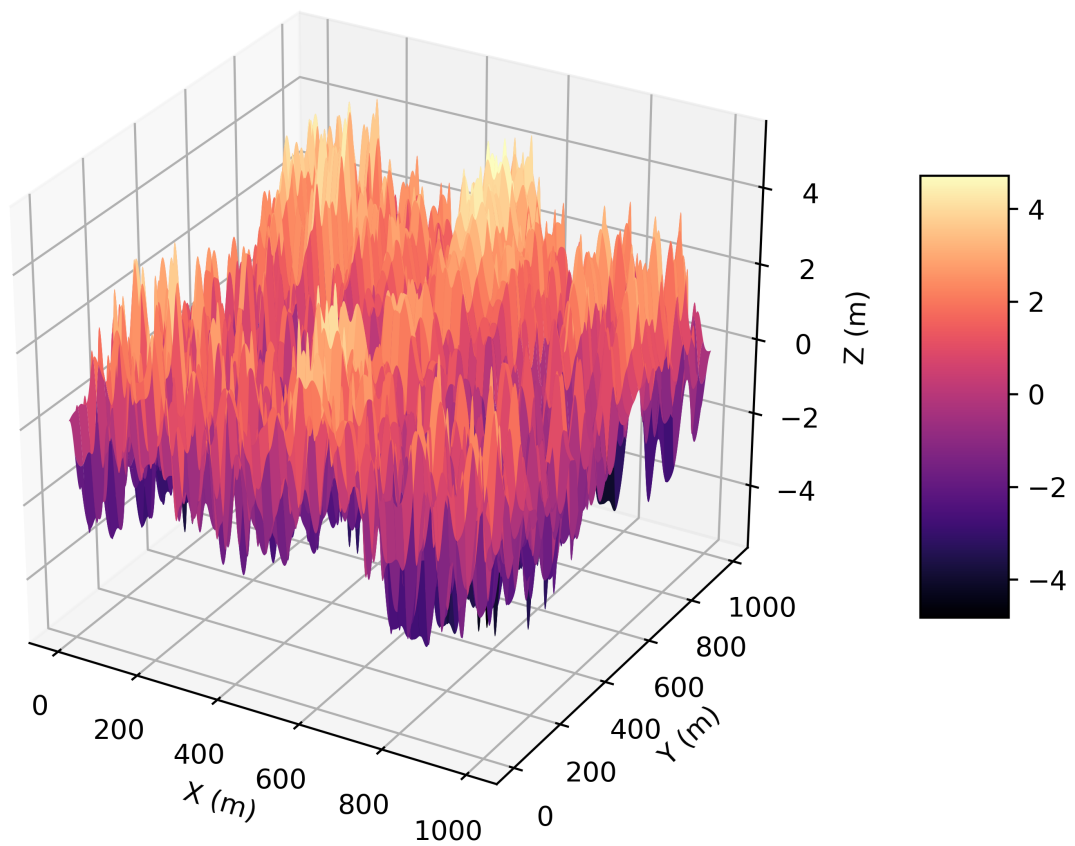


Figure 3.9: A 3-D rendition of a magma ocean surface generated using the methods given in sect. 3.2.4 and 3.2.5. Note that the x-axis and y-axis do not have the same scale, so surface features may seem distorted. It is also important to consider that in our albedo simulator, we used 2-D surfaces as they were less computationally expensive.

Parameter	$H \leq 0.95$
α_1	-0.397910
α_2	0.149320
α_3	0.388928
α_4	0.852872
β_1	1.594982
β_2	-3.375571
β_3	2.437896
β_4	-0.881001
β_5	0.194354
β_6	-0.041750
β_7	-0.081323

Table 3.1: Parameters for Eq. (3.12a) and (3.12b)

3.2.6 The Albedo Simulator

Once we had the fractal surface generator, we created a basic simulator that would throw 10,000 light rays with uniformly sampled initial locations. Each of these light rays interacted specularly with the surface according to the approximate Fresnel equations (Eq. 3.7) and the refractive index equations listed in Table 5 of [Modirrousta-Galian et al. \(2021\)](#). By recording how much of the incident light was reflected, we constrained the Bond albedo of the surfaces for different compositions and roughnesses. We set the condition that if a light ray lost more than 99.99% of its intensity, it got fully absorbed. This assumption was made to increase the efficiency of our code. We fitted the results from our simulations with analytic functions that we show in Eq. 3.12a and 3.12b. In conjunction, these analytic fits give the spherical albedo of a planar surface as a function of the Hurst exponent (a measure of the surface roughness) and the synthetic refractive index (a measure of the composition of the surface and wavelength of the light).

$$A \approx (\alpha_1 H + \alpha_2) + (\alpha_3 H + \alpha_4)(1 - e^{\Psi \cdot n_{sy}}) \quad (3.12a)$$

with

$$\Psi = \beta_1 H^6 + \beta_2 H^5 + \beta_3 H^4 + \beta_4 H^3 + \beta_5 H^2 + \beta_6 H + \beta_7, \quad (3.12b)$$

where $\alpha_{1 \rightarrow 4}$ and $\beta_{1 \rightarrow 7}$ are the coefficients listed in Table 3.1. With this equation, the planar albedo can be predicted as shown by Fig. 3.10. However, planets are spherical, not flat; 3-D effects must therefore be incorporated into the simulations. The influence of the

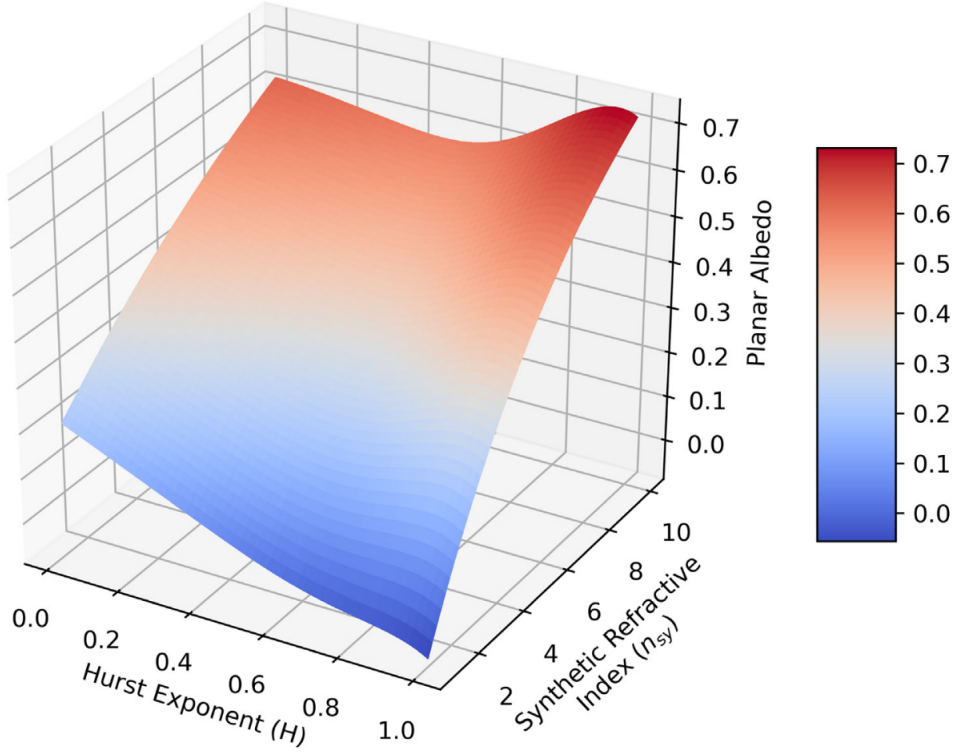


Figure 3.10: The planar albedo as a function of the synthetic refractive index (n_{sy}) and the Hurst exponent (H). This figure was generated with Eq. 3.12a and 3.12b.

sub-stellar latitude, $q(\phi)$, on the albedo is required to convert the planar albedo into the spherical albedo. From our simulations (see Supplementary File 2 that is found on the online version of [Modirrousta-Galian et al., 2021](#), containing raw data and χ^2 values) it was found that $q(\phi)$ is well approximated as,

$$q(\phi) \approx 1 - \frac{1 - A_{pla}}{1 + \left(\frac{\phi}{C_1(H)}\right)^{C_2(H)}}, \quad (3.13a)$$

where,

$$\begin{aligned} C_1(H) &= 0.320717H + 1.14083 \\ C_2(H) &= 8.54326 + 82.6376H^{3.88648}. \end{aligned} \quad (3.13b)$$

This can be combined with the equation for the spherical albedo of a planet,

$$A_S = \int_0^{\pi/2} \sin 2\phi \cdot q(\phi) d\phi. \quad (3.14)$$

From Eq. 3.13a it follows that as $\phi \rightarrow \pi/2$, $q(\phi) \rightarrow 1$ because at the terminator the planet

is fully reflecting (at right angles there is no absorption). Conversely, when $\phi \rightarrow 0$, the local albedo becomes identical to the planar albedo as the light is interacting with the sub-stellar point. Combining Eq. 3.14 with Eq. 3.12a, 3.12b, 3.13a, and 3.13b gives the spherical albedo of a planet. Hence, it is now possible to explore the reflective properties of planets with different magma ocean properties.

A comparison between different materials can be found in Fig. 3.11. Planets composed of common Earth minerals and rocks typically have spherical albedo values of $\sim 10\%$ that tend to decrease as the wavelength increases from $0.5 \mu\text{m}$ to $7.8 \mu\text{m}$. The only exceptions are SiO_2 (i.e., rhyolites) and komatiites, which have sudden increases in their spherical albedos at $\sim 7.2 \mu\text{m}$.

Pure metal planets would have very high spherical albedos, especially if they were made of Ag, Al, Au, Cu, Fe, Mg, Mo, or Ni, as they would reach values close to 100% at larger wavelengths. Metalloids (Ge and Si) would produce lower spherical albedos, and, in the wavelengths of interest, they appear to stabilize at 30 – 50%.

The reflective properties of metal oxides vary significantly depending on the species considered. FeO is the shiniest oxidized material analyzed in this study, with values reaching as high as 45%. Conversely, Al_2O_3 and MgO are the least reflective oxidized metallic species with spherical albedo values close to common Earth minerals and rocks such as the ones explained above.

We present two carbonaceous minerals; CaCO_3 and SiC. SiC's spherical albedo decreases from $\sim 20\%$ to $\sim 15\%$ from $0.5 - 7.8 \mu\text{m}$ respectively. Conversely, CaCO_3 has a spherical albedo $\lesssim 10\%$ for wavelengths below $\sim 6.2\mu\text{m}$, but beyond this, it quickly increases to a maximum of almost $\sim 90\%$ at $\sim 6.8\mu\text{m}$. This peak decreases to $\sim 15\%$ for wavelengths greater than $\sim 7.5\mu\text{m}$.

An analysis of pure materials is useful as a benchmark test for the composition of exoplanets; however, real systems have more complex compositions. Therefore, it is important to find geochemically self-consistent mixtures of the aforementioned materials so that, from an observed albedo spectrum, one can categorize the composition of an exoplanet. For a thorough analysis of different geochemical compositions, see sect. 4 of [Modirrousta-Galian et al. \(2021\)](#). Note that our focus is on airless magma ocean planets that will have surface

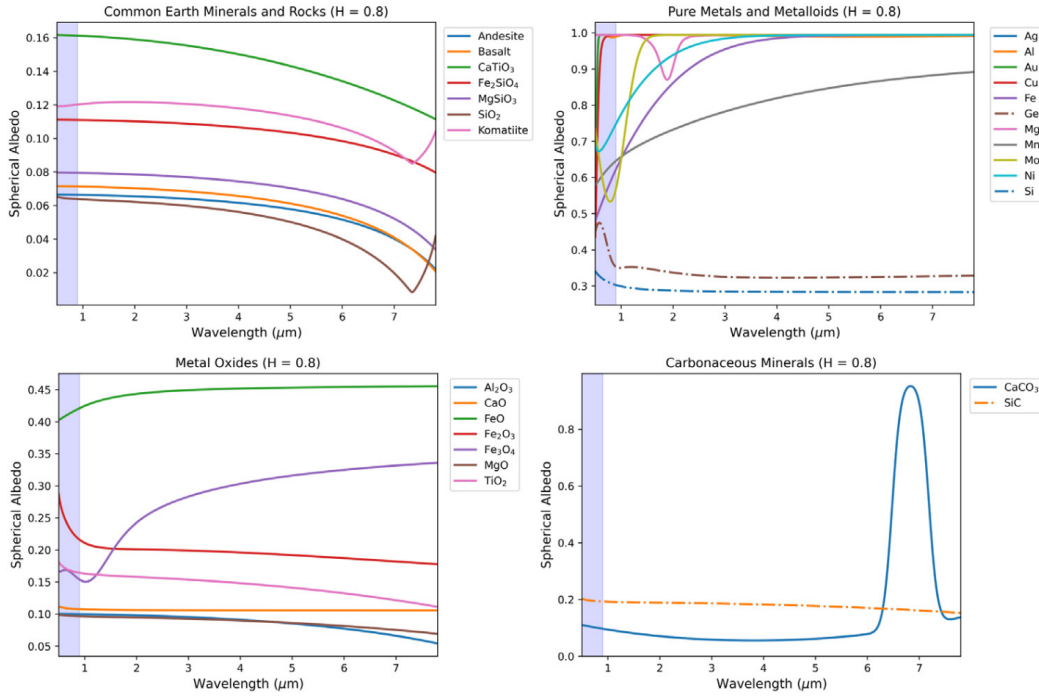


Figure 3.11: The spherical albedo values of common Earth minerals and rocks, metals and metalloids, metal oxides, and two carbonaceous minerals, for a Hurst exponent of 0.8. The light-blue section is Kepler’s band-pass. This figure was generated with Eqs. 3.14, Eq. 3.12a, 3.12b, 3.13a, and 3.13b.

textures described by the turbulence of the ocean surface; comparing our results to bodies with solid surfaces such as asteroids or comets would be incommensurable. We provide a summary of our results below:

Evolved planets: These are airless tidally-locked bodies with Earth-like compositions that have had their surfaces heavily processed by the formation of mineral atmospheres. The mineral atmospheres form on the day-side and then expand rapidly into their night-side, where they condense. Since different minerals condense at different temperatures (Lodders, 2003), this will cause the day-side’s surface to experience a geochemical evolution (assuming weak magma ocean convection Kite et al., 2016). For example, refractory materials, like metals, condense at higher temperatures than volatiles like ices, so hotter sections of the magma ocean (close to the substellar point) would become metal-rich and ice-poor, whereas the opposite would occur at latitudes close to the terminator. Our results show that the Bond albedo will remain $\lesssim 10\%$, which is consistent with experimental data (Essack et al., 2020). Fig. 3.12 shows our results.

Metallic planet: The albedo of metallic planets (i.e., planets with large metal abundances)

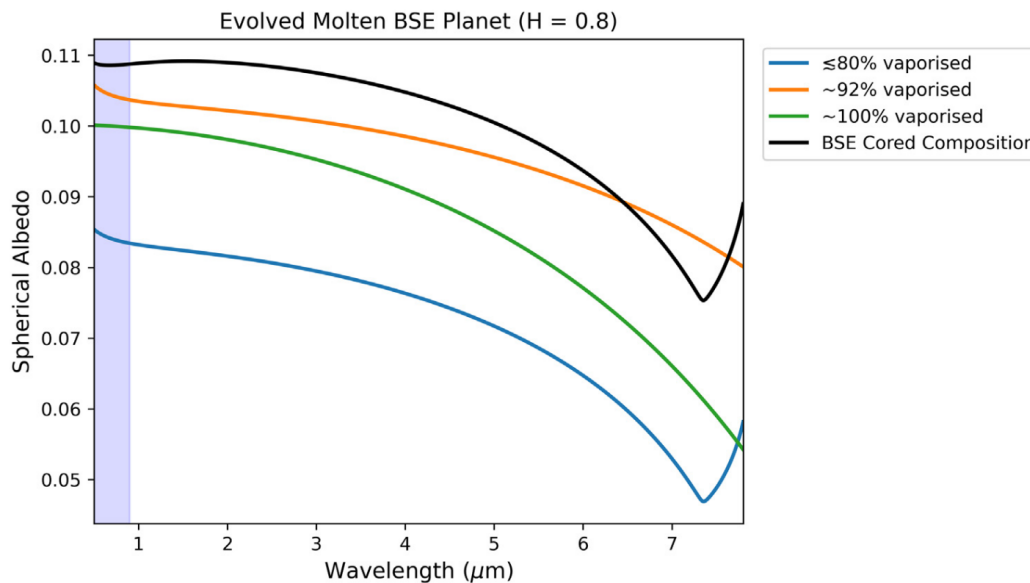


Figure 3.12: The spherical albedo for a terrestrial planet with an initial composition corresponding to the BSE that has been evolved due to chemical interactions between the magma and the mineral atmosphere. Four different spherical albedo spectrums are shown corresponding to varying levels of vaporization. The BSE composition is from [O’Neill and Palme \(1998\)](#), while the vaporized compositions were taken from [Kite et al. \(2016\)](#). The light-blue section is Kepler’s band-pass. This figure was generated with Eqs. 3.14, Eq. 3.12a, 3.12b, 3.13a, and 3.13b.

depends on the oxidation state of the metals. For instance, if a metallic planet formed under very oxidized conditions, most of the metals would combine with oxygen to form species like FeO, Fe₂O₃, Fe₃O₄, MgO. These minerals have high Bond albedo values, so the planet would have a high reflectance (see Fig. 3.11). Conversely, if the planet formed under very reduced conditions, some metals would remain relatively pure (notably iron). However, because pure metals are heavy relative to silicate species such as olivines and pyroxenes, they would sink to the center of the planet and form a core ([Elkins-Tanton and Seager, 2008](#)). Among the various explanations for Mercury’s formation, this prescription (i.e., [Lewis, 1972, 1974](#); [Cameron, 1985](#)) could explain why Mercury has an iron-poor regolith ([Evans et al., 2012](#); [Weider et al., 2014](#)) and the solar system’s largest (relatively) iron core ([Riner et al., 2008](#); [Malavergne et al., 2010](#); [Hauck et al., 2013](#); [Chabot et al., 2014](#)). It is, therefore, impossible to constrain the Bond albedo values of metallic planets as it depends strongly on their redox state and not on their metallic mass fractions.

Coreless terrestrial planet: These are planets that formed under heavily oxidized conditions. Because of this, most metals would combine with oxygen to form species such as FeO, Fe₂O₃, Fe₃O₄ and MgO. Since they have similar masses to rocky species (e.g., olivines

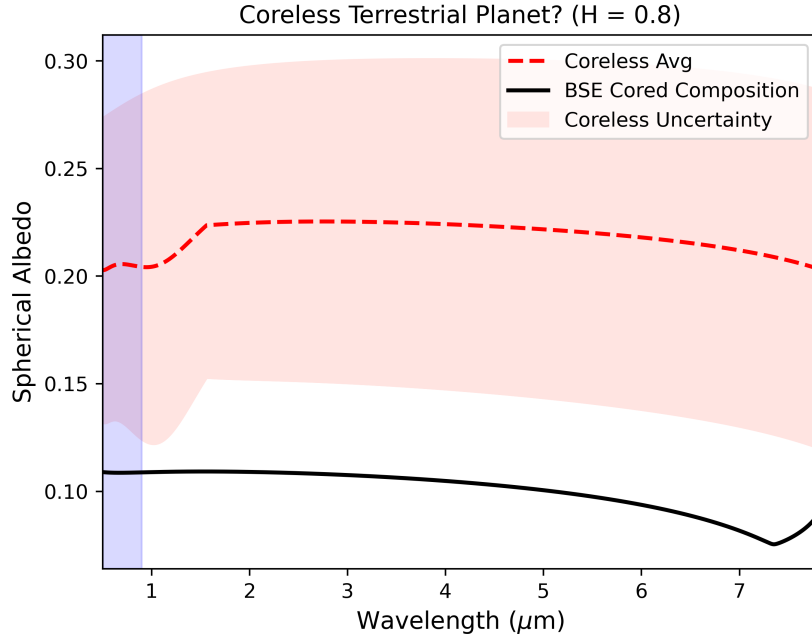


Figure 3.13: The spherical albedo of a coreless terrestrial planet with the composition given by [Elkins-Tanton and Seager \(2008\)](#). The red dotted line is the average coreless spherical albedo value for $H = 0.8$, the red shaded region represents the uncertainty, and the black line is for the spherical albedo value of a cored BSE planet [O’Neill and Palme \(1998\)](#). The light-blue section is Kepler’s band-pass. This figure was generated with Eqs. 3.14, Eq. 3.12a, 3.12b, 3.13a, and 3.13b.

and pyroxenes), they would get incorporated in the crust and mantle, resulting in metal-rich magmas. Adjusting the surface roughness parameter (H) and maximizing the FeO abundance allows for a theoretically maximum Bond albedo of $\sim 55\%$. Fig. 3.13 shows our results.

Reduced planets: Enstatite chondrites are among the most reduced, naturally occurring rocks; Mercury is believed to have formed from meteorites of this type (e.g., [Nittler et al., 2011](#); [Malavergne et al., 2014](#); [Nittler and Weider, 2019](#)). Hence, the Bond albedo values of reduced planets that form from enstatite chondrites should be very low ($\sim 10\%$ [Essack et al., 2020](#)) as their surfaces are expected to be rich in silicate species (e.g., [Namur et al., 2016](#)). We find that the amount of light they reflect is similar to typical bulk silicate Earth composition (BSE) planets, albeit with slightly different spectrum shapes. However, one cannot rule out the possibility of more unusual reduced compositions as these could lead to ambiguities in the predicted Bond albedos. One such example is carbon-rich planets that we explain below.

Carbon planets: These are planets that are rich in carbonaceous species such as graphite

or SiC. For this to be the case, the planet must have formed under significantly reduced conditions. For instance, if a planet were composed of equal parts Si-O-C, most of the silicon would bind with the oxygen to form silicates such as SiO₂ and SiO. The carbon would then bond with itself to form graphite in the planet's outer layers and diamond at greater depths. Due to graphite being less dense than SiO₂ and having a higher melting temperature, it would rise to the top layers of the mantle in the form of solid graphitic grains. This simple analogy is supported by high-pressure, high-temperature (high P-T) laboratory experiments (e.g., [Hakim et al., 2018, 2019](#)) that arrived at the same conclusion. These high P-T experiments predict that extremely reduced conditions are required to maintain SiC in a geochemically stable condition. Therefore, despite SiC planets being theoretically plausible, they may be unlikely. On that account, it seems more probable that carbon-rich worlds will be composed of silicate mantles covered in solid graphite. The Bond albedo values of these planets would be dominated by the graphitic layer that we cannot model with our code because it is adapted for fluid systems. Ignoring surface roughness, the Bond albedo of a graphite layer in the range of 0.5 – 7.8 μm would vary from 30 – 80% (e.g., [Taft and Philipp, 1965](#); [Philipp, 1977](#); [Querry, 1985](#); [Djurišić and Li, 1999](#); [Kuzmenko et al., 2008](#); [Papoular and Papoular, 2014](#)), making carbon-rich super-Earths the brightest airless bodies.

3.2.7 Summary

In this chapter (see also [Modirrousta-Galian et al., 2021](#)) we provide an analytic model for the spherical albedo of molten, airless, or near-airless super-Earths. We developed this model by fitting the simulations of photons interacting with magma ocean surfaces with varying reliefs and geochemical compositions. Our list, shown in Table 5 of [Modirrousta-Galian et al. \(2021\)](#), is not comprehensive as more chemicals could be added to the collection. Due to being analytic, our model could be adopted in a computationally inexpensive manner to constrain the surface composition of airless super-Earths.

3.2.8 Future Work

There is a bimodal distribution of exoplanet radii with one peak at $\sim 1.3R_{\oplus}$, the other at $\sim 1.75R_{\oplus}$, and the minimum at $\sim 2.4R_{\oplus}$ (see sect. 2). According to theoretical modeling (e.g., [Owen and Wu, 2013, 2017](#); [Jin and Mordasini, 2018](#); [Modirrousta-Galian et al.,](#)

2020a) and observational data (e.g. Swain et al., 2019), most planets in the first peak lack primordial atmospheres, whereas most planets in the second peak have them. For planets with such atmospheres, it is more straightforward to constrain their compositions as atmospheric species can be detected (Tsiaras et al., 2016; Ridden-Harper et al., 2016; Esteves et al., 2017) and then used to infer the interior properties. However, if a planet lacks a primordial atmosphere, spectroscopy is not feasible, leaving one with fewer data to deduce the interior properties. In the case of molten, airless super-Earths (located mostly in the first peak) the Bond albedo can be used in an analogous manner to spectroscopic data to deduce the surface composition and constrain the interior. Hence, exotic bodies like 55 Cancri e could be tested to see whether they are a coreless body (Bourrier et al., 2018a), a graphitic planet (Madhusudhan et al., 2012; Miozzi et al., 2018), an icy planet (Zeng and Sasselov, 2013; Zeng et al., 2016), a planet with a hydrogen atmosphere partially confined to the night-side and with a day-side that is near-airless (Modirrousta-Galian et al., 2020b), or none of the above.

In addition, due to our model being analytic, it could be implemented into atmospheric general circulation models (GCMs) and spectral retrieval codes. Such integration may provide a more holistic analysis of a planet because the effects of an atmosphere and surface could be coupled. Furthermore, it would be interesting to expand our work to non-molten surfaces such as desert planets; in theory, solid surfaces can also be described with fractal mathematics (e.g., Mandelbrot, 1975; Shelberg et al., 1983). We also welcome more experimental data on the refractive indices of materials at different temperatures, pressures, and phases to better model the Bond albedo values of exoplanet surfaces.

4 Constraining Super-Earths with Envelopes

As explained in sect. 1.3, together with information on the bulk average density, atmospheric spectroscopy can be used to constrain the properties of exoplanets. However, before the connection between the atmospheric composition and interior structure is discussed, we explore the atmospheric composition, determined by spectroscopy, of examples of representative planets in the following order: sect. 4.0.1 ultra-hot Jupiters (Edwards et al., 2020; Pluriel et al., 2020), sect. 4.0.2 hot Jupiters (Skaf et al., 2020), sect. 4.0.3 hot sub-Neptunes (Guilluy et al., 2021), and sect. 4.0.4 a warm super-Earth (Mugnai et al., 2021). After this section, we present the RAPOC code that converts wavelength-dependent opacities into Rosseland and Planck mean opacities that facilitate modeling efforts. By using the realizations of RAPOC to build synthetic exoplanet atmospheres, we show that the atmospheric enrichment can be used to constrain the composition of super-Earth interiors.

4.0.1 Two Ultra-Hot Jupiters

WASP-76 b and KELT-7 b are two ultra-hot Jupiters with temperatures of ~ 2800 K and ~ 2100 K, respectively. WASP-76 b has a mass and radius of $\simeq 0.9M_J$ and $\simeq 1.85R_J$ (Ehrenreich et al., 2020) orbiting an F7V-type star that is $5.30^{+6.10}_{-2.90}$ Gyr old (West et al., 2016). Regarding KELT-7 b, its mass and radius are $\simeq 1.28M_J$ and $\simeq 1.533R_J$, respectively, with its host star being an F2-type with an age of 1.3 ± 0.2 Gyr (Bieryla et al., 2015). WASP-76 b and KELT-7 b have significantly lower densities than what planetary equations of state predict for hot Jupiters (Fortney et al., 2007). The current best explanation for the extended radii of some hot Jupiters is ohmic heating (Batygin and Stevenson, 2010). This mechanism occurs when magnetic interactions between the host star and the planet trigger electrothermic heating within. The resultant inflated radii make these planets optimum targets for atmospheric spectroscopy. In Edwards et al. (2020) and Pluriel et al. (2020) we performed an atmospheric spectroscopic analysis of these planets using transmission and emission spectroscopy. For both planets we used Hubble Space Telescope’s (HST) Wide Field Camera 3 (WFC3) data that reduced and fit for each observation using the open-source software Iraclis¹¹. After this, a full Bayesian retrieval

¹¹<https://github.com/ucl-exoplanets/Iraclis>

was performed using the publicly available analysis suite TauREx3¹².

From the transmission analysis, we found a spectrum consistent with grey clouds and a strong water feature, whereas in the emission spectrum, we found spectral features that indicate a low TiO abundance with water and evidence of a thermal inversion. With the exception of water, the presence of the other chemical species is weakly constrained due to their low abundances. Our results are consistent with previous spectroscopic studies (Tsiaras et al., 2018) and theoretical chemical equilibrium models (Mollière et al., 2015, 2017). In Table 4.1 we present our best fit results for the atmospheric properties of WASP-76 b.

Parameter	Transmission	Emission
$\log_{10}(\text{H}_2\text{O})$	$-2.85^{+0.42}_{-0.71}$	$-2.81^{+0.51}_{-0.65}$
$\log_{10}(\text{TiO})$	< -6.1	$-5.62^{+0.71}_{-1.57}$
$\log_{10}(\text{VO})$	< -6.9	< -7.9
$\log_{10}(\text{FeH})$	< -7.3	< -7
$\log_{10}(P_{\text{clouds}})$	$0.91^{+0.70}_{-0.46}$	N.A.
T (K)	$2231.16^{+265.22}_{-283.51}$	$3146.76^{+189.33}_{-168.50}$

Table 4.1: Retrieved atmospheric composition of WASP-76 b from transmission and emission spectroscopy

Regarding KELT-7 b, our spectroscopic analysis found a cloud-free atmosphere with H₂O and H⁻ with log abundances of $-4.34^{+1.41}_{-4.45}$ and $-4.26^{+1.41}_{-2.42}$ respectively. This result is consistent with the equilibrium chemistry predicted by the petitCODE¹³: a 1D pressure-temperature iterator that solves radiative-convective and chemical processes. An attempt was made to include Spitzer IRAC data, but this gave rise to almost identical transmission and emission results with the exception that carbon monoxide was now constrained to $\log_{10}(\text{CO}) = -4.56^{+1.72}_{-4.69}$. However, adding TESS data to our analysis drastically changed the results as it negated the H⁻ detection and instead preferred FeH as an atmospheric component; this disparity shows that there are uncertainties in the composition and properties of KELT-7 b’s atmosphere that can only be overcome with more data.

¹²https://github.com/ucl-exoplanets/TauREx3_public

¹³https://petitradtrans.readthedocs.io/en/latest/content/notebooks/poor_man.html

4.0.2 Three Hot Jupiters

In Skaf et al. (2020) we analyzed three exoplanets: WASP-127 b ($M_p \simeq 0.18M_J$, $R_p \simeq 1.37R_J$, $T \simeq 1400$ K; [Palle et al., 2017](#)), WASP-79 b ($M_p \simeq 0.85M_J$, $R_p \simeq 1.53R_J$, $T \simeq 1716$ K; [Brown et al., 2017](#)), and WASP-62 b ($M_p \simeq 0.58M_J$, $R_p \simeq 1.34R_J$, $T \simeq 1475$ K; [Brown et al., 2017](#)). WASP-127 b, WASP-79 b, and WASP-62 b orbit G5-, F3-, and F7-type stars, respectively; like the planets mentioned in sect. 4.0.1, the bulk densities of these hot Jupiters are significantly lower than pure (cold) hydrogen ([Fortney et al., 2007](#)). Such densities are not caused by the high (> 1000 K) effective temperatures, but by the star-planet magnetic interactions triggering interior ohmic heating ([Batygin and Stevenson, 2010](#)), thus explaining why these planets have very low densities despite being colder than those shown in sect. 4.0.1. The low densities make these planets optimum targets for atmospheric spectroscopy, which was a strong motivating factor for our work.

We made use of the spectroscopic data from the G141 grism ($1.088 - 1.68\mu\text{m}$) of the Wide Field Camera 3 on board the Hubble Space Telescope. We adopted the same methodology as the previously mentioned paper, where we processed the data using the Iraclis pipeline and the TauREx3 retrieval code. Our derived chemical abundances were as follows: All planets are consistent with chemical equilibrium models; however, we note

	WASP-127 b	WASP-79 b	WASP-63 b
$\log_{10}(\text{H}_2\text{O})$	$-2.71^{+0.57}_{-0.76}$	$-2.43^{+0.57}_{-0.76}$	$-2.03^{+0.52}_{-1.27}$
$\log_{10}(\text{FeH})$	$-5.25^{+0.88}_{-1.10}$	$-4.42^{+0.91}_{-1.18}$	$-3.04^{+2.18}_{-2.27}$
$\log_{10}(P_{\text{clouds}})$	$1.7^{+0.93}_{-0.66}$	> 4	$3.63^{+1.46}_{-1.29}$

Table 4.2: Retrieved atmospheric composition of WASP-127 b, WASP-62 b and WASP-62 b from transmission spectroscopy

that WASP-79 b showed a hint of non-equilibrium because when an attempt was made to fit the chemical equilibrium model to the data, the solution gave anomalously low temperatures. Including FeH as an opacity source provided a more realistic temperature solution that allowed for chemical equilibrium at ~ 1000 K. Even so, this temperature is still lower than the effective temperature of the planet, which is ~ 1700 K. This anomaly suggests that other opacity sources could be present but have yet to be found. Another possible explanation for the low temperatures is the significant uncertainties in the 10 bar radius; a better-constrained radius may rectify this issue.

4.0.3 Two Hot Sub-Neptunes

In [Guilluy et al. \(2021\)](#), we analyzed two hot sub-Neptunian exoplanets: HD 106315 c and HD 3167 c. The first of which has a mass, radius and temperature of $14.6 \pm 4.7M_{\oplus}$, $4.98 \pm 0.23R_{\oplus}$, and $\simeq 900$ K, respectively ([Guilluy et al., 2021](#); [Barros et al., 2017](#)). The other planet, HD 3167 c, has a mass, radius and temperature of $8.33^{+1.79}_{-1.85}M_{\oplus}$, $2.740^{+0.106}_{-0.100}R_{\oplus}$, and $\simeq 530$ K, respectively ([Gandolfi et al., 2017](#)). HD 106315 c and HD 3167 c orbit F5V- and K0V-type stars, at distances of 0.1536 ± 0.0017 AU ([Barros et al., 2017](#)) and 0.1806 ± 0.0080 AU ([Gandolfi et al., 2017](#)), respectively. Their close orbits suggest that atmospheric evaporation from XUV-irradiation was probable in their pasts ([Modirrousta-Galian et al., 2020a](#)); atmospheric spectroscopy can be used to constrain the degree of atmospheric processing that took place and, therefore, constrain the histories of these bodies.

We performed a transmission spectroscopic analysis with the G141 grism ($1.125 - 1.650\mu\text{m}$) of the Wide Field Camera 3 (WFC3) onboard the Hubble Space Telescope. With this approach, water vapor was detected on both planets with an abundance of $\log_{10}(\text{H}_2\text{O}) = -2.1^{+0.7}_{-1.3}$ ($\sim 5.68\sigma$) and $\log_{10}(\text{H}_2\text{O}) = -4.1^{+0.9}_{-0.9}$ ($\sim 3.17\sigma$) for HD 106315 c and HD 3167 c, respectively. The transmission spectrum of HD 106315 c also shows possible evidence of ammonia absorption ($\log_{10}(\text{NH}_3) = -4.3^{+0.7}_{-2.0}$, $\sim 1.97\sigma$), although it is not statistically significant. HD 3167 c has statistically significant carbon dioxide absorption features in the $1.1 - 1.6\mu\text{m}$ wavelength range ($\log_{10}(\text{CO}_2) = -2.4^{+0.7}_{-1.0}$, $\sim 3.28\sigma$). However, CO_2 cannot be explained by 1D equilibrium chemistry models, so it may be due to possible systematic errors.

4.0.4 One Warm Super-Earth

In [Mugnai et al. \(2021\)](#), we present a study on the spectroscopic transit observations of the warm (~ 500 K) super-Earth GJ 1132 b, which orbits an M4.5V-type star ([Berta-Thompson et al., 2015](#)). Having a mass and radius of $1.66 \pm 0.23M_{\oplus}$ and $1.13 \pm 0.056R_{\oplus}$ respectively ([Bonfils et al., 2018](#)), the bulk density is consistent with a rocky composition that is denser than Earth (see Fig. 1 of [Mugnai et al., 2021](#)). However, spectroscopic data from [Swain et al. \(2021\)](#) suggested that GJ 1132 b has a hydrogen-rich tenuous atmosphere. This puzzling and contradictory finding warranted further investigation, which is why we

characterized the atmosphere of this planet using atmospheric spectroscopy.

In our work, all of the data was obtained with the G141 grism (1.125 - 1.650 μm) on the Wide Field Camera 3 (WFC3) onboard the Hubble Space Telescope. We used the publicly available Iraclis pipeline to extract the planetary transmission spectra from the five visits and produce a precise transmission spectrum. These data were then analyzed using the TauREx3 atmospheric retrieval code, with which it is shown that the spectrum does not contain discernible molecular signatures in the investigated wavelength range. The spectrum is instead best-fit with a flat-line model. Therefore, our results suggest that GJ 1132 b does not have a clear primordial atmosphere and may host a cloudy or very enriched atmosphere, be airless, or have a tenuous atmosphere that has not been detected. Due to the limited wavelength coverage of WFC3, it is not possible to decide among these scenarios, but the James Webb Space Telescope or Ariel may resolve the atmospheric features.

Final Remarks – Because atmospheric spectroscopic data of exoplanets are so far limited, overarching conclusions cannot yet be made; our results do, however, support the premise that water is a common molecule in planetary atmospheres and that such atmospheres are typically in thermodynamic equilibrium. These results raise new questions such as under what conditions atmospheres are in disequilibrium and where the water reservoir originated.

The findings of atmospheric characterization studies are sometimes assumed to reflect the bulk composition of the total planetary envelope. This assumption fails to recognize the effects of condensation in setting an upper limit for what species can exist above their respective cloud layer. In the following section, we present RAPOC, a tool that facilitates the opacity treatment for atmospheric modeling. In the section after, we use the realizations of RAPOC to show under what conditions spectroscopic data can reveal insights on the properties of planetary interiors.

4.1 Opacities and the RAPOC Code

Atmospheric spectroscopy is essential for determining the chemical constituents of exoplanet atmospheres. However, to infer the temperature structure and location of the radiative-convective boundary, modeling is required. When modeling atmospheres,

knowing how to evaluate opacities is essential. The most appropriate approach would use wavelength-dependent opacities; in the case of atomic hydrogen, for example, the Rydberg formula is a reasonable approximation for calculating the regions in the electromagnetic spectrum that are opaque,

$$\frac{1}{\lambda} = R_{\infty} \left(\frac{1}{n_1^2} - \frac{1}{n_2^2} \right), \quad (4.1)$$

where λ is the wavelength, R_{∞} is the Rydberg constant ($1.09737316 \times 10^7 \text{ m}^{-1}$), and n is the energy level. From Eq. 4.1, one can see that from the Paschen series onwards ($n_1 \geq 3$), there is absorption in the infrared wavelengths. However, hydrogen is generally found in molecular form under typical planetary conditions and rarely as a single atom. When dealing with molecules, the treatment of opacities is more complex as electronic, vibrational, and rotational transitions can co-occur. Furthermore, collision-induced emission and absorption can be important opacity sources for dense gases; this is the process in which inelastic collisions between molecules result in quantum transitions or the formation of transient supramolecular complexes with spectral features distinct from the original mixture. To model such effects, an extensive list of opacities is required, which is provided by several repositories such as *ExoMol*¹⁴, *HITRAN*¹⁵, and *HITEMP*¹⁶. After a careful opacity treatment, the next step is to consider the stellar host's emission (reasonably approximated as a blackbody) to calculate what fraction of incoming energy the atmosphere absorbs. However, such modeling can be complicated because the planetary albedo and the gas opacities are wavelength-dependent. In addition, clouds of different compositions may form at different altitudes that further complicates modeling efforts because the chemistry and opacity of the atmosphere is not homogenous (Fortney et al., 2007; Nettelmann et al., 2011; Petralia et al., 2020).

One commonly used method for simplifying the treatment of opacities is to remove the wavelength dependence through averaging. There are several possible approaches, but the main two concern with generating Rosseland and Planck mean opacities (abbreviated to RM, PM, and RPM when referring to both). The Rosseland mean opacity is defined as (Lenzuni et al., 1991),

$$\frac{1}{\kappa_r} = \frac{\int_0^{\infty} \kappa_{\nu}^{-1} u(\nu, T) d\nu}{\int_0^{\infty} u(\nu, T) d\nu}, \quad (4.2)$$

¹⁴www.exomol.com

¹⁵hitran.org

¹⁶<https://hitran.org/hitemp/>

where κ_ν is the opacity at a given frequency ν , and $u(\nu, T)$ is the Planck black body derivative with respect to the temperature T . Since opacity data is not available across the entirety of the electromagnetic spectrum, a shorter range is selected (i.e., multigroup opacities). Eq. 4.2 can therefore be rewritten as,

$$\frac{1}{\kappa_r} \simeq \frac{\int_{\nu_1}^{\nu_2} \kappa_\nu^{-1} u(\nu, T) d\nu}{\int_{\nu_1}^{\nu_2} u(\nu, T) d\nu}. \quad (4.3)$$

The Planck mean opacity is defined as (Lenzuni et al., 1991),

$$\kappa_p = \frac{\int_0^\infty \kappa_\nu B_\nu(T) d\nu}{\int_0^\infty B_\nu(T) d\nu}, \quad (4.4)$$

where $B_\nu(T)$ is the Planck black body law at temperature T . Eq. 4.4 is rewritten as,

$$\kappa_p \simeq \frac{\int_{\nu_1}^{\nu_2} \kappa_\nu B_\nu(T) d\nu}{\int_{\nu_1}^{\nu_2} B_\nu(T) d\nu}. \quad (4.5)$$

The Rosseland and Planck mean opacities are different averages; the former is the harmonic mean (favoring smaller opacities) and the latter is the arithmetic mean (favoring larger opacities). Depending on the context and the wavelength range considered, the most relevant opacity is selected. For example, when dealing with relatively transparent gases like primordial mixtures of hydrogen and helium, the Rosseland mean opacity may represent the true opacities better because it predicts lower values. Conversely, if one wants to model an atmosphere rich in H₂O, the Planck mean opacity may be the better choice as it can account for the strong absorption peaks in the infrared. These two opacity approximations are widely used in the literature, inspiring the creation of the RAPOC code.

Developed in collaboration with Lorenzo V. Mugnai, the RAPOC code is the product of a joint effort between Sapienza Università di Roma, Università degli Studi di Palermo, and INAF - Osservatorio Astronomico di Palermo. RAPOC uses molecular absorption data (i.e., wavelength-dependent opacities) to calculate Rosseland and Planck mean opacities that are commonly used in atmospheric modeling. RAPOC is designed to be simple, straightforward, and easily incorporated into other codes; it is completely written in Python and documented with docstrings^{17,18}. The motivation for the creation of

¹⁷<https://rapoc-public.readthedocs.io/en/latest/>

¹⁸<https://github.com/ExObsSim/Rapoc-public>

this code is that no publicly available program fulfilled this task, meaning that many researchers had to use Rosseland and Planck mean opacities from limited databases in their models. Using RAPOC, it is possible to estimate the opacities at different pressures and temperatures as well as finding the mean opacities for the Rayleigh scattering of 102 built-in atomic species, without requiring input data from the user. Incorporating the opacity from Rayleigh scattering can be particularly important as some species such as Na can contribute considerably to the opacity of planetary atmospheres.

4.1.1 Comparison With Values in the Literature

To demonstrate the efficacy of the RAPOC code, we compare its predicted Rosseland and Planck mean opacities, with several reference values in the literature. Most studies, however, focus on primordial gas mixtures with different metallicities (Cox and Tabor, 1976; Alexander et al., 1989; Lenzuni et al., 1991; Alexander and Ferguson, 1994; Iglesias and Rogers, 1996; Mayer and Duschl, 2005; Freedman et al., 2008, 2014). Whereas the values of mixtures are useful for modeling planetary formation or stellar interiors, they are not as applicable to planetary atmospheres. We, therefore, focus on papers providing RPMs for individual molecules because they allow for a straightforward comparison with the RPM values provided by RAPOC. Most of the individual molecule RPM values present in the literature are estimated directly from line-lists (Badescu, 2010; Kurosaki et al., 2014). Alternatively, RAPOC uses precomputed opacities for single molecules to estimate their wavelength-averaged values, which allows for faster and easier computations, and a straightforward integration into other codes. RAPOC, therefore, relies on precomputed data, such as the one provided by *ExoMol* and *DACE*, instead of line lists. Furthermore, if the opacities of a gas mixture are required, the user can manually combine the contributions of the individual species calculate by RAPOC.

We compare our RPM opacity estimations for water vapor with those of Hottel (1954), Abu-Romia and Tien (1967), and Kurosaki et al. (2014). Hottel (1954) estimated the IR Planck mean opacities from emissivity data, whereas Abu-Romia and Tien (1967) found IR RPMs from spectral data using selected bands in the $2.7 - 20 \mu\text{m}$ range. Kurosaki et al. (2014), however, produces a monotonic power-law fit (their Eqs. A.5–8) for estimating water RPMs in the visible and thermal wavelengths using *HITRAN* data. The power-law approximation presented in Kurosaki et al. (2014) has been tuned for two wavelength

ranges: visible ($0.4 - 0.7 \mu m$) and thermal ($0.7 - 100 \mu m$). For a comparison with RAPOC, we estimate RPMs with $0.4 - 0.7 \mu m$ and $0.7 - 50 \mu m$ wavelength ranges for visible and thermal range respectively. Our comparison is found in Fig. 4.1. Because Abu-Romia and Tien (1967) and Hottel (1954) only provide results the IR range, we only show Kurosaki et al. (2014) for the visible range. We are aware that for simple molecules such as H_2 that are weakly absorbing in the infrared and visible wavelengths, the collisional absorption may be crudely approximately by a power law as a function of pressure and temperature. However, as soon as a hydrogen gas is slightly enriched by other molecules, the power-law approximation begins to fail (Freedman et al., 2008, 2014). In addition, for molecules like H_2O and CO_2 , there are other sources of opacity such as electronic transitions, molecular rotations, and vibrations, meaning that the opacity is not at all monotonic. Because of this, and the different wavelength ranges considered, the model by Kurosaki et al. predicts opacities that differ by up to five orders of magnitude from what is estimated by RAPOC. Fig. 4.1 shows how Kurosaki et al. (2014) predicts opacities that are significantly greater than the wavelength-dependent values available from *ExoMol*. In addition, Fig. 4.1 shows that RAPOC's Planck Mean Opacity estimate is compatible with the value reported in Abu-Romia and Tien (1967) and Hottel (1954). The Rosseland Mean Opacity given by Abu-Romia and Tien (1967) is, however, several orders of magnitudes larger than the value estimated by Kurosaki et al. (2014) and RAPOC.

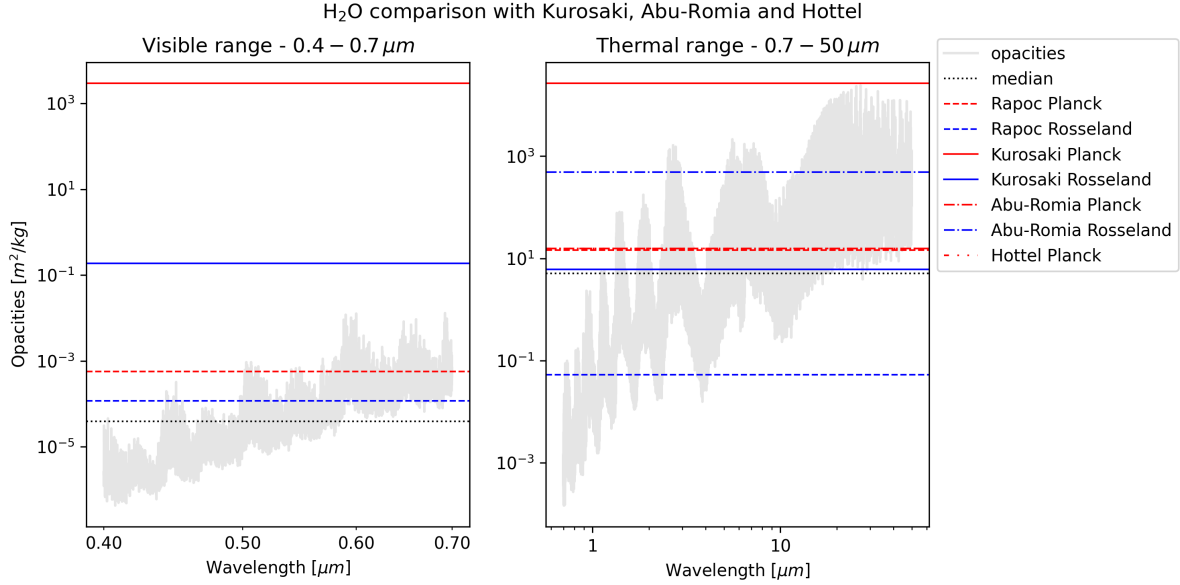


Figure 4.1: Comparison between Kurosaki et al. (2014), Abu-Romia and Tien (1967), Hottel (1954), and RAPOC. The shaded lines in both plots represent the raw data loaded from *ExoMol*'s water opacities (Polyansky et al., 2018). The blue lines are Rosseland mean opacities with the filled lines being from Kurosaki et al. (2014), the dash-dotted line from Abu-Romia and Tien (1967), and the dashed lines from RAPOC. The red lines are Planck Mean Opacities with the filled lines being from Kurosaki et al. (2014), the dash-dotted line from Abu-Romia and Tien (1967), the dash-dot-dotted line from Hottel (1954), and the dashed lines from RAPOC. The black dotted line is the median value of the raw wavelength dependent opacities. The left panel is for the visible wavelength range (0.3 to 0.7 μm) and right panel is for the IR wavelength range (0.7 to 50 μm). Both panels use the same pressure (1.01325 bar) and temperature (1500 K).

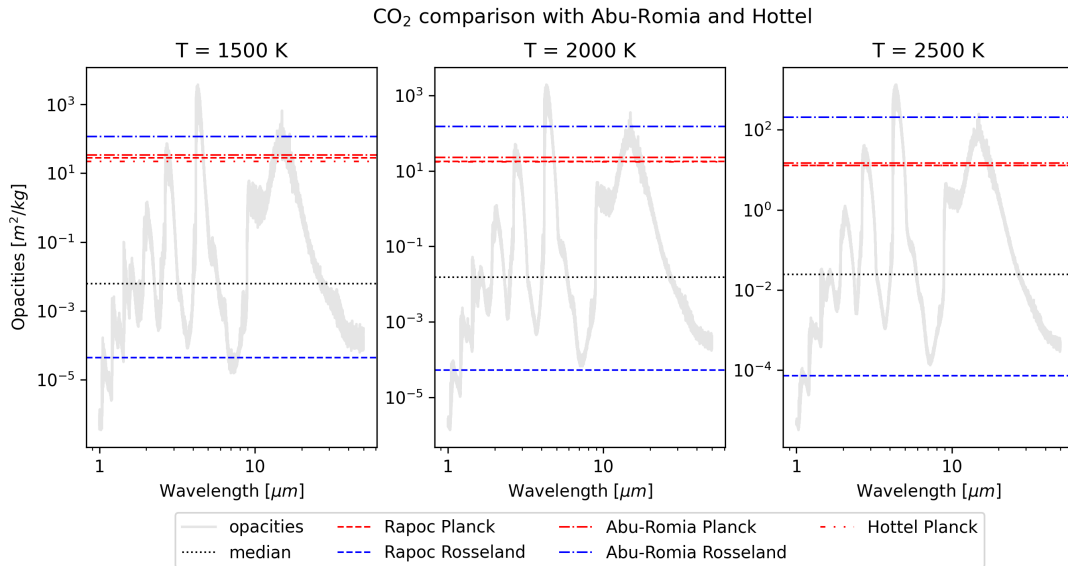


Figure 4.2: Comparison between [Abu-Romia and Tien \(1967\)](#), [Hottel \(1954\)](#), and RAPOC. The shaded lines in all plots represent the raw data loaded from *ExoMol*'s carbon dioxide opacities ([Yurchenko et al., 2020](#)). The blue lines are Rosseland mean opacities with the dash-dotted lines being from [Abu-Romia and Tien \(1967\)](#), and the dashed lines from RAPOC. The red lines are Planck Mean Opacities with the dash-dot-dotted lines being from [Hottel \(1954\)](#), the dash-dotted lines from [Abu-Romia and Tien \(1967\)](#), and the dashed being from RAPOC. The black dotted line is the median value of the raw wavelength dependent opacities. The three panels refer to different gas temperatures: right is for $T = 1500\text{ K}$, center is for $T = 2000\text{ K}$, and right is for $T = 2500\text{ K}$. All panels use the same pressure (1.01325 bar).

Regarding CO₂, we compare the Planck opacities calculated by RAPOC with those given in [Abu-Romia and Tien \(1967\)](#) and [Hottel \(1954\)](#); the Rosseland opacities are compared to those of [Badescu \(2010\)](#). The comparison for the Planck opacities is shown in Fig. 4.2 for three different temperatures. As shown in Fig. 4.2, the RAPOC values are consistent with those of [Abu-Romia and Tien \(1967\)](#) and [Hottel \(1954\)](#).

For the Rosseland mean opacities, Table 6 of [Badescu \(2010\)](#) is considered. In their calculation, a wavelength range of 0.5–100 μm was used, which is beyond the limit provided by *ExoMol* data ([Yurchenko et al., 2020](#)). Hence, a wavelength range of 0.5 – 50 μm will be adopted when making the comparison. The results are shown in the first row of Fig. 4.3. The figure shows that estimates of [Badescu \(2010\)](#) are closer to the median value of the wavelength dependent opacities from *ExoMol* than what RAPOC calculates. The bottom row of the same figure reports the same estimates performed on the 5 – 10 μm wavelength range. A major advantage of the RAPOC code is that the wavelength range can

be specified, whereas the values from [Badescu \(2010\)](#) are given for a set wavelength range.

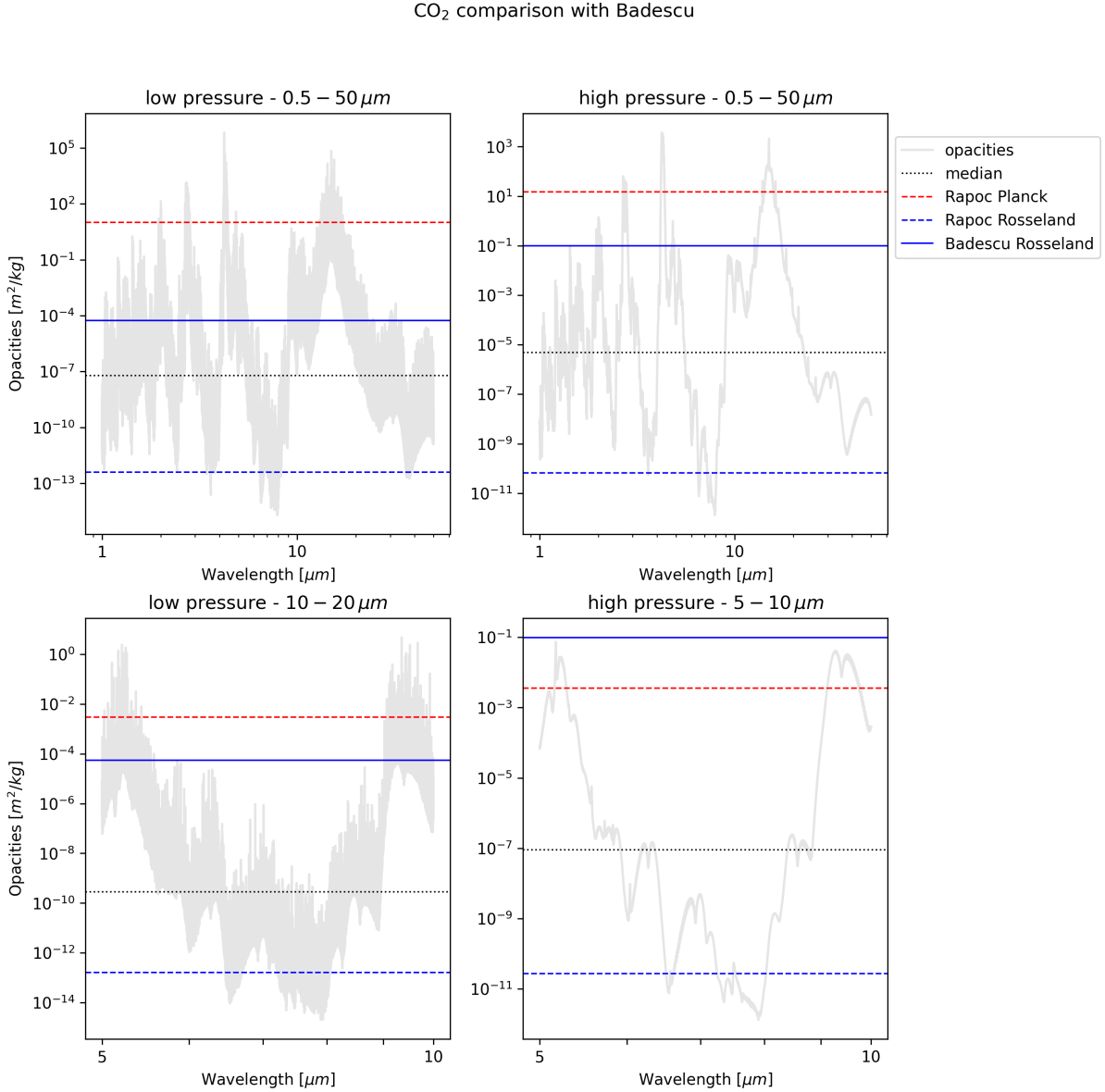


Figure 4.3: Comparison between [Badescu \(2010\)](#) and RAPOC estimates. The shaded lines in all plots represent the raw data loaded from *ExoMol*'s carbon dioxide opacities ([Yurchenko et al., 2020](#)). The blue lines are Rosseland Mean Opacities with the filled lines from Badescu and the dashed lines from RAPOC. The red dashed lines are RAPOC's Planck Mean opacities, and the black dotted lines are the median value of the raw wavelength dependent opacities. The left column is for low pressure ($567 \cdot 10^{-3}$ bar) and the right column is for high pressure (11.467 bar); both columns use the same temperature (300 K). The wavelength range is different in the two rows as the top row uses 0.5 to $50 \mu\text{m}$ range, while the bottom row uses 5 to $10 \mu\text{m}$.

For the water and carbon dioxide cases, there are significant differences between the RPMs given by RAPOC and those available in the literature; the only exception being the Planck

mean opacities that are consistent with those of [Abu-Romia and Tien \(1967\)](#) and [Hottel \(1954\)](#). These differences are the result of different wavelength ranges investigated, or the adoption of simple analytic approximations, such as the power-law fit introduced in [Kurosaki et al. \(2014\)](#). The major advantage of RAPOC is that it provides a flexible and systematic avenue for calculating RPMs with widely available input data. As shown in the above, this flexibility is coupled with RAPOC's ability to better represent the weighted mean opacity of a gaseous species at a given spectral window, or across a large range than the other approaches in the literature. Despite these advantages, RAPOC is dependent on the input data (excluding the Rayleigh scattering opacities), and it cannot extrapolate outside the given wavelength, temperature, and pressure bounds.

4.1.2 Limitations with Rosseland and Planck Mean Opacities

Whereas RPMs have their uses, they are also limited. For instance, in optically-thin environments, RPMs may overestimate the opacities present as photons could traverse through 'spectral windows' that might be very different from a few strong opacity regions. Furthermore, RM and PM have different functional forms corresponding to the different averages they are providing. The RM opacity uses the derivative of the Planck distribution as the weighting function, which it then uses to find the harmonic mean of the opacity. Consequently, RMs are extremely sensitive to the opacity minima and can provide erroneous values if a molecule is fully transparent at a given wavelength. Conversely, PM opacity uses the Planck function as the weighting function and then finds the arithmetic mean, so it is strongly affected by the more opaque regions of the spectrum. Due to their different averaging prescriptions, RM and PM opacities can differ by over two orders of magnitude which, depending on thermodynamic properties of the system, could lead to substantially different temperature profiles.

4.1.3 Summary and Conclusion

In this work we present the RAPOC code that is able to convert wavelength-dependent opacity data into Rosseland and Planck mean opacities (RPMs) in an efficient manner. Our code is fully written in Python and publicly available on GitHub and Pypi. RAPOC uses *ExoMol* and *DACE* data, but user-defined data can also be used as an input as long as it is within a readable format. By incorporating the pressure and temperature dependence

of RPMs, `RAPOC` provides a more complex treatment of the mean opacities than what is sometimes used in the literature, notably, assuming constant values or adopting simple analytic formulations. Whereas RPMs should not be used as a replacement for more rigorous opacity analyses, they have certain benefits. For example, RPMs allow one to use Grey or semi-Grey models when analysing gaseous environments, which are simpler and have exact solutions. We note that `RAPOC` should not be used as an alternative to more thorough approaches such as those using wavelength-dependent opacities. However, for simpler models, `RAPOC` provides a prescription for evaluating wavelength-dependent opacities, which can be used for exploring a larger parameter space, as well as benchmark testing.

In the next section, we use the `RAPOC` code to model the opacities of super-Earths that experience the core-erosion mechanism; this being an interior-atmosphere exchange in which material from the central embryo enriches the envelope, leading to an evolution of its chemistry, interior dynamics, and presumably the detectable species in the upper atmosphere.

4.2 Exploring Super-Earth Interiors

Unlike Earth, massive planets with Earth-like compositions often accumulate substantial hydrogen-dominated atmospheres from the nebula in which they form because their formation time is less than or comparable to the survival time of the nebula (Ida and Lin, 2004, 2008, 2005; Ikoma and Hori, 2012). In the most simplistic (and incorrect) view, one could imagine aggregating solids and then enveloping them with a primordial atmosphere that has been sequestered from the surrounding nebula and is of sufficient pressure to balance the gravity of the newly formed planet. This picture would suggest that the atmosphere has the same metallicity as the parent star or lower. However, observations and associated modeling indicate that super-Earths often have hydrogen atmospheres enriched in heavy elements (e.g., Tsiaras et al., 2019; Benneke et al., 2019; Guilluy et al., 2021). This enrichment can arise in six ways: (1) direct accretion of enriched nebula gas (e.g., Ikoma et al., 2000; Ikoma and Hori, 2012); (2) chemical reactions of incoming planetesimals with the co-accreting gas (Kimura and Ikoma, 2020), (3) preferential escape of hydrogen, leaving behind an enriched gas (e.g., Kubyshkina et al., 2018a,b; Modirrousta-

Galian et al., 2020a); (4) volcanism from the core¹⁹ (e.g., Noack et al., 2017; Dorn et al., 2018; Spaargaren et al., 2020); (5) pollution, that is, impacts of solid bodies such as planetesimals into a hydrogen-dominated atmosphere (e.g., Shiraishi and Ida, 2008; Turrini et al., 2021); and (6) core erosion, the convective entrainment of core material into the overlying envelope. In this paper, we focus on the core erosion process even though we argue that current observations provide no basis for deciding among the other alternatives. However, these mechanisms could result in different enrichment trends and potentially different enrichment compositions that could be used to infer the structure and history of some super-Earths.

Before proceeding further, it is essential to recognize that for the most common case of all, supersaturation, there is no straightforward distinction to be made among the other enrichment mechanisms. If an atmosphere becomes saturated (i.e., forms clouds), the mole fraction of the saturated species (e.g., water or silicates) will be independent of the mixing ratio deeper down. A relevant example comes from Jupiter, where one cannot determine the total bulk amount of water from measuring the low water abundance in its photosphere as water has condensed far below (e.g., Atreya et al., 1999; Guillot et al., 2020). Exoplanets may frequently be in a similar situation to Earth, but with silicates condensing and forming clouds instead of water. It may be tempting to include water into this prescription because water condenses at significantly lower temperatures, and exoplanets typically have higher temperatures than Earth, but these are precisely the bodies that are unlikely to possess water except through secondary processes (the case for Earth, presumably). In addition, one should be cautious when incorporating metals into atmospheric models as they do not behave as a single substance and are therefore likely to form clouds even if each metal is below its respective saturation level. The above prescription is, therefore, most significant for hot bodies and silicate abundances in the atmosphere. Therefore, this paper aims to determine whether the abundance of heavy species in an unsaturated atmosphere is largely the result of convective transport from the core rather than the other previously mentioned mechanisms.

As suggested for Jupiter (e.g., Guillot and Hueso, 2006), directly accreting gas that is enriched relative to the parent star composition is possible but requires special pleading or

¹⁹In the current context, “core” refers to the entire condensed part of the super-Earth, possibly including water ice or liquid, and not just what we mean when we speak of Earth’s core.

a preferential loss of hydrogen from the nebula. Oxidation reactions between a primordial atmosphere and a rocky central embryo could produce enough water to enrich the envelope substantially (Kimura and Ikoma, 2020); this scenario relies on the probable chemical disequilibrium between the embryo and nebula material and uses the accretional energy to mix incoming vaporized solids with the atmosphere. Regarding atmospheric evaporation, hydrodynamic models suggest that planets either lose the entirety of their primordial envelopes or only a negligible amount (Kubyskhina et al., 2018a,b; Modirrousta-Galian et al., 2020a). This prediction is supported by the presence of the bimodal distribution in exoplanet radii (see sect. 2). This kind of modeling does not necessarily imply the loss of the residual (high molecular weight) atmosphere, although some hydrodynamic losses of the heavier species would be expected (e.g., Hunten et al., 1987; Luger and Barnes, 2015; Johnstone, 2020).

Volcanism is difficult to quantify and may not be relevant to many exoplanets because the presence of a thick atmosphere would cause high basal temperatures and pressures that significantly influence surface properties. Surfaces may therefore vaporize (e.g., Mizuno et al., 1980) or become highly compressed (e.g., Mocquet et al., 2014), such situations differ significantly from the surface conditions relevant to the solar system. However, planetesimal accretion is accepted by many to have the capacity to enrich primordial exoplanet atmospheres greatly (e.g., Shiraishi and Ida, 2008; Shibata and Ikoma, 2019). The amount of pollution that a primordial atmosphere can experience depends on the original enrichment of the pre-stellar nebula, the processing and evolution that takes place in the pre-stellar nebula, the amount of migration the protoplanet experienced, and the intrinsic properties of the planet, such as its mass and radius; this is a complicated dynamic problem, but analytic approximations are available (Shiraishi and Ida, 2008),

$$\frac{M_z}{M_\oplus} \propto \left(\frac{R_p}{R_\oplus}\right)^2 \left(\frac{a_p}{5 \text{ AU}}\right)^{1.2} \left(\frac{M_p}{M_\oplus}\right)^{-0.3} \left(\frac{t_{acc}}{10^4}\right)^{-0.8}, \quad (4.6)$$

where M_z is the heavy material mass (i.e., the total accreted mass of pollutants), R_p is the planetary radius, R_\oplus is Earth's radius, a_p is the orbital distance, M_p is the planetary mass, M_\oplus is Earth's mass, and t_{acc} is the timescale during which the accretion process occurs, which is of the same order as the dissipation timescale of the protoplanetary disk. We acknowledge that our understanding on the formation of super-Earths remains

nebulous, and that the planetary accretion and disk dissipation timescales may not fully coincide as is believed to be the case for Earth; this is an assumption that warrants further investigation. While planetesimal accretion can significantly pollute a primordial atmosphere, it would follow a different trend than the other enrichment mechanisms.

In summary, all the other enrichment processes have been explored in the literature, and their effectiveness has been quantified. However, the significance of core erosion in super-Earths has not been modeled yet; this is the objective of this work. We show by simple physical modeling that core erosion is readily able to provide the observed high enrichments and is a highly plausible, indeed inescapable, process for any planet whose basal temperature allows for substantial evaporation of core material and whose overlying atmosphere is sufficiently hot to prevent the formation of clouds. The core erosion model also makes testable predictions (given sufficient data for many exoplanets): (1) a robust correlation between atmospheric enrichment and inferred basal atmospheric temperature; this correlation would not exist for the other mechanisms. (2) Some correlation with age because the core erosion process depends on the integrated core luminosity over the planet's age. Future data is expected to tell us about the age through precise asteroseismology of the central star.

4.2.1 How Core Erosion Works

Core erosion takes place because the surface immediately below the atmosphere vaporizes and then gets redistributed in the atmosphere by turbulent convection. Surface vaporization always occurs because it is an inescapable thermodynamic process that can be demonstrated by considering the Gibbs free energy:

$$G = U + PV - TS, \quad (4.7a)$$

differentiating this and inserting the first law of thermodynamics ($dU = PdV - TdS$) leads to

$$\begin{aligned} dG &= (TdS - PdV) + (PdV + VdP) - (TdS + SdT) \\ &= VdP - SdT. \end{aligned} \quad (4.7b)$$

The change in the Gibbs free energy across a single phase is, by definition, zero, so we select two arbitrary points and solve,

$$\begin{aligned}
 dG_1 &= dG_2 \\
 V_1 dP - S_1 dT &= V_2 dP - S_2 dT \\
 S_2 dT - S_1 dT &= V_2 dP - V_1 dP \\
 \frac{dP}{dT} &= \frac{\Delta S}{\Delta V}
 \end{aligned} \tag{4.7c}$$

The phase change from a solid or liquid to gas results in a significant volume change where $\Delta V \simeq V_{gas} = RT/P$. Furthermore, the change in the entropy is $\Delta S = L/T$; this is also a definition. Putting this together gives,

$$\frac{dP}{dT} = \frac{PL}{RT^2}, \tag{4.7d}$$

that can then be integrated, leading to

$$\ln \left(\frac{P}{P_0} \right) = \frac{L}{RT_0} - \frac{L}{RT}. \tag{4.7e}$$

Hence, the vapor pressure equation is retrieved,

$$P_v(T) = A \exp \left(-\frac{L}{RT} \right). \tag{4.7f}$$

The mole fraction of heavy materials at the bottom boundary is given by the balance between the partial pressure and the vapor pressure,

$$x = \frac{P_v(T)}{P}, \tag{4.8}$$

where x is the mole fraction and P is the total pressure. In other words,

$$x = \frac{A}{P} \exp \left(-\frac{L}{RT} \right). \tag{4.9}$$

Therefore, the bottom boundary of the atmosphere must get constantly enriched by eroded materials from the core because it has a non-zero temperature. The type of convection

that occurs when there is a temperature contrast between a hotter lower layer and a colder upper layer is called Rayleigh-Bénard convection; this is the simplest form of convection. To establish whether convection occurs, the most efficient energy-loss mechanism has to be determined because nature always wants to minimize the potential energy of a given system. Generally, two transitions occur in atmospheres: (1) radiative-convective and (2) convective-conductive. Radiative-conductive transitions are possible but rare in gaseous systems and will therefore not be explored in this thesis.

An atmosphere's upper region is relatively transparent so internal energy is most easily lost through radiation; this layer is usually called the 'radiative region.' The radiative-convective boundary (rcb) is located at the point where the internal energy flux is equal to the stellar irradiation flux,

$$\mathcal{F}_{int} = \mathcal{F}_{irr}. \quad (4.10)$$

When the internal flux is greater, convection ensues. However, the gas opacity also needs to be incorporated into this prescription because the greenhouse effect leads to greater internal temperatures. Hence, $\mathcal{F}_{int} \rightarrow F_{int}\tau$, where τ is the optical depth. The energy from stellar irradiation is $\mathcal{F}_{irr} \simeq \sigma T_{eff}^4$ (ignoring albedo). Putting this all together, the point at which these two fluxes are equal is where the system transitions from losing energy through radiation to losing it through convection,

$$F_{int}\tau = F_{irr}, \quad (4.11)$$

whence we obtain,

$$\tau \approx \frac{\sigma T_{eff}^4}{F_{int}}. \quad (4.12)$$

If a planet has an effective temperature of $T_{eff} = 400$ K and an internal energy similar to Earth's ($F_{int} = 0.1 \text{ W m}^{-2}$), according to Eq. 4.12, the atmosphere will transition from being radiative to convective at an optical depth of $\tau \sim 10^4$. If this opacity cannot be reached because, for example, the atmosphere is tenuous or too transparent, energy will be lost through radiation. A more rigorous approach would be to solve the following differential equation,

$$\left. \frac{dT}{dP} \right|_T - \left. \frac{dT}{dP} \right|_{ad} < \frac{d\mu}{dP} \frac{P}{\mu}, \quad (4.13)$$

where the first differential is the temperature gradient, the second is the adiabatic

temperature gradient, and the third is the compositional gradient. This prescription is the Ledoux criterion for convection that gives solutions for non-chemically homogeneous environments. If the system is chemically homogeneous, the above differential can be simplified into the Schwarzschild criterion by setting the last term to zero.

A fluids convective regime is expressed by the Rayleigh number (see sect. A.3 of the appendix for a derivation),

$$Ra = \frac{\rho\alpha\Delta T\delta^3g}{\eta\kappa}, \quad (4.14)$$

where ρ is the density, α is the volumetric thermal expansion coefficient, ΔT is the temperature contrast across a distance δ , η is the dynamic viscosity, and κ is the thermal diffusivity. For a Rayleigh-Bénard configuration, convection begins when the Rayleigh number exceeds a value of ~ 1000 (dimensionless). If, however, the value is below ~ 1000 , the system has a conductive temperature gradient. To include compositional effects, Eq. 4.14 can be changed to,

$$Ra = \frac{\rho\delta^3g}{\eta} \left(\frac{\alpha\Delta T}{\kappa} + \frac{\beta\Delta\mu}{D} \right), \quad (4.15)$$

where β is the rate at which the volume changes as the mean molecular weight of the gas changes, $\Delta\mu$ is the mean molecular weight contrast, and D is the molecular diffusivity. The left fraction in the brackets is substantially larger (typically by two orders of magnitude or more) than the right fraction, so it is not necessary to use Eq. 4.15 because Eq. 4.14 is a good approximation.

4.2.2 Modeling Core Erosion

Core erosion occurs when the basal atmospheric temperature is high enough to vaporize the surface significantly. Vaporized materials get redistributed by turbulent convection throughout the atmosphere. Two approaches can be taken: a global analysis of the atmosphere or an analysis of the core-atmosphere boundary layer. A global analysis would suggest that the heat flux is,

$$F = \rho c_p \langle v\delta T \rangle, \quad (4.16)$$

where ρ is the density of the gas, c_p is the specific heat, v is the convective velocity, and δT is a temperature anomaly. We also know that the buoyant thermal mass flux arising

from this heat flux is

$$F_{b,th} = \rho\alpha\langle v\delta T\rangle, \quad (4.17)$$

where α is the volumetric thermal expansion coefficient. If some of this rising gas contains heavy materials dissolved within it (from surface vaporization) then,

$$\begin{aligned} F_z &= fF_{b,th} \\ &= f\rho\alpha\langle v\delta T\rangle, \end{aligned} \quad (4.18)$$

where f is an efficiency constant. Combining Eq. 4.16 with Eq. 4.18 gives,

$$F_z = f\frac{F\alpha}{c_p}. \quad (4.19)$$

The efficiency f cannot be derived from the global analysis, but a close look at the boundary layer can provide this information. At the boundary layer, heat and matter are transferred through diffusion (by definition as convection does not occur at boundaries). The equation for diffusive heat flow is,

$$F = \frac{\kappa\rho c_p\delta T}{\delta}, \quad (4.20a)$$

and the equation for matter diffusion is,

$$F_z = \frac{D\delta z\rho}{\delta_z}, \quad (4.20b)$$

where δz is the compositional contrast across the compositional boundary layer δ_z . Note that the thermal boundary layer (δ) is larger than the compositional boundary layer because heat can transfer faster than matter (i.e., $\kappa \gg D$, where κ and D are the thermal and compositional diffusivities). Combining Eq. 4.20a and Eq. 4.20b gives,

$$F_z = \frac{\delta z}{c_p\delta T} \cdot \frac{D}{\kappa} \cdot \frac{\delta_z}{\delta}. \quad (4.20c)$$

$\delta \sim (\kappa\tau)^{1/2}$ and $\delta_z \sim (D\tau)^{1/2}$, where τ is the diffusive or convective timescales, so

$$F_z = \left(\frac{D}{\kappa}\right)^{1/2} \frac{F\delta z}{c_p\delta T}, \quad (4.20d)$$

this can be combined with the global analysis result (Eq. 4.19) to find the efficiency f ,

$$f = \left(\frac{D}{\kappa}\right)^{1/2} \frac{\delta z}{\alpha \delta T}. \quad (4.21)$$

Therefore, the core erosion efficiency is a measure of the relative velocity of the compositional to thermal diffusivities and the amount of heavy material carried by thermal buoyancy. From Eq. 4.19 we can estimate the total amount of eroded materials as $M_z \simeq F_z \cdot 4\pi R_c^2 \cdot \tau_{age}$, where M_z is the total mass of eroded materials, R_c is the radius of the core, and τ_{age} is the age of the planet;

$$\frac{M_z}{M_\oplus} \simeq \mathcal{A} \left(\frac{R_c}{R_\oplus}\right)^2 \left(\frac{F}{F_\oplus}\right) \left(\frac{T_b}{1000}\right)^{-1} \left(\frac{\tau_{age}}{1 \text{ Gyr}}\right), \quad (4.22)$$

where F_\oplus is Earth's surface flux, T_b is the planet's temperature at the bottom of the atmosphere, and τ_{age} is the age of the planet. \mathcal{A} is a collection of constants, normalization factors, and parameters,

$$\mathcal{A} = \left(\frac{D}{\kappa}\right)^{1/2} \left(\frac{L_\oplus \tau_{Gyr}}{1000 M_\oplus c_p}\right). \quad (4.23)$$

The problem with only relying on Eq. 4.22 and \mathcal{A} is that the system is dynamic, so the parameters evolve with time. For example, core erosion is fueled by the planet's internal energy that will decrease with time. The four primary sources of internal heat are (1) core accretion, (2) differentiation, (3) radiogenic heating, and (4) tidal flexing. Core accretion is the energy that a planet gets from its formation, that correlates with the gravitational binding energy,

$$E_{c.a} \sim \frac{3GM_p^2}{5R_p}. \quad (4.24)$$

Eq. 4.24 is the maximum energy attainable from core accretion because planets do not form instantaneously; radiative cooling plays an important role that should not be ignored. The energy from differentiation can be approximated by assuming that the planet is initially chemically homogeneous and slowly separates into distinct layers over time. For a binary (rock+iron) mixture one finds (see sect. 4.2 of [Hussmann et al., 2010](#), for the derivation),

$$E_d = (E_c + E_m) - E_{c.a} \quad (4.25)$$

where E_c and E_m are the potential energies of the core and mantle, respectively, that are given by,

$$E_c \sim \frac{3GM_c^2}{5R_c} \quad (4.26)$$

and

$$E_m \sim \frac{16}{15}\pi^2 G \left[\frac{5}{2}\rho_c\rho_m R_c^3 (R_p^5 - R_c^5) + \rho_m^2 (R_p^5 - R_c^5) - \frac{5}{2}\rho_m^2 R_m^2 R_c^3 (R_p^2 - R_c^2) \right], \quad (4.27)$$

where ρ_m and ρ_c are the bulk average densities of the mantle and core respectively. Evaluating the above equations for typical terrestrial planet values shows that the energy released from differentiation is usually one order of magnitude lower than that of accretion (Hussmann et al., 2010). The above model is, however, rudimentary and lacks many of the complexities associated with more realistic geochemical compositions and planetary formation pathways.

Energy from radiogenic heating typically comes from ^{40}K , ^{232}Th , ^{235}U , and ^{238}U . For planets with a similar geochemical composition to the Earth, the amount of radiogenic energy can be approximated with the following scaling arguments that have been fit from the data given in Frank et al. (2014),

$$E_{rad} \sim \frac{M_{\oplus}R_{\oplus}}{g_{\oplus}} \left(\frac{M_p}{M_{\oplus}} \right) \left(\frac{t_{age}}{\text{Gyr}} \right)^{1/1.86}, \quad (4.28)$$

where M_{\oplus} , R_{\oplus} , and g_{\oplus} are Earth's mass, radius, and gravitational acceleration respectively, and t_{age} is the age of the planet. Solving Eq. 4.24 with Eq. 4.28 for a timescale of $t_{age} = 1$ Gyr makes it possible to estimate the crossover mass at which radioactivity is no longer the dominant energy source; this being, approximately, the mass of Ganymede. However, the calculation above can be misleading as it fails to show the timescales of each energy source. Although the total radiogenic energy may be less than that of accretion, some radioactive species have long half-lives so they may begin releasing energy after a large proportion of the original formational energy has been lost. Hence, radiogenic heating can be a large source of internal energy over billion year timescales.

The final major heat source is tidal heating (or tidal flexing). This heat source arises from the differential stresses experienced by a planet as it orbits around its host star (assuming it has a non-zero eccentricity). The equation for tidal dissipation is (Segatz et al., 1988;

Hussmann et al., 2010),

$$\dot{E} = -\frac{21R_p^5 n^5 e^2}{2G} \text{Im}(k_2), \quad (4.29)$$

where n is the angular velocity,

$$n = \sqrt{\frac{GM}{a_p^3}}, \quad (4.30)$$

e is the eccentricity of the planet, $\text{Im}(k_2)$ is the imaginary component of the second degree potential Love number,

$$k_2 = \frac{3}{2 + 19 \frac{\mu_c}{\rho_p g_p R_p}}, \quad (4.31)$$

ρ_p is the bulk average density of the planet, g_p is its gravitational acceleration, and μ_c is the rigidity of the planet that has a real and imaginary component:

$$\text{Re}(\mu_c) = \frac{\eta^2 n^2 \mu}{\mu^2 + \eta^2 n^2} \quad (4.32)$$

and

$$\text{Im}(\mu_c) = \frac{\eta n \mu^2}{\mu^2 + \eta^2 n^2}, \quad (4.33)$$

with η and μ being the bulk average elastic rigidity and viscosity of the body respectively. Considering all of the above mentioned energy sources, it follows that simulations are required so that the influence of core erosion can be evaluated; this is the main objective of our ongoing paper. The critical point is that core erosion could directly link the photospheric enrichment of the planet with the composition of the core. However, this connection will only exist provided that the planet is cloudless:

$$x \leq \frac{P_v(T)}{P}. \quad (4.34)$$

If the mole fraction x is greater than Eq. 4.34, clouds will form. Note that T is the temperature of the radiative section of the atmosphere that is approximately $T \simeq T_{eq}$. If clouds form, the atmospheric enrichment would be set by condensation and not the core erosion process.

5 A Note on Astrobiology

5.1 Motivation

Before my current research on exoplanets, my focus was abiogenesis and astrobiology. While under the supervision of Dr. Dominic Papineau during the first part of my Masters' degree in Planetary Science, I analyzed billion-year-old rocks and searched for biosignatures such as molecular biomarkers, elemental CHNOPS, isotopic ratios, and morphology concretions. By way of illustration, I show below two rock slabs from geothermal vents that were examined in transmitted and reflected light. Fig. 5.1 is an Archean-aged rock that contains

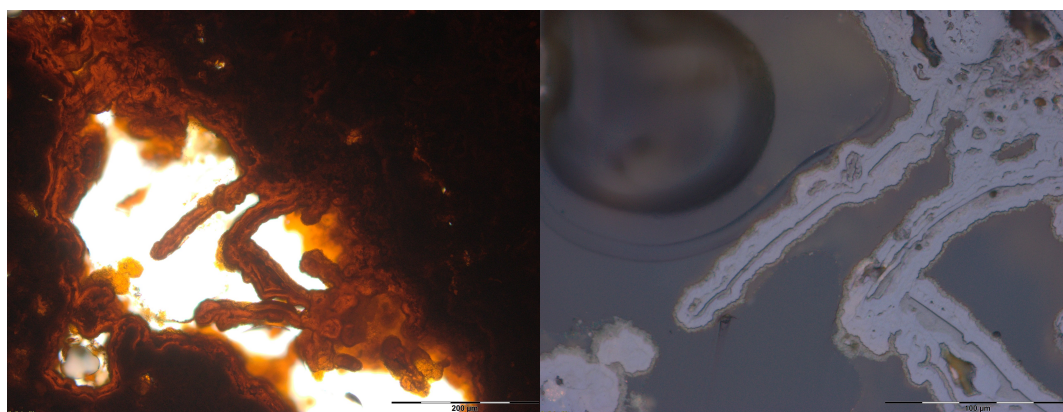


Figure 5.1: *Left:* $\times 20$ transmitted light photo of haematite strings. *Right:* $\times 50$ reflected light photo of haematite strings.

complex morphologies but, upon closer inspection, does not appear to have evidence of ancient life.

My previous experience and interest in astrobiology and abiogenesis have motivated me to dedicate a small section of my Ph.D. work to the subject of alien life and its relevance to exoplanet science. One of the central questions in astrobiology originates back to the summer of 1950 when Enrico Fermi asked his colleagues Edward Teller, Herbert York, and Emil Konopinski "But where is everybody?" when discussing the existence of extraterrestrial life. This question has now become known as the Fermi paradox, and it encompasses various fields such as biology, chemistry, physics, geology, and mathematics. With the drastic increase in exoplanets discovered, and new astronomical missions such as the JWST that are now active, it is natural to ponder whether extraterrestrial life may

be discovered in the near future. Such possibilities have motivated some researchers to explore more quixotic pathways for the formation of life by removing water as a necessary ingredient for abiogenesis. I am critical of this position, which is why I wrote a critical essay/review with my friend and colleague Giovanni Maddalena ([Modirrousta-Galian and Maddalena, 2021](#)) that was published in the journal *JBIS: Journal of the British Interplanetary Society*. Below I report the content of the review article. We note that the journal takes a more colloquial approach to essay-writing, so the rhetoric below will deviate from the rest of this thesis.

5.2 Of Aliens and Exoplanets: Why the search for life, probably, requires the search for water

It is not currently possible to create a living organism *ab initio* due to the overwhelming complexity of biological systems. In fact, the origin of life mechanism, this being how biological organisms form from non-living matter, is unknown. To better understand how abiogenesis can occur, some researchers have taken water out of their models and instead opted for more exotic approaches. These assumptions will have substantial implications for astronomical observations and potential future space exploration. By breaking down water's properties to the physical, chemical, and biological levels, herewith, it is demonstrated to be the most adequate medium for the formation of life.

In 1995, the first exoplanet orbiting a Sun-like star, 51 Pegasi b (also known as *Dimidium*), was officially discovered by Michel Mayor and Didier Queloz ([Mayor and Queloz, 1995](#)). Over two decades later, in 2019, they earned a Nobel prize, which was a historic moment for the exoplanetary community. As of April 2021, over 4000 exoplanets have been discovered, which is expected to grow as our astronomical instruments improve and our methodologies become more refined. Given the large number of newly discovered worlds, many have considered the possibility of extraterrestrial life. This inquiry is fundamentally critical because of its implications for upcoming astronomical missions such as Ariel and JWST, as well as future interstellar space exploration. Knowing where extraterrestrial life forms and thrives may coincide with planets more favorable to human life, which may be critical for the human race to survive. The late Stephen Hawking, who was a theoretical physicist, cosmologist, and director of research at the Centre for Theoretical Cosmology

at the University of Cambridge, highlighted the importance of space travel and human survival as such *“I don’t think the human race will survive the next thousand years, unless we spread into space. There are too many accidents that can befall life on a single planet. But I’m an optimist. We will reach out to the stars.”* Because of the vastness of the universe, it is impossible to explore all or most planetary systems to find the optimum one for future human exploration, so it is essential to have a solid theoretical foundation that can be used to inform our decisions. For instance, knowing when to launch a spacecraft to reach its destination at an optimum time is necessary. Sending it too early means that future technological advances may produce vehicles that would overtake it centuries or millennia after it had been launched. Sending it too late means that a previously sent spacecraft, perhaps less technologically advanced, would have reached the destination earlier. This conundrum is avoided by performing a theoretical ‘wait calculation’ that considers several parameters such as the growth of technology and the evolution of Earth’s economy (Kennedy, 2006). However, if the destination has been erroneously selected, all of the previous planning would be rendered useless. When it comes to interstellar space travel in search of habitable or inhabited planets, having a robust understanding of how biological systems form and thrive is vital for the efficacy of the mission.

Incidentally, several papers are focusing on the search for extraterrestrial life that claim, either directly or indirectly, that life (including Earth’s) forms in the absence of water. This argument is incompatible with most lines of evidence and data. Liquid water is essential to life and should be the direction to follow in future space flight missions to improve the likelihood of finding extraterrestrial life. In order to tackle this argument, it is appropriate to begin at the cosmochemical level as life is made of matter, so the provenance and abundance of water are relevant for understanding the formation of life. Before progressing, it is essential to issue the caveat that only the usefulness of liquid water is explored instead of vapor or solid ice. This position is taken as gases are relatively light, so they may not be efficient at mixing different constituents (i.e., weak buoyancy), and solids are typically too viscous for efficient convective mixing within a reasonably short timescale.

5.2.1 Cosmochemical level

13.8 billion years ago, the Universe began from a very hot state that gradually cooled down. Soon after the Big Bang, the Universe was dominated by hydrogen and helium with trace amounts of lithium and beryllium. Gravitational instabilities caused a small fraction of the total hydrogen to form stars. Nuclear fusion within stars led to the eventual chemical enrichment of the Universe. Although there are varying chemical compositions amongst stars, a common practice in astronomy is to adopt our Sun as a reference point. Through astronomical observations of our Sun's photosphere and laboratory experiments on meteorites, our solar system's elemental abundances have been determined (Lodders, 2010),

Element	Number Fraction	Mass Fraction
H	0.92	0.71
He	0.08	0.27
O	5.4×10^{-4}	8.6×10^{-3}
C	2.5×10^{-4}	3×10^{-3}
Ne	1.1×10^{-4}	2.2×10^{-3}
N	7.2×10^{-5}	10^{-3}
Mg	3.5×10^{-5}	9×10^{-4}
Si	3.4×10^{-5}	9×10^{-4}
Fe	2.9×10^{-5}	1.6×10^{-3}
S	1.5×10^{-5}	5×10^{-4}
Ar	3×10^{-6}	10^{-4}
Al	3×10^{-6}	10^{-4}
Ca	2×10^{-6}	10^{-4}

Table 5.1: The cosmochemical composition of our solar-system according to Lodders (2010).

From Table 5.1 it becomes immediately apparent how common water is in the Universe as the two elemental constituents of water, hydrogen, and oxygen, are the first and third most common elements. It follows that from a purely statistical perspective, a strong argument can be made that if life were to exist elsewhere in the Universe, it would have most probably interacted with water in a certain manner. However, a large elemental abundance does not imply biological utility. For example, despite being the second most common element in the Universe, helium is not largely present within biological systems as it is chemically inert. In order to explore the usefulness of water, one must examine its properties on a physical, chemical, and biological level.

5.2.2 Planetary level

For a planet of a given composition to form, its constituents must be condensed (i.e., icy). Therefore, for a water-rich planet to form, it has to be located in a region within the protoplanetary disc where water vapor can form ice (there is no liquid water in the near-vacuum of space because it is thermodynamically forbidden). From fundamental thermodynamic principles, it is known that water vapor can only condense when its vapor pressure is less than its partial pressure, $P_v(T) < fP$, where $P_v(T)$ is the vapor pressure at temperature T , f is the number fraction of water, and P is the total gas pressure. In our solar system the condensation temperature of H₂O is ~ 150 K (Podolak and Zucker, 2004; D’Angelo and Podolak, 2015), which corresponds to a distance of approximately ~ 3 AU from the Sun (Martin and Livio, 2012). This location is called the ‘frost line,’ and its properties will vary depending on the nature of the protoplanetary disc from which the planet forms as well as the spectral type of the host star. Notwithstanding, a value of ~ 150 K is a reasonable benchmark to adopt for purely illustrative purposes. Therefore, for planets that formed at temperatures below ~ 150 K, there is a very high probability that water is present in large amounts, such as Uranus and Neptune that are rich in water ice. In contrast, planets formed at hotter temperatures are unlikely to have a significant abundance of water unless it came from external sources. Earth, for example, is believed to have received most of its water from comets and asteroids (Shiraishi and Ida, 2008). While the precise mechanism is not fully understood, it is generally accepted to be due to the period of late heavy bombardment (Matter et al., 2009). With its weak gravitational field, even Mars shows very strong evidence that it once hosted a substantial amount of water. For instance, high-resolution data from the Mars Reconnaissance Orbiter Context Camera has found topographical evidence for a paleo-fluvial channel system in the Arabia Terra Martian region (Davis et al., 2016). This indicates a “warm and wet” Noachian climate model for Mars where abundant precipitation was common. This is further supported by the presence of water-rich materials, such as clays and sulfates on the Martian surface (Sautter et al., 2015). Despite being controversial, another example worth mentioning is the discovery of water in the atmosphere of the exoplanet K2-18b (Tsiaras et al., 2019; Benneke et al., 2019). This is a super-Earth with a mass and radius of $\sim 8.6M_{\oplus}$ and $\sim 2.6R_{\oplus}$, respectively, that has a temperature well above the condensation point of water

(~ 265 K, [Benneke et al., 2019](#)). Water has also been found on other hot small exoplanets such as HD 106315c and HD 3167c ([Guilluy et al., 2021](#)). This is strong evidence that water delivery by comets and asteroids could be common not just in our solar system but elsewhere in the universe. In other words, due to the copious cosmic presence of water, whether a planet formed within or outside the frost line appears to have little influence on whether it has come into contact with water.

However, to get a more holistic understanding of the presence of water on planetary surfaces, its thermodynamic stability must also be considered. Referring back to Mars, although there is strong evidence supporting the presence of liquid water in its past, it currently has an arid surface. This is believed to be due to solar winds, X-rays and ultraviolet irradiation that stripped away the Martian atmosphere. Therefore, a planet may lose its surface water due to atmospheric erosion. This effect is especially strong if the planet in question has a small mass like Mars. Under those circumstances, life may adapt to its new arid environment through various means, such as evolving to thrive deep in the regolith where water may be stored in underground reservoirs. This would result in planets that harbor life but have no surface or atmospherically detectable water. Unfortunately, if the atmosphere has been lost, there is no known way of detecting potential biosignatures, thus rendering atmospheric spectroscopy obsolete.

Planets are also susceptible to atmospheric evaporation if they orbit too close to their host star ([Zahnle and Kasting, 1986](#); [Hunten et al., 1987](#)). Water is not stable when exposed to high temperatures and stellar X-ray and ultraviolet irradiation, thus resulting in its eventual removal ([Kurosaki et al., 2014](#); [Kimura and Ikoma, 2020](#)). This is why water is scarce on Venus. The problem with this scenario is that life is very sensitive to high temperatures, so it may not survive. For example, to get water to vaporize efficiently so that it remains stably in the atmosphere (i.e., no surface condensation), one requires surface temperatures $\gtrsim 100^\circ\text{C}$ (this will vary depending on the ambient pressure). At these temperatures, only some extremophiles would survive. However, water is a greenhouse gas, so its presence in the atmosphere would increase surface temperatures, potentially leading to a runaway greenhouse. In other words, to get water into the atmosphere so that it is more easily destroyed by stellar irradiation, one risks increasing surface temperatures to lethal levels. Instead, the system would need to be in a subtle (delicate) equilibrium

in which water can be removed without leading to extreme surface conditions. Similarly, it can be argued that life may adapt by living underground where the temperatures are favorable, but this would result in the same testability problem.

5.2.3 Micropalaeontological level

The story of life on Earth undoubtedly contradicts the hypothesis that abiogenesis typically occurs under non-aqueous conditions. This prescription is incompatible with, for example, the oldest known microfossils that are from hydrothermal vents in the Nuvvuagittuq belt in Quebec, Canada. These are filamentous, fossilized microorganisms that are at least 3.77 billion years old but could be as old as 4.28 billion years (Dodd et al., 2017). Conversely, the oldest verified life on land is from 3.5 billion-year-old stromatolites found in the Dresser Formation, Pilbara Craton, in Western Australia (Djokic et al., 2017; Baumgartner et al., 2019). Furthermore, biases in the data must also be considered. For instance, the proportion of Earth's 'dry' surface that has been investigated is much more significant than the equivalent of Earth's oceans. Even with this strong bias, the oldest known microfossils have still been found in the oceans. In addition, considering that most of Earth's surface is covered by water (approximately 70%), it must be acknowledged that there is a strong statistical argument for life's oldest fossils being located underwater.

Moreover, there is a rich body of scientific literature that discusses the many biologically advantageous properties of hydrothermal vents that may have resulted in autocatalytic chemical reactions that contributed to the formation of the first primitive living organisms (Wächtershauser, 1990; Hordijk et al., 2010). Some dismiss this evidence with arguments such as that researchers have been unable to form life in hydrous conditions artificially. This is a misleading argument as scientists have never been able to form life *ab initio* under any conditions. However, the field of synthetic biology and, more specifically, its subfield xenobiology are bringing us closer to this goal.

5.2.4 Earth is the average planet

The Rare Earth Hypothesis postulates that life on Earth is unique and therefore not a good representation of life elsewhere in the universe. However, a more statistically robust argument would be to assume that Earth's position is 'average' amongst other

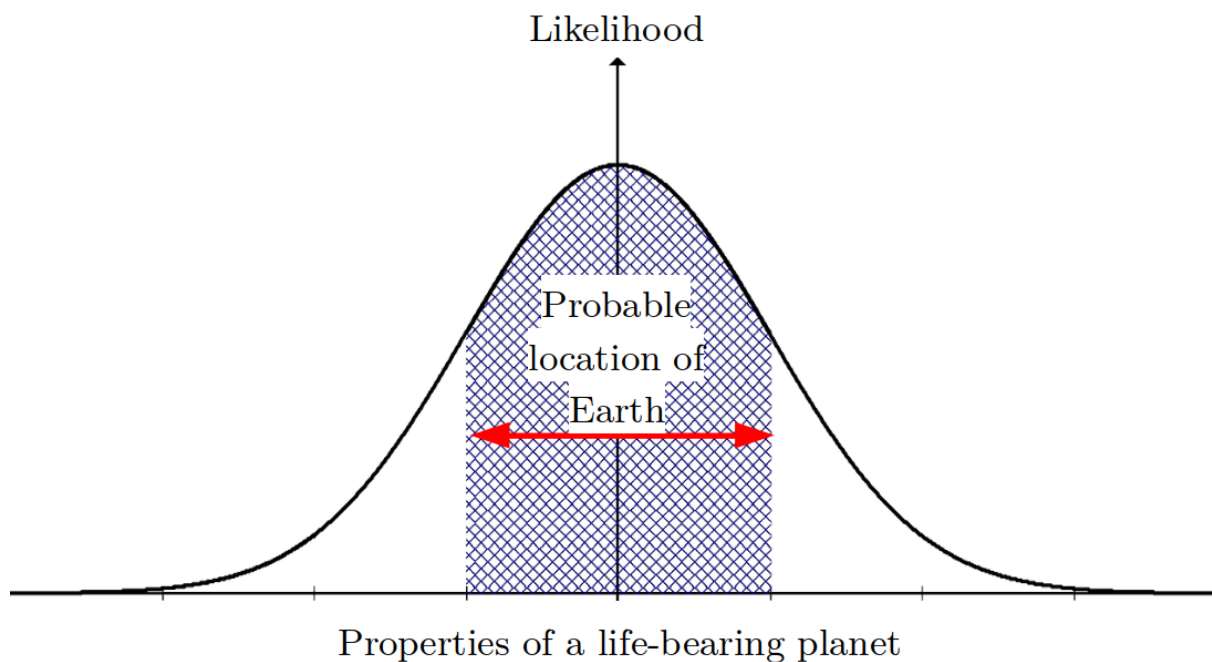


Figure 5.2: If we plotted the properties of life-bearing planets on a graph, Earth would most probably be located somewhere in the center. Note, this figure assumes that such properties would be distributed in a Gaussian-like manner; the actual distribution is unknown.

life-bearing planets (i.e., the *Copernican principle*, see Fig. 5.2). Astrophysicist, planetary scientist, author, and science communicator Neil deGrasse Tyson, who is the Frederick P. Rose Director of the Hayden Planetarium at the Rose Center for Earth and Space in New York City, phrased this issue as such: “*Had we been made of some rare isotope of bismuth, you would have an argument to say [that] we are something special.*” Precisely as deGrasse Tyson explained, there is little evidence that supports the argument that biology on Earth is unique within the cosmos. The example given was how the four most common non-inert elements in the universe (hydrogen, oxygen, carbon, and nitrogen) are also the most common elements within biology on Earth. Most biological scientists accept these elements, which have the mnemonic acronym of CHON, as the building blocks of life. This is why it is common for many within the petrological community to search for these elements when trying to detect microfossils in billion-year-old rocks when using, for instance, Raman spectroscopy.

5.2.5 Physicochemical level

To better understand the importance of water in finding extraterrestrial life, the following definition, adapted from commonly used principles, will be applied – ‘*an enclosed membrane which produces energy, and transfers information*’ (Dzieciol and Mann, 2012). Present-day terrestrial biology consists of a membrane made of phospholipids and energy in the form of ATP (Adenosine triphosphate). Within this framework, information is transferred by DNA (Deoxyribonucleic acid) getting transcribed to RNA (Ribonucleic acid) and then translated to proteins. This prescription is central to molecular biology (Crick, 1970). However, it is worth considering that this optimized process includes billions, or at the very least, hundreds of millions of years of evolution and selective pressures.

Interestingly, water may have acted indirectly as a catalyst for the evolution of prebiotic molecules, converse to The Water Paradox, which states water breaks down biopolymers (such as proteins and DNA). Mounting evidence suggests that prebiotic chemistry may have originated from wet-dry cycles in shallow sources of water (Frenkel-Pinter et al., 2019). In the dry phase, water-forming condensation reactions would produce chains between biomolecules, like amino acids and bases for proteins or RNA, respectively, with the water then quickly evaporating away. In the wet phase, water returns to the system and breaks down any ‘weak’ links in the biopolymer chains. Regular cycling applies a selection pressure that facilitates the evolution of stable complexes (Frenkel-Pinter et al., 2020). These biomolecules would interact with each other or with themselves to create a steric hindrance that restricts water’s access to easily hydrolyzed chemical bonds.

The ‘wet-dry’ hypothesis suggests that water was a catalyst for the formation of primordial cells in the early Earth due to the prevalence of hydrolysis-condensation reactions found in nature. However, this description cannot fully encapsulate the unique physicochemical properties of water, which may be crucial for abiogenesis. A more holistic analysis can be attained by considering the electronic properties of a H₂O molecule. Water consists of two hydrogens and one oxygen. Oxygen is strongly electronegative, second-most to fluorine (3.440 and 3.980 respectively), meaning that it tends to attract electrons away from partnered hydrogens (Fig. 5.3A). The H-O-H bond angle is 104.5° which, when combined with the high disparity in electronegativity, generates a polar molecule with a negative charge density at the oxygen and a positive charge density at the hydrogen.

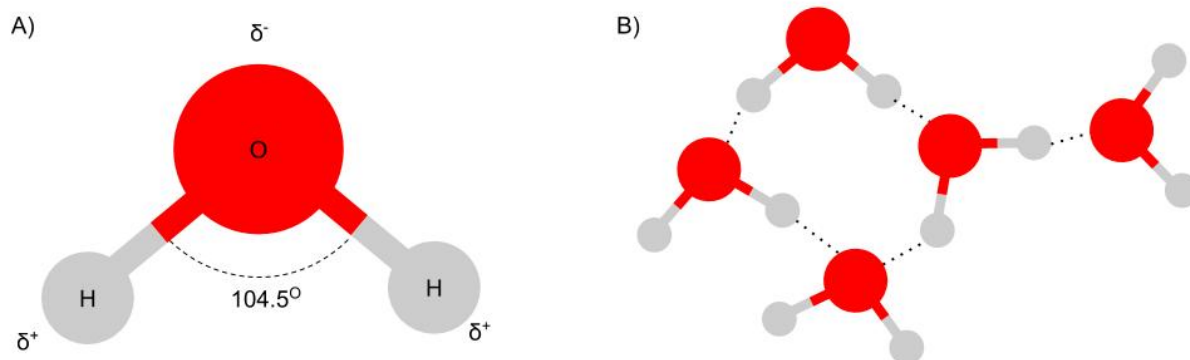


Figure 5.3: The physicochemical properties of water can be explained by the high electronegativity of oxygen, and the low electronegativity of hydrogen, which give it two dipoles capable of hydrogen bonding. The polar nature of the molecule is due to the 104.5° angle that forms.

The highly polar nature of water makes it a universal solvent allowing it to dissolve an extensive range of inorganic and organic molecules. Wet-dry cycles taking place on mineral deposits would benefit from this property as they can solubilize metal ions such as iron and arsenic, which were relatively abundant in the early Earth (Enriquez and Do, 2012). The varying redox states of these metals allow them to transfer electrons to other molecules and act as a source of energy (Roden, 2012; Sforza et al., 2014). The dissolution of these metal ions is an example of how the polar behavior of water facilitated primordial reactions. The dielectric constant of water is very high (with a value of 81), and it is responsible for weakening the bonds between other molecules such as metal salts in minerals. For comparison, ammonia has a dielectric constant of 16, and hydrocarbons, such as ethane, are nonpolar with a significantly lower constant. The two aforementioned compounds are popular alternatives to water-based life, but their poor ability to solubilize organic and inorganic molecules may prevent this (McKay, 2014).

Hydrophobicity is another physicochemical property that is important in sustaining life. This behavior is crucial to forming an enclosed membrane, a prerequisite to forming enclosed cellular life (Tanford, 1978; Dzieciol and Mann, 2012). A semi-permeable barrier controls the movement of molecules, either produced inside the cell, such as proteins, or carried into the cell, such as metal ions. In aqueous solutions, amphiphilic molecules (containing one charged hydrophilic end and one hydrophobic moiety) will form liposomes, micelles, or bilayers as the most thermodynamically favorable structure (Fig. 5.4). These shapes reduce the surface area in contact with water, minimizing the system's free energy.

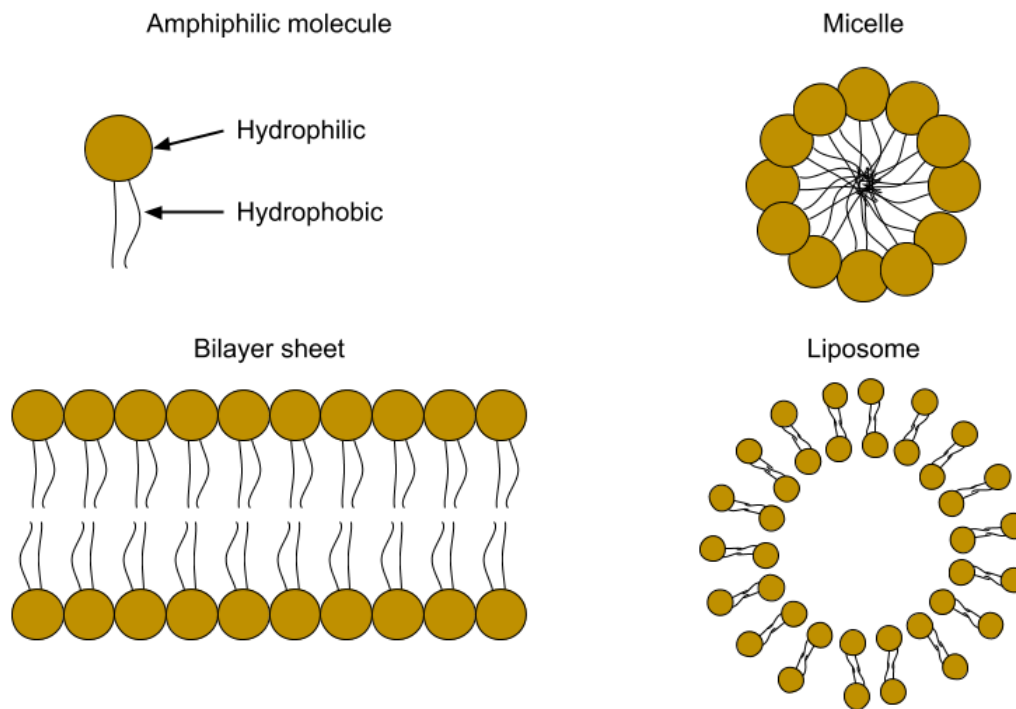


Figure 5.4: The most thermodynamically favourable shapes for amphiphilic molecules to take in water are micelles, bilayer sheets and liposomes. These forms are driven by the hydrophobic effect and may have facilitated the evolution of cellular membranes.

The high electronegativity of oxygen in the molecular structure of water allows it to form hydrogen bonds (Fig. 5.4B). These can form between other water molecules or other molecules containing highly electronegative atoms, such as peptides. Hydrogen bonds play a chaperone-like role in biomolecular topography, meaning that they assist in folding biological molecules such as proteins and DNA. The shape of these molecules is key to regulating processes inside and outside of the cell. For example, an enzyme has a very precise and defined shape that dictates its biochemical functions. As protein folding occurs, water forms hydrogen bonds with peptides in a rapid cycle of breaking and reforming, following a folding-funnel mechanism. This mechanism causes the potential and configurational energy of a protein to decrease as its native state is approached, following a funnel-like direction as various folding conformations are trialed (Collet, 2011). It is the polar nature of water that allows for this process to take place. Without hydrogen bonding and water as a solvent to chaperone, proteins would have many probable folding patterns, leading to imprecise folding or no folding at all; this may result in a complete

loss of function.

5.2.6 Conclusion

The only evidence available for life in the universe is that of planet Earth. This limited data sample will result in an unavoidable ‘Earth-centric’ bias, which may have motivated some researchers to opt for more quixotic theories for the formation and evolution of life. Given the vastness of the universe (perhaps being infinite in size), even the least probable events are bound to happen. Therefore, the formation and evolution of exotic forms of life are possible, given that they do not violate the laws of nature. However, just because an event is possible does not mean that it is probable. When it comes to interstellar space travel, one must be as practical as possible due to technological and financial restrictions. Hence, it may be unwise to reject our one single data point in favor of more speculative models for life as these have practical consequences. Whether most life forms on dry land or in liquid conditions will determine the type of exoplanets worth investigating spectroscopically and then, potentially, being visited.

For this reason, it is essential to select one’s assumptions sensibly and base them on as much evidence as possible. Understanding the origin of life on Earth and how it could form on other planets is certainly not an easy task, so we admire and encourage those who investigate this issue. However, we are cautioning others not to assume, perhaps erroneously, that life formed without water just because the origin of life mechanism has not been discovered yet. Obstacles are expected, after all, nature is mysterious.

6 Future Work

In this thesis, a holistic exploration of the physics of exoplanets was pursued with the aim of providing a theoretical foundation to observable data. To understand exoplanets in their totality, star-planet interactions through XUV irradiation, atmospheric physics, and geological principles were combined; this allowed me to better constrain the formation and evolution of super-Earths and sub-Neptunes.

Due to being a relatively new field, it is interesting and meaningful to discuss where the field of exoplanets will be in the future and the type of research that may take place. Like all fields of science, exoplanetology is limited by the available data. As of the writing of this thesis, spectroscopic studies of super-Earths and sub-Neptunes are restricted to the narrow range of the Hubble space telescope ($0.1 - 1.7 \mu\text{m}$) and the multi-band photometry of Spitzer ($3 - 180 \mu\text{m}$). Whereas high-resolution ground-based instrumentation exists, it is most applicable to gas giants and rarely for small-mass exoplanets. These data limitations make atmospheric characterization troublesome, with many studies disagreeing with each other. For example, K2-18 b could either have a water-rich (Tsiaras et al., 2019; Benneke et al., 2019) or carbon-rich atmosphere (Bézard et al., 2020; Blain et al., 2021), whereas GJ 1132 b may have a flat spectrum or a primordial envelope rich in HCN and CH₄. Such puzzling results show that our data is substandard and open to interpretation. With upcoming missions such as Ariel, JWST, Twinkle, and the ELT, more accurate and precise spectroscopic and transit measurements will be possible so that planetary properties will be better constrained. With new data, superior theoretical models will be possible such as constraining the interior composition and structure of super-Earths and sub-Neptunes. However, more advanced instrumentation will require at least several months to become operational, so, in the meantime, the objective is to prepare a more robust theoretical framework.

There has been a growing interest in the atmosphere-interior connection of super-Earths and sub-Neptunes, which can be seen in the white paper published by the Ariel interiors' working group (Helled et al., 2021). To effectively establish this connection, it may first be necessary to analyze simpler planets like airless magma-ocean super-Earths (AMOSEs) that are more straightforward to observe and model. Though it has been suggested that

some tight-orbiting planets may form *in situ* (e.g., [Batygin et al., 2016](#)), many are thought to have formed farther out and then migrated inwards (e.g., [Mordasini et al., 2009](#)), so analyzing such bodies may provide new insights into not only AMOSEs but also more typical super-Earths. Once a theoretical framework has been built for these simpler systems, the next stage would be to explore more normal super-Earths and sub-Neptunes. Such research will require a multidisciplinary approach that involves the collaboration of experts from various fields.

7 Summary and Conclusion

Theoretical exoplanetology requires the development of modeling techniques to understand the properties of exoplanets. Because planets are complex, exoplanetology encompasses many fields such as astrobiology, astrophysics, astronomy, astrochemistry, astrogeology, geochemistry, and planetary science. These fields use different approaches and sometimes do not interact much, making it cumbersome to attain a complete picture of the analyzed planet. This thesis has tackled this problem by analyzing exoplanets as a population and individually. Our analysis of the bimodal distribution of exoplanet radii incorporates different geological compositions, varying atmospheric sizes, and a thorough analysis of the XUV irradiation of stars; from this, we were able to reproduce the bimodal trend. We then analyzed exoplanets individually like 55 Cancri e, in which we show that inconspicuous effects like tidal forces could partially shield primordial atmospheres from harmful XUV-irradiation. We used a simple 2D analysis to demonstrate this, although a 3D analysis would be the next step in improving our models. GJ 357 b was also analyzed, and we showed that atmospheric evaporation could remove atmospheres even when the star has an anomalously low activity; this contrasts strongly with previous works suggesting that atmospheric evaporation is slow and gradual for super-Earths and sub-Neptunes.

After analyzing XUV photoevaporation, we explore a novel technique for constraining the properties of airless magma ocean super-Earths. Atmospheric spectroscopy is impossible because these planets are airless (except for a tenuous vaporized mineral atmosphere); any surface vaporized gases would not be detectable even with future instruments like Ariel or the JWST unless temperatures are above ~ 3000 K, which is uncommon. Instead, our proposed method involves detecting the planetary albedo and, from this, inferring the surface composition. Combining mass and radius measurements with the surface composition will provide unprecedented constraints on the inner working of these mysterious worlds.

In the sect. 3, we provide a new method for inferring the interior structure of planets with primordial atmospheres. Large primordial envelopes insert significant degeneracies, so it is impossible to know whether, for example, the planet has a rocky or icy core. Furthermore, including a high interior heat flux makes such analyses even harder as this could make a

planet seem like it has a larger primordial envelope than reality. Because core erosion directly links the photospheric enrichment with the core composition, it can be used to constrain planetary interiors from atmospheric spectroscopic data. We note, however, that this condition only holds if the atmosphere is unsaturated (i.e., no clouds).

In sect. 4, we briefly explore where alien life is likely to form in the universe. Our published paper, which was co-written with a biologist, shows that water is the optimum medium for the formation of life and should therefore be a central focus of future astrobiological missions. Missions such as Ariel and the JWST will actively search for H₂O in exoplanet atmospheres suggesting that there may be some exciting discoveries to be made.

Finally, I conclude this thesis with the following: In the 10th and 11th centuries AD, Hāmid al-Ghazālī's said²⁰ that mathematics and science were tools used by scientists for "*sinister mischief*." According to him, anyone who tried to investigate science outside the scope he deemed allowable was performing "*a very serious evil*." Because of this, he recommended that "*one should warn off anyone who would embark upon the study of those mathematical sciences*."

I am not a philosopher or anyone of a particularly high moral standard, so I cannot comment on whether my research can be classified as "*mathematics and its evil consequences*." The ethics, however, are irrelevant to me. I do science because there is nothing in life that brings me more joy than research. Therefore, if indeed I am doing an act of evil, let it be so because –

"heaven for climate, hell for company!" – Mark Twain²¹

²⁰Hāmid al-Ghazālī Deliverance from Error, Translated by Richard J. MCCARTHY, S.J.: 1980

²¹Mark Twain's Notebooks and Journals, Volume III: 1883-1891

References

- Abe, Y. (1993). Physical state of the very early Earth. *Lithos*, 30(3):223–235.
- Abraham, M. and Becker, R. (1950). *The Classical Theory of Electricity and Magnetism*. Blackie and Son, 2 edition.
- Abu-Romia, M. M. and Tien, C. L. (1967). Appropriate mean absorption coefficients for infrared radiation of gases. *Journal of Heat Transfer*, 89(4):321–327.
- Al-Refaie, A. F., Changeat, Q., Waldmann, I. P., and Tinetti, G. (2019). TauREx III: A fast, dynamic and extendable framework for retrievals. *arXiv e-prints*, page arXiv:1912.07759.
- Alexander, D. R., Augason, G. C., and Johnson, H. R. (1989). An Opacity-sampled Treatment of Water Vapor. *ApJ*, 345:1014.
- Alexander, D. R. and Ferguson, J. W. (1994). Low-Temperature Rosseland Opacities. *ApJ*, 437:879.
- Armstrong, D. J., Lopez, T. A., Adibekyan, V., Booth, R. A., Bryant, E. M., Collins, K. A., Emsenhuber, A., Huang, C. X., King, G. W., Lillo-box, J., Lissauer, J. J., Matthews, E. C., Mousis, O., Nielsen, L. D., Osborn, H., Otegi, J., Santos, N. C., Sousa, S. G., Stassun, K. G., Veras, D., Ziegler, C., Acton, J. S., Almenara, J. M., Anderson, D. R., Barrado, D., Barros, S. C. C., Bayliss, D., Belardi, C., Bouchy, F., Briceno, C., Brogi, M., Brown, D. J. A., Burleigh, M. R., Casewell, S. L., Chaushev, A., Ciardi, D. R., Collins, K. I., Colón, K. D., Cooke, B. F., Crossfield, I. J. M., Díaz, R. F., Deleuil, M., Delgado Mena, E., Demangeon, O. D. S., Dorn, C., Dumusque, X., Eigmüller, P., Fausnaugh, M., Figueira, P., Gan, T., Gandhi, S., Gill, S., Goad, M. R., Guenther, M. N., Helled, R., Hoggatpanah, S., Howell, S. B., Jackman, J., Jenkins, J. S., Jenkins, J. M., Jensen, E. L. N., Kennedy, G. M., Latham, D. W., Law, N., Lendl, M., Lozovsky, M., Mann, A. W., Moyano, M., McCormac, J., Meru, F., Mordasini, C., Osborn, A., Pollacco, D., Queloz, D., Raynard, L., Ricker, G. R., Rowden, P., Santerne, A., Schlieder, J. E., Seager, S., Sha, L., Tan, T.-G., Tilbrook, R. H., Ting, E., Udry, S., Vanderspek, R., Watson, C. A., West, R. G., Wilson, P. A., Winn, J. N., Wheatley, P., Villaseñor, J. N., Vines, J. I., and Zhan, Z. (2020). A remnant planetary core in the hot-Neptune desert. *arXiv e-prints*, page arXiv:2003.10314.
- Astropy Collaboration, Price-Whelan, A. M., Sipőcz, B. M., Günther, H. M., Lim, P. L., Crawford, S. M., Conseil, S., Shupe, D. L., Craig, M. W., Dencheva, N., Ginsburg, A., VanderPlas, J. T., Bradley, L. D., Pérez-Suárez, D., de Val-Borro, M., Aldcroft, T. L., Cruz, K. L., Robitaille, T. P., Tollerud, E. J., Ardelean, C., Babej, T., Bach, Y. P., Baccetti, M., Bakanov, A. V., Bamford, S. P., Barentsen, G., Barmby, P., Baumbach, A., Berry, K. L., Biscani, F., Boquien, M., Bostroem, K. A., Bouma, L. G., Brammer, G. B., Bray, E. M., Breytenbach, H., Buddelmeijer, H., Burke, D. J., Calderone, G., Cano Rodríguez, J. L., Cara, M., Cardoso, J. V. M., Cheedella, S., Copin, Y., Corrales, L., Crichton, D., D’Avella, D., Deil, C., Depagne, É., Dietrich, J. P., Donath, A., Droettboom, M., Earl, N., Erben, T., Fabbro, S., Ferreira, L. A., Finethy, T., Fox, R. T., Garrison, L. H., Gibbons, S. L. J., Goldstein, D. A., Gommers, R., Greco, J. P., Greenfield, P., Groener, A. M., Grollier, F., Hagen, A., Hirst, P., Homeier, D., Horton, A. J., Hosseinzadeh, G., Hu, L., Hunkeler, J. S., Ivezić, Ž., Jain, A., Jenness,

- T., Kanarek, G., Kendrew, S., Kern, N. S., Kerzendorf, W. E., Khvalko, A., King, J., Kirkby, D., Kulkarni, A. M., Kumar, A., Lee, A., Lenz, D., Littlefair, S. P., Ma, Z., Macleod, D. M., Mastropietro, M., McCully, C., Montagnac, S., Morris, B. M., Mueller, M., Mumford, S. J., Muna, D., Murphy, N. A., Nelson, S., Nguyen, G. H., Ninan, J. P., Nöthe, M., Ogaz, S., Oh, S., Parejko, J. K., Parley, N., Pascual, S., Patil, R., Patil, A. A., Plunkett, A. L., Prochaska, J. X., Rastogi, T., Reddy Janga, V., Sabater, J., Sakurikar, P., Seifert, M., Sherbert, L. E., Sherwood-Taylor, H., Shih, A. Y., Sick, J., Silbiger, M. T., Singanamalla, S., Singer, L. P., Sladen, P. H., Sooley, K. A., Sornarajah, S., Streicher, O., Teuben, P., Thomas, S. W., Tremblay, G. R., Turner, J. E. H., Terrón, V., van Kerkwijk, M. H., de la Vega, A., Watkins, L. L., Weaver, B. A., Whitmore, J. B., Woillez, J., Zabalza, V., and Astropy Contributors (2018). The Astropy Project: Building an Open-science Project and Status of the v2.0 Core Package. *AJ*, 156:123.
- Astropy Collaboration, Robitaille, T. P., Tollerud, E. J., Greenfield, P., Droettboom, M., Bray, E., Aldcroft, T., Davis, M., Ginsburg, A., Price-Whelan, A. M., Kerzendorf, W. E., Conley, A., Crighton, N., Barbary, K., Muna, D., Ferguson, H., Grollier, F., Parikh, M. M., Nair, P. H., Unther, H. M., Deil, C., Woillez, J., Conseil, S., Kramer, R., Turner, J. E. H., Singer, L., Fox, R., Weaver, B. A., Zabalza, V., Edwards, Z. I., Azalee Bostroem, K., Burke, D. J., Casey, A. R., Crawford, S. M., Dencheva, N., Ely, J., Jenness, T., Labrie, K., Lim, P. L., Pierfederici, F., Pontzen, A., Ptak, A., Retsdal, B., Servillat, M., and Streicher, O. (2013). Astropy: A community Python package for astronomy. *A&A*, 558:A33.
- Atreya, S. K., Wong, M. H., Owen, T. C., Mahaffy, P. R., Niemann, H. B., de Pater, I., Drossart, P., and Encrenaz, T. (1999). A comparison of the atmospheres of Jupiter and Saturn: deep atmospheric composition, cloud structure, vertical mixing, and origin. *P&SS*, 47(10-11):1243–1262.
- Badescu, V. (2010). Tables of Rosseland mean opacities for candidate atmospheres of life hosting free-floating planets. *Central European Journal of Physics*, 8(3):463–479.
- Barros, S. C. C., Almenara, J. M., Deleuil, M., Diaz, R. F., Csizmadia, S., Cabrera, J., Chaintreuil, S., Collier Cameron, A., Hatzes, A., Haywood, R., Lanza, A. F., Aigrain, S., Alonso, R., Bordé, P., Bouchy, F., Deeg, H. J., Erikson, A., Fridlund, M., Grziwa, S., Gandolfi, D., Guillot, T., Guenther, E., Leger, A., Moutou, C., Ollivier, M., Pasternacki, T., Pätzold, M., Rauer, H., Rouan, D., Santerne, A., Schneider, J., and Wuchterl, G. (2014). Revisiting the transits of CoRoT-7b at a lower activity level. *A&A*, 569:A74.
- Barros, S. C. C., Gosselin, H., Lillo-Box, J., Bayliss, D., Delgado Mena, E., Brugger, B., Santerne, A., Armstrong, D. J., Adibekyan, V., Armstrong, J. D., Barrado, D., Bento, J., Boisse, I., Bonomo, A. S., Bouchy, F., Brown, D. J. A., Cochran, W. D., Collier Cameron, A., Deleuil, M., Demangeon, O., Díaz, R. F., Doyle, A., Dumusque, X., Ehrenreich, D., Espinoza, N., Faedi, F., Faria, J. P., Figueira, P., Foxell, E., Hébrard, G., Hojjatpanah, S., Jackman, J., Lendl, M., Ligi, R., Lovis, C., Melo, C., Mousis, O., Neal, J. J., Osborn, H. P., Pollacco, D., Santos, N. C., Sefako, R., Shporer, A., Sousa, S. G., Triaud, A. H. M. J., Udry, S., Vigan, A., and Wyttenbach, A. (2017). Precise masses for the transiting planetary system HD 106315 with HARPS. *A&A*, 608:A25.
- Batalha, N. M., Rowe, J. F., Bryson, S. T., Barclay, T., Burke, C. J., Caldwell, D. A., Christiansen, J. L., Mullally, F., Thompson, S. E., and Brown, T. M. (2013). Planetary

- Candidates Observed by Kepler. III. Analysis of the First 16 Months of Data. *ApJS*, 204(2):24.
- Batygin, K., Bodenheimer, P. H., and Laughlin, G. P. (2016). In Situ Formation and Dynamical Evolution of Hot Jupiter Systems. *ApJ*, 829(2):114.
- Batygin, K. and Stevenson, D. J. (2010). Inflating Hot Jupiters with Ohmic Dissipation. *ApJL*, 714(2):L238–L243.
- Baumgartner, R. J., Van Kranendonk, M. J., Wacey, D., Fiorentini, M. L., Saunders, M., Caruso, S., Pages, A., Homann, M., and Guagliardo, P. (2019). Nano-porous pyrite and organic matter in 3.5-billion-year-old stromatolites record primordial life. *Geology*, 47(11):1039–1043.
- Becker, A., Lorenzen, W., Fortney, J. J., Nettelmann, N., Schöttler, M., and Redmer, R. (2014). Ab Initio Equations of State for Hydrogen (H-REOS.3) and Helium (He-REOS.3) and their Implications for the Interior of Brown Dwarfs. *ApJS*, 215(2):21.
- Benatti, S., Nardiello, D., Malavolta, L., Desidera, S., Borsato, L., Nascimbeni, V., Damasso, M., D’Orazi, V., Mesa, D., Messina, S., Esposito, M., Bignamini, A., Claudi, R., Covino, E., Lovis, C., and Sabotta, S. (2019). A possibly inflated planet around the bright young star DS Tucanae A. *A&A*, 630:A81.
- Benneke, B., Wong, I., Piaulet, C., Knutson, H. A., Lothringer, J., Morley, C. V., Crossfield, I. J. M., Gao, P., Greene, T. P., Dressing, C., Dragomir, D., Howard, A. W., McCullough, P. R., Kempton, E. M. R., Fortney, J. J., and Fraine, J. (2019). Water Vapor and Clouds on the Habitable-zone Sub-Neptune Exoplanet K2-18b. *ApJL*, 887(1):L14.
- Bercovici, D. (2003). The generation of plate tectonics from mantle convection. *Earth and Planetary Science Letters*, 205(3-4):107–121.
- Berta-Thompson, Z. K., Irwin, J., Charbonneau, D., Newton, E. R., Dittmann, J. A., Astudillo-Defru, N., Bonfils, X., Gillon, M., Jehin, E., Stark, A. A., Stalder, B., Bouchy, F., Delfosse, X., Forveille, T., Lovis, C., Mayor, M., Neves, V., Pepe, F., Santos, N. C., Udry, S., and Wünsche, A. (2015). A rocky planet transiting a nearby low-mass star. *Natur*, 527(7577):204–207.
- Bézard, B., Charnay, B., and Blain, D. (2020). Methane as a dominant absorber in the habitable-zone sub-Neptune K2-18 b. *arXiv e-prints*, page arXiv:2011.10424.
- Bieryla, A., Collins, K., Beatty, T. G., Eastman, J., Siverd, R. J., Pepper, J., Gaudi, B. S., Stassun, K. G., Cañas, C., Latham, D. W., Buchhave, L. A., Sanchis-Ojeda, R., Winn, J. N., Jensen, E. L. N., Kielkopf, J. F., McLeod, K. K., Gregorio, J., Colón, K. D., Street, R., Ross, R., Penny, M., Mellon, S. N., Oberst, T. E., Fulton, B. J., Wang, J., Berlind, P., Calkins, M. L., Esquerdo, G. A., DePoy, D. L., Gould, A., Marshall, J., Pogge, R., Trueblood, M., and Trueblood, P. (2015). KELT-7b: A Hot Jupiter Transiting a Bright $V = 8.54$ Rapidly Rotating F-star. *AJ*, 150(1):12.
- Bitsch, B., Lambrechts, M., and Johansen, A. (2015). The growth of planets by pebble accretion in evolving protoplanetary discs. *A&A*, 582:A112.
- Blain, D., Charnay, B., and Bézard, B. (2021). 1D atmospheric study of the temperate sub-Neptune K2-18b. *A&A*, 646:A15.

- Bonfils, X., Almenara, J. M., Cloutier, R., Wünsche, A., Astudillo-Defru, N., Berta-Thompson, Z., Bouchy, F., Charbonneau, D., Delfosse, X., Díaz, R. F., Dittmann, J., Doyon, R., Forveille, T., Irwin, J., Lovis, C., Mayor, M., Menou, K., Murgas, F., Newton, E., Pepe, F., Santos, N. C., and Udry, S. (2018). Radial velocity follow-up of GJ1132 with HARPS. A precise mass for planet b and the discovery of a second planet. *A&A*, 618:A142.
- Bonomo, A. S., Desidera, S., Benatti, S., Borsa, F., Crespi, S., Damasso, M., Lanza, A. F., Sozzetti, A., Lodato, G., Marzari, F., Boccato, C., Claudi, R. U., Cosentino, R., Covino, E., Gratton, R., Maggio, A., Micela, G., Molinari, E., Pagano, I., Piotto, G., Poretti, E., Smareglia, R., Affer, L., Biazzo, K., Bignamini, A., Esposito, M., Giacobbe, P., Hébrard, G., Malavolta, L., Maldonado, J., Mancini, L., Martinez Fiorenzano, A., Masiero, S., Nascimbeni, V., Pedani, M., Rainer, M., and Scandariato, G. (2017). The GAPS Programme with HARPS-N at TNG . XIV. Investigating giant planet migration history via improved eccentricity and mass determination for 231 transiting planets. *A&A*, 602:A107.
- Bourrier, V., Dumusque, X., Dorn, C., Henry, G. W., Astudillo-Defru, N., Rey, J., Benneke, B., Hébrard, G., Lovis, C., and Demory, B. O. (2018a). The 55 Cancri system reassessed. *A&A*, 619:A1.
- Bourrier, V., Ehrenreich, D., Lecavelier des Etangs, A., Louden, T., Wheatley, P. J., Wyttenbach, A., Vidal-Madjar, A., Lavie, B., Pepe, F., and Udry, S. (2018b). High-energy environment of super-Earth 55 Cancri e. I. Far-UV chromospheric variability as a possible tracer of planet-induced coronal rain. *A&A*, 615:A117.
- Bourrier, V., Lovis, C., Beust, H., Ehrenreich, D., Henry, G. W., Astudillo-Defru, N., Allart, R., Bonfils, X., Ségransan, D., Delfosse, X., Cegla, H. M., Wyttenbach, A., Heng, K., Lavie, B., and Pepe, F. (2018c). Orbital misalignment of the Neptune-mass exoplanet GJ 436b with the spin of its cool star. *Nature*, 553(7689):477–480.
- Brown, D. J. A., Triaud, A. H. M. J., Doyle, A. P., Gillon, M., Lendl, M., Anderson, D. R., Collier Cameron, A., Hébrard, G., Hellier, C., Lovis, C., Maxted, P. F. L., Pepe, F., Pollacco, D., Queloz, D., and Smalley, B. (2017). Rossiter-McLaughlin models and their effect on estimates of stellar rotation, illustrated using six WASP systems. *MNRAS*, 464(1):810–839.
- Burke, C. J., Bryson, S. T., Mullally, F., Rowe, J. F., Christiansen, J. L., Thompson, S. E., Coughlin, J. L., Haas, M. R., Batalha, N. M., and Caldwell, D. A. (2014). Planetary Candidates Observed by Kepler IV: Planet Sample from Q1-Q8 (22 Months). *ApJS*, 210(2):19.
- Cameron, A. G. W. (1985). The partial volatilization of Mercury. *Icarus*, 64(2):285–294.
- Chabot, N. L., Wollack, E. A., Klima, R. L., and Minitti, M. E. (2014). Experimental constraints on Mercury’s core composition. *Earth and Planetary Science Letters*, 390:199–208.
- Chachan, Y. and Stevenson, D. J. (2018). On the Role of Dissolved Gases in the Atmosphere Retention of Low-mass Low-density Planets. *ApJ*, 854:21.
- Charbonneau, D., Brown, T. M., Noyes, R. W., and Gilliland, R. L. (2002). Detection of an Extrasolar Planet Atmosphere. *ApJ*, 568(1):377–384.

- Cloud, P. (1972). A working model of the primitive Earth. *American Journal of Science*, 272(6):537–548.
- Collet, O. (2011). How does the first water shell fold proteins so fast? *The Journal of Chemical Physics*, 134(8):085107.
- Collins, G. S., Melosh, H. J., and Marcus, R. A. (2005). Earth Impact Effects Program: A Web-based computer program for calculating the regional environmental consequences of a meteoroid impact on Earth. *Meteoritics and Planetary Science*, 40:817.
- Cox, A. N. and Tabor, J. E. (1976). Radiative opacity tables for 40 stellar mixtures. *ApJS*, 31:271–312.
- Crick, F. (1970). Central Dogma of Molecular Biology. *Nature*, 227(5258):561–563.
- Crida, A., Ligi, R., Dorn, C., Borsa, F., and Lebreton, Y. (2018). Mass, Radius, and Composition of the Transiting Planet 55 Cnc e: Using Interferometry and Correlations - A Quick Update. *Research Notes of the American Astronomical Society*, 2(3):172.
- D’Angelo, G. and Podolak, M. (2015). Capture and Evolution of Planetesimals in Circumjovian Disks. *ApJ*, 806(2):203.
- Davies, R. B. and Harte, D. S. (1987). Tests for hurst effect. *Biometrika*, 74(1):95–101.
- Davis, J. M., Balme, M., Grindrod, P. M., Williams, R. M. E., and Gupta, S. (2016). Extensive Noachian fluvial systems in Arabia Terra: Implications for early Martian climate. *Geology*, 44(10):847–850.
- Demory, B.-O. (2014). The Albedos of Kepler’s Close-in Super-Earths. *ApJL*, 789:L20.
- Demory, B.-O., Gillon, M., de Wit, J., Madhusudhan, N., Bolmont, E., Heng, K., Kataria, T., Lewis, N., Hu, R., Krick, J., Stamenković, V., Benneke, B., Kane, S., and Queloz, D. (2016). A map of the large day-night temperature gradient of a super-Earth exoplanet. *Nature*, 532:207–209.
- Djokic, T., van Kranendonk, M. J., Campbell, K. A., Walter, M. R., and Ward, C. R. (2017). Earliest signs of life on land preserved in ca. 3.5 Ga hot spring deposits. *Nature Communications*, 8:15263.
- Djurišić, A. B. and Li, E. H. (1999). Optical properties of graphite. *Journal of Applied Physics*, 85(10):7404–7410.
- Dodd, M. S., Papineau, D., Grenne, T., Slack, J. F., Rittner, M., Pirajno, F., O’Neil, J., and Little, C. T. S. (2017). Evidence for early life in Earth’s oldest hydrothermal vent precipitates. *Nature*, 543(7643):60–64.
- Doering, C. R. (2020). Absence of evidence for the ultimate state of turbulent rayleigh-bénard convection. *Phys. Rev. Lett.*, 124:229401.
- Doering, C. R., Toppaladoddi, S., and Wettlaufer, J. S. (2019). Absence of evidence for the ultimate regime in two-dimensional rayleigh-bénard convection. *Phys. Rev. Lett.*, 123:259401.
- Dorn, C., Noack, L., and Rozel, A. B. (2018). Outgassing on stagnant-lid super-Earths. *A&A*, 614:A18.

- Dorn, C., Venturini, J., Khan, A., Heng, K., Alibert, Y., Helled, R., Rivoldini, A., and Benz, W. (2017). A generalized Bayesian inference method for constraining the interiors of super Earths and sub-Neptunes. *A&A*, 597:A37.
- Durst, P., Mason, G., McKinley, B., and Baylot, A. (2011). Predicting RMS surface roughness using fractal dimension and PSD parameters. *Journal of Terramechanics*, 48(2):105 – 111.
- Dziociol, A. J. and Mann, S. (2012). Designs for life: protocell models in the laboratory. *Chem. Soc. Rev.*, 41:79–85.
- Edgett, K. S. and Rice, J. W., J. (1997). Geologic Signature of Life on Mars: Low-Albedo Lava Flows and the Search for “Warm Havens”. In Clifford, S. M., Treiman, A. H., Newsom, H. E., and Farmer, J. D., editors, *Early Mars: Geologic and Hydrologic Evolution, Physical and Chemical Environments, and the Implications for Life*, volume 916, page 29.
- Edwards, B., Changeat, Q., Baeyens, R., Tsiaras, A., Al-Refaie, A., Taylor, J., Yip, K. H., Bieger, M. F., Blain, D., Gressier, A., Guilluy, G., Jaziri, A. Y., Kiefer, F., Modirrousta-Galian, D., Morvan, M., Mugnai, L. V., Pluriel, W., Poveda, M., Skaf, N., Whiteford, N., Wright, S., Zingales, T., Charnay, B., Drossart, P., Leconte, J., Venot, O., Waldmann, I., and Beaulieu, J.-P. (2020). ARES I: WASP-76 b, A Tale of Two HST Spectra. *Aj*, 160(1):8.
- Edwards, B., Changeat, Q., Mori, M., Anisman, L. O., Morvan, M., Yip, K. H., Tsiaras, A., Al-Refaie, A., Waldmann, I., and Tinetti, G. (2021). Hubble WFC3 Spectroscopy of the Habitable-zone Super-Earth LHS 1140 b. *AJ*, 161(1):44.
- Ehrenreich, D., Bourrier, V., Bonfils, X., Lecavelier des Etangs, A., Hébrard, G., Sing, D. K., Wheatley, P. J., Vidal-Madjar, A., Delfosse, X., Udry, S., Forveille, T., and Moutou, C. (2012). Hint of a transiting extended atmosphere on 55 Cancri b. *A&A*, 547:A18.
- Ehrenreich, D., Bourrier, V., Wheatley, P. J., Lecavelier des Etangs, A., Hébrard, G., Udry, S., Bonfils, X., Delfosse, X., Désert, J.-M., Sing, D. K., and Vidal-Madjar, A. (2015). A giant comet-like cloud of hydrogen escaping the warm Neptune-mass exoplanet GJ 436b. *Nature*, 522(7557):459–461.
- Ehrenreich, D. and Désert, J.-M. (2011). Mass-loss rates for transiting exoplanets. *A&A*, 529:A136.
- Ehrenreich, D., Lovis, C., Allart, R., Zapatero Osorio, M. R., Pepe, F., Cristiani, S., Rebolo, R., Santos, N. C., Borsa, F., Demangeon, O., Dumusque, X., González Hernández, J. I., Casasayas-Barris, N., Ségransan, D., Sousa, S., Abreu, M., Adibekyan, V., Affolter, M., Allende Prieto, C., Alibert, Y., Aliverti, M., Alves, D., Amate, M., Avila, G., Baldini, V., Bandy, T., Benz, W., Bianco, A., Bolmont, É., Bouchy, F., Bourrier, V., Broeg, C., Cabral, A., Calderone, G., Pallé, E., Cegla, H. M., Cirami, R., Coelho, J. M. P., Conconi, P., Coretti, I., Cumani, C., Cupani, G., Dekker, H., Delabre, B., Deiries, S., D’Odorico, V., Di Marcantonio, P., Figueira, P., Fragoso, A., Genolet, L., Genoni, M., Génova Santos, R., Hara, N., Hughes, I., Iwert, O., Kerber, F., Knudstrup, J., Landoni, M., Lavie, B., Lizon, J.-L., Lendl, M., Lo Curto, G., Maire, C., Manescau, A., Martins, C. J. A. P., Mégevand, D., Mehner, A., Micela, G., Modigliani, A., Molaro,

- P., Monteiro, M., Monteiro, M., Moschetti, M., Müller, E., Nunes, N., Oggioni, L., Oliveira, A., Pariani, G., Pasquini, L., Poretti, E., Rasilla, J. L., Redaelli, E., Riva, M., Santana Tschudi, S., Santin, P., Santos, P., Segovia Milla, A., Seidel, J. V., Sosnowska, D., Sozzetti, A., Spanò, P., Suárez Mascareño, A., Tabernero, H., Tenegi, F., Udry, S., Zanutta, A., and Zerbi, F. (2020). Nightside condensation of iron in an ultrahot giant exoplanet. *Nature*, 580(7805):597–601.
- Elkins-Tanton, L. T. and Seager, S. (2008). Coreless Terrestrial Exoplanets. *ApJ*, 688(1):628–635.
- Enriquez, R. P. H. and Do, T. N. (2012). Bioavailability of metal ions and evolutionary adaptation. *Life*, 2(4):274–285.
- Espinoza, N., Brahm, R., Jordán, A., Jenkins, J. S., Rojas, F., Jofré, P., Mädler, T., Rabus, M., Chanamé, J., Pantoja, B., Soto, M. G., Morzinski, K. M., Males, J. R., Ward-Duong, K., and Close, L. M. (2016). Discovery and Validation of a High-Density sub-Neptune from the K2 Mission. *ApJ*, 830(1):43.
- Essack, Z., Seager, S., and Pajusalu, M. (2020). Low-albedo Surfaces of Lava Worlds. *ApJ*, 898(2):160.
- Esteves, L. J., de Mooij, E. J. W., Jayawardhana, R., Watson, C., and de Kok, R. (2017). A Search for Water in a Super-Earth Atmosphere: High-resolution Optical Spectroscopy of 55Cancer e. *AJ*, 153:268.
- Evans, L. G., Peplowski, P. N., Rhodes, E. A., Lawrence, D. J., McCoy, T. J., Nittler, L. R., Solomon, S. C., Sprague, A. L., Stockstill-Cahill, K. R., Starr, R. D., Weider, S. Z., Boynton, W. V., Hamara, D. K., and Goldsten, J. O. (2012). Major-element abundances on the surface of Mercury: Results from the MESSENGER Gamma-Ray Spectrometer. *Journal of Geophysical Research (Planets)*, 117:E00L07.
- Fairbairn, M. B. (2005). Planetary Photometry: The Lommel-Seeliger Law. *Journal of the Royal Astronomical Society of Canada*, 99(3):92.
- Fortes, A. D. (2012). Titan’s internal structure and the evolutionary consequences. *Planetary and Space Science*, 60(1):10–17.
- Fortney, J. J., Marley, M. S., and Barnes, J. W. (2007). Planetary Radii across Five Orders of Magnitude in Mass and Stellar Insolation: Application to Transits. *ApJ*, 659(2):1661–1672.
- Fossati, L., Erkaev, N. V., Lammer, H., Cubillos, P. E., Odert, P., Juvan, I., Kislyakova, K. G., Lendl, M., Kubyschkina, D., and Bauer, S. J. (2017). Aeronomical constraints to the minimum mass and maximum radius of hot low-mass planets. *A&A*, 598:A90.
- Frank, E. A., Meyer, B. S., and Mojzsis, S. J. (2014). A radiogenic heating evolution model for cosmochemically Earth-like exoplanets. *Icarus*, 243:274–286.
- Freedman, R. S., Lustig-Yaeger, J., Fortney, J. J., Lupu, R. E., Marley, M. S., and Lodders, K. (2014). Gaseous Mean Opacities for Giant Planet and Ultracool Dwarf Atmospheres over a Range of Metallicities and Temperatures. *ApJS*, 214(2):25.
- Freedman, R. S., Marley, M. S., and Lodders, K. (2008). Line and Mean Opacities for Ultracool Dwarfs and Extrasolar Planets. *ApJS*, 174(2):504–513.

- French, M., Becker, A., Lorenzen, W., Nettelmann, N., Bethkenhagen, M., Wicht, J., and Redmer, R. (2012). Ab Initio Simulations for Material Properties along the Jupiter Adiabatic. *ApJS*, 202(1):5.
- Frenkel-Pinter, M., Haynes, J. W., C, M., Petrov, A. S., Burcar, B. T., Krishnamurthy, R., Hud, N. V., Leman, L. J., and Williams, L. D. (2019). Selective incorporation of proteinaceous over nonproteinaceous cationic amino acids in model prebiotic oligomerization reactions. *Proceedings of the National Academy of Sciences*, 116(33):16338–16346.
- Frenkel-Pinter, M., Haynes, J. W., Mohyeldin, A. M., C, M., Sargon, A. B., Petrov, A. S., Krishnamurthy, R., Hud, N. V., Williams, L. D., and Leman, L. J. (2020). Mutually stabilizing interactions between proto-peptides and RNA. *Nature Communications*, 11:3137.
- Fulton, B. J., Petigura, E. A., Howard, A. W., Isaacson, H., Marcy, G. W., Cargile, P. A., Hebb, L., Weiss, L. M., Johnson, J. A., Morton, T. D., Sinukoff, E., Crossfield, I. J. M., and Hirsch, L. A. (2017). The California-Kepler Survey. III. A Gap in the Radius Distribution of Small Planets. *AJ*, 154:109.
- Gandolfi, D., Barragán, O., Hatzes, A. P., Fridlund, M., Fossati, L., Donati, P., Johnson, M. C., Nowak, G., Prieto-Arranz, J., Albrecht, S., Dai, F., Deeg, H., Endl, M., Grziwa, S., Hjorth, M., Korth, J., Nespral, D., Saario, J., Smith, A. M. S., Antoniciello, G., Alarcon, J., Bedell, M., Blay, P., Brems, S. S., Cabrera, J., Csizmadia, S., Cusano, F., Cochran, W. D., Eigmüller, P., Erikson, A., González Hernández, J. I., Guenther, E. W., Hirano, T., Suárez Mascareño, A., Narita, N., Palle, E., Parviainen, H., Pätzold, M., Persson, C. M., Rauer, H., Saviane, I., Schmidtbreick, L., Van Eylen, V., Winn, J. N., and Zakhzhay, O. V. (2017). The Transiting Multi-planet System HD 3167: A 5.7 M_⊕ Super-Earth and an 8.3 M_⊕ Mini-Neptune. *Aj*, 154(3):123.
- García Muñoz, A. (2007). Physical and chemical aeronomy of HD 209458b. *Planet. Space Sci.*, 55(10):1426–1455.
- Ginzburg, S., Schlichting, H. E., and Sari, R. (2016). Super-Earth Atmospheres: Self-consistent Gas Accretion and Retention. *ApJ*, 825:29.
- Ginzburg, S., Schlichting, H. E., and Sari, R. (2018). Core-powered mass-loss and the radius distribution of small exoplanets. *MNRAS*, 476:759–765.
- Grainger, D., Peters, D., Clarisse, L., and Herbin, H. (2014). Aerosol refractive index archive.
- Guillot, T. and Hueso, R. (2006). The composition of Jupiter: sign of a (relatively) late formation in a chemically evolved protosolar disc. *MNRAS*, 367(1):L47–L51.
- Guillot, T., Stevenson, D. J., Atreya, S. K., Bolton, S. J., and Becker, H. N. (2020). Storms and the Depletion of Ammonia in Jupiter: I. Microphysics of “Mushballs”. *Journal of Geophysical Research (Planets)*, 125(8):e06403.
- Guilluy, G., Gressier, A., Wright, S., Santerne, A., Jaziri, A. Y., Edwards, B., Changeat, Q., Modirrousta-Galian, D., Skaf, N., Al-Refaie, A., Baeyens, R., Bieger, M. F., Blain, D., Kiefer, F., Morvan, M., Mugnai, L. V., Pluriel, W., Poveda, M., Zingales, T., Whiteford, N., Yip, K. H., Charnay, B., Leconte, J., Drossart, P., Sozzetti, A., Marcq,

- E., Tsiaras, A., Venot, O., Waldmann, I., and Beaulieu, J.-P. (2021). ARES IV: Probing the Atmospheres of the Two Warm Small Planets HD 106315c and HD 3167c with the HST/WFC3 Camera. *AJ*, 161(1):19.
- Gupta, A. and Schlichting, H. E. (2019). Sculpting the valley in the radius distribution of small exoplanets as a by-product of planet formation: the core-powered mass-loss mechanism. *MNRAS*, 487(1):24–33.
- Hakim, K., Spaargaren, R., Grewal, D. S., Rohrbach, A., Berndt, J., Dominik, C., and van Westrenen, W. (2019). Mineralogy, Structure, and Habitability of Carbon-Enriched Rocky Exoplanets: A Laboratory Approach. *Astrobiology*, 19(7):867–884.
- Hakim, K., van Westrenen, W., and Dominik, C. (2018). Capturing the oxidation of silicon carbide in rocky exoplanetary interiors. *A&A*, 618:L6.
- Hamano, K., Kawahara, H., Abe, Y., Onishi, M., and Hashimoto, G. L. (2015). Lifetime and Spectral Evolution of a Magma Ocean with a Steam Atmosphere: Its Detectability by Future Direct Imaging. *ApJ*, 806(2):216.
- Hapke, B. (2012). *Theory of Reflectance and Emittance Spectroscopy*. Cambridge University Press, 2 edition.
- Hauck, S. A., Margot, J.-L., Solomon, S. C., Phillips, R. J., Johnson, C. L., Lemoine, F. G., Mazarico, E., McCoy, T. J., Padovan, S., Peale, S. J., Perry, M. E., Smith, D. E., and Zuber, M. T. (2013). The curious case of Mercury’s internal structure. *Journal of Geophysical Research (Planets)*, 118(6):1204–1220.
- Hayashi, C., Nakazawa, K., and Adachi, I. (1977). Long-Term Behavior of Planetesimals and the Formation of the Planets. *PASJ*, 29:163–196.
- He, X., Funfschilling, D., Nobach, H., Bodenschatz, E., and Ahlers, G. (2012). Transition to the Ultimate State of Turbulent Rayleigh-Bénard Convection. *Phys. Rev. Lett.*, 108(2):024502.
- Helled, R., Werner, S., Dorn, C., Guillot, T., Ikoma, M., Ito, Y., Kama, M., Lichtenberg, T., Miguel, Y., Shorttle, O., Tackley, P. J., Valencia, D., and Vazan, A. (2021). Ariel planetary interiors White Paper. *Experimental Astronomy*.
- Hordijk, W., Hein, J., and Steel, M. (2010). Autocatalytic Sets and the Origin of Life. *Entropy*, 12(7):1733–1742.
- Hottel, H. C. (1954). Radiant-heat transmission. In McAdams, W. and on Heat Transmission, N. R. C. U. C., editors, *Heat Transmission*, International student edition. McGraw-Hill.
- Howard, A. W., Marcy, G. W., Johnson, J. A., Fischer, D. A., Wright, J. T., Isaacson, H., Valenti, J. A., Anderson, J., Lin, D. N. C., and Ida, S. (2010). The Occurrence and Mass Distribution of Close-in Super-Earths, Neptunes, and Jupiters. *Science*, 330:653.
- Hunten, D. M., Pepin, R. O., and Walker, J. C. G. (1987). Mass fractionation in hydrodynamic escape. *Icarus*, 69:532–549.
- Hussmann, H., Choblet, G., Lainey, V., Matson, D. L., Sotin, C., Tobie, G., and van Hoolst, T. (2010). Implications of Rotation, Orbital States, Energy Sources, and Heat Transport for Internal Processes in Icy Satellites. *SSRv*, 153:317–348.

- Ida, S. and Lin, D. N. C. (2004). Toward a Deterministic Model of Planetary Formation. I. A Desert in the Mass and Semimajor Axis Distributions of Extrasolar Planets. *ApJ*, 604:388–413.
- Ida, S. and Lin, D. N. C. (2005). Toward a Deterministic Model of Planetary Formation. III. Mass Distribution of Short-Period Planets around Stars of Various Masses. *ApJ*, 626:1045–1060.
- Ida, S. and Lin, D. N. C. (2008). Toward a Deterministic Model of Planetary Formation. V. Accumulation Near the Ice Line and Super-Earths. *ApJ*, 685:584–595.
- Iglesias, C. A. and Rogers, F. J. (1996). Updated Opal Opacities. *ApJ*, 464:943.
- Ikoma, M. and Hori, Y. (2012). In Situ Accretion of Hydrogen-rich Atmospheres on Short-period Super-Earths: Implications for the Kepler-11 Planets. *ApJ*, 753:66.
- Ikoma, M., Nakazawa, K., and Emori, H. (2000). Formation of Giant Planets: Dependences on Core Accretion Rate and Grain Opacity. *ApJ*, 537(2):1013–1025.
- Ito, Y., Changeat, Q., Edwards, B., Al-Refaie, A., Tinetti, G., and Ikoma, M. (2021). Detectability of Rocky-Vapour atmospheres on super-Earths with Ariel. *Experimental Astronomy*.
- Ito, Y., Ikoma, M., Kawahara, H., Nagahara, H., Kawashima, Y., and Nakamoto, T. (2015). Theoretical Emission Spectra of Atmospheres of Hot Rocky Super-Earths. *ApJ*, 801(2):144.
- Iyer, K. P., Scheel, J. D., Schumacher, J., and Sreenivasan, K. R. (2020). Classical $1/3$ scaling of convection holds up to $ra = 1015$. *Proceedings of the National Academy of Sciences*, 117(14):7594–7598.
- Jenkins, J. S., Pozuelos, F. J., Tuomi, M., Berdiñas, Z. M., Díaz, M. R., Vines, J. I., Suárez, J. C., and Peña Rojas, P. A. (2019). GJ 357: a low-mass planetary system uncovered by precision radial velocities and dynamical simulations. *MNRAS*, 490(4):5585–5595.
- Jespersen, C. K. and Stevenson, D. J. (2020). Investigating Radius Increases in Hot Exoplanets. In *American Astronomical Society Meeting Abstracts #235*, volume 235 of *American Astronomical Society Meeting Abstracts*, page 174.07.
- Jin, S. and Mordasini, C. (2018). Compositional Imprints in Density-Distance-Time: A Rocky Composition for Close-in Low-mass Exoplanets from the Location of the Valley of Evaporation. *ApJ*, 853(2):163.
- Jin, S., Mordasini, C., Parmentier, V., van Boekel, R., Henning, T., and Ji, J. (2014). Planetary Population Synthesis Coupled with Atmospheric Escape: A Statistical View of Evaporation. *ApJ*, 795:65.
- Jindal, A., de Mooij, E. J. W., Jayawardhana, R., Deibert, E. K., Brogi, M., Rustamkulov, Z., Fortney, J. J., Hood, C. E., and Morley, C. V. (2020). Characterization of the Atmosphere of Super-Earth 55 Cancri e Using High-resolution Ground-based Spectroscopy. *AJ*, 160(3):101.
- Johansen, A., Ida, S., and Brasser, R. (2019). How planetary growth outperforms migration. *A&A*, 622:A202.

- Johnstone, C. P. (2020). Hydrodynamic Escape of Water Vapor Atmospheres near Very Active Stars. *ApJ*, 890(1):79.
- Jontof-Hutter, D., Ford, E. B., Rowe, J. F., Lissauer, J. J., Fabrycky, D. C., Van Laerhoven, C., Agol, E., Deck, K. M., Holczer, T., and Mazeh, T. (2016). Secure Mass Measurements from Transit Timing: 10 Kepler Exoplanets between 3 and 8 M_{\oplus} with Diverse Densities and Incident Fluxes. *ApJ*, 820(1):39.
- Kennedy, A. (2006). Interstellar Travel - The Wait Calculation and the Incentive Trap of Progress. *Journal of the British Interplanetary Society*, 59:239–246.
- Kimura, T. and Ikoma, M. (2020). Formation of aqua planets with water of nebular origin: effects of water enrichment on the structure and mass of captured atmospheres of terrestrial planets. *MNRAS*, 496(3):3755–3766.
- Kite, E. S., Fegley, Jr., B., Schaefer, L., and Gaidos, E. (2016). Atmosphere-interior Exchange on Hot, Rocky Exoplanets. *ApJ*, 828:80.
- Kite, E. S., Fegley, Bruce, J., Schaefer, L., and Ford, E. B. (2020). Atmosphere Origins for Exoplanet Sub-Neptunes. *ApJ*, 891(2):111.
- Korenaga, J. (2007). Thermal cracking and the deep hydration of oceanic lithosphere: A key to the generation of plate tectonics? *Journal of Geophysical Research (Solid Earth)*, 112(B5):B05408.
- Korenaga, J. (2010). On the Likelihood of Plate Tectonics on Super-Earths: Does Size Matter? *APJL*, 725(1):L43–L46.
- Korenaga, J. (2017). On the extent of mantle hydration caused by plate bending. *Earth and Planetary Science Letters*, 457:1–9.
- Korenaga, J. (2021). Hadean geodynamics and the nature of early continental crust. *Precambrian Research*, 359:106178.
- Kraus, R., Root, S., Lemke, R., Stewart, S., Jacobsen, S., and Mattsson, T. (2015). Impact vaporization of planetesimal cores in the late stages of planet formation. *Nature Geoscience*, 8:269–272.
- Kubyshkina, D., Fossati, L., Erkaev, N. V., Cubillos, P. E., Johnstone, C. P., Kislyakova, K. G., Lammer, H., Lendl, M., and Odert, P. (2018a). Overcoming the Limitations of the Energy-limited Approximation for Planet Atmospheric Escape. *ApJL*, 866:L18.
- Kubyshkina, D., Fossati, L., Erkaev, N. V., Johnstone, C. P., Cubillos, P. E., Kislyakova, K. G., Lammer, H., Lendl, M., and Odert, P. (2018b). Grid of upper atmosphere models for 1-40 M_{\oplus} planets: application to CoRoT-7 b and HD 219134 b,c. *A&A*, 619:A151.
- Kurosaki, K., Ikoma, M., and Hori, Y. (2014). Impact of photo-evaporative mass loss on masses and radii of water-rich sub/super-Earths. *A&A*, 562:A80.
- Kuzmenko, A. B., van Heumen, E., Carbone, F., and van der Marel, D. (2008). Universal Optical Conductance of Graphite. *Physical Review Letters*, 100(11):117401.
- Lammer, H., Erkaev, N. V., Fossati, L., Juvan, I., Odert, P., Cubillos, P. E., Guenther, E., Kislyakova, K. G., Johnstone, C. P., Lüftinger, T., and Güdel, M. (2016). Identifying

- the ‘true’ radius of the hot sub-Neptune CoRoT-24b by mass-loss modelling. *MNRAS*, 461(1):L62–L66.
- Lammer, H., Erkaev, N. V., Odert, P., Kislyakova, K. G., Leitzinger, M., and Khodachenko, M. L. (2013). Probing the blow-off criteria of hydrogen-rich ‘super-Earths’. *MNRAS*, 430:1247–1256.
- Lazányi, I. and Szirmay-Kalos, L. (2005). Fresnel term approximations for metals. In *WSCG’2005: Short Papers Proceedings*, pages 77–80, University of West Bohemia, Plzen, Czech Republic. University of West Bohemia.
- Lecavelier Des Etangs, A. (2007). A diagram to determine the evaporation status of extrasolar planets. *A&A*, 461:1185–1193.
- Leconte, J. and Chabrier, G. (2012). A new vision of giant planet interiors: Impact of double diffusive convection. *A&A*, 540:A20.
- Lenzuni, P., Chernoff, D. F., and Salpeter, E. E. (1991). Rosseland and Planck Mean Opacities of a Zero-Metallicity Gas. *ApJS*, 76:759.
- Lewis, J. S. (1972). Metal/silicate fractionation in the Solar System. *Earth and Planetary Science Letters*, 15(3):286–290.
- Lewis, J. S. (1974). The Temperature Gradient in the Solar Nebula. *Science*, 186(4162):440–443.
- Li, J. and Agee, C. B. (1996). Geochemistry of mantle-core differentiation at high pressure. *Nature*, 381(6584):686–689.
- Locci, D., Cecchi-Pestellini, C., and Micela, G. (2019). Photo-evaporation of close-in gas giants orbiting around G and M stars. *A&A*, 624:A101.
- Lodders, K. (2003). Solar System Abundances and Condensation Temperatures of the Elements. *ApJ*, 591:1220–1247.
- Lodders, K. (2010). Solar System Abundances of the Elements. *Astrophysics and Space Science Proceedings*, 16:379.
- Lopez, E. D. and Fortney, J. J. (2014). Understanding the Mass-Radius Relation for Sub-neptunes: Radius as a Proxy for Composition. *ApJ*, 792:1.
- Luger, R. and Barnes, R. (2015). Extreme Water Loss and Abiotic O₂ Buildup On Planets Throughout the Habitable Zones of M Dwarfs. In *American Astronomical Society Meeting Abstracts #225*, volume 225 of *American Astronomical Society Meeting Abstracts*, page 407.04.
- Lupu, R. E., Zahnle, K., Marley, M. S., Schaefer, L., Fegley, B., Morley, C., Cahoy, K., Freedman, R., and Fortney, J. J. (2014). The Atmospheres of Earthlike Planets after Giant Impact Events. *ApJ*, 784:27.
- Luque, R., Pallé, E., Kossakowski, D., Dreizler, S., Kemmer, J., Espinoza, N., Burt, J., Anglada-Escudé, G., Béjar, V. J. S., Caballero, J. A., Collins, K. A., Collins, K. I., Cortés-Contreras, M., Díez-Alonso, E., Feng, F., Hatzes, A., Hellier, C., Henning, T., Jeffers, S. V., Kaltenegger, L., Kürster, M., Madden, J., Molaverdikhani, K., Montes, D., Narita, N., Nowak, G., Ofir, A., Oshagh, M., Parviainen, H., Quirrenbach, A., Reffert,

- S., Reiners, A., Rodríguez-López, C., Schlecker, M., Stock, S., Trifonov, T., Winn, J. N., Zapatero Osorio, M. R., Zechmeister, M., Amado, P. J., Anderson, D. R., Batalha, N. E., Bauer, F. F., Bluhm, P., Burke, C. J., Butler, R. P., Caldwell, D. A., Chen, G., Crane, J. D., Dragomir, D., Dressing, C. D., Dynes, S., Jenkins, J. M., Kaminski, A., Klahr, H., Kotani, T., Lafarga, M., Latham, D. W., Lewin, P., McDermott, S., Montañés-Rodríguez, P., Morales, J. C., Murgas, F., Nagel, E., Pedraz, S., Ribas, I., Ricker, G. R., Rowden, P., Seager, S., Shectman, S. A., Tamura, M., Teske, J., Twicken, J. D., Vanderspeck, R., Wang, S. X., and Wohler, B. (2019). Planetary system around the nearby M dwarf GJ 357 including a transiting, hot, Earth-sized planet optimal for atmospheric characterization. *A&A*, 628:A39.
- Madhusudhan, N., Lee, K. K. M., and Mousis, O. (2012). A Possible Carbon-rich Interior in Super-Earth 55 Cancri e. *ApJ*, 759(2):L40.
- Malavergne, V., Cordier, P., Righter, K., Brunet, F., Zanda, B., Addad, A., Smith, T., Bureau, H., Surblé, S., Raepsaet, C., Charon, E., and Hewins, R. H. (2014). How Mercury can be the most reduced terrestrial planet and still store iron in its mantle. *Earth and Planetary Science Letters*, 394:186–197.
- Malavergne, V., Toplis, M. J., Berthet, S., and Jones, J. (2010). Highly reducing conditions during core formation on Mercury: Implications for internal structure and the origin of a magnetic field. *Icarus*, 206(1):199–209.
- Malavolta, L. (2018). Ultra-short Period Rocky Super-Earths. *European Planetary Science Congress*, 12:EPSC2018–1115.
- Malhotra, R. (2015). The Mass Distribution Function of Planets. *ApJ*, 808:71.
- Mandelbrot, B. B. (1975). Stochastic Models for the Earth’s Relief, the Shape and the Fractal Dimension of the Coastlines, and the Number-Area Rule for Islands. *Proceedings of the National Academy of Science*, 72(10):3825–3828.
- Marcy, G. W., Isaacson, H., Howard, A. W., Rowe, J. F., Jenkins, J. M., Bryson, S. T., Latham, D. W., Howell, S. B., Gautier, III, T. N., Batalha, N. M., Rogers, L., Ciardi, D., Fischer, D. A., Gilliland, R. L., Kjeldsen, H., Christensen-Dalsgaard, J., Huber, D., Chaplin, W. J., Basu, S., Buchhave, L. A., Quinn, S. N., Borucki, W. J., Koch, D. G., Hunter, R., Caldwell, D. A., Van Cleve, J., Kolbl, R., Weiss, L. M., Petigura, E., Seager, S., Morton, T., Johnson, J. A., Ballard, S., Burke, C., Cochran, W. D., Endl, M., MacQueen, P., Everett, M. E., Lissauer, J. J., Ford, E. B., Torres, G., Fressin, F., Brown, T. M., Steffen, J. H., Charbonneau, D., Basri, G. S., Sasselov, D. D., Winn, J., Sanchis-Ojeda, R., Christiansen, J., Adams, E., Henze, C., Dupree, A., Fabrycky, D. C., Fortney, J. J., Tarter, J., Holman, M. J., Tenenbaum, P., Shporer, A., Lucas, P. W., Welsh, W. F., Orosz, J. A., Bedding, T. R., Campante, T. L., Davies, G. R., Elsworth, Y., Handberg, R., Hekker, S., Karoff, C., Kawaler, S. D., Lund, M. N., Lundkvist, M., Metcalfe, T. S., Miglio, A., Silva Aguirre, V., Stello, D., White, T. R., Boss, A., Devore, E., Gould, A., Prsa, A., Agol, E., Barclay, T., Coughlin, J., Brugamyer, E., Mullally, F., Quintana, E. V., Still, M., Thompson, S. E., Morrison, D., Twicken, J. D., Désert, J.-M., Carter, J., Crepp, J. R., Hébrard, G., Santerne, A., Moutou, C., Sobeck, C., Hudgins, D., Haas, M. R., Robertson, P., Lillo-Box, J., and Barrado, D. (2014). Masses, Radii, and Orbits of Small Kepler Planets: The Transition from Gaseous to Rocky Planets. *ApJS*, 210:20.

- Markham, S. and Stevenson, D. (2018). Excitation mechanisms for Jovian seismic modes. *Icarus*, 306:200–213.
- Martin, R. G. and Livio, M. (2012). On the evolution of the snow line in protoplanetary discs. *MNRAS*, 425:L6–L9.
- Martins, J. H. C., Santos, N. C., Figueira, P., Faria, J. P., Montalto, M., Boisse, I., Ehrenreich, D., Lovis, C., Mayor, M., Melo, C., Pepe, F., Sousa, S. G., Udry, S., and Cunha, D. (2015). Evidence for a spectroscopic direct detection of reflected light from 51 Pegasi b. *A&A*, 576:A134.
- Masuda, K. (2014). Very Low Density Planets around Kepler-51 Revealed with Transit Timing Variations and an Anomaly Similar to a Planet-Planet Eclipse Event. *ApJ*, 783(1):53.
- Matsui, T. and Abe, Y. (1986a). Evolution of an impact-induced atmosphere and magma ocean on the accreting Earth. *Nature*, 319(6051):303–305.
- Matsui, T. and Abe, Y. (1986b). Formation of a ‘magma ocean’ on the terrestrial planets due to the blanketing effect of an impact-induced atmosphere. *Earth Moon and Planets*, 34(3):223–230.
- Matt, S. P., Brun, A. S., Baraffe, I., Bouvier, J., and Chabrier, G. (2015). The Mass-dependence of Angular Momentum Evolution in Sun-like Stars. *ApJL*, 799(2):L23.
- Matter, A., Guillot, T., and Morbidelli, A. (2009). Calculation of the enrichment of the giant planet envelopes during the “late heavy bombardment”. *Annual Review of Earth and Planetary Sciences*, 57(7):816–821.
- Mayer, M. and Duschl, W. J. (2005). Rosseland and Planck mean opacities for primordial matter. *MNRAS*, 358(2):614–631.
- Mayor, M. and Queloz, D. (1995). A Jupiter-mass companion to a solar-type star. *Nature*, 378(6555):355–359.
- McKay, C. P. (2014). Requirements and limits for life in the context of exoplanets. *Proceedings of the National Academy of Science*, 111(35):12628–12633.
- Met Office (2010). National Meteorological Library and Archive Fact Sheet 6 - The Beaufort Scale.
- Miozzi, F., Morard, G., Antonangeli, D., Clark, A. N., Mezouar, M., Dorn, C., Rozel, A., and Fiquet, G. (2018). Equation of State of SiC at Extreme Conditions: New Insight Into the Interior of Carbon-Rich Exoplanets. *Journal of Geophysical Research (Planets)*, 123(9):2295–2309.
- Mizuno, H. (1980). Formation of the Giant Planets. *Progress of Theoretical Physics*, 64(2):544–557.
- Mizuno, H., Nakazawa, K., and Hayashi, C. (1978). Instability of a gaseous envelope surrounding a planetary core and formation of giant planets. *Progress of Theoretical Physics*, 60:699–710.
- Mizuno, H., Nakazawa, K., and Hayashi, C. (1980). Dissolution of the primordial rare gases into the molten Earth’s material. *Earth and Planetary Science Letters*, 50(1):202–210.

- Mocquet, A., Grasset, O., and Sotin, C. (2014). Very high-density planets: a possible remnant of gas giants. *Philosophical Transactions of the Royal Society of London Series A*, 372:20130164–20130164.
- Modirrousta-Galian, D., Ito, Y., and Micela, G. (2021). Exploring super-Earth surfaces: Albedo of near-airless magma ocean planets and topography. *Icarus*, 358:114175.
- Modirrousta-Galian, D., Locci, D., and Micela, G. (2020a). The Bimodal Distribution in Exoplanet Radii: Considering Varying Core Compositions and H₂ Envelope’s Sizes. *ApJ*, 891(2):158.
- Modirrousta-Galian, D., Locci, D., Tinetti, G., and Micela, G. (2020b). Hot Super-Earths with Hydrogen Atmospheres: A Model Explaining Their Paradoxical Existence. *ApJ*, 888(2):87.
- Modirrousta-Galian, D. and Maddalena, G. (2021). Of Aliens And Exoplanets: Why The Search For Life, Probably, Requires The Search For Water. *Journal of the British Interplanetary Society*, 74:238–242.
- Modirrousta-Galian, D., Stelzer, B., Magaudda, E., Maldonado, J., Güdel, M., Sanz-Forcada, J., Edwards, B., and Micela, G. (2020c). GJ 357 b: A Super-Earth Orbiting an Extremely Inactive Host Star. *arXiv e-prints*, page arXiv:2007.10262.
- Mollière, P., van Boekel, R., Bouwman, J., Henning, T., Lagage, P. O., and Min, M. (2017). Observing transiting planets with JWST. Prime targets and their synthetic spectral observations. *A&A*, 600:A10.
- Mollière, P., van Boekel, R., Dullemond, C., Henning, T., and Mordasini, C. (2015). Model Atmospheres of Irradiated Exoplanets: The Influence of Stellar Parameters, Metallicity, and the C/O Ratio. *ApJ*, 813(1):47.
- Mordasini, C. (2020). Planetary evolution with atmospheric photoevaporation. I. Analytical derivation and numerical study of the evaporation valley and transition from super-Earths to sub-Neptunes. *A&A*, 638:A52.
- Mordasini, C., Alibert, Y., and Benz, W. (2009). Extrasolar planet population synthesis. I. Method, formation tracks, and mass-distance distribution. *A&A*, 501:1139–1160.
- Moresi, L. and Solomatov, V. (1998). Mantle convection with a brittle lithosphere: thoughts on the global tectonic styles of the Earth and Venus. *Geophysical Journal International*, 133(3):669–682.
- Mousis, O., Deleuil, M., Aguichine, A., Marcq, E., Naar, J., Aguirre, L. A., Brugger, B., and Gonçalves, T. (2020). Irradiated Ocean Planets Bridge Super-Earth and Sub-Neptune Populations. *ApJL*, 896(2):L22.
- Mugnai, L. V., Modirrousta-Galian, D., Edwards, B., Changeat, Q., Bouwman, J., Morello, G., Al-Refai, A., Baeyens, R., Bieger, M. F., Blain, D., Gressier, A., Guilluy, G., Jaziri, Y., Kiefer, F., Morvan, M., Pluriel, W., Poveda, M., Skaf, N., Whiteford, N., Wright, S., Yip, K. H., Zingales, T., Charnay, B., Drossart, P., Leconte, J., Venot, O., Waldmann, I., and Beaulieu, J.-P. (2021). ARES. V. No Evidence For Molecular Absorption in the HST WFC3 Spectrum of GJ 1132 b. *AJ*, 161(6):284.
- Namur, O., Charlier, B., Holtz, F., Cartier, C., and McCammon, C. (2016). Sulfur solubility

- in reduced mafic silicate melts: Implications for the speciation and distribution of sulfur on Mercury. *Earth and Planetary Science Letters*, 448:102–114.
- Nettelmann, N., Fortney, J. J., Kramm, U., and Redmer, R. (2011). Thermal Evolution and Structure Models of the Transiting Super-Earth GJ 1214b. *ApJ*, 733(1):2.
- Nittler, L. R., Starr, R. D., Weider, S. Z., McCoy, T. J., Boynton, W. V., Ebel, D. S., Ernst, C. M., Evans, L. G., Goldsten, J. O., Hamara, D. K., Lawrence, D. J., McNutt, R. L., Schlemm, C. E., Solomon, S. C., and Sprague, A. L. (2011). The Major-Element Composition of Mercury’s Surface from MESSENGER X-ray Spectrometry. *Science*, 333(6051):1847.
- Nittler, L. R. and Weider, S. Z. (2019). The Surface Composition of Mercury. *Elements*, 15(1):33–38.
- Noack, L., Rivoldini, A., and Van Hoolst, T. (2017). Volcanism and outgassing of stagnant-lid planets: Implications for the habitable zone. *Physics of the Earth and Planetary Interiors*, 269:40–57.
- O’Neill, H. S. C. and Palme, H. (1998). Composition of the silicate earth: implications for accretion of and core formation. In Jackson, I., editor, *The Earth’s mantle; composition, structure, and evolution*, volume 264, pages 3–126, Cambridge. Cambridge University Press.
- O’Rourke, J. G. and Korenaga, J. (2012). Terrestrial planet evolution in the stagnant-lid regime: Size effects and the formation of self-destabilizing crust. *Icarus*, 221(2):1043–1060.
- Owen, J. E. and Adams, F. C. (2019). Effects of magnetic fields on the location of the evaporation valley for low-mass exoplanets. *MNRAS*, 490(1):15–20.
- Owen, J. E. and Lai, D. (2018). Photoevaporation and high-eccentricity migration created the sub-Jovian desert. *MNRAS*, 479(4):5012–5021.
- Owen, J. E. and Wu, Y. (2013). Kepler Planets: A Tale of Evaporation. *ApJ*, 775:105.
- Owen, J. E. and Wu, Y. (2016). Atmospheres of Low-mass Planets: The “Boil-off”. *ApJ*, 817(2):107.
- Owen, J. E. and Wu, Y. (2017). The Evaporation Valley in the Kepler Planets. *ApJ*, 847:29.
- Palle, E., Chen, G., Prieto-Arranz, J., Nowak, G., Murgas, F., Nortmann, L., Pollacco, D., Lam, K., Montanes-Rodriguez, P., Parviainen, H., and Casasayas-Barris, N. (2017). Feature-rich transmission spectrum for WASP-127b. Cloud-free skies for the puffiest known super-Neptune? *A&A*, 602:L15.
- Papoular, R. J. and Papoular, R. (2014). Some optical properties of graphite from IR to millimetric wavelengths. *MNRAS*, 443(4):2974–2982.
- Peale, S. J. (1999). Origin and Evolution of the Natural Satellites. *Annu. Rev. Astron. Astrophys.*, 37:533–602.
- Penz, T. and Micela, G. (2008). X-ray induced mass loss effects on exoplanets orbiting dM stars. *A&A*, 479:579–584.

- Penz, T., Micela, G., and Lammer, H. (2008). Influence of the evolving stellar X-ray luminosity distribution on exoplanetary mass loss. *A&A*, 477:309–314.
- Perri, F. and Cameron, A. G. W. (1974). Hydrodynamic Instability of the Solar Nebula in the Presence of a Planetary Core. *Icarus*, 22(4):416–425.
- Petralia, A., Alei, E., Aresu, G., Locci, D., Cecchi-Pestellini, C., Micela, G., Claudi, R., and Ciaravella, A. (2020). A systematic study of CO₂ planetary atmospheres and their link to the stellar environment. *MNRAS*, 496(4):5350–5359.
- Philipp, H. R. (1977). Infrared optical properties of graphite. *Physical Review B (Solid State)*, 16(6):2896–2900.
- Pluriel, W., Marcq, E., and Turbet, M. (2019). Modeling the albedo of Earth-like magma ocean planets with H₂O-CO₂ atmospheres. *Icarus*, 317:583–590.
- Pluriel, W., Whiteford, N., Edwards, B., Changeat, Q., Yip, K. H., Baeyens, R., Al-Refaie, A., Fabienne Bieger, M., Blain, D., Gressier, A., Guilluy, G., Yassin Jaziri, A., Kiefer, F., Modirrousta-Galian, D., Morvan, M., Mugnai, L. V., Poveda, M., Skaf, N., Zingales, T., Wright, S., Charnay, B., Drossart, P., Leconte, J., Tsiaras, A., Venot, O., Waldmann, I., and Beaulieu, J.-P. (2020). ARES. III. Unveiling the Two Faces of KELT-7 b with HST WFC3. *Aj*, 160(3):112.
- Podolak, M. and Zucker, S. (2004). A note on the snow line in protostellar accretion disks. *Meteoritics and Planetary Science*, 39:1859–1868.
- Polyanskiy, M. N. (2010). Refractive index database.
- Polyansky, O. L., Kyuberis, A. A., Zobov, N. F., Tennyson, J., Yurchenko, S. N., and Lodi, L. (2018). ExoMol molecular line lists XXX: a complete high-accuracy line list for water. *MNRAS*, 480(2):2597–2608.
- Querry, M. R. (1985). Optical constants. Technical report.
- Ridden-Harper, A. R., Snellen, I. A. G., Keller, C. U., de Kok, R. J., Di Gloria, E., Hoeijmakers, H. J., Brogi, M., Fridlund, M., Vermeersen, B. L. A., and van Westrenen, W. (2016). Search for an exosphere in sodium and calcium in the transmission spectrum of exoplanet 55 Cancri e. *A&A*, 593:A129.
- Righter, K., Drake, M. J., and Yaxley, G. (1997). Prediction of siderophile element metal-silicate partition coefficients to 20 GPa and 2800°C: the effects of pressure, temperature, oxygen fugacity, and silicate and metallic melt compositions. *Physics of the Earth and Planetary Interiors*, 100(1):115–134.
- Riner, M. A., Bina, C. R., Robinson, M. S., and Desch, S. J. (2008). Internal structure of Mercury: Implications of a molten core. *Journal of Geophysical Research (Planets)*, 113(E8):E08013.
- Roden, E. (2012). Microbial iron-redox cycling in subsurface environments. *Biochemical Society Transactions*, 40(6):1249–1256.
- Rogers, L. A. and Seager, S. (2010). A Framework for Quantifying the Degeneracies of Exoplanet Interior Compositions. *ApJ*, 712:974–991.

- Rouan, D., Deeg, H. J., Demangeon, O., Samuel, B., Cavarroc, C., Fegley, B., and Léger, A. (2011). The Orbital Phases and Secondary Transits of Kepler-10b. A Physical Interpretation Based on the Lava-ocean Planet Model. *ApJL*, 741(2):L30.
- Safronov, V. S. and Zvjagina, E. V. (1969). Relative Sizes of the Largest Bodies during the Accumulation of Planets. *Icarus*, 10(1):109–115.
- Sanz-Forcada, J., Micela, G., Ribas, I., Pollock, A. M. T., Eiroa, C., Velasco, A., Solano, E., and García-Álvarez, D. (2011). Estimation of the XUV radiation onto close planets and their evaporation. *A&A*, 532:A6.
- Sautter, V., Toplis, M. J., Wiens, R. C., Cousin, A., Fabre, C., Gasnault, O., Maurice, S., Forni, O., Lasue, J., Ollila, A., Bridges, J. C., Mangold, N., Le Mouélic, S., Fisk, M., Meslin, P. Y., Beck, P., Pinet, P., Le Deit, L., Rapin, W., Stolper, E. M., Newsom, H., Dyar, D., Lanza, N., Vaniman, D., Clegg, S., and Wray, J. J. (2015). In situ evidence for continental crust on early Mars. *Nature Geoscience*, 8(8):605–609.
- Schaefer, L. and Fegley, B. (2009). Chemistry of Silicate Atmospheres of Evaporating Super-Earths. *ApJl*, 703:L113–L117.
- Schaefer, L., Lodders, K., and Fegley, B. (2012). Vaporization of the Earth: Application to Exoplanet Atmospheres. *ApJ*, 755:41.
- Schlichting, H. E., Fuentes, C. I., and Trilling, D. E. (2013). Initial Planetesimal Sizes and the Size Distribution of Small Kuiper Belt Objects. *AJ*, 146(2):36.
- Schlick, C. (1994). An inexpensive brdf model for physically-based rendering. *Computer Graphics Forum*, 13(3):233–246.
- Seager, S., Kuchner, M., Hier-Majumder, C. A., and Militzer, B. (2007). Mass-Radius Relationships for Solid Exoplanets. *ApJ*, 669:1279–1297.
- Seeliger, H. (1884). Zur photometrie des saturnringes. *Astronomische Nachrichten*, 109(20):305–314.
- Segatz, M., Spohn, T., Ross, M. N., and Schubert, G. (1988). Tidal dissipation, surface heat flow, and figure of viscoelastic models of Io. *Icarus*, 75:187–206.
- Sforna, M. C., Philippot, P., Somogyi, A., van Zuilen, M. A., Medjoubi, K., Schoepp-Cothenet, B., Nitschke, W., and Visscher, P. T. (2014). Evidence for arsenic metabolism and cycling by microorganisms 2.7 billion years ago. *Nature Geoscience*, 7(11):811–815.
- Shelberg, M., Lam, N., and Moellering, H. (1983). Measuring the fractal dimensions of surfaces. *Proceedings: Auto-Carlo Six*, pages 319–328.
- Shibata, S. and Ikoma, M. (2019). Capture of solids by growing proto-gas giants: effects of gap formation and supply limited growth. *MNRAS*, 487(4):4510–4524.
- Shiraishi, M. and Ida, S. (2008). Infall of Planetesimals onto Growing Giant Planets: Onset of Runaway Gas Accretion and Metallicity of Their Gas Envelopes. *ApJ*, 684(2):1416–1426.
- Simon, J. B., Armitage, P. J., Li, R., and Youdin, A. N. (2016). The Mass and Size Distribution of Planetesimals Formed by the Streaming Instability. I. The Role of Self-gravity. *ApJ*, 822(1):55.

- Sinukoff, E., Howard, A. W., Petigura, E. A., Fulton, B. J., Crossfield, I. J. M., Isaacson, H., Gonzales, E., Crepp, J. R., Brewer, J. M., Hirsch, L., Weiss, L. M., Ciardi, D. R., Schlieder, J. E., Benneke, B., Christiansen, J. L., Dressing, C. D., Hansen, B. M. S., Knutson, H. A., Kosiarek, M., Livingston, J. H., Greene, T. P., Rogers, L. A., and Lépine, S. (2017). K2-66b and K2-106b: Two Extremely Hot Sub-Neptune-size Planets with High Densities. *AJ*, 153(6):271.
- Skaf, N., Bieger, M. F., Edwards, B., Changeat, Q., Morvan, M., Kiefer, F., Blain, D., Zingales, T., Poveda, M., Al-Refaie, A., Baeyens, R., Gressier, A., Guilluy, G., Jaziri, A. Y., Modirrousta-Galian, D., Mugnai, L. V., Pluriel, W., Whiteford, N., Wright, S., Yip, K. H., Charnay, B., Leconte, J., Drossart, P., Tsiraras, A., Venot, O., Waldmann, I., and Beaulieu, J.-P. (2020). ARES. II. Characterizing the Hot Jupiters WASP-127 b, WASP-79 b, and WASP-62b with the Hubble Space Telescope. *Aj*, 160(3):109.
- Sotin, C., Gasset, O., and Mocquet, A. (2007). Mass radius curve for extrasolar Earth-like planets and ocean planets. *Icarus*, 191(1):337–351.
- Spaargaren, R. J., Ballmer, M. D., Bower, D. J., Dorn, C., and Tackley, P. J. (2020). The influence of bulk composition on the long-term interior-atmosphere evolution of terrestrial exoplanets. *A&A*, 643:A44.
- Stevenson, D. J. (1982a). Formation of the giant planets. *Annual Review of Earth and Planetary Sciences*, 30(8):755–764.
- Stevenson, D. J. (1982b). Interiors of the Giant Planets. *Annual Review of Earth and Planetary Sciences*, 10:257.
- Stevenson, D. J. (2020). Jupiter’s Interior as Revealed by Juno. *Annual Review of Earth and Planetary Sciences*, 48:465–489.
- Stiassnie, M. (1991). The fractal dimension of the ocean surface. *Proceedings of the International School of Physics Enrico Fermi*, pages 633–647.
- Stiassnie, M., Agnon, Y., and Shemer, L. (1991). Fractal dimensions of random water surfaces. *Physica D Nonlinear Phenomena*, 47(3):341–352.
- Swain, M. R., Estrela, R., Roudier, G. M., Sotin, C., Rimmer, P. B., Valio, A., West, R., Pearson, K., Huber-Feely, N., and Zellem, R. T. (2021). Detection of an Atmosphere on a Rocky Exoplanet. *AJ*, 161(5):213.
- Swain, M. R., Estrela, R., Sotin, C., Roudier, G. M., and Zellem, R. T. (2019). Two Terrestrial Planet Families with Different Origins. *ApJ*, 881(2):117.
- Taft, E. A. and Philipp, H. R. (1965). Optical Properties of Graphite. *Physical Review*, 138(1A):197–202.
- Tanford, C. (1978). The Hydrophobic Effect and the Organization of Living Matter. *Science*, 200(4345):1012–1018.
- Tian, F., Kasting, J. F., Liu, H.-L., and Roble, R. G. (2008). Hydrodynamic planetary thermosphere model: 1. Response of the Earth’s thermosphere to extreme solar EUV conditions and the significance of adiabatic cooling. *Journal of Geophysical Research (Planets)*, 113(E5):E05008.

- Timms, N., Erickson, T., Zanetti, M., Pearce, M., Cayron, C., Cavosie, A., Reddy, S., Wittmann, A., and Carpenter, P. (2017). Cubic zirconia in $> 2370^\circ$ C impact melt records Earth's hottest crust. *Earth and Planetary Science Letters*, 477:52–58.
- Tobie, G., Lunine, J. I., and Sotin, C. (2006). Episodic outgassing as the origin of atmospheric methane on Titan. *Nature*, 440(7080):61–64.
- Tsiaras, A., Rocchetto, M., Waldmann, I. P., Venot, O., Varley, R., Morello, G., Damiano, M., Tinetti, G., Barton, E. J., Yurchenko, S. N., and Tennyson, J. (2016). Detection of an Atmosphere Around the Super-Earth 55 Cancri e. *ApJ*, 820:99.
- Tsiaras, A., Waldmann, I. P., Tinetti, G., Tennyson, J., and Yurchenko, S. N. (2019). Water vapour in the atmosphere of the habitable-zone eight-Earth-mass planet K2-18 b. *Nature Astronomy*, 3:1086–1091.
- Tsiaras, A., Waldmann, I. P., Zingales, T., Rocchetto, M., Morello, G., Damiano, M., Karpouzias, K., Tinetti, G., McKemmish, L. K., Tennyson, J., and Yurchenko, S. N. (2018). A Population Study of Gaseous Exoplanets. *Aj*, 155(4):156.
- Turrini, D., Schisano, E., Fonte, S., Molinari, S., Politi, R., Fedele, D., Panić, O., Kama, M., Changeat, Q., and Tinetti, G. (2021). Tracing the Formation History of Giant Planets in Protoplanetary Disks with Carbon, Oxygen, Nitrogen, and Sulfur. *ApJ*, 909(1):40.
- Urban, P., Musilová, V., and Skrbek, L. (2011). Efficiency of heat transfer in turbulent rayleigh-bénard convection. *Phys. Rev. Lett.*, 107:014302.
- Vaiana, G. S., Cassinelli, J. P., Fabbiano, G., Giacconi, R., Golub, L., Gorenstein, P., Haisch, B. M., Harnden, F. R., J., Johnson, H. M., Linsky, J. L., Maxson, C. W., Mewe, R., Rosner, R., Seward, F., Topka, K., and Zwaan, C. (1981). Results from an extensive Einstein stellar survey. *ApJ*, 245:163–182.
- Valencia, D., Guillot, T., Parmentier, V., and Freedman, R. S. (2013). Bulk Composition of GJ 1214b and Other Sub-Neptune Exoplanets. *ApJ*, 775:10.
- Valencia, D., O'Connell, R. J., and Sasselov, D. (2006). Internal structure of massive terrestrial planets. *Icarus*, 181(2):545–554.
- Valencia, D., O'Connell, R. J., and Sasselov, D. D. (2007a). Inevitability of Plate Tectonics on Super-Earths. *ApJL*, 670(1):L45–L48.
- Valencia, D., Sasselov, D. D., and O'Connell, R. J. (2007b). Detailed Models of Super-Earths: How Well Can We Infer Bulk Properties? *ApJ*, 665(2):1413–1420.
- Wächtershauser, G. (1990). Evolution of the First Metabolic Cycles. *Proceedings of the National Academy of Science*, 87(1):200–204.
- Watson, A. J., Donahue, T. M., and Walker, J. C. G. (1981). The dynamics of a rapidly escaping atmosphere - Applications to the evolution of earth and Venus. *Icarus*, 48:150–166.
- Weider, S. Z., Nittler, L. R., Starr, R. D., McCoy, T. J., and Solomon, S. C. (2014). Variations in the abundance of iron on Mercury's surface from MESSENGER X-Ray Spectrometer observations. *Icarus*, 235:170–186.

- West, R. G., Hellier, C., Almenara, J. M., Anderson, D. R., Barros, S. C. C., Bouchy, F., Brown, D. J. A., Collier Cameron, A., Deleuil, M., Delrez, L., Doyle, A. P., Faedi, F., Fumel, A., Gillon, M., Gómez Maqueo Chew, Y., Hébrard, G., Jehin, E., Lendl, M., Maxted, P. F. L., Pepe, F., Pollacco, D., Queloz, D., Ségransan, D., Smalley, B., Smith, A. M. S., Southworth, J., Triaud, A. H. M. J., and Udry, S. (2016). Three irradiated and bloated hot Jupiters: WASP-76b, WASP-82b, and WASP-90b. *A&A*, 585:A126.
- Whitworth, A. P., Bhattal, A. S., Francis, N., and Watkins, S. J. (1996). Star formation and the singular isothermal sphere. *MNRAS*, 283(3):1061–1070.
- Wood, A. T. A. and Chan, G. (1994). Simulation of stationary gaussian processes in $[0,1]^d$. *Journal of Computational and Graphical Statistics*, 3(4):409–432.
- Xie, J.-W. (2014). Transit Timing Variation of Near-resonance Planetary Pairs. II. Confirmation of 30 Planets in 15 Multiple-planet Systems. *ApJS*, 210(2):25.
- Yurchenko, S. N., Mellor, T. M., Freedman, R. S., and Tennyson, J. (2020). ExoMol line lists - XXXIX. Ro-vibrational molecular line list for CO₂. *MNRAS*, 496(4):5282–5291.
- Zahnle, K. J. and Kasting, J. F. (1986). Mass fractionation during transonic escape and implications for loss of water from Mars and Venus. *Icarus*, 68(3):462–480.
- Zapolsky, H. S. and Salpeter, E. E. (1969). The Mass-Radius Relation for Cold Spheres of Low Mass. *ApJ*, 158:809.
- Zeng, L., Jacobsen, S. B., Sasselov, D. D., Petaev, M. I., Vanderburg, A., Lopez-Morales, M., Perez-Mercader, J., Mattsson, T. R., Li, G., Heising, M. Z., Bonomo, A. S., Damasso, M., Berger, T. A., Cao, H., Levi, A., and Wordsworth, R. D. (2019). Growth model interpretation of planet size distribution. *Proceedings of the National Academy of Science*, 116(20):9723–9728.
- Zeng, L. and Sasselov, D. (2013). A Detailed Model Grid for Solid Planets from 0.1 through 100 Earth Masses. *PASP*, 125(925):227.
- Zeng, L., Sasselov, D. D., and Jacobsen, S. B. (2016). Mass-Radius Relation for Rocky Planets Based on PREM. *ApJ*, 819:127.
- Zhang, M., Knutson, H. A., Wang, L., Dai, F., Oklopcic, A., and Hu, R. (2021). No Escaping Helium from 55 Cnc e. *AJ*, 161(4):181.
- Zilinskas, M., Miguel, Y., Mollière, P., and Tsai, S.-M. (2020). Atmospheric compositions and observability of nitrogen-dominated ultra-short-period super-Earths. *MNRAS*, 494(1):1490–1506.

Appendix

A Equations

A.1 Why Remnant Cores Matter – Calculation

A.1.1 Simple Radiative Model (after; [Stevenson, 1982a](#))

We begin by considering hydrostatic equilibrium,

$$\frac{dP}{dr} = -\rho g, \quad (\text{A.1})$$

optical depth,

$$\frac{d\tau}{dr} = -\rho k, \quad (\text{A.2})$$

temperature change,

$$\frac{dT}{d\tau} = \frac{3}{16} \frac{T_{eff}^4}{T^3}, \quad (\text{A.3})$$

and the ideal gas equation,

$$P = \frac{\rho}{\mu} k_B T, \quad (\text{A.4})$$

where P is the pressure, r is the distance, g is the gravitational acceleration, τ is the optical depth, ρ is the density, k is the opacity, T_{eff} and T are the effective and true temperatures, μ is the mean molecular mass, and k_B is the Boltzmann constant. One can now combine Eq A.2 and A.3 together,

$$\frac{dT}{dr} = -\frac{3}{16} \rho k \frac{T_{eff}^4}{T^3}. \quad (\text{A.5a})$$

Substituting in Eq A.1,

$$\frac{dT}{dP} = \frac{3}{16} \frac{k}{g} \frac{T_{eff}^4}{T^3}, \quad (\text{A.5b})$$

and integrating the above equation one arrives at,

$$\frac{T}{4P} = \frac{3}{16} \frac{k}{g} \frac{T_{eff}^4}{T^3}. \quad (\text{A.5c})$$

However, this is identical to dT/dP (as shown above), so ,

$$\frac{dT}{dP} = \frac{T}{4P}, \quad (\text{A.5d})$$

Re-inserting the equation for hydrostatic equilibrium (Eq A.1) with the ideal gas equation (Eq A.4) provides,

$$\frac{dT}{dr} = -\frac{GM}{4k_B r^2}. \quad (\text{A.5e})$$

By assuming that T and P are much larger than their outer boundary values, and integrating with respect to distance, one obtains the temperature as a function of the radius,

$$T \simeq \frac{GM\mu}{4k_B r}. \quad (\text{A.6})$$

An almost identical equation can be acquired through the virial theorem. For the next part of the derivation we take Eq A.5c and substitute in the luminosity ($L = 4\pi r^2 \sigma T_{eff}^4$),

$$\frac{T}{4P} = \frac{3}{16} \frac{k}{g} \frac{1}{T^3} \frac{L}{4\pi r^2 \sigma}, \quad (\text{A.7a})$$

The ideal gas equation (Eq A.4) is then inserted, and the equation for the gravitational acceleration can be substituted in. This can be solved for the density,

$$\rho = \frac{64\pi\sigma}{3kL} T^4 r. \quad (\text{A.7b})$$

We then insert Eq A.6,

$$\rho \simeq \frac{64\pi\sigma}{3kL} \left(\frac{GM\mu}{4k_B} \right)^4 \frac{1}{r^3}. \quad (\text{A.7c})$$

With the density known, it is possible to calculate the mass of the envelope as such,

$$\begin{aligned} M_{atm} &\simeq \int_{R_{core}}^{R_{Hill}} 4\pi r^2 \rho(r) dr \\ &\simeq \frac{256\pi^2 \sigma}{3kL} \left(\frac{GM\mu}{4k_B} \right)^4 \ln \left(\frac{R_{Hill}}{R_{core}} \right). \end{aligned} \quad (\text{A.8})$$

This is the equation for the atmospheric mass. Note how the mass is incredibly insensitive to the thickness of the atmosphere. Assume that the majority of the luminosity of the

embryo comes from its formational energy,

$$L \simeq \frac{GM_c}{R_c} \frac{dM_c}{dt}, \quad (\text{A.9a})$$

hence,

$$L \propto M_c^{2/3}, \quad (\text{A.9b})$$

where M_c and R_c are the core mass and radius, respectively. Therefore, Eq A.8 can be simplified as follows,

$$M_{atm} \propto \alpha \cdot \frac{M_p^4}{M_c^{2/3}}, \quad (\text{A.10})$$

where M_p is the total planetary mass and α is a constant that incorporates many of the parameters in Eq A.8. Its value is approximately $\sim 10^{-61}$. Since we know $M_p = M_{atm} + M_c$,

$$M_p \simeq M_c + \alpha \cdot \frac{M_p^4}{M_c^{2/3}}. \quad (\text{A.11})$$

we are interested in finding the maximum possible core mass (i.e., the critical core mass) beyond which runaway accretion occurs. We therefore set $dM_c/dM_p = 0$,

$$M_c \simeq 0.38 \left(\frac{1}{\alpha} \right)^{3/7}. \quad (\text{A.12})$$

Inputting $\alpha \sim 10^{-61}$ gives $M_c \sim 10M_\oplus$. This simple model shows that at $\sim 10M_\oplus$ one expects runaway accretion to commence. This model provides an oversimplified prescription of the physics taking place, so one should be cautious when adopting it. Nevertheless, more advanced models show similar behavior (e.g. [Ikoma et al., 2000](#)).

A.1.2 Radius Derivation (after; [Stevenson, 1982b](#))

We begin with the equation of state,

$$P = K\rho^2, \quad (\text{A.13a})$$

that we differentiate with respect to radius,

$$\frac{dP}{dr} = 2K\rho \frac{d\rho}{dr}. \quad (\text{A.13b})$$

We now insert the equation for hydrostatic equilibrium and divide by ρ ,

$$2K \frac{d\rho}{dr} = -g(r). \quad (\text{A.13c})$$

The gravitational acceleration can be rewritten as,

$$2K \frac{d\rho}{dr} = -\frac{G}{r^2} \int_0^r 4\pi r^2 \rho \, dr. \quad (\text{A.13d})$$

We then multiply by r^2 ,

$$2K r^2 \frac{d\rho}{dr} = -G \int_0^r 4\pi r^2 \rho \, dr. \quad (\text{A.13e})$$

The integral can be removed by differentiating by respect to the radius,

$$\frac{d}{dr} \left(r^2 \frac{d\rho}{dr} \right) = -\frac{2\pi G}{K} r^2 \rho. \quad (\text{A.13f})$$

We then define $k^2 = \frac{2\pi G}{K}$ and solve, yielding the density,

$$\rho = A \frac{\sin kr}{kr} + B \frac{\cos kr}{kr}. \quad (\text{A.14})$$

Because the planet is assumed to be homogeneous and has a finite radius, it can be deduced that $B = 0$. If B is non-zero, then the density approaches infinity at small radii. Therefore, when $kr = \pi$ the density is zero, marking the end of the planet's radius, so,

$$R_{H_2/He} = \sqrt{\frac{\pi K}{2G}}. \quad (\text{A.15})$$

A.1.3 Well-Mixed Model (after; [Stevenson, 1982b](#))

For the well-mixed (eroded) mode, one can consider *volume additivity*, where the total volume of the planet is assumed to equal the volume occupied by the primordial gas plus the volume of the heavy materials:

$$V_t = V_{H_2/He} + V_{Heavy}, \quad (\text{A.16a})$$

however, volume is mass over density,

$$\frac{M_t}{\rho_{avg}} = \frac{M_{H_2/He}}{\rho_{H_2/He}} + \frac{M_{heavy}}{\rho_{heavy}}, \quad (\text{A.16b})$$

but we can write $M_{H_2/He}$ and M_{heavy} as functions of the total mass,

$$\frac{M_t}{\rho_{avg}} = \frac{(1-z) \cdot M_t}{\rho_{H_2/He}} + \frac{z \cdot M_t}{\rho_{heavy}}, \quad (\text{A.16c})$$

where z is the heavy material mass fraction. Now we cancel through by M_t ,

$$\frac{1}{\rho_{avg}} = \frac{1-z}{\rho_{H_2/He}} + \frac{z}{\rho_{heavy}}. \quad (\text{A.16d})$$

Because $(1-z) \gg z$ and $\rho_{heavy} \gg \rho_{H_2/He}$ the equation can be approximated as,

$$\frac{1}{\rho_{avg}} = \frac{1-z}{\rho_{H_2/He}}. \quad (\text{A.16e})$$

We now replace $\rho_{H_2/He}$ with Eq 2.20,

$$\frac{1}{\rho_{avg}} = \frac{1-z}{\sqrt{P/K}}. \quad (\text{A.16f})$$

This can now be solved,

$$P = (1-z)^2 K \rho^2, \quad (\text{A.16g})$$

meaning that the constant K has been reduced by $(1-z)^2$, so that the total radius decreases,

$$R_{H_2/He} = (1-z) \sqrt{\frac{\pi K}{2G}}. \quad (\text{A.17})$$

A.1.4 Cored Model

We begin with the equation of state,

$$P = K \rho^2. \quad (\text{A.18a})$$

We then differentiate with respect to ρ ,

$$\frac{dP}{d\rho} = 2K\rho, \quad (\text{A.18b})$$

and multiply by the equation for hydrostatic equilibrium,

$$\frac{d\rho}{dr} = -\frac{g}{2K}. \quad (\text{A.18c})$$

After this, we insert $k^2 = \frac{2\pi G}{K}$. For the case of $r \sim R_c$, where R_c is the radius of the core, the gravitational acceleration $\approx GM_c/R_c^2$, so,

$$\frac{d\rho}{dr} \approx -\frac{M_c k^2}{4\pi R_c^2}. \quad (\text{A.18d})$$

Next, we Taylor expand the density given by Eq A.14,

$$\rho \simeq A + \frac{B}{kr}, \quad (\text{A.18e})$$

and differentiate with respect to the radius,

$$\frac{d\rho}{dr} \simeq -\frac{B}{kr^2}. \quad (\text{A.18f})$$

Equating Eq A.18d with Eq A.18f and solving for B leads to,

$$B \simeq M_c \frac{k^3}{4\pi}. \quad (\text{A.18g})$$

Knowing B we can solve Eq A.14 for the radius. Note that unlike the well-mixed case (see sect. A.1.3), $B \neq 0$, so $kr \neq \pi$. Instead, $kr = \pi(1 - \delta)$, where δ is a small deviation:

$$\rho = A \frac{\sin \pi(1 - \delta)}{\pi(1 - \delta)} + B \frac{\cos \pi(1 - \delta)}{\pi(1 - \delta)}. \quad (\text{A.19a})$$

Using trigonometric identities,

$$\rho = A \frac{\sin(\pi\delta)}{\pi\delta} - B \frac{\cos(\pi\delta)}{\pi\delta}, \quad (\text{A.19b})$$

that can be simplified as,

$$\begin{aligned}\delta &= \frac{1}{\pi} \arctan\left(\frac{B}{A}\right) \\ &\simeq \frac{B}{\pi A}.\end{aligned}\tag{A.19c}$$

Solving for the radius gives,

$$\begin{aligned}kr &= \pi(1 - \delta) \\ &= \pi\left(1 - \frac{B}{\pi A}\right),\end{aligned}\tag{A.19d}$$

hence,

$$R = \frac{\pi\left(1 - \frac{B}{\pi A}\right)}{k}.\tag{A.19e}$$

Inserting the equation of state $k^2 = 2\pi G/K$ provides,

$$R = \left(1 - \frac{B}{\pi A}\right) \sqrt{\frac{\pi K}{2G}},\tag{A.19f}$$

where B/A is proportional to the mass of the core divided by the mass of the planet; this has the same functional form as Eq A.17 and, hence, predicts an almost identical radius.

A.2 Derivation of Compressed Cores

We begin with the definition of a polytrope,

$$P \propto \rho^n.\tag{A.20}$$

Because there is a pressure contribution from the overlying atmosphere, we slightly alter the equation,

$$P + \Delta P \propto \rho^n.\tag{A.21}$$

We make the following substitutions: $P \propto M_c^2/R_c^4$, $\Delta P \propto M_{atm}M_c/R_c^4$, and $\rho \propto M_c/R_c^3$.

We also insert numerical constants in the form of c_i ,

$$\frac{M_c^2}{R_c^4} + c_1 \frac{M_c M_{atm}}{R_c^4} = c_2 \left(\frac{M_c}{R_c^3}\right)^n.\tag{A.22}$$

Solving for R_c gives,

$$R_c = c_3 M_c^{\frac{2-n}{4-3n}} \left(1 + c_4 \frac{M_{atm}}{M_c} \right)^{\frac{1}{4-3n}}, \quad (\text{A.23})$$

where c_3 and n are given by the equations of state from [Zeng et al. \(2016\)](#). c_4 accounts for the compression from the overlying envelope and is given by fitting the models of [Mocquet et al. \(2014\)](#). Therefore,

$$\frac{R_c}{R_\oplus} = \frac{1.07 - 0.21 \cdot f_{Fe}}{(1 + 1.2 \cdot (M_{atm}/M_c))^{0.1}} \cdot \left(\frac{M_c}{M_\oplus} \right)^{1/3.7} \quad (\text{A.24})$$

A.3 Derivation of the Rayleigh Number

Before deriving the Rayleigh number, it is necessary to delineate the conditions required for convection. This being that the convective timescale is less than the diffusive timescale,

$$t_{conv} < t_{diff}. \quad (\text{A.25})$$

The diffusive timescale can be derived by finding the diffusive velocity, which can be found equating the diffusive flux with the heat flux,

$$\frac{\kappa \rho c_p \Delta T}{\delta} = \rho c_p \langle v \Delta T \rangle, \quad (\text{A.26})$$

where κ is the thermal diffusivity, ρ is the density, c_p is the specific heat, ΔT is the temperature contrast, δ is the boundary layer thickness, and v is the velocity of the flow, so,

$$v = \frac{\kappa}{\delta}. \quad (\text{A.27})$$

The timescale is defined as the distance, δ , divided by the velocity,

$$t_{diff} = \frac{\delta^2}{\kappa}. \quad (\text{A.28})$$

The convective timescale is also found by equating Stokes law with the buoyancy force,

$$F_s \approx \eta v \delta, \quad (\text{A.29a})$$

and

$$F_b \approx \rho\alpha\Delta T\delta^3g, \quad (\text{A.29b})$$

hence,

$$v \approx \frac{\rho\alpha\Delta T\delta^2g}{\eta}, \quad (\text{A.29c})$$

so the timescale is,

$$t_{conv} \approx \frac{\eta}{\rho\alpha\Delta T\delta g}. \quad (\text{A.30})$$

Inputting Eq. A.28 and A.30 into Eq. A.25 gives,

$$\frac{\eta}{\rho\alpha\Delta T\delta g} < \frac{\delta^2}{\kappa}, \quad (\text{A.31a})$$

such that,

$$\frac{\rho\alpha\Delta T\delta^3g}{\eta\kappa} > 1. \quad (\text{A.31b})$$

The collection of parameters on the left-hand side is the Rayleigh number. The reason for the number 1 is that numerical constants were not included within the calculation. Careful consideration of the constants (for a Rayleigh-Bénard configuration) would give,

$$\frac{\rho\alpha\Delta T\delta^3g}{\eta\kappa} \gtrsim 1000, \quad (\text{A.32})$$

where the left-hand side is the Rayleigh number, and the right-hand side is the critical value required for convection.

A.4 Classical vs Ultimate Theory of Rayleigh-Bénard Convection

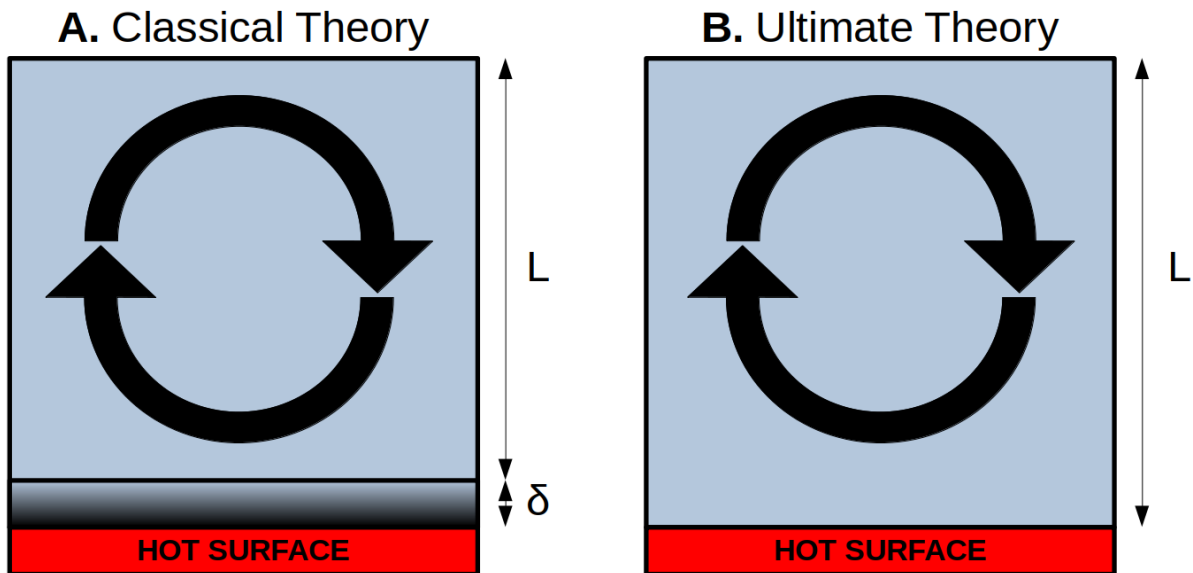


Figure A.1: Not-to-scale cartoon depicting the classical vs. ultimate theory of Rayleigh-Bénard convection. L is the thickness of the convective section, whereas δ is the thickness of the boundary layer.

A.4.1 Classical Derivation

The classical theory of Rayleigh-Bénard convection works under the assumption that there is a thin boundary layer at the bottom of the fluid (see A of Fig. A.1). In this boundary, energy is transported through conduction into the overlying fluid. Using this assumption, the relationship between the Rayleigh number (tells us the fluids flow regime) and the Nusselt number (the ratio of the convective-to-conductive energy flux) is $Nu \propto Ra^{1/3}$. The derivation is as follows:

$$Nu \equiv \frac{F_{conv}}{F_{cond}}, \quad (\text{A.33a})$$

that is,

$$Nu \approx \frac{\rho c_p \Delta T v}{\kappa \rho c_p \Delta T / \delta}, \quad (\text{A.33b})$$

where ρ is the density, c_p is the specific heat, ΔT is the temperature contrast, v is the velocity of convection, κ is the thermal diffusivity. Therefore,

$$Nu \approx \frac{v\delta}{\kappa}. \quad (\text{A.33c})$$

Because the system is in equilibrium, we know that the convective and diffusive timescales are equal so,

$$\frac{L}{v} = \frac{\delta^2}{\kappa}, \quad (\text{A.33d})$$

where the left-hand side is the convective timescale, the right-hand side is the diffusive timescale, and L is the thickness of the convecting system. Solving for δ gives,

$$\delta \sim \left(\frac{L\kappa}{v}\right)^{1/2}, \quad (\text{A.33e})$$

whence,

$$v \sim \frac{L\kappa}{\delta^2}, \quad (\text{A.33f})$$

meaning that,

$$Nu \approx \frac{L}{\delta}, \quad (\text{A.33g})$$

this is a fundamental identity that has many applications in the sciences. We know from the definition of the Rayleigh number that,

$$L \equiv \left(\frac{\eta\kappa}{\rho\alpha\Delta Tg}\right)^{1/3} Ra^{1/3}, \quad (\text{A.33h})$$

that can be inserted into Eq. A.33g,

$$Nu \approx \left(\frac{\eta\kappa}{\rho\alpha\Delta T\delta^3g}\right)^{1/3} Ra^{1/3}. \quad (\text{A.33i})$$

Note that the bracketed term is the inverse Rayleigh number of the bottom boundary. By definition, the bottom boundary is the immediate location below where convection takes place, so its value is roughly the critical value ~ 1000 ,

$$Nu \sim 0.1Ra^{1/3}, \quad (\text{A.33j})$$

and this is the classical relation between the Nusselt number and the Rayleigh number.

A.4.2 Ultimate Derivation

The derivation of the ultimate theory assumes that once the Rayleigh number is large, convection is so turbulent that rising plumes will dominate heat transfer. These plumes will move at velocities close to the buoyancy free-fall limit and will destroy the boundary layers. To derive this relation, we begin by deriving the Nusselt number, but for the entire fluid:

$$Nu \equiv \frac{F_{conv}}{F_{cond}}, \quad (\text{A.34a})$$

such that,

$$Nu \approx \frac{\rho c_p \Delta T v}{\kappa \rho c_p \Delta T / L} \quad (\text{A.34b})$$

where ρ is the density, c_p is the specific heat, ΔT is the temperature contrast, v is the velocity of convection, and κ is the thermal diffusivity. We can therefore simplify the above equation as follows,

$$Nu \approx \frac{vL}{\kappa}. \quad (\text{A.34c})$$

To calculate the velocity, we use Newton's laws of motion,

$$v \approx (\alpha \Delta T g L)^{1/2}, \quad (\text{A.34d})$$

hence,

$$Nu \approx \left(\frac{\alpha \Delta T g L^3}{\kappa^2} \right)^{1/2}, \quad (\text{A.34e})$$

but we know that,

$$L \equiv \left(\frac{\eta \kappa}{\rho \alpha \Delta T g} \right)^{1/3} Ra^{1/3}, \quad (\text{A.34f})$$

so putting this all together gives,

$$Nu \approx \left(\frac{\alpha \Delta T g \eta \kappa}{\rho \alpha \Delta T g \kappa^2} \right)^{1/2} Ra^{1/2}, \quad (\text{A.34g})$$

hence,

$$Nu \approx \left(\frac{\eta}{\rho \kappa} \right)^{1/2} Ra^{1/2}. \quad (\text{A.34h})$$

Assuming that the ultimately convective system is an ideal gas (reasonable, due to the high Ra arising from the low viscosity), then,

$$Nu \sim Ra^{1/2}. \tag{A.34i}$$